Defect Mediated Photoluminescence and Solar Cell from Colloidal I-III-VI Semiconductor Nanocrystals

A thesis
submitted in partial fulfilment of the requirements
for the degree of

Doctor of Philosophy

By

METIKOTI JAGADEESWARARAO

(ID: 20133238)

Indian Institute of Science Education and Research (IISER)-Pune

2018

Dedicated to

My family, Teachers

&

My friends

(Especially to Bendi Bhaskararao)

भारतीय विज्ञान शिक्षा एवं अनुसंधान संस्थान, पुणे
INDIAN INSTITUTE OF SCIENCE EDUCATION AND RESEARCH (IISER) PUNE
(An Autonomous Institution of Ministry of Human Resource Development, Govt. of India)
Dr. Homi Bhabha Road, Pune - 411008.

DECLARATION

I declare that this written submission represents my ideas in my own words and wherever other's ideas have been included; I have adequately cited and referenced the original sources. I also declare that I have adhered to all principles of academic honesty and integrity and have not misrepresented or fabricated or falsified any idea / data / fact / source in my submission. I understand that violation of the above will cause for disciplinary action by the Institute and can also evoke penal action from the sources which have thus not been properly cited or from whom proper permission has not been taken when needed.

Mr. Metikoti Jagadeeswararao
(ID: 20133238)

Date: 11th January 2018

भारतीय विज्ञान शिक्षा एवं अनुसंधान संस्थान, पुणे
INDIAN INSTITUTE OF SCIENCE EDUCATION AND RESEARCH (IISER) PUNE
(An Autonomous Institution of Ministry of Human Resource Development, Govt. of India)
Dr. Homi Bhabha Road, Pune - 411008.

Dr. Angshuman Nag
Assistant Professor
Department of Chemistry,
IISER Pune

CERTIFICATE

Certified that the work incorporated in the thesis entitled "***Defect Mediated Photoluminescence and Solar Cell from Colloidal I-III-VI Semiconductor Nanocrystals***" submitted by **Mr. Metikoti Jagadeeswararao** was carried out by the candidate, under my supervision. The work presented here or any part of it has not been included in any other thesis submitted previously for the award of any degree or diploma from any other university or institution.

Angshuman Nag

Dr. Angshuman Nag
(Research Supervisor)

Date: 11th January 2018

Acknowledgements

First and foremost, I want to express gratitude towards my thesis supervisor Dr. Angshuman Nag for his excellent guidance, care, support, and encouragement. I am very much thankful to him for being his first Ph.D student. I admire him in most of the cases. I am always wondering the way he does data analysis and his thinking at each and every aspect. After I interacted with him during my Ph.D, I must say that, whatever I do in my future his role will be always there because he introduced myself basically what I am and what I can do (potential). He builds confidence in me. One more thing I adopted from him is one should listen to all but you should be able to think which is more appropriate (final decision should come from our side) whether it is science or real life, simply do not follow others unless your wisdom allows you.

I would like to thank my Research Advisory Committee (RAC) members Dr. B. L. V. Prasad and Dr. Nirmalya Ballav for their valuable comments and suggestions during my RAC meetings. I am thankful to Dr. Shouvik Datta, Prof. D. D. Sarma, and Prof. C. N. R. Rao for giving me the opportunity to collaborate with them on various research projects. I am also thankful to Prof. S. B. Ogale for allowing me to use their solar simulator.

I would like to acknowledge Dr. Padmashri Patil, Dr. Sunita Dey and Somnath Pal for fruitful collaboration during my Ph.D. I also owe gratitude to Umesh and Satyawan, for introducing me to carry out solar cell measurements.

I would like to thank faculty members whoever taught in my Ph.D. course work Dr. Angshuman Nag, Dr. Anirban Hazra, Dr. Seema Verma, Dr. Nirmalya Ballav, and others.

I acknowledge all the lab members particularly Kiran, Shiva, Abhishek, Wasim, Bharat, Vikas, Tariq, Dr. Ganesh, and all MS student coworkers Bala Gopal, Nila, Ashutosh and project students for their support. It is being nice interaction with all Ph.D labmates for learning many things from them in terms of discussion and fun I got from everybody that made everyone’s role special to me.

I would like to thank Dr. Pankaj Mondal and Dr. Nirmalya Ballav for giving us space to work in their lab and sitting place during initial period of my Ph.D. It was a good time to learn many things from different group members, Gopal anna, Satish anna, Kiran anna, Ranguwar,

Dinesh, Aravind, Ashok, Mahesh, Barun, Somu, Panchal, Sohini, Plawan. Krishna, Rajkumar, Sandeep, Abhigyan, Dhaneswar, Kavitha, Satish, Arundati, and Tanmay.

I acknowledge FESEM operators Mr. Yathish (special thanks) and Mr. Anil. I am thankful to all the administrative staff, IT, store and purchase people particularly, Nitin, Mahesh Jadhav, Ganesh Dimber, Megha, Mr. Mayuresh, and Mr. Tushar.

I owe special thanks to Gurivi Reddy anna for his crucial help from starting days of my Ph.D. I think he is the first best person ever I met in IISER-Pune. I would like to thank all the Telugu family in IISER and NCL Pune, for their encouragement and support whenever I needed.

I am thankful to the IPL cricket team captains of Nanosoldiers (Gurivi reddy), Resonance (Ravi Raut and Moreswar), Furji (Shammi and Rakesh), and Finex (Saleem) for giving me chance to play in their teams. I am thankful to other friends in IISER, Pune specially Rohit, Panja, and Bagh. I am very much thankful to Rahul, Sourabh, Pramod, Indu, and many others for being my fans as a singer.

I would like to thank all the roommates Nilesh, Nanda kumar, Chennakesava reddy, and Vandana didi for making tasty food for us. I am thankful to Sambu, Tripura for their support.

I am thankful to my friends Khagesh (special thanks), Purushottam, Suresh, Samba, VS, for helping me in terms of discussion for CSIR preparation when we were in Hyderabad. I am thankful to my M.Sc friends Bhaskararao, Durga Prasad, Hari Prasad, Venky, Vasu, Govind, Srinu, Ramarao, Kasim. I miss you so much Bhaskar, I cannot pay back to you the love, care and support you showed me apart from mentioning your name in my thesis. Other close friends Bolla Govindarao, Madhu Babu, Ramu etc.

Last but not least, My all teachers Apparao Sir, Narayanarao Sir, Sailaja Madam, Usha Madam, Sirisha madam, Shobharani Madam, Suryanarayana Sir, R.V.R. Sir, Dr. Vayukumar Sir, Ramesh Sir, Vilasamurthy Sir, K.V.S. Sir, Tagore Sir, Dr. Syambab Sir, and Prof. Ramana Sir and many others who taught us good quality education (at school, college, and University) and inspiring me to reach up to this stage from a small village that too with a poor back ground.

synopsis

This thesis focuses on $AgInS_2$ and $CuInSe_2$ based I-III-VI semiconductor nanocrystals (NCs). Colloidal synthesis of NCs, surface modification, understanding of luminescence, and fabrication of NC sensitized solar cells are the major topics discussed in this thesis. Particular emphasis is on studying how the defect levels, both inside and on the surface of I-III-VI NCs, govern the photophysics and optoelectronic properties. Throughout the thesis, advantages and disadvantages in optoelectronic properties of our NCs have been compared with those of II-VI semiconductor NCs. Some of these I-III-VI semiconductor NCs have the potential to be environment friendly efficient optoelectronic materials, in comparison to Cd and Pb based NCs. At last, the comparison between Ag-based and Cu-based I-III-VI NCs have been made in the outlook and future direction section.

Chapter 1. Introduction: In this chapter, a brief introduction about various topics related to semiconductor NCs have been discussed. Only those topics were chosen which are relevant to this thesis. We have started discussing from basics such as the effect of size on optical properties of II-VI semiconductor NCs through quantum confinement effect. The detrimental effect of surface of NC on photoluminescence (PL) properties and strategies to improve the PL efficiency by making hetero structures are discussed. Tuning optical properties by changing the composition of NC, and Mn doping are discussed. I-III-VI NCs have tunable band gaps in the visible to near infrared region and reasonably small effective masses of charge carriers similar to that of II-VI NCs. But, some of the intrinsic photophysics are different. A detailed comparison between the photophysics and optoelectronic properties of II-VI and I-III-VI semiconductor NCs has been studied. In I-III-VI, luminescence is governed by defects, unlike the band-edge or excitonic emission in II-VI semiconductor NCs. The point defects located inside the NC are more abundant in I-III-VI NCs compared to II-VI NCs. Finally we have discussed the scope of my thesis work, where the effect of defects on luminescence and solar cell properties of $AgInS_2$ and $CuInSe_2$ based I-III-VI NCs have been studied and optimized for better performance. Moreover, we have discussed the principles of quantum dot sensitized solar cell, and photocatalytic H_2 evolution.

Chapter 2: Origin of Photoluminescence in $AgInS_2$ Nanocrystals: In this chapter, we have studied the origin of PL in $AgInS_2$ NCs. Bulk $AgInS_2$ has a band gap of ~2 eV. $AgInS_2$ NCs absorbs visible light and exhibit reasonably high PL quantum yield. However, the understanding of photophysics is far from being complete. For example, $AgInS_2$ NCs exhibit

>300 meV (~100 nm) broad PL with large Stoke's shift (200-300 meV) compared to absorption spectrum. In prior literature, this broad PL has been assigned to transitions between localised states (Donor-Acceptor (D-A)) within the band gap with PL lifetime >250 ns. However, D-A model could not explain the size dependent shift in PL peak by 0.35 eV. In order to understand the origin of PL in $AgInS_2$ NCs, we have prepared $(ZnS)_{1-x}(AgInS_2)_x$ alloy NCs keeping size of all the samples constant ~5 nm. This constant size allows us to assume that the D-A distance is similar in all the samples. These NCs show a shift in PL peak by 0.57 eV for x = 1 to 0.33, which cannot be explained by D-A model. Interestingly, the shift in PL of alloy NCs is similar to shift in their optical band gap. PL decay profile of these NCs show two radiative lifetimes ~25 ns and ~250 ns. We have assigned these two radiative lifetimes to two paths. Path-1 corresponds to ~25 ns lifetime where at least one delocalised state (conduction band (CB) or valance band (VB)) is involved in the PL. Path-2 correspond to ~250 ns lifetime, in which localised (D-A) states are involved. Moreover, for x = 0.33 composition, the contribution from path-2 decreased significantly, with path-1 being the major contributor. Therefore, we concluded that, the PL in $AgInS_2$ NCs is originating from the contribution of at least one delocalised state (CB/VB) along with D-A states. Typically, participation of such delocalized states lead to efficient charge transfer from NC to electron and/or hole acceptors in solar cells and other photocatalytic processes.

Chapter 3. Synthesis of Organic-Free $AgInS_2$ and Other Metal Sulfide Nanocrystals for Solar Cell: In this chapter, we have synthesized organic-free $AgInS_2$ NCs along with with other organic-free CdS, ZnS, $Zn_{1-x}Cd_xS$, and Mn-doped $Zn_{1-x}Cd_xS$ NCs. Quantum dot sensitized solar cell (QDSSC) using organic-free $AgInS_2$ NCs has also been prepared. Typically, colloidal NCs are capped with long hydrocarbon ligand. Such insulating ligands inhibit the charge transfer from NC to TiO_2 resulting into poor photoconversion efficiency (PCE). In order to overcome this problem, we have synthesized organic-free $AgInS_2$ NCs for the first time using a direct method that does not require post-synthesis surface modification. To establish and understand the synthesis, initially we prepared simpler metal sulfide like CdS NCs. Then the generic nature of the synthesis protocol was verified by preparing variety of other metal sulfide NCs, including $AgInS_2$ NCs. The essential parameter for the preparation of stable organic-free $AgInS_2$ NCs (and other metal sulfides) is their non-stoichiometric surface. Excess sulphur on the surface provides negative charge to these NCs and get stabilised by electrostatic repulsive forces among NCs in polar solvents. We made QDSSC with organic-free $AgInS_2$ NCs. Our best solar cell shows better PCE (0.8%),

compared with prior report of organic cap $AgInS_2$ NCs (0.06%). However, the obtained PCE from organic-free $AgInS_2$ NCs is still far behind than that of II-VI based NCs. This is because of both insufficient absorption of near infrared solar light and high defect density in $AgInS_2$ NCs. The advantage of our organic-free NCs is better charge transfer at device interface, but these NCs suffer from higher level of defect density compared to organic capped NCs.

Chapter 4. Photoluminescence and Solar Cell from Ag_2S-$AgInS_2$ Hetero Dimer Nanocrystals: In this chapter, we have prepared oleylamine capped Ag_2S-$AgInS_2$ hetero dimer NCs (HDNCs) in order to absorb both visible and near infrared (NIR) light, and to explore the possibility of nanoscale p-n junction at Ag_2S-$AgInS_2$ interface. In Ag_2S-$AgInS_2$ HDNCs, $AgInS_2$ can act as n-type semiconductor and Ag_2S may act as p-type semiconductor. However, cyclic voltammetry (CV) results indicate that the band alignment is type-I at the Ag_2S-$AgInS_2$ interface. Steady state PL of Ag_2S-$AgInS_2$ HDNCs show peak at a lower energy than that of $AgInS_2$ NCs and at a higher energy than that of Ag_2S band gap. This suggests that mid-gap defects are responsible for PL in Ag_2S-$AgInS_2$ HDNCs. Interestingly Ag_2S-$AgInS_2$ HDNCs show 13 μs long PL lifetime suggesting effective electron hole separation, similar to type-II band alignment. Such defect mediated type-II alignment or possibility of p-n junction can also be beneficial for solar cell applications. Therefore, we have fabricated QDSSC using Ag_2S-$AgInS_2$ HDNCs along with $AgInS_2$ NCs for a comparative study. The obtained PCE from Ag_2S-$AgInS_2$ HDNCs and $AgInS_2$ NCs (different fabrication from chapter 3) stands at 1.3% and 0.4% with external quantum efficiency (EQE) of 25% and 10% at 500 nm, respectively. Indeed, the improvement in PCE of Ag_2S-$AgInS_2$ HDNCs compared to $AgInS_2$ NCs indicates that the defect mediated electron hole separation helps in achieving higher PCE. However, the obtained PCE values from Ag_2S-$AgInS_2$ HDNCs are still low. This is due to the fact that the EQE spectrum showed no photocurrent in NIR region corresponding to Ag_2S, which is a consequence of conduction band minimum (CBM) of Ag_2S is lower in energy than that of TiO_2. This improper band alignment of Ag_2S with respect to TiO_2 does not allow the electron injection from Ag_2S to TiO_2.

Chapter 5. Colloidal $CuInSe_2$ Based Nanocrystals for Solar Cell: In this chapter we have fabricated $CuInSe_2$ based NC sensitized solar cell. To circumvent the problem, which rose in Ag_2S-$AgInS_2$ HDNC sensitized solar cell (chapter 4), oleylamine capped $CuInSe_2$ based NCs have been prepared. $CuInSe_2$ NCs absorbs from visible to NIR region along with suitable band alignment with respect to TiO_2. However, as prepared $CuInSe_2$ NCs show PL with less efficiency, which is not a good indicator for solar cell applications. In order to

enhance the PL efficiency, we have extended our synthesis to other compositions like $(Zn)_{0.24}(CuIn)_{0.76}Se_2$ and $(Zn)_{0.42}(CuIn)_{0.58}Se_2$ NCs. Among these, $(Zn)_{0.24}(CuIn)_{0.76}Se_2$ NCs with optical band gap of 1.5 eV show the highest PL intensity. Therefore, $(Zn)_{0.24}(CuIn)_{0.76}Se_2$ NCs were chosen for making of QDSSC. Surface of $(Zn)_{0.24}(CuIn)_{0.76}Se_2$ NCs were modified from oleylamine to mercapto propanoic acid capped NCs. This facilitates both NC loading and injection of photo-generated electrons from NC to TiO_2. In order to reduce the recombinations at NC sensitised TiO_2 electrodes (photoanode) and electrolyte interface, photoanode was treated with 8 cycles of ZnS by employing successive ionic layer adsorption and reaction (SILAR). Using these photoanodes, we achieved PCE 3.6% using Cu_2S as a counter electrode.

Appendix. Visible Light Induced Hydrogen Generation Using Colloidal $(ZnS)_{0.4}(AgInS2)_{0.6}$ Nanocrystals Capped by S^{2-} Ions: In this appendix we have used S^{2-} capped $(ZnS)_{0.4}(AgInS_2)_{0.6}$ NCs (discussed in chapter 2) for visible light driven H_2 generation owing to their suitable band gap and band alignment. Here, we have modified the surface of $(ZnS)_{0.4}(AgInS2)_{0.6}$ NCs from oleylamine to S^{2-} capped. S^{2-} capping helps in better charge extraction and injection at the NC surface, along with dispersion of NCs in water medium, required for reduction of H^+ to H_2. A high activity of 5.0 $mmolg^{-1}h^{-1}$ is achieved using S^{2-} capped $(ZnS)_{0.4}(AgInS2)_{0.6}$ NCs as photocatalyst without using any co-catalyst.

Contents

List of Abbreviations

QDs: Quantum dots

NCs: Nanocrystals

CB: Conduction band

CBM: Conduction band minimum

VBM: Valance band maximum

VB: Valance band

EQE: External quantum efficiency

CV: Cyclic voltammetry

PL QY: Photoluminescence quantum yield

TCSPC: Time correlated single photon counting

QDSSC: Quantum dot sensitized solar cell

D-A: Donor-Acceptor

NIR: Near infrared

SILAR: Successive ionic layer adsorption and reaction

FWHM: Full width at half maximum

MPA: 3-Mercaptopropionic acid

SAED: Selected area electron diffraction

TEM: Transmission electron microscopy

HRTEM: High resolution transmission electron microscopy

FESEM: Field emission scanning electron microscopy

EDS: Energy dispersive X-ray spectroscopy

XRD: Powder X-ray diffraction

STEM - ADF: Scanning transmission electron microscope - annular dark field

STS: Scanning tunnelling spectroscopy

DPP: Diphenyl phosphine

DDT: Dodecane thiol

DDAB: Didecyldimethylammonium bromide

FFT: Fast fourier transform

TGA: Thermogravimetric analysis

FTIR: Fourier-transform infrared

FA: Formamide

FET: Filed effect transistor

J_{sc} : Short circuit current density

V_{oc}: Open circuit voltage

FF: Fill factor

PCE: Photo conversion efficiency

HDNCs: Hetero dimer nanocrystals

DDTC: Sodium diethyldithiocarbamate

RB: Round bottom

ODE: 1-octadecene

RPM - Rotation per minute

TBAP: Tetrabutyl ammonium perchlorate

NHE: Normal hydrogen electrode

FTO: F-doped SnO_2

MEG: Multiple exciton generation

TOF: Turn over frequency

TON: Turn over number

AQY: Apparent quantum yield

FRET: Forster resonance energy transfer

LSCs: Luminescent solar concentrators

LED: Light emitting diode

Chapter 1
Introduction

Semiconductor nanocrystals (NCs) are tiny crystalline particles at the nanoscale regime (less than 100 nm in diameter). Typically, semiconductor NCs exhibit fascinating properties compared to their bulk counterparts. One of such property is tuning the band gap by changing the size of NC within quantum confinement regime.[1] These NCs exhibit high absorption coefficient values and result into high photoluminescence quantum yield (PL QY). Consequently, NCs have been used in various applications such as light emitting diode (LED), lasing, bio-imaging, photodetector, photocatalysis, and solar cell.[2-7] Furthermore, NCs show multiple exciton generation (MEG) where using one photon more than one exciton can be formed. Thus, using NCs, there is a theoretical possibility to achieve higher solar cell efficiency than the Shockley-Queisser limit.[8] In addition to all these interesting properties, solution processability of NCs enables the NC based devices cost-effective along with ease of processing.[9]

Research in the field of nanoscience was started in early 1980s by few pioneers such as Ekimov,[10] Hanglein,[11] Efros,[12] and Brus.[13] Since then, researchers are finding ways to synthesize high quality nanomaterials and investigating their photophysical properties. 30 years of research on semiconductors lead to commercial applications of semiconductor NCs. For example, Sony Company in 2013 announced the incorporation of semiconductor NCs in television technology for high definition display.[14]

Since last three decades, researchers have explored different compound semiconductor NCs such as group II(Zn, Cd, Hg)-VI (S, Se), IV (Pb)-VI (S, Se) and III (In, Ga)-V (P, As). These NCs showed promising applications in opical and opto-electronic properties.[15-18] However, the toxicity of Cd and Pb is a concern. Later, group I (Cu, Ag)-III (In, Ga)-VI (S, Se) semiconductor NCs have emerged as potential alternative to II-VI NCs due to the following reasons. I-III-VI semiconductors are analogues to II-VI in terms of their crystal structure. The band gap can be tuned in the visible to near infrared (NIR) region and these semiconductors have high (10^5 cm^{-1}) absorption coefficient values and high PL QY (>50%).[19] Moreover, the small effective masses of charge carriers of I-III-VI semiconductors may lead to high carrier mobility, which is an essential parameter for opto-electronic applications. Thus, being environmentally benign nature I-III-VI based semiconductors are an interesting system for opto-electronic applications.[7]

My thesis work is on synthesis, photophysics, solar cell and photo-catalytic applications of I-III-VI semiconductor NCs. Particularly, we worked on $AgInS_2$ and $CuInSe_2$ based NCs. In

the subsequent sections of this chapter 1 will discuss a few topics of semiconductor NCs that are relevant to my research area followed by discussion on the scope of my thesis work.

1.1 Effect of nanocrystal size on optical properties

Bulk semiconductors contain a forbidden energy gap between valance band maximum (VBM) and conduction band minimum (CBM), known as the band gap. When a semiconductor absorbs a photon with energy greater than or equal to band gap, an electron get promoted to the conduction band (CB) leaving behind a hole in the valance band (VB) as shown by the Figure 1.1.

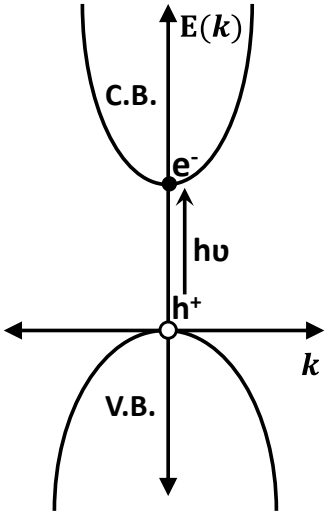

Figure 1.1: Schematic of energy-momentum (*E-k*) diagram of a bulk semiconductor, representing electron at the conduction band minimum and hole at the valance band maximum which was created by photo-excitation.

Coulombic attraction force between electron and hole leads to the formation of electron-hole pair termed as exciton. This electron-hole pair can be treated as analogous to a simple Hydrogen atom model where electron and proton are bound to each other by Coulombic forces. The distance between the electron and proton in the Hydrogen atom is known as Bohr radius (a_o) whereas the distance between electron and hole in a bulk semiconductor is called Bohr exciton radius (a_B). It can be calculated using the following equation.

$$a_B = \frac{\hbar^2 \varepsilon}{\mu e^2} \tag{1.1}$$

Where ε dielectric constant of the material, μ reduced mass of electron and hole, and e is charge of an electron. Typically, high dielectric constant of semiconductors leads to larger Bohr exciton radius for semiconductors than that of Bohr radius of Hydrogen atom (0.529 Å).

In other words, the binding energy of electron-hole pair in a bulk semiconductor is lesser than the binding energy of electron and proton in a Hydrogen atom.

Interestingly, when the size (radius) of the bulk semiconductor is smaller than that of Bohr exciton radius of a particular semiconductor, then the charge carriers become spatially confined. Consequently, following changes takes place relative to bulk semiconductor; i) band gap increases, ii) continuum energy levels become discrete atomic like energy levels in the electronic band structure as shown in Figure 1.2, and iii) increase in the transition probability for absorption and emission across the optical band gap. This phenomenon is known as the quantum confinement effect.[20] Usually, the Bohr exciton radius for different semiconductors is in the range of 2-50 nm. Semiconductor NCs which exhibit confinement effect in all three dimensions are called quantum dots (QDs). The band gap of a QD can be calculated by following the Brus and Kayanuma equation based on the effective mass approximation model.[21,22,23]

$$E_{g(QD)} = E_{bulk} + \frac{h^2}{8R^2}\left(\frac{1}{m_e^*} + \frac{1}{m_h^*}\right) - \frac{1.786e^2}{4\pi\varepsilon_o\varepsilon_r R} - 0.248\left(E_{Ry}^*\right) \qquad (1.2)$$

where h- Plank`s constant

R- radius of the QD

m_e^*- effective mass of excited electron

m_h^* - effective mass of excited hole

ε_o- permittivity of vacuum

ε_r- relative permittivity

E_{Ry}^*- Rydberg energy

First term of the right side of equation 1.2 represents the band gap of a bulk semiconductor, which is fixed for a particular material at a given temperature. Second term is the additional energy because of quantum confinement effect, in which energy is inversely proportional to both R^2 and effective masses of charge carriers. Therefore, change in the size of a QD results in a considerable shift in the band gap. Third term corresponds to the Coulombic attraction between electron and hole (excitonic binding energy) with dependence of 1/R. Therefore, excitonic binding energy of NCs are greater than the corresponding bulk semiconductor. Higher excitonic binding energy increases both the cross section of light absorption and PL QY of NCs compared to bulk semiconductors.[1, 24] The last term in the equation 1.2

corresponds to spatial correlation effect which is significant only in the case of low dielectric constant materials. Often, the band gap of a QD is governed by the first two terms in the right side of equation 1.2.

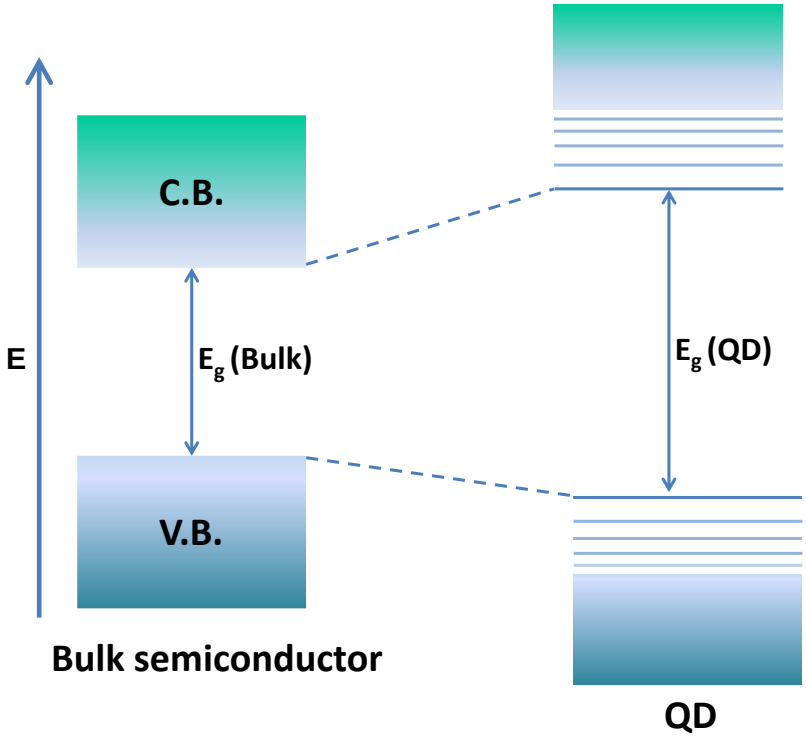

Figure 1.2: Schematic representation of flat band diagram for bulk semiconductor (left) and QD (right).

Figure 1.3a-b shows absorption and PL spectra for different sizes of CdSe NCs. The Bohr exciton radius of CdSe is ~6 nm.[1] Therefore, CdSe NCs with size less than its Bohr exciton diameter show quantum confinement effect. In Figure 1.3a, 20 nm sized CdSe NCs show optical band gap ~700 nm, similar to that of bulk CdSe (band gap of bulk CdSe is 712 nm). On the other hand, the absorption spectra for NCs with size less than 7.3 nm show blue shift in band gap compared to the band gap of bulk CdSe. Thus, the optical band gap of CdSe NCs can be tuned in the entire visible range by controlling the size of NCs. Absorption of a photon results in the formation of an electron-hole pair, if the electron and hole recombination takes place via radiative pathway then it gives emission of photon. Thus, different sized NCs with different optical band gap emit lights of different colours under the quantum confinement region. Therefore, the PL also can be tuned throughout the entire visible range by controlling the size of NCs. Figure 1.3b shows the PL tunability of different sizes of CdSe NCs.[25] CdSe NCs exhibit PL with small (<100 meV) Stoke's shift with respect to the corresponding

excitonic absorption. Such a PL is called excitonic or band-edge emission with a full width at half maximum (FWHM) 25-35 nm.

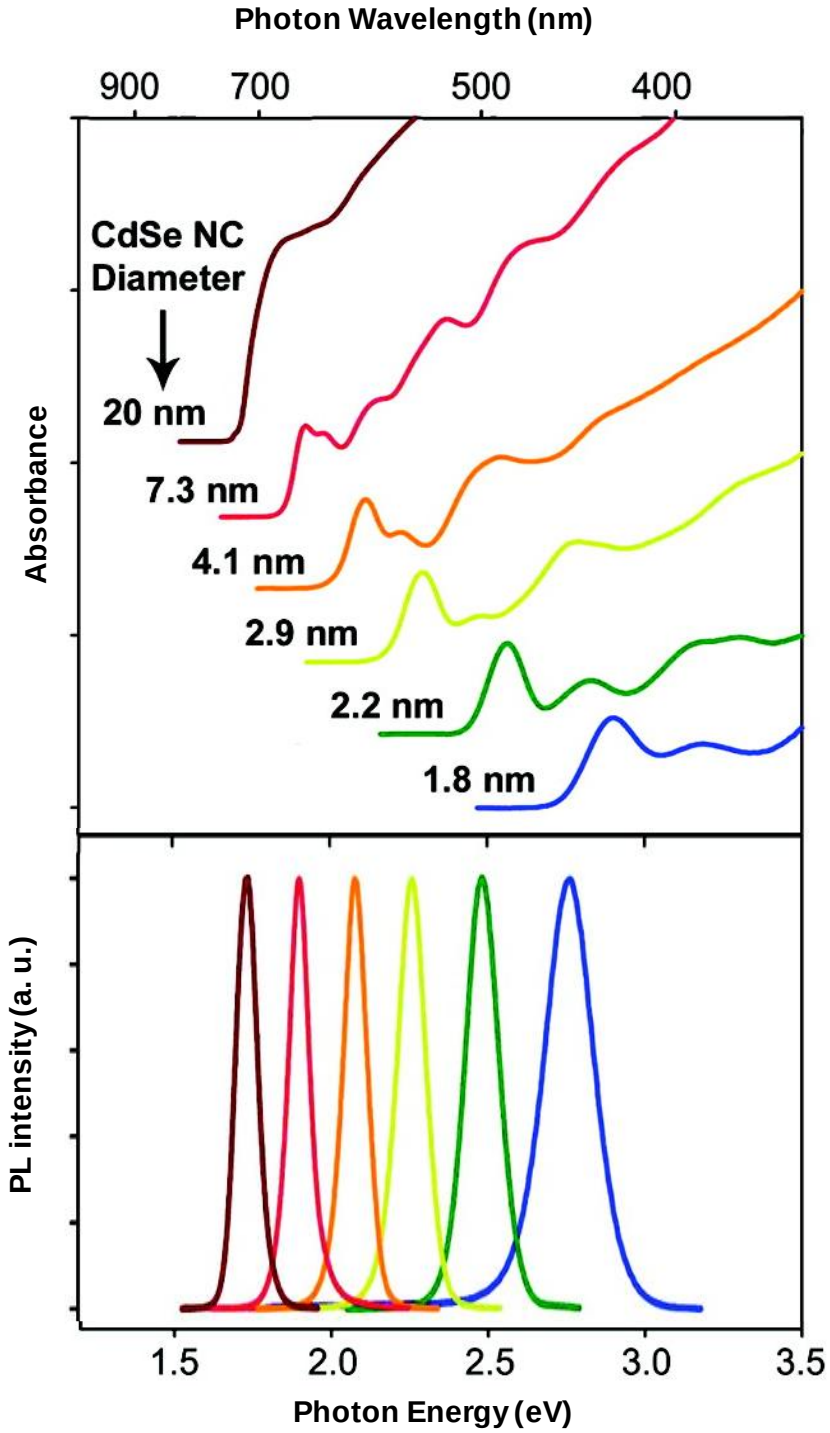

Figure 1.3: (a) Absorption spectra of different sizes of CdSe NCs, and (b) the corresponding photoluminescence of CdSe NCs showing quantum confinement effect. Reprinted with permission from ref.[25] Copy right @ 2010, American Chemical Society.

1.2 Effect of surface of nanocrystal on optical properties

Optical properties such as band gap and PL depend mainly on the core of the NC. For example, size dependent optical properties due to quantum confinement effect. However, as the size of the NC decreases the contribution from NC surface increases, which can also influence the optical properties. Surface of a crystal means the termination of periodic arrangement of atoms, so it can be considered as defects. Atoms present on the surface are left-off with unsaturated chemical bonds known as dangling bonds.[26] Often, these dangling bonds give rise to energy states within the conduction band minimum (CBM) and valance band maximum (VBM) of NC. Such kinds of defect states act as traps for charge carriers at the surface, thereby increasing the non-radiative decay of excitons reducing the PL QY.[25, 27] In order to passivate these dangling bonds on the surface of NCs, basic ligands with long hydrocarbon chain (organic capping) are typically used during synthesis of NCs. These ligands bind with cations at the surface of NCs as shown in Figure 1.4a for CdSe NCs. Thus, organic capping have the potential to remove Cd dangling bonds (electron traps) from the intra band gap region.[25] However, organic capping is ineffective in removing Se dangling bonds (hole traps).[28] For example, very small (2.1 nm) organic capped CdSe NCs often show two kinds of PL: one due to excitonic recombination, and the other due to recombination at sub band gap defect sites located on the surface shown by Figure 1.4b. However, addition of excess Cd^{2+} ions to the above sample can passivate some of the Se dangling bonds yielding cationic surfaces that can strongly bind to organic ligands. Figure 1.4b shows only single PL peak corresponds to band edge emission after treating with Cd^{2+} ions suppressing the hole trap emission at lower energy. Furthermore, organic capping provides stability to NCs in non-polar solvents through hydrophobic interactions with the alkyl chain on the ligands.[29]

However, it is not possible to passivate all kinds of trap states by organic capping ligands, because it depends on the nature of the passivating ligands[30-31] and the steric hindrance of long alkyl chain.[27] These residual traps results in reducing the PL QY. This problem can be largely overcome by making an inorganic shell of another semiconductor on top of the core part of a NC, which lead to the formation of hetero structured (core/shell) NCs.

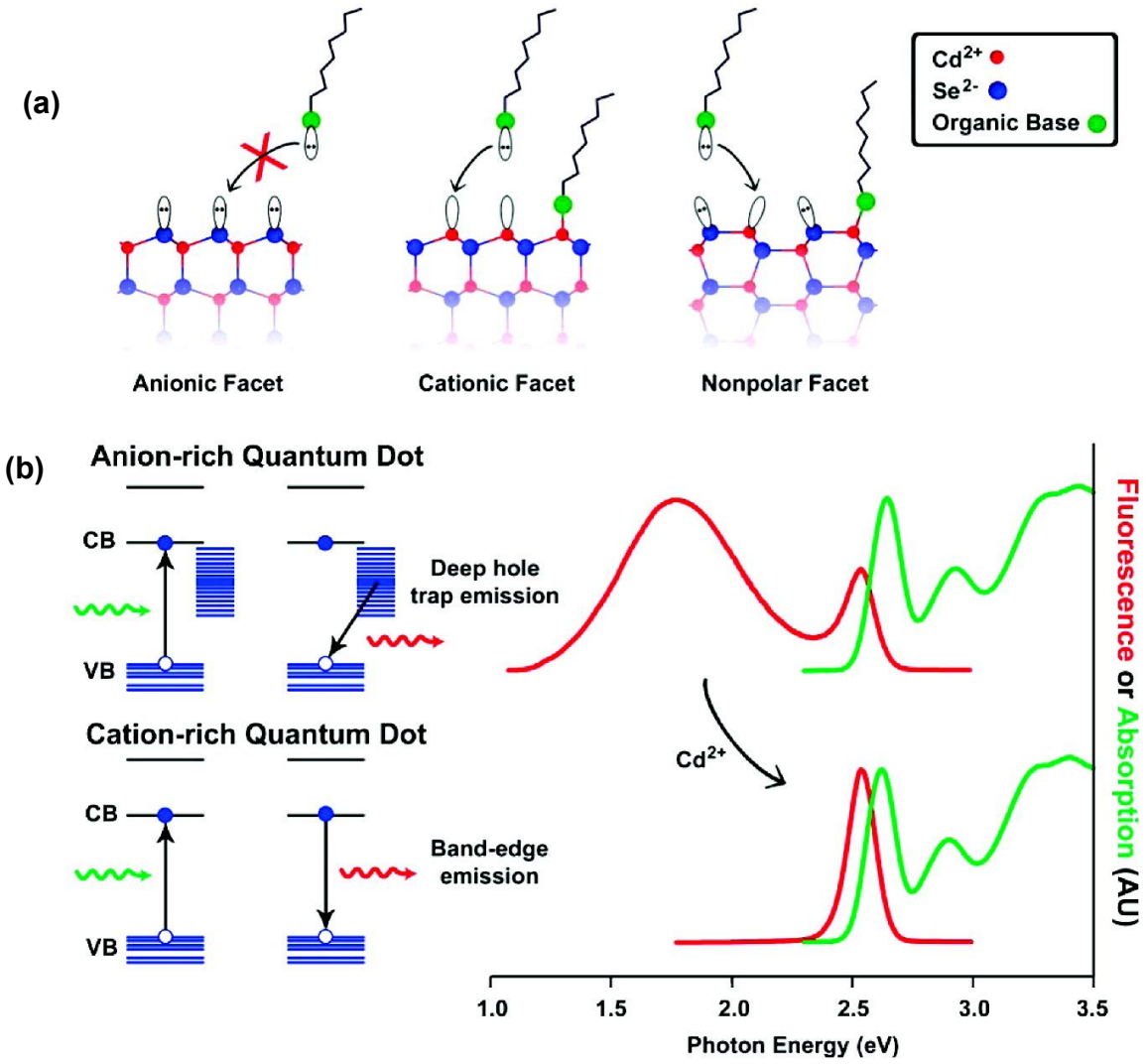

Figure 1.4: Surface properties of CdSe NCs. (a) Illustrates the terminal dangling orbitals on different types of facets. (b) Schematic representation (left) showing the effects of surface hole traps on the photoluminescence spectra (right) of small 2.1 nm NCs. Reprinted with permission from ref.[25] Copy right @ 2010, American Chemical Society.

1.3 Tunability of optical properties by making hetero-structured nanocrystals

In order to overcome the surface defects which are energetically located within the mid-gap region, researchers developed hetero structured NCs. In a hetero structured NC more than one kind of inorganic part is present. The most popular variety of hetero structured NCs is core/shell NCs, where the core and shell materials are formed by different inorganic semiconductors. Depending on the band gaps and the relative band edge positions of the involved semiconductors, these core/shell materials are mainly classified into type-I, inverse

type-I, type-II and quasi type-II structures. The classification is depicted in the scheme shown in Figure 1.5.

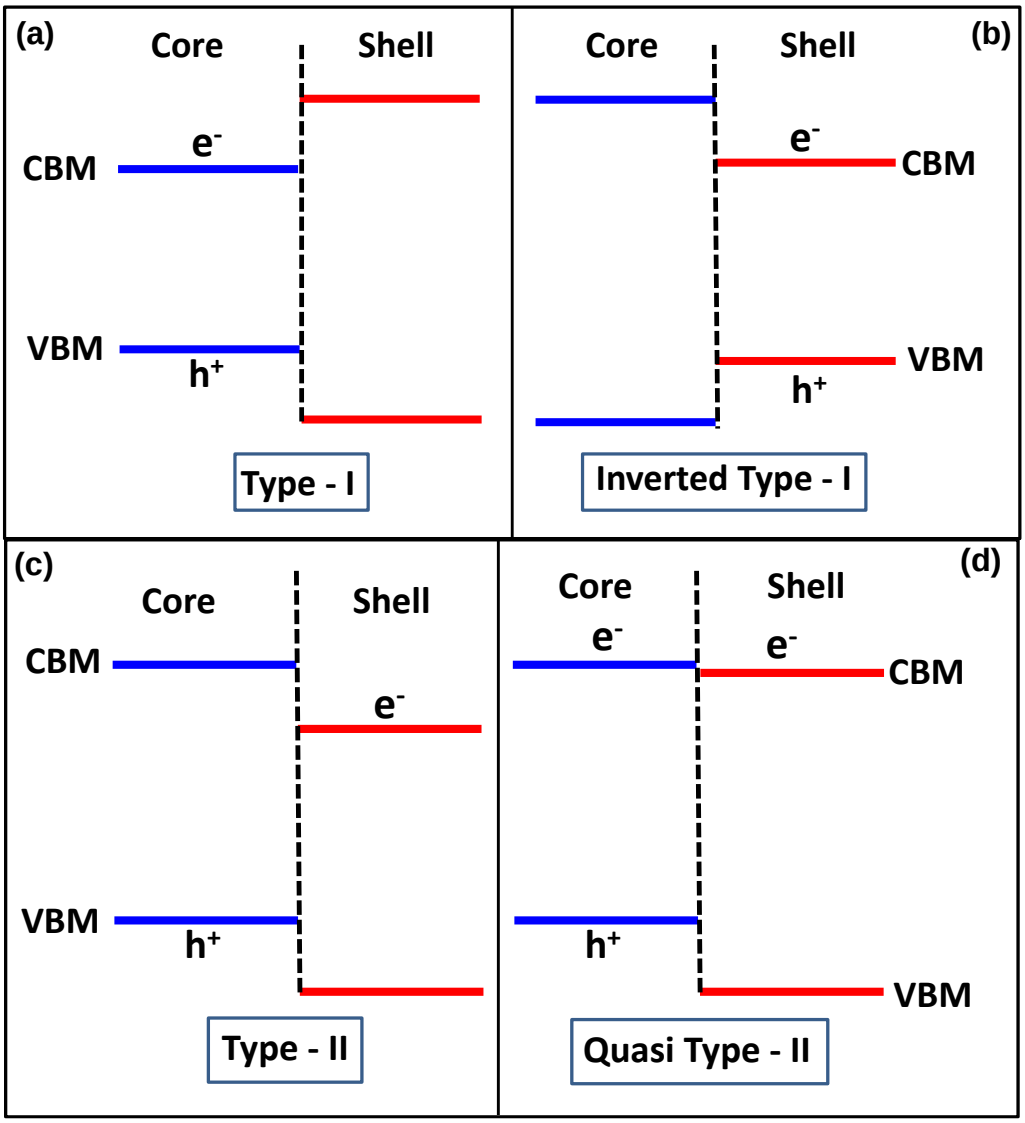

Figure 1.5: Band alignment of (a) type-I, (b) inverse type-I, (c) type-II and (d) quasi type-II core/shell NCs and (a, b, c, and d) representing the localisation of electron and hole in the respective VBM or CBM after excitation.

In type-I core/shell NCs, band gap of shell material is larger than that of the core and CBM and VBM of core have higher and lower energies respectively, with respect to the CBM and VBM of shell material as shown in Figure 1.5a. Thus, the non-radiative states arising from dangling bonds on the surface of core part are passivated. On the other hand, both the electron and hole are confined in the core part, because both kinds of carriers have large energy barriers to transfer from core to shell part. Therefore, photogenerated electron and hole are spatially isolated from non-radiative defects located on the surface of shell material,

enhancing the PL efficiency. CdSe/ZnS and CdSe/ZnSe NCs are the examples for type-I core/shell NCs,[32,33] in which electron and hole both are confined in CdSe core part. Thus, ZnS shell on CdSe NCs enhances the PL QY from <5% to 50%.[34] In type-I systems, radiative recombination of electron and hole takes place with PL lifetime ~20 ns similar to that of core only NC. Shell growth leads to a small red shift in both excitonic absorption and the PL peak position. This small red-shift in absorption and PL can be attributed to the partial leakage of charge carriers into the shell material.

In inverse type-I core/shell NCs the CBM and VBM of shell material lies within the band gap of core part as shown by the figure 1.5b. As a result, electron and hole wave functions are confined to shell material, and the emission takes place in shell material. CdS/CdSe,[35] and ZnSe/CdSe[36] core/shell NCs exhibit inverse type-I band alignment, in which by tuning shell thickness one can tune the emission wavelength in the broad range. In order to enhance PL QY and photostability of CdS/CdSe core/shell NCs another shell with wide band gap is coated on these NCs. These, CdS/CdSe/CdS NCs exhibit PL QYs over 40%. Therefore, this kind of band alignment is good for LED application because of the effective radiative recombination of electron- hole pair can lead to high intensity emitting diodes.[36-38]

In type-II core/shell NCs, one of the charge carrier is located in the core and the other one is located in the shell material. Figure 1.5c shows one possibility where VBM and CBM of core are higher in energy compared to VBM and CBM of shell material, respectively. Similarly, VBM and CBM of core material can also be of lower energies than the CBM and VBM of shell material, respectively. Due to this band alignment, electron (hole) confined to core (shell) or vice versa, which leads to reduction in the spatial overlap between electron and hole wavefunction. Consequently, the transition probability of radiative recombination of electron and hole reduces resulting into long PL lifetime (~1 μs).[39] The long excited state lifetime of type-II core/shell NCs helps collection of charge carriers from type-II systems, enabling them in solar cell application.[40-41] CdSe/ZnTe,[40] CdTe/CdSe,[42] CdSe/CdTe,[39] and CdTe/CdS[43] are the examples for type-II core/shell NCs. If there is small energy barrier between CBM of core and shell material as shown in the Figure 1.5d, then electrons can delocalise in both core and shell material whereas hole remains confined in core material. This kind of band alignment is called quasi type-II alignment. CdTe/CdSe Core/Shell NCs is an example for quasi type-II core/shell NCs. Hetero structures with quasi type-II band alignment also can be used for solar cell application. However, type-II systems are preferable.[44]

1.4 Effect of composition on optical properties of semiconductor nanocrystals

In section 1.1 it was discussed that the band gap engineering can be done by changing the size of the NCs. However, very smaller size of NCs prepared to exhibit PL in the higher energy range of visible spectrum suffer from problems of large density of surface defects (as a consequence of high surface to volume ratio) leading to lower PL QY.[45] One can overcome this issue by changing the composition of NCs, where band gap can be increased with composition without decreasing the size of NCs. Therefore, making a solid solution with higher band gap semiconductor allows us tuning of band gap while maintaining high PL QY.

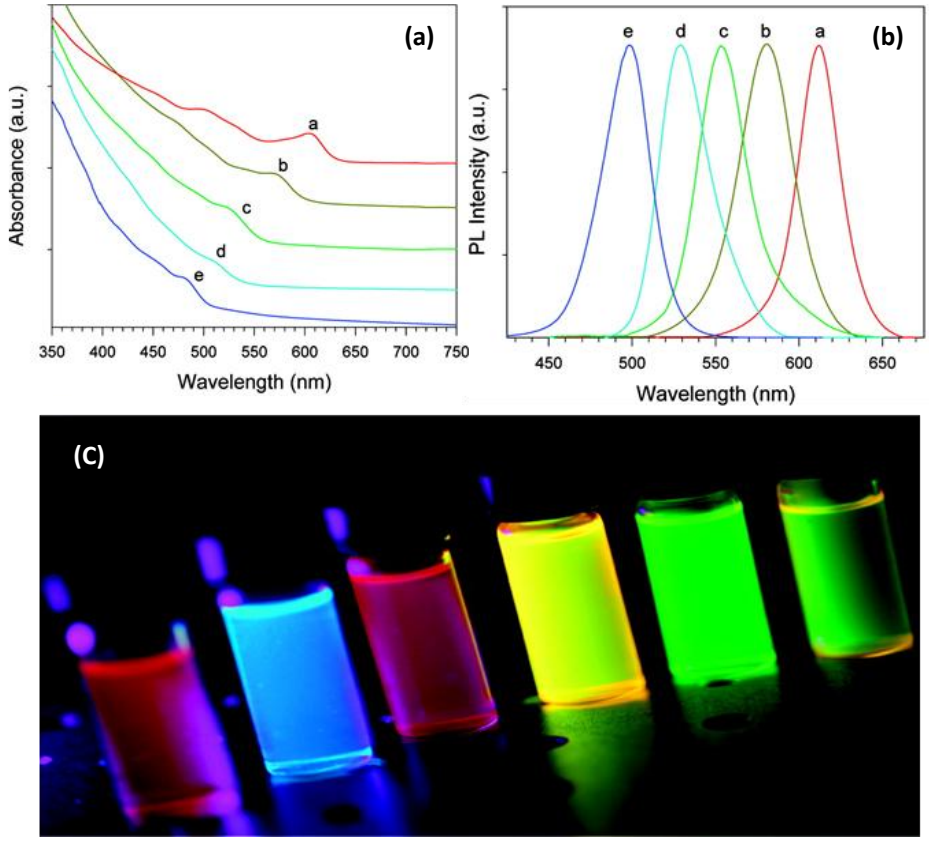

Figure1.6: a) Absorption b) emission spectra of $Zn_xCd_{1-x}Se$ NCs with Zn mole fractions of a (0), b (0.28), c (0.44), d (0.55) and e (0.67). c) Photograph of composition tunable emission-color of alloy $Zn_xCd_{1-x}Se$ NCs under UV light. Reprinted with permission from ref.[45] Copyright 2010, American Chemical Society.

Figure 1.6 shows that the band gap can be tuned from blue to the red region of visible spectra by making an alloy of CdSe and ZnSe. For this, CdSe NCs were synthesized first by hot injection technique followed by the addition of Zn and Se precursors to the synthesized CdSe NCs at a high temperature (~300 ^{o}C).[46] The amount of Zn and Se mole fractions can be

varied in the reaction mixture to prepare different compositions of $Zn_xCd_{1-x}Se$ NCs. Figure 1.6a-b show the corresponding change in the absorption and emission for $Zn_xCd_{1-x}Se$ NCs with Zn mole fractions 0. 0.28, 0.44, 0.55, and 0.67. By increasing the Zn mole fraction from 0 to 0.67 in $Zn_xCd_{1-x}Se$ NCs, both the excitonic absorption and PL peaks were shifted by ~120 nm. Also, the excitonic peak in the absorption spectra got broadened with increasing Zn content. Figure 1.6c shows photographs of composition-tunable emission of $Zn_xCd_{1-x}Se$ alloy NCs across the visible spectral window. It is clear that the systematic shift in the absorption onset and PL peak maxima is indicating the formation of a $Zn_xCd_{1-x}Se$ solid solution, rather than the formation of separate individual NCs of CdSe and ZnSe or hetero structures such as core-shell (CdSe/ZnSe). Thus, the optical properties can be tuned by changing the composition of the NCs.

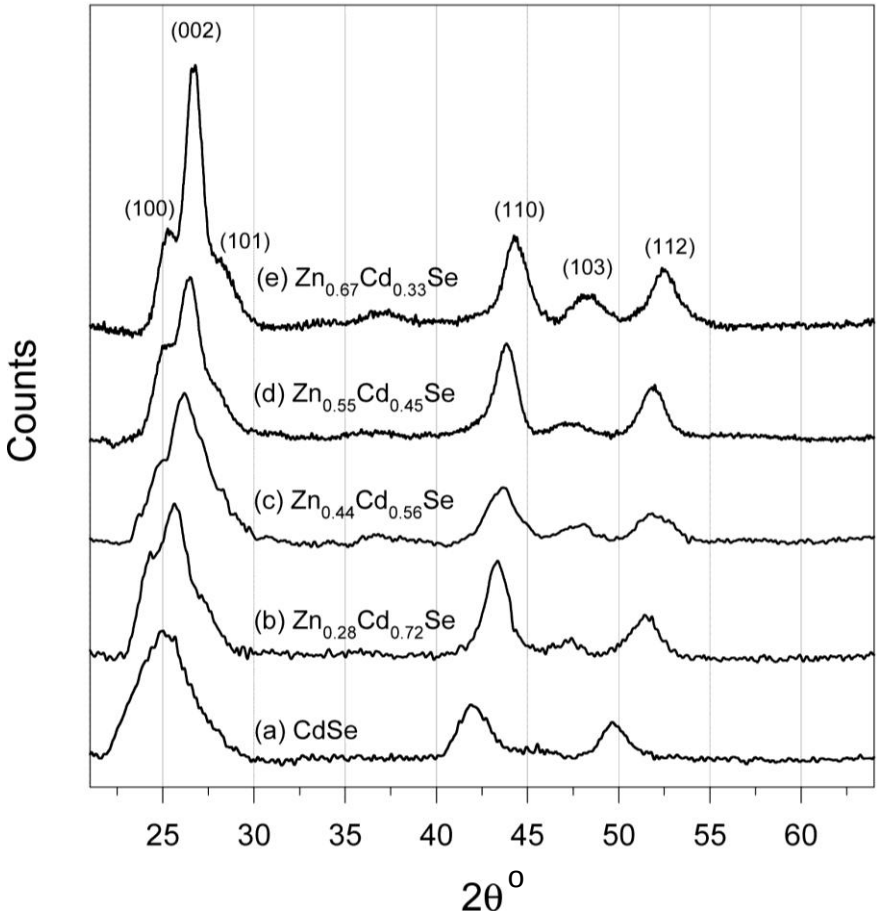

Figure1.7: Powder X-ray diffraction patterns of $Zn_xCd_{1-x}Se$ NCs with different Zn mole fractions of (a) 0, (b) 0.28, (c) 0.44, (d) 0.55, and (e) 0.67. Reprinted with permission from ref.[45] Copyright 2010, American Chemical Society.

Figure 1.7 shows the powder X-ray diffraction (XRD) pattern of $Zn_xCd_{1-x}Se$ NCs. An increase in the Zn content in CdSe NCs shifts XRD peaks to higher 2Θ values. This is because of the contraction of lattice parameter with incorporation of Zn. Further, change in inter planar spacing with Zn concentration follows the Vegard's law suggesting homogeneous alloy formation. This ruled out the possibility of forming impurity phases corresponding to CdSe and ZnSe separately.

The alloy of CdSe and ZnSe formation takes place by two step processes. Initially there is formation of core/shell NCs of CdSe/ZnSe with the addition of ZnSe to CdSe. Then further increase in the temperature leads to the diffusion of Zn^{2+} cations into the CdSe matrix resulting in the formation of $Zn_xCd_{1-x}Se$ alloy NCs.[47]

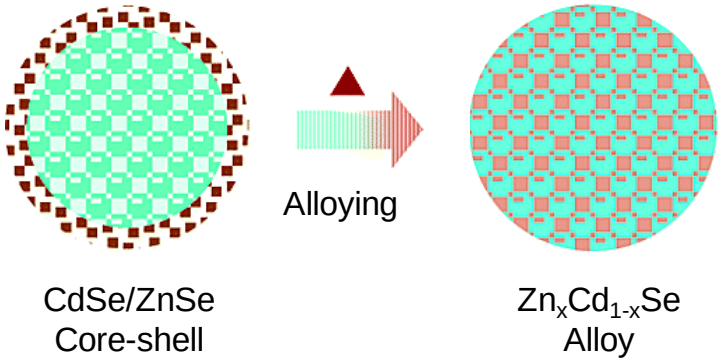

Figure1.8: A schematic representation of the kinetic alloying process from core-shell CdSe/ZnSe to alloyed $Zn_xCd_{1-x}Se$ NCs. Reprinted with permission from ref.[47] Copyright 2003, American Chemical Society.

The process of alloy formation of $Zn_xCd_{1-x}Se$ NCs can also be done by taking ZnSe NCs as starting material followed by the addition of Cd. Consequently, the absorption onset and PL peak position shift to red region of the visible region.[48] But, the formation of $Zn_xCd_{1-x}Se$ alloy from ZnSe NCs was observed at lower temperature than that of CdSe NCs. This suggest that the cation exchange of Cd^{2+} ions in ZnSe lattice is more favourable than Zn^{2+} ions in CdSe lattice probably because of lower dissociation energy for Zn-Se (136 KJ/mole) bond than that of Cd-Se (310 KJ/mole). The emission from alloy NCs can be extended to NIR region (750-1200 nm) by making $Cd_xHg_{1-x}Te$ alloy NCs.[49] The alloy formation can also takes place between two different anions with same oxidation state which allows us to tune the band gap. For example, CdS_xSe_{1-x} and $CdSe_xTe_{1-x}$ alloy NCs emits in the range 600- 850 nm.[50-51]

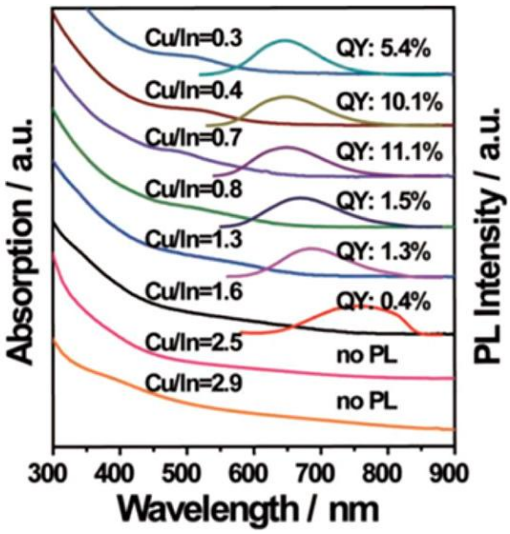

Figure1.9: Absorption and photoluminescence spectra of $CuInS_2$ NCs with different [Cu]/[In] molar ratios. Reprinted from permission from ref.[52] Copyright 2012 WILEY-VCH Verlag GmbH & Co.

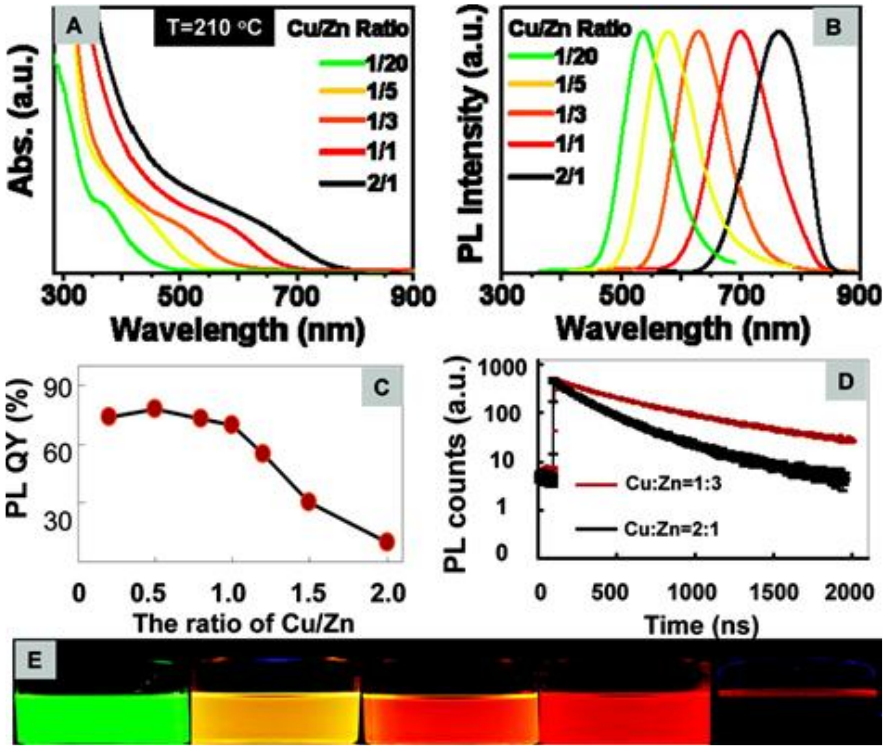

Figure1.10: (A) Absorption and (B) emission spectra of the Cu-Zn-In-S NCs with different Cu/Zn ratios prepared at 210 °C. (C) Photoluminescence quantum yield of the plain NCs vs the ratio of Cu to Zn. (D) PL lifetime decays of two typical samples with Cu to Zn ratios of 1:3 and 2:1 under excitation wavelengths of 405 nm. (E) Digital pictures of the samples with different Cu/Zn ratios were taken under a 365 nm UV lamp (from left to right, 1:20, 1:5, 1:3, 1:1, and 2:1). Reprinted with permission from ref.[53] Copyright 2011, American Chemical Society.

Band gap of I-III-VI semiconductor NCs can also be tuned in the visible to NIR range maintaining high PL QY by controlling the composition. Along with these interesting optical properties, I-III-VI NCs are non-toxic in nature, motivating the use of these NCs in LED and biomedical imaging.[2, 52-57] Unlike II-VI, I-III-VI semiconductors possess large structural tolerance to the off-stoichiometry; I-III-VI semiconductor like $CuInSe_2$ and $AgInSe_2$ are examples for this category. $CuInSe_2$ and $AgInSe_2$ can exist in different forms such as $CuIn_5Se_8$, $CuIn_3Se_5$, $Cu_2In_4Se_7$ and $Ag_{0.85}In_{1.05}Se_2$, $Ag_3In_5Se_9$, $AgIn_3Se_5$, and $AgIn_{11}Se_{17}$.[58-59]

Thus, by varying the amount of Cu in $CuInS_2$ and Ag in $AgInS_2$, the absorption and emission can be tuned. For example, Figure 1.9 shows the tunability of absorption and emission spectra of $CuInS_2$ NCs with the change in the Cu:In ratio.[60] Typically, Cu deficient NCs exhibit high PL QY. But still the obtained PL QYs from these NCs are lower (up to 11%) suggesting the presence of high density of non-radiative trap states. Along with the band gap tunability, the PL QY of $CuInS_2$ NCs can be enhanced by minimising the trap states by making Cu-Zn-In-S alloy NCs and $CuInS_2$/ZnS core/shell NCs. For example, figure 1.10A-B show the tuning of absorption and emission by varying Cu:Zn ratio in the Cu-Zn-In-S NCs. In addition to this, the incorporation of Zn with respect to Cu in $CuInS_2$ NCs eliminates the non-radiative trap states which leads to enhancement in the PL QY up to ~90% as evidenced by figure 1.10 C-D.[53] Similarly, the trap states can be minimised by preparing core/shell NCs. For example, >80% PL QY can be obtained from core/shell NCs of $CuInS_2$/CdS or $CuInS_2$/ZnS.[56] This, composition tuning can be extended to Ag based I-III-VI semiconductor NCs as well.[61-63] Typically, I-III-VI semiconductor NCs exhibit PL with ~100 nm full width at half maximum (FWHM) in contrast to II-VI semiconductor NCs which exhibit PL with FWHM ~30 nm.[64] In II-VI NCs, PL arises due to excitonic emission whereas in I-III-VI NCs sub-band gap states participate in PL along with VBM and CBM. Further details of PL mechanism of I-III-VI NCs will be discussed in the 2nd chapter of this thesis.

1.5 Effect of Mn-doping on optical properties of semiconductor nanocrystals

Purposeful incorporation of impurities into the lattice of a crystalline material is known as doping. Doping of a semiconductor with a heterovalent ion often provides extra electrons or holes that can lead to either n-type or p-type doping respectively, and thus an increase in carrier density. This high carrier concentration often leads to high conductivities in semiconductors. For example, doping boron and phosphorous in silicon gives rise to p-type

and n-type conductivities respectively. Such high conducting semiconductors are required for electronic device applications. On the other hand, doping semiconductor with a homovalent ion can also provide new properties. One benchmark example of such doping is incorporation of Mn^{2+} in group II-VI semiconductors including both bulk and NCs that can lead to novel magnetic, electronic, magneto optic and opto-electronic properties.[65,66-68] Compared to bulk semiconductors, Mn^{2+}-doping in quantum confined NCs exhibit superior optical properties. For example, Mn-doping in ZnS NCs exhibit stronger interaction of Mn localised *d*-states with *s-p* electronic states of the host. Quantum confinement of host electronic wavefunction results into efficient energy transfer from host to the dopant as shown in Figure 1.11a. Doping Mn^{2+} in group II-VI semiconductor NCs such as ZnS, ZnSe, CdSe and CdS have been extensively studied. Mn-doped NCs emit distinct PL peak at ~585 nm with high (>50%) PL QY.[69] These highly luminescent NCs have been used in electroluminescent display technology and biological labelling.[70-71]

The PL mechanism for Mn-doped NCs is as follows. Mn^{2+} has five d-electrons, and according to Hund's rule, the ground state of Mn^{2+} is $^6A_1$ in both tetrahedral and octahedral weak field geometries. The lowest energy excited state is $^4T_1$. We have shown the ground state for total energy of the Mn-doped system in Figure1.11b as < 1 >. This energy level corresponds to host in the ground state (no electron-hole excitation) along with the ground state multiplet configuration of Mn^{2+} state, which is the $^6A_1$ state. After excitation, electron-hole pair formation takes place in host whereas Mn^{2+} is in its ground state configuration ($^6A_1$ state), which is shown as energy level < 2 >. Then, in the de-excitation process, system goes to < 3 > state where host goes to ground state by non-radiative recombination of electron and hole. The energy during de-excitation process of host gets transferred to Mn^{2+} ground state ($^6A_1$) which in turn results in the population of $^4T_1$ state of Mn^{2+}. Eventually, excited state Mn^{2+} $^4T_1$ state decays radiatively to ground state configuration of the $^6A_1$ state by emitting yellow-orange light at ~585 nm.

Often, surface and defect states in semiconductor NCs give rise to PL at lower energy than the band-edge emission. Such PL arise from the excited states which are populated by electrons or holes at total energy lower than electron-hole excitation of host as shown in Figure 1.11c. This population of defect states are attained by electron or hole or energy transfer. Therefore, one can show such transitions between these states in terms of total energy diagram shown in Figure 1.11c. This diagram does not distinguish between

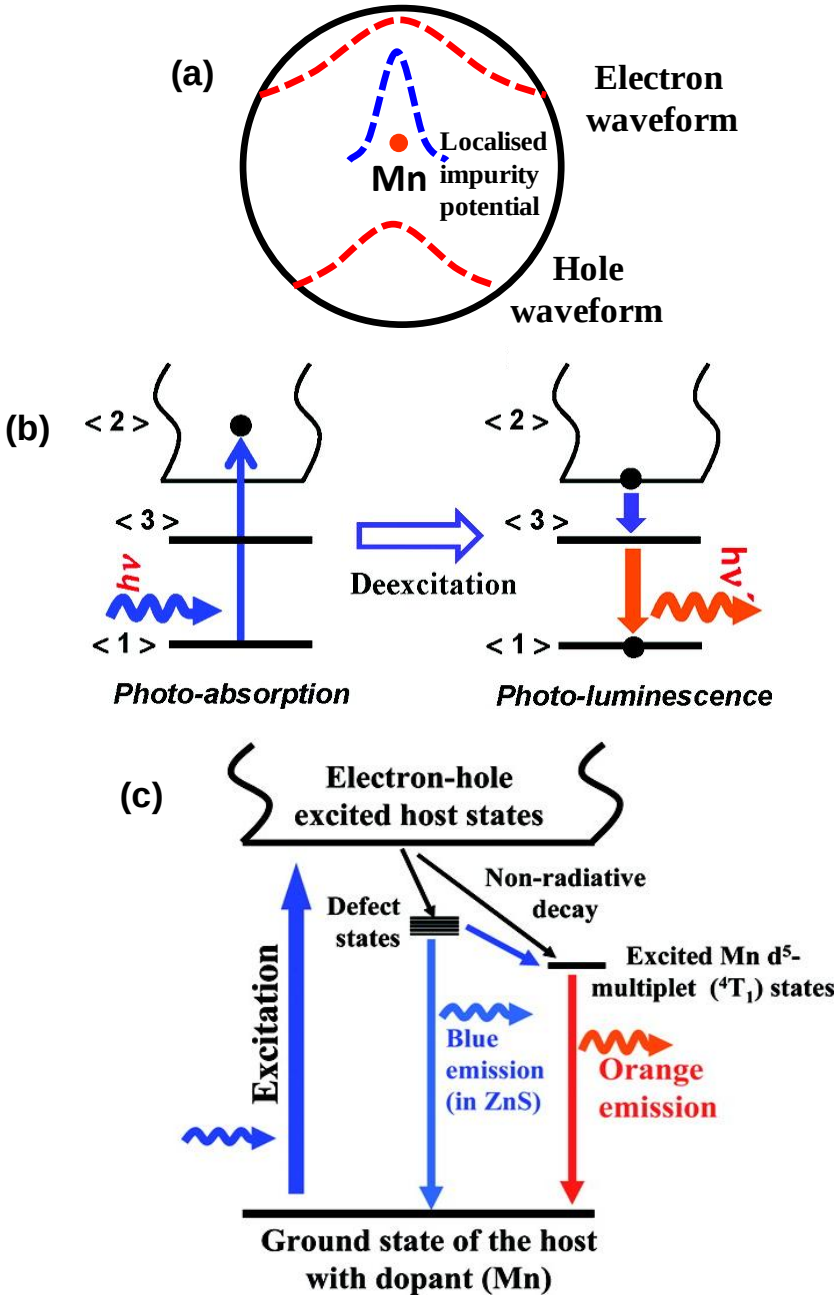

Figure 1.11: (a) A model depicting the overlap of electron-hole wave function with a localized impurity potential in a nanocrystal. Adapted from ref.[67] (b) Total energy diagram of (left) the excitation and (right) the de-excitation processes in Mn-doped NCs, as discussed in the text. < 1 > represents the ground state of the NC with Mn^{2+} in $^6A_1$ state, < 2 > represents the host with an electron-hole excitation and the Mn^{2+} in the $^6A_1$ state. < 3 > represents the total energy of Mn^{2+} in the $^4T_1$ state but the host without any electron-hole excitation. States corresponding to < 1 >, < 2 >, and < 3 > can be thought of as (host + Mn), (host* + Mn) and (host + Mn*), respectively, where the * denotes an excited state. (c) Schematic representation of the total energy diagram of Mn-doped ZnS NCs in presence of surface/defect states: excitation and de-excitation processes for doped NCs. Figures b and c are adopted from ref.[72] Copyright 2011, American Chemical Society.

electron/hole/energy transfer and hence the same diagram can be represented in a compact way wherein all possible surface and defect state related emissions are depicted. When these excited defect states decay radiatively to ground state which results in emission of light at lower energy than that of optical gap as shown by blue arrow in Figure 1.11c. However, in Mn-doped NCs, Mn d-states undergo competition with the excited surface states as shown by blue diagonal arrow in Figure 1.11c leading to both surface and dopant state emission. However, excited state of Mn^{2+} is populated by both energy transfer from band gap excitations, and decay of excited surface states (depending on the energy difference of surface states).[73] Therefore, NCs containing more number of surface states are able to exhibit intense Mn d-d emission. Thus, the population of Mn excited state ($^4T_1$) in both ways results in giving PL peak with high PL QY.

Unlike the delocalized CB and VB states, the localised atomic like Mn d-states are spatially separated from the surface states. Therefore, surface states are less detrimental for PL arising from Mn d-d transition. Typically the PL lifetime of the Mn d-d emission are in few milliseconds owing to their spin-forbidden transitions.[74] The long PL lifetime of Mn-doped NCs are now being utilized to enhance solar cell efficiency in the quantum dot based solar cell.[68, 75]

1.6 Electronic band structure of II-VI and I-III-VI semiconductors

I-III-VI semiconductors are analogous to II-VI semiconductors in terms of their crystal structure. In the unit cell of zinc blende crystal structure of ZnS, if the two Zn atoms are replaced by one Ag and one In and double the unit cell in the Z-direction then we get the unit cell of chalcopyrite $AgInS_2$ as shown by the Figure 1.12.[76] The lattice parameter c for $AgInS_2$ is not exactly 2a, due to the difference in the bond strengths and bond length of Ag-S and In-S.

Optical properties such as absorption and PL of a semiconductor are governed by the electronic band structure. In II-VI based semiconductors, for example in CdS, the VBM is mainly formed from the bonding orbitals of Cd (5s)-orbital and S (3p)-orbital whereas CBM is formed from the antibonding orbitals of Cd (5s)-orbital and S (3p)-orbital.[1] The schematic representation for CdS is shown in the left side figure1.13. The band gap is governed by the bonding and antibonding orbitals of Cd and S. Therefore, Cd and S unpassivated bonds have more probability to lie energetically deep within the band gap. In II-VI semiconductors there are more chances of formation of trap states which are detrimental for efficient optical

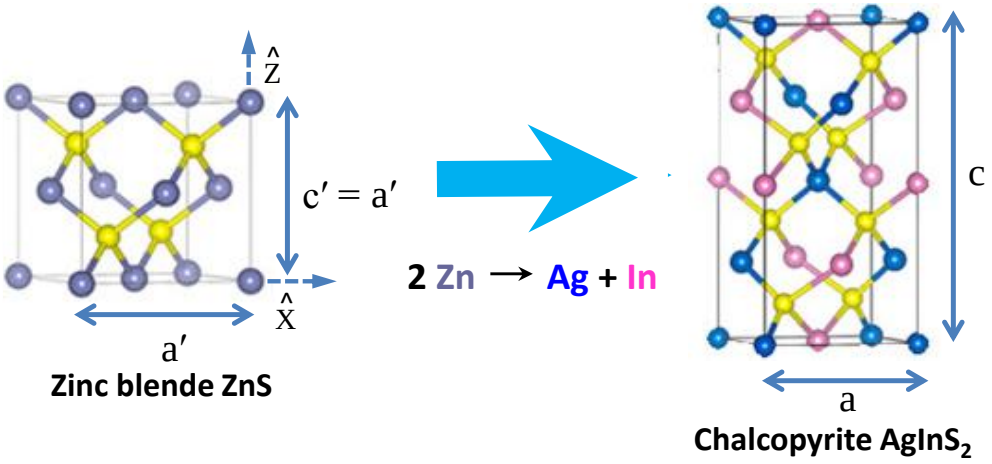

Figure1.12: Unit cell of ZnS and $AgInS_2$ where two Zn atoms have been replaced by one Ag and one In atoms. Reprinted with permission from ref.[76] Copyright 2017, American Chemical Society.

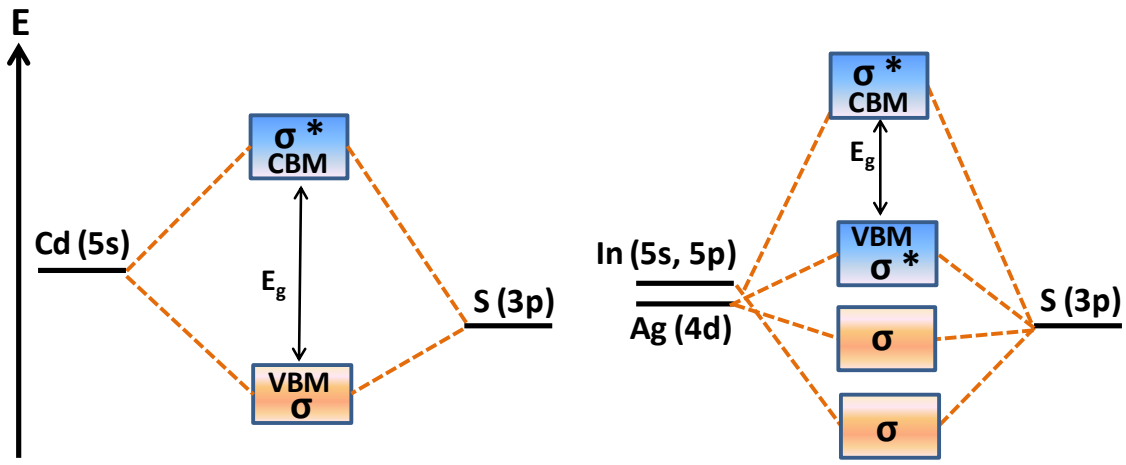

Figure 1.13: Schematic of bulk band structure of CdS and $AgInS_2$, made from the refs. [1, 77]

properties such as high PL QY (as discussed in section 1.2). On the other hand, in I-III-VI semiconductors, there are two metal ions present. The valance orbitals of these metal ions undergo hybridization with valance orbitals of Se resulting in the formation of corresponding bonding and antibonding orbitals. For example, in $AgInS_2$ the VBM is formed from antibonding orbital of Ag (4d)- and S (3p)-orbitals, whereas CBM is formed from the antibonding orbitals In(5s, 5p)- and S(3p)-orbitals.[77] Thus, unlike II-VI semiconductors, in I-III-VI semiconductors the band gap is governed only by the antibonding states. Consequently, chances of non-bonding (unpassivated) states from Ag, In and S forming deep trap states in the mid-gap region is less. Thus, I-III-VI system can be treated as a defect tolerant system, which is good for opto-electronic applications.[78]

1.7 Quantum dot sensitized solar cell

Solar cell is a device which converts solar energy into electricity by photovoltaic effect. One of the effective way of utilisation of solar light is using semiconductors with band gap 1.1 to 1.5 eV as photo absorbers. In this regard, crystalline silicon (Si) and gallium arsenide (GaAs) based solar cells are well known examples. Single p-n junction Si and GaAs cells show PCE ~30%.[79] Si is an indirect band gap semiconductor (electron momentum state is different at VBM and CBM). Therefore, in order to absorb sufficient amount of sun light a thick (100-500 µm) film of Si is needed. Preparation of crystalline Si requires expensive depositing techniques. On the other hand, GaAs is a direct band gap semiconductor so thin films (tens of µm) are sufficient enough to absorb good amount of sun-light. However, preparation of crystalline GaAs is also expensive. In order to prepare less expensive solar cells researchers developed poly-crystalline Si, CIGS, and copper zinc tin sulphide selinide (CZTSSe) based solar cells. These solar cells cost relatively lesser than single crystalline Si and GaAs based solar cell. In order to reduce the solar cell cost further down, different solution processable semiconductor came into the picture which are often NC based solar cell, or dye sensitized solar cell.[80-81] NC based solar cells are promising because of large absorption coefficient, and tunable band gap. Also MEG process and utilisation of hot electrons (electrons which possess high kinetic energy) leaves room to increase the photo conversion efficiency (PCE) higher than the Shockley-Queisser limit (the maximum PCE 33.7% one can get from a single junction solar cell with a band gap 1.34 eV).[8]

In my thesis, we have worked on semiconductor NC sensitised solar cell often termed as QD sensitized solar cell. So, here I will discuss about basic structure of a QD sensitized solar cell. Schematic of solar cell device of a QD sensitized solar cell is given below Figure 1.16.[82] In which mainly three parts are there namely photo-anode, cathode, and electrolyte solution. Photo anode consists of NCs sensitized mesoporous TiO_2 on conducting glass. Cathode material can be Pt or Au or Cu_2S electrode and poly sulphide is used as electrolyte. Photo-anode and cathode are assembled in sandwich fashion by keeping spacer in between for addition of few drops of polysulfide electrolyte solution. Then, anode and cathode electrodes connected to Keithley I-V source meter. The cell tested by illuminating the top of photo-anode using a solar simulator (Xe-lamp).

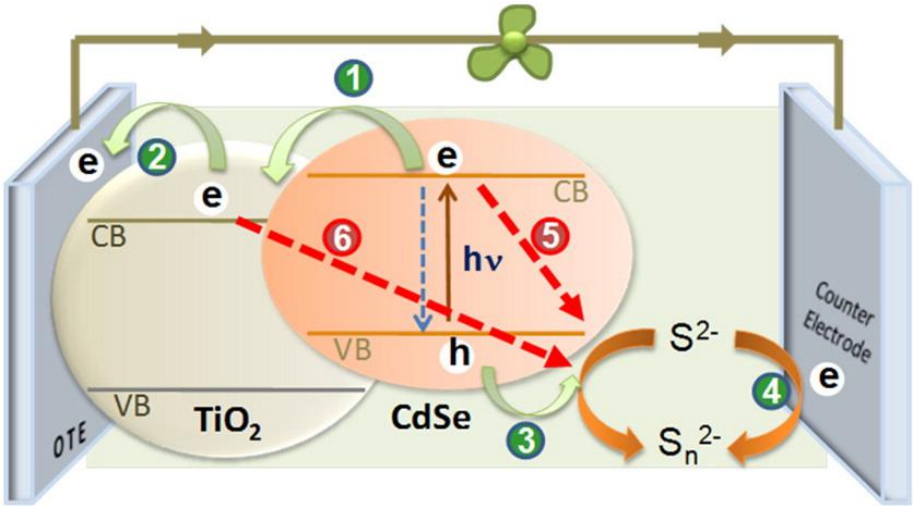

Figure1.16: Schematic illustration of a function of quantum dot sensitised solar cell. Reprinted with permission from ref.[82] Copyright © 2013, American Chemical Society

Upon irradiation of solar cell by a Xe lamp, absorption of a photon takes place by a NC and generates an electron-hole pair. Electron from the CBM of a NC will get transferred to CBM of TiO_2.The separation of electron and hole occur at the interface of NC and TiO_2. This process has been shown in Figure 1.16 as step 1. From TiO_2 electrons will reach to conducting glass, as shown by step 2 in Figure 1.16. On the other hand, hole at VBM will be regenerated by oxidising poly sulphide electrolyte as shown by step 3 in Figure 1.16. Electrolyte will be regenerated by the electron coming through outer circuit which is shown by step 4 in Figure 1.16. Thus, the separation and collection of charge carriers result in the creation of voltage and current from a NC based solar cell device. However, along with the above mentioned process there are some undesired recombination processes also take place in the device. Those are the recombination between electrons from the CBM of NC to electrolyte shown by step 5 in Figure 1.16. The recombination between electrons from the CBM of TiO_2 to electrolyte shown by step 6 in Figure 1.16. Of course there are additional inherent recombination processes within the NC. These recombinations lead to reduction of efficient charge carrier separation and collection. Thus, recombination processes affects the final device performance. Solar cell can be characterised by current-voltage (*I-V*) plot which provides the efficiency of a solar cell.

1.7.1 I-V characteristics of a solar cell device

I-V characteristic of a solar cell under illumination is shown in Figure 1.17. Typically, the PCE is dependent on three parameters, short circuit current (I_{sc}), open circuit voltage (V_{oc})

and fill factor (*FF*). I_{sc} is the maximum current obtained from a solar cell at the short circuit condition (at $V = 0$). On the other hand, the maximum voltage obtained from a solar cell at condition $I_{sc} = 0$ is called V_{oc}. Power of a solar cell is the product of current and voltage. The maximum power obtained theoretically (P_T) from a solar cell is the product of I_{sc} and V_{oc}. However, in practical the power obtained at I_{sc} and V_{oc} is zero. So the maximum power obtained from a solar cell is given by P_m and the corresponding current and voltage are shown in the Figure 1.17 are I_m and V_m.

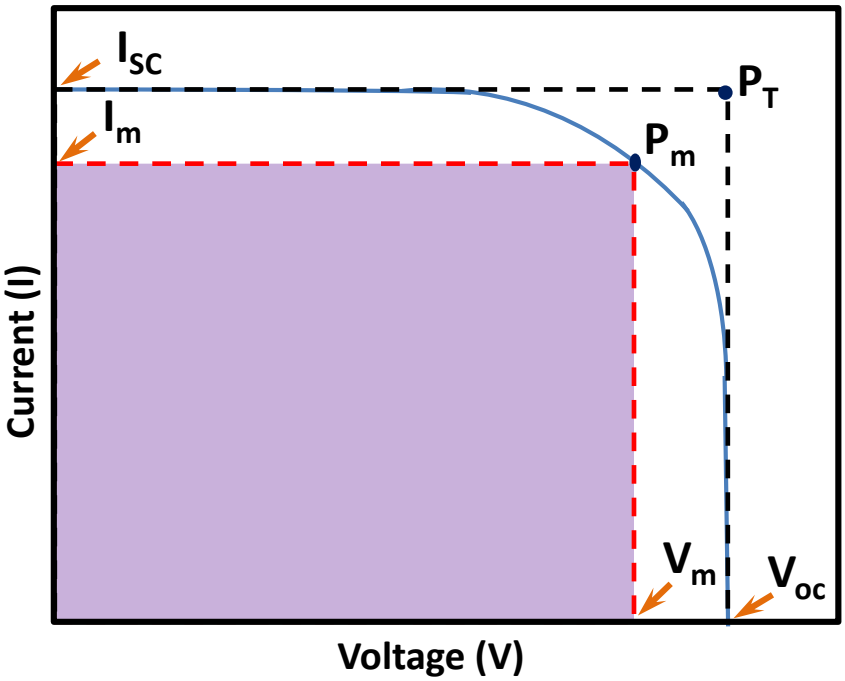

Figure1.17: Schematic of *I-V* characteristic of a typical solar cell under illumination.

FF is the ratio of maximum power (P_m) to the theoretical power (P_T) or the small area under the curve to that of large area as shown in the Figure 1.17. *FF* indicates the Maximum output of a solar cell.

$$FF = \frac{P_m}{P_T} = \frac{I_m V_m}{I_{sc} V_{oc}} \tag{1.3}$$

The efficiency of a solar cell (η) is the ratio between the output power (P_{out}) of a solar cell and input power (P_{in}) of sun light. Typically, in laboratory Xe lamp is used for illumination with 1 sun intensity (100 mW/cm^2) under air mass 1.5 global illumination.

$$\eta = \frac{P_{out}}{P_{in}} = \frac{P_m}{P_{in}} \tag{1.4}$$

In the above equation P_{in} is constant and if we substitute the value of P_m using the equation 1.3, then the final expression turns out to be

$$\eta = \frac{FF \times V_{oc} \times I_{sc}}{P_{in}} \quad (1.5)$$

Where, P_{in} is constant which is treated as 1 owing to their 1 sun intensity. Therefore, η is only depends on the product of *FF*, V_{oc}, and I_{sc}.

1.8 Effective mass (m*) of electrons and hole of II-VI and I-III-VI semiconductors

One of the important parameter which determines the performance of solar cell devices is the mobility of charge carriers (electrons and holes). Since mobility depends on effective mass (m*) of charge carriers, it is essential to have lower m* values for solar absorbing materials. For example, CdTe possess lower m* value along with suitable band gap for solar cell application. Indeed, CdTe based thin film solar cell shows the PCE 22.1%.[83] I-III-VI semiconductors also exhibit similar m* values to that of II-VI semiconductors as given in the Table 1.1.[84] $CuIn_xGa_{1-x}Se_2$ (CIGS) thin film solar cell also shows the PCE 22.6%.[83] This suggests that similar to II-VI semiconductors, I-III-VI semiconductors are also a potential candidate for solar cell application. Along with strong absorption in the visible to NIR region, the low m* of charge carriers play a crucial role in achieving the high PCE.

Table1.1: Comparison of effective masses of electron and hole of II-VI and I-III-VI semiconductor NCs.[84,85,86-87] Bulk band gap values have been given in parenthesis of each system. In the Table, m_o = rest mass of electron.

Effective mass of charge carrier (m*)	II-VI semiconductors		I-III-VI semiconductors			
	CdSe (1.74 eV)	CdTe (1.5 eV)	$CuInSe_2$ (1.1 eV)	$CuGaSe_2$ (1.64 eV)	$AgInS_2$ (1.87 eV)	$AgInSe_2$ (1.2 eV)
Electron	0.12 m_o	0.096 m_o	0.08 m_o	0.14 m_o	0.12 m_o	0.2 m_o
Hole	0.4 m_o	0.4 m_o	0.71 m_o	1.2 m_o	0.59 m_o	~0.39 m_o

1.9 Surface modification of nanocrystals

Organic ligands with long hydrocarbon chains are typically used during the synthesis of NCs to passivate the surface of NCs.[9] However, such organic ligands are typically insulating in nature and creates high energy barrier for charge transport in a NC film. Therefore, organic

capped NCs often show poor electronic and opto-electronic properties. For example, oleylamine capped $AgInS_2$ NCs show poor PCE of 0.06 %. After removal of organic ligands from the surface of the NCs by annealing, the PCE was increased to 0.5 %.[88] It proves that, the removal of organic ligands enhances the performance of a solar cell. Annealing of NCs at high temperature (>300 ^oC) may lead to cracks in the film which hinders the transport of charge carriers. Also such annealing may lead to a significant increase in the size of NCs. In order to improve the transport of the charge carriers in NC films without losing their intrinsic properties, researchers have developed post synthesis modification to get organic-free NCs. In this regard, Talapin *et al*; developed a protocol for II-VI type semiconductor NCs.[89] The long chain hydrocarbon organic ligands were replaced by electronically conducting smaller inorganic ligands. As a result, NCs in a film come closer to each other reducing the barrier for charge transport as schematically shown in Figure 1.14a. Consequently, the mobility of charge carriers increases leading to an increase in conductivity values. For example, the films of dodecanethiol (DDT) capped Au nanoparticles show conductivity of 10^{-9} S/cm whereas $Sn_2S_6^{4-}$ capped Au nanoparticles exhibit conductivity of 10^3 S/cm.[89] The corresponding TEM

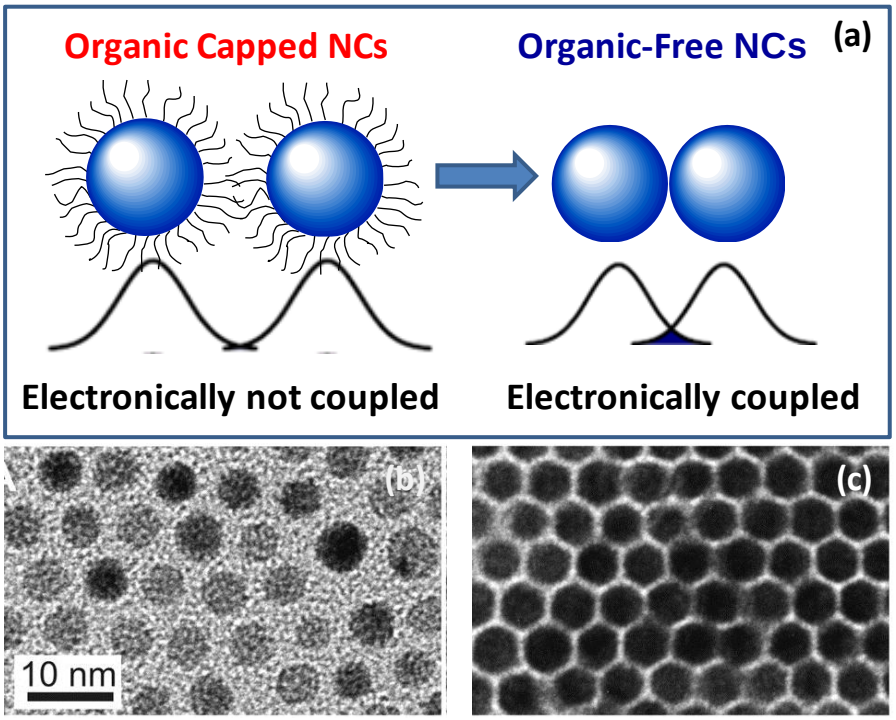

Figure1.14: (a) Schematic representation of the electronic coupling of organic capped and organic-free NCs. TEM images for (b) DDT-capped Au nanoparticles, and (c) $Sn_2S_6^{4-}$capped Au nanoparticles. (b) and (c) are reprinted with permission from the ref.[89] Copyright 2009, American Association for the Advancement of Science.

images of DDT capped Au nanoparticles and $Sn_2S_6^{4-}$ capped Au nanoparticles shown in figure 1.14b-c. The strong electronic coupling among $Sn_2S_6^{4-}$ capped Au NCs allows the enormous increase in the conductivity indicating the importance of organic-free NCs for electronic and opto-electronic applications.

In order to prepare organic-free NCs, one has to synthesise good quality organic capped NCs as shown by the Figure 1.15a and then surface modification has to be employed in the second step. Surface modification can be done by following three ways. i) Solution processing, in which NCs dispersed in a non polar solvents are treated with inorganic ligands in a polar solvent, for example, Figure 1.15b shows the surface modification of organic capped CdSe NCs to S^{2-} capped CdSe NCs.[90] ii) Film processing, in which films of organic capped NCs are treated with smaller organic ligands (L) such as L = $C_2H_4(SH)_2$, N_2H_4N. iii) Simply annealing of NC based films at higher temperatures. Nevertheless, these post synthesis modifications are developed mostly for II-VI type semiconductor NCs. This sort of ligand exchange reactions have to be explored for I-III-VI type semiconductor NCs. Moreover, it would be better if one can synthesize organic-free NCs in a single step, which is not significantly even for well established II-VI NCs.

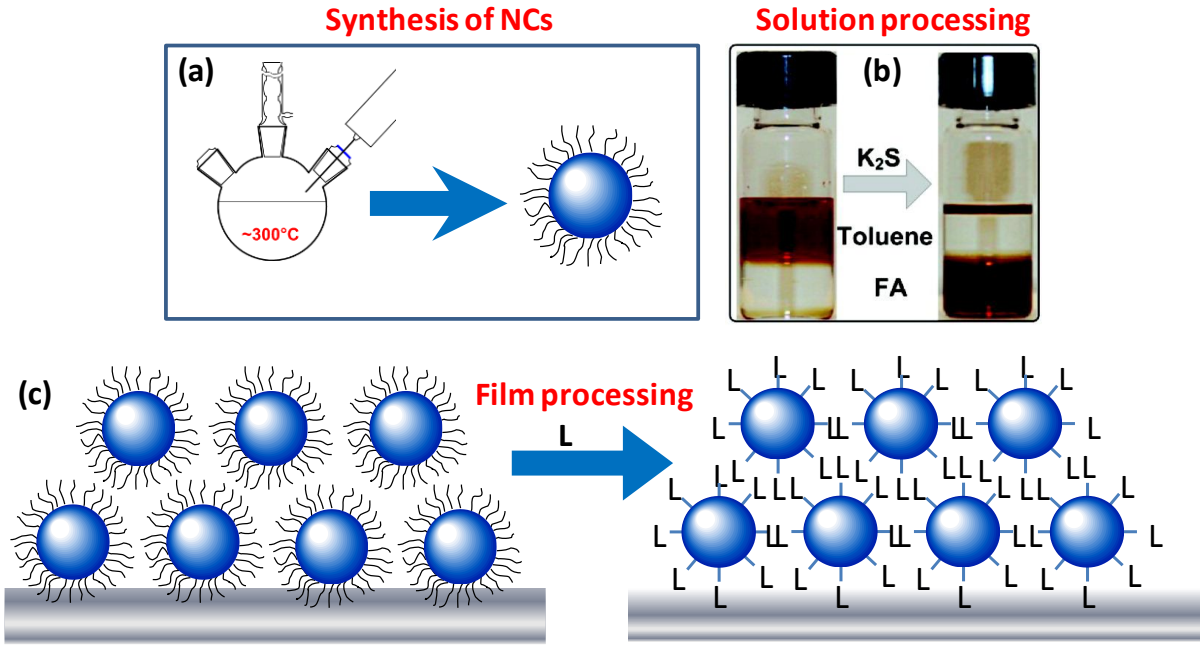

Figure 1.15: (a) Schematic representation of synthesis of organic capped NCs. surface modification of organic capped NCs through (b) solution processing and (c) film processing. Figure (b) reprinted with permission from ref.[90] Copyright © 2011, American Chemical Society.

1.10 Photocatalytic H_2 generation using semiconductor nanocrystals

The decomposition of water into H_2 and O_2 was first demonstrated by Fujishima and Honda through photoelectrochemical method using TiO_2 as anode and Pt as cathode.[91] A potential difference more than 1.23 V between the anode and cathode electrodes is necessary for electrochemical decomposition of water as shown in Figure 1.19. It corresponds to the positive free energy change $\Delta G^0 = 237$ kJmol^{-1} for decomposition of water $2H_2O \longrightarrow 2H_2 + O_2$, indicating a non-spontaneous process. In order to drive this reaction, semiconductors with band gap >1.23 eV is required. CBM of the semiconductor should be more negative potential than the reduction potential of water (0 V with respect to normal hydrogen electrode (NHE)) and VBM should be more positive than the oxidation potential of water (1.23 V with respect to NHE). Since, the band gap of bulk TiO_2 is 3.2 eV,[92] energy more than 3.2 eV is required to excite the electrons from VB to the CB. The electrons then reach to the Pt electrode through external circuit where the reduction of H^+ to H_2 takes place whereas at TiO_2 electrode water gets oxidised to O_2. This was the first demonstration of water splitting using a semiconductor.[99]

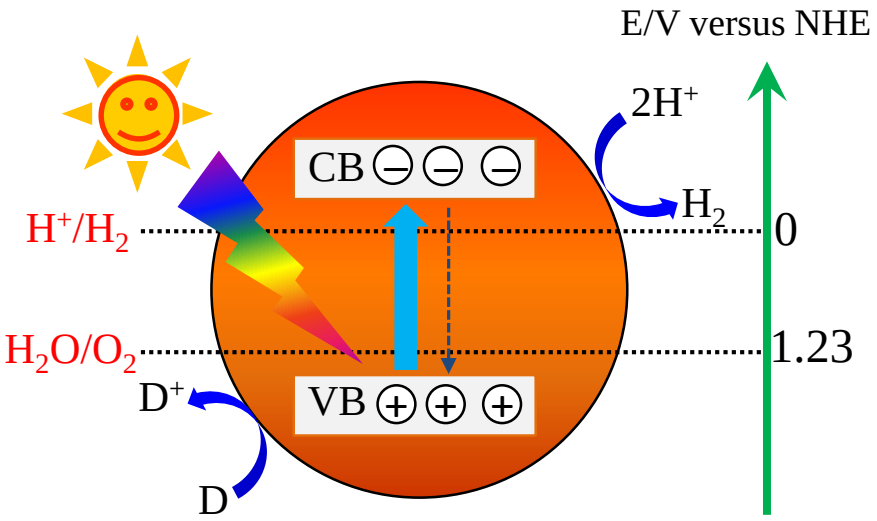

Figure 1.18: Schematic description of photocatalytic H_2 evolution using a semiconductor nanocrystal under illumination. Figure is adopted from the ref.[93]

However, for TiO_2 the band gap is 3.2 eV (380 nm) which is in the UV region.[92] Due to the less availability of UV light (<5%) in the solar spectrum wide band gap semiconductors are not suitable for solar light driven photo-catalytic water splitting. In order to make the photocatalyst visible-light active, researchers focussed on the semiconductors with narrower

band gap. Band gap of semiconductor NCs can be tuned by controlling size and composition, which shifts the CBM typically higher in energy above the reduction potential of water. Moreover, high surface to volume ratio of NCs creates more number of active sites on the surface for water splitting. In my thesis we focus only on H_2 evolution reaction using semiconductor NCs as photocatalyst. The Figure 1.18 shows the working mechanism of H_2 evolution using NC. Upon excitation of NC with appropriate wavelength of light, electron will go to the CB leaving behind hole in the VB. Then electrons move onto the surface of NCs where the reduction of H^+ to H_2 takes place and holes formed in the VB get reduced by sacrificial electron donors. Size of the NCs used for photocatalyst are typically in terms of nm, so the photogenerated electrons have to travel a smaller distance to reach surface. Thus, NCs can be a better visible light driven photocatalyst for H_2 production.

1.11 Scope of the present work

I-III-VI semiconductor NCs exhibit optical band gap and PL QY similar to that of II-VI semiconductor NCs as shown in the Table 1.2, and seems promising alternative to II-VI semiconductor NCs. There are also interesting intrinsic differences in the optical properties of both kinds of NCs. For example, II-VI NCs exhibit narrow PL width (FWHM 25-35 nm)

Table1.2: Comparison of optical properties of II-VI and I-III-VI semiconductor NCs, taken from ref. [94]

Properties	II-VI NCs	I-III-VI NCs
Spectral tunable window	UV-vis-NIR	UV-vis-NIR
PL QY%	Oil-soluble >50% Water-soluble >30%	Oil-soluble >50% Water-soluble 20-50%
PL FWHM	25-35 nm	80-120 nm
PL life times	~20 ns	100-300 ns
Stokes Shift	< 100 meV	200-300 meV

with Stoke's shift < 100 meV whereas I-III-VI NCs exhib it broad PL width (FWHM 80-120 nm) with Stoke's shift 200-300 meV. Such differences in optical properties indicate that the origin of PL in I-III-VI NCs is intrinsically different than that of II-VI NCs. Such differences in PL properties needs to be understood. The large Stoke's shift of PL peak in I-III-VI NCs ruled out the possibilities of self-absorption and foster resonance energy transfer (FRET) which are often detrimental for opto-electronic applications. Furthermore, the long PL lifetimes (100-300 ns) of I-III-VI NCs is expected to be beneficial for separation of charge carriers which is desired for solar cell and photocatalytic applications. Due to the fascinating optical properties of I-III-VI NCs, we got motivated to work on I-III-VI semiconductor NCs. Importantly, I-III-VI NCs are environmentally benign compared to II-VI semiconductors.

This thesis mainly deals with the understanding of photophysics of colloidal I-III-VI semiconductor NCs and their application in solar cell. Often, it is essential to have suitable optical properties for solar cell materials such as narrow band gap, high PL QY, long PL lifetime. CBM of NC should be above than CBM of TiO_2 for efficient charge separation. Overall, point defects in I-III-VI semiconductor NCs are critical to control the optical and opto-electronic properties.

$AgInS_2$ NCs exhibit broad PL with large Stoke's shift and it could not be explained based on size distribution. Prior literature assigned this broad PL of $AgInS_2$ NCs to donor-acceptor transition. Donor (D) and acceptor (A) states lies in the mid gap region. However, D-A model failed to explain the size and composition dependent PL properties of $AgInS_2$ NCs with shift in PL peak by 0.35 eV. This indicates that other states such as CB or VB are involved in the PL of $AgInS_2$ NCs. In order to confirm the involvement of CB or VB in the PL mechanism of $AgInS_2$ NCs, we have synthesized NCs with similar size but varying the CB and VB edges by changing the composition, x in $(ZnS)_{1-x}(AgInS_2)_x$ alloyed NCs. These alloys allow us to assume not much change in distance between Donor and Acceptor. But shift in VBM and CBM allowed us to know the involvement of CB and VB in PL mechanism of $AgInS_2$ NCs. The complete details will be discussed in chapter 2.

Surface of NCs are passivated by organic ligands containg long hydrocarbon chain. Such ligands are insulating in nature. Therefore, efficiencies of opto-electronic properties decreases significantly because of such organic ligands. In order to overcome this problem, surface of NCs has to be modified. In this regard, we have reported for the first time organic-free

$AgInS_2$ NCs and studied their optical properties. We have fabricated solar cell device out of these organic-free $AgInS_2$ NCs. The obtained PCE from organic-free $AgInS_2$ NCs is 0.8% which is more than ten times greater compared with organic capped $AgInS_2$ NCs. But, still the obtained PCE values are lower than II-VI semiconductor NCs. The lower PCE values can be attributed to the higher density of defects in $AgInS_2$ NCs. Also, the band gap of $AgInS_2$ is relatively high and therefore do not absorb NIR light. Complete details will be discussed in chapter 3.

In order to absorb sun light in both visible and NIR spectral region, we have synthesized Ag_2S-$AgInS_2$ hetero dimer NCs (HDNCs) where band gap of bulk $AgInS_2$ is ~2 eV and that of Ag_2S is 1.1 eV.[77, 95] Therefore, these HDNCs can absorb light from the NIR to visible range. Prior literature suggests that the band alignment of HDNCs at the interface is a quasi-type II which can partially separate electrons and holes in these HDNCs.[96] After excitation, holes may stay in VB of Ag_2S whereas electrons stay in CB of both $AgInS_2$ and Ag_2S Thus, Ag_2S-$AgInS_2$ HDNCs are potential material to form pseudo p-n junction at the interface of Ag_2S and $AgInS_2$. In our study we have observed type-I band alignment at the interface of HDNCs. Despite of having type-I band alignment at the interface, PL decay profile of HDNCs show defect mediated 13 μs long PL lifetime. Such long lifetime enhances the ease of charge carrier separation in solar cell device. We have checked this possibility by preparing QD sensitized solar cell. Complete details will be discussed in chapter 4.

Though Ag_2S-$AgInS_2$ HDNCs absorb in the visible and NIR region, but the photocurrent in NIR region corresponding to Ag_2S is negligible. This is because of the CBM of Ag_2S is lower than that of TiO_2 CBM. Therefore, inefficient electron injection takes place from Ag_2S to TiO_2. In order to absorb both visible and NIR photons, along with proper band alignment with respect to TiO_2, we have chosen $CuInSe_2$ based NCs exhibiting a band gap of 1.05 eV. Incorporation of Zn into $CuInSe_2$ lattice and surface decreases the non-radiative trap states and shifts in the CBM to higher energy enhancing the efficiency of electron injection to TiO_2. We have used mercaptopropionic acid capped $(Zn)_{0.24}(CuIn)_{0.76}Se_2$ NCs in solar cell. However, the obtained values are still low (0.8 %) due to recombination of electrons from NC and TiO_2 with electrolyte. In order to overcome this problem, ZnS treatment has been done over the photo-anode increasing the PCE of $(Zn)_{0.24}(CuIn)_{0.76}Se_2$ NCs up to 3.6%. Inexpensive Cu_2S was used as a counter electrode. Complete details will be discussed in chapter 5.

In addition to the five chapters, there is an appendix in my thesis showing the visible-light driven photocatalytic H_2 generation using $(ZnS)_{0.4}(AgInS_2)_{0.6}$ NCs. $(ZnS)_{0.4}(AgInS_2)_{0.6}$ NCs exhibits band gap in the visible range along with its CBM energy higher than that of H^+/H_2 reduction potential. So, photogenerated electrons can reduce H^+ to H_2 efficiently. Further, high surface area of NCs provides more active sites for H^+ adsorption. However, $(ZnS)_{0.4}(AgInS_2)_{0.6}$ NCs capped by oleylamine inhibit charge extraction and dispersion of these NCs in water. In order overcome these problems we have modified the surface of NCs from oleylamine to S^{2-} capping. These S^{2-} capped, non-toxic $(ZnS)_{0.4}(AgInS_2)_{0.6}$ NCs have been used it for photocatalytic H_2 generation. Complete details will be discussed in the appendix.

References

1. Nirmal, M.; Brus, L. Luminescence Photophysics in Semiconductor Nanocrystals. *Acc. Chem. Res.* **1999**, *32*, 407-414.

2. Zhang, Y.; Xie, C.; Su, H.; Liu, J.; Pickering, S.; Wang, Y.; Yu, W. W.; Wang, J.; Wang, Y.; Hahm, J.-i.; Dellas, N.; Mohney, S. E.; Xu, J. Employing Heavy Metal-Free Colloidal Quantum Dots in Solution-Processed White Light-Emitting Diodes. *Nano Lett.* **2011**, *11*, 329-332.

3. Klimov, V. I.; Ivanov, S. A.; Nanda, J.; Achermann, M.; Bezel, I.; McGuire, J. A.; Piryatinski, A. Single-Exciton Optical Gain in Semiconductor Nanocrystals. *Nature* **2007**, *447*, 441.

4. Michalet, X.; Pinaud, F. F.; Bentolila, L. A.; Tsay, J. M.; Doose, S.; Li, J. J.; Sundaresan, G.; Wu, A. M.; Gambhir, S. S.; Weiss, S. Quantum Dots for Live Cells, in Vivo Imaging, and Diagnostics. *Science* **2005**, *307*, 538-544.

5. Saran, R.; Curry, R. J. Lead Sulphide Nanocrystal Photodetector Technologies. *Nat. Photonics* **2016**, *10*, 81.

6. Ma, D.; Shi, J.-W.; Zou, Y.; Fan, Z.; Ji, X.; Niu, C. Highly Efficient Photocatalyst Based on a CdS Quantum Dots/ZnO Nanosheets 0D/2D Heterojunction for Hydrogen Evolution from Water Splitting. *ACS Appl. Mater. Interfaces* **2017**, *9*, 25377-25386.

7. Gur, I.; Fromer, N. A.; Geier, M. L.; Alivisatos, A. P. Air-Stable All-Inorganic Nanocrystal Solar Cells Processed from Solution. *Science* **2005**, *310*, 462-465.

8. Stolle, C. J.; Harvey, T. B.; Pernik, D. R.; Hibbert, J. I.; Du, J.; Rhee, D. J.; Akhavan, V. A.; Schaller, R. D.; Korgel, B. A. Multiexciton Solar Cells of $CuInSe_2$ Nanocrystals. *J. Phys. Chem. Lett.* **2014**, *5*, 304-309.

9. Talapin, D. V.; Lee, J.-S.; Kovalenko, M. V.; Shevchenko, E. V. Prospects of Colloidal Nanocrystals for Electronic and Optoelectronic Applications. *Chem. Rev.* **2010**, *110*, 389-458.

10. Ekimov, A. I.; Onushchenko, A. A. Quantum Size Effect in Three-Dimensional Microscopic Semiconductor Crystals, *J. Exp. Theor. Phys* 1981, 34, 363.

11. Henglein, A. Photochemistry of Colloidal Cadmium Sulfide. 2. Effects of Adsorbed Methyl Viologen and of Colloidal Platinum. *J. Phys. Chem.* **1982**, *86*, 2291-2293.

12. Ekimov, A. I.; Efros, A. L.; Onushchenko, A. A. Quantum Size Effect in Semiconductor Microcrystals. *Solid State Commun.* **1985**, *56*, 921-924.

13. Brus, L. E. A Simple Model for the Ionization Potential, Electron Affinity, and Aqueous Redox Potentials of Small Semiconductor Crystallites. *J. Chem. Phys.* **1983**, *79*, 5566-5571.

14. Bourzac, K. Quantum Dots Go on Display. *Nature* **2013**, *493*, 283.

15. Reiss, P.; Protière, M.; Li, L. Core/Shell Semiconductor Nanocrystals. Small **2009**, *5*, 154-168.

16. Zhang, Z.; Chen, Z.; Zhang, J.; Chen, W.; Yang, J.; Wen, X.; Wang, B.; Kobamoto, N.; Yuan, L.; Stride, J. A.; Conibeer, G. J.; Patterson, R. J.; Huang, S. Significant Improvement in the Performance of PbSe Quantum Dot Solar Cell by Introducing a $CsPbBr_3$ Perovskite Colloidal Nanocrystal Back Layer. Adv. Energy Mater **2017**, *7*, 1601773.

17. Yang, Z.; Chang, H.-T. CdHgTe and CdTe Quantum Dot Solar Cells Displaying an Energy Conversion Efficiency Exceeding 2%. *Sol. Energy Mater Sol. Cells* **2010**, *94*, 2046-2051.

18. Kim, S.; Kim, T.; Kang, M.; Kwak, S. K.; Yoo, T. W.; Park, L. S.; Yang, I.; Hwang, S.; Lee, J. E.; Kim, S. K.; Kim, S.-W. Highly Luminescent InP/GaP/ZnS Nanocrystals and Their Application to White Light-Emitting Diodes. *J. Am. Chem. Soc.* **2012**, *134*, 3804-3809.

19. Sandroni, M.; Wegner, K. D.; Aldakov, D.; Reiss, P. Prospects of Chalcopyrite-Type Nanocrystals for Energy Applications. *ACS Energy Lett.* **2017**, *2*, 1076-1088.

20. Brus, L. Electronic Wave Functions in Semiconductor Clusters: Experiment and Theory. *J. Phys. Chem.* **1986**, *90*, 2555-2560.

21. Brus, L. E. Electron–Electron and Electron- Hole Interactions in Small Semiconductor Crystallites: The Size Dependence of the Lowest Excited Electronic State. *J. Chem. Phys.* **1984**, *80*, 4403-4409.

22. Kayanuma, Y. Quantum-Size Effects of Interacting Electrons and Holes in Semiconductor Microcrystals with Spherical Shape. *Phys. Rev. B* **1988**, *38*, 9797-9805.

23. Chukwuocha, E. O.; Onyeaju, M. C.; Harry, T. S. T. Theoretical Studies on the Effect of Confinement on Quantum Dots Using the Brus Equation. *World Journal of Condensed Matter Physics*, **2012**, 2, 96-100

24. McBride, J.; Treadway, J.; Feldman, L. C.; Pennycook, S. J.; Rosenthal, S. J. Structural Basis for Near Unity Quantum Yield Core/Shell Nanostructures. *Nano Lett.* **2006**, *6*, 1496-1501.

25. Smith, A. M.; Nie, S. Semiconductor Nanocrystals: Structure, Properties, and Band Gap Engineering. *Acc. Chem. Res.* **2010**, *43*, 190-200.

26. Pokrant, S.; Whaley, K. B. Tight-binding studies of surface effects on electronic structure of CdSe nanocrystals: the role of organic ligands, surface reconstruction, and inorganic capping shells. *Eur. Phys. J. D* **1999**, *6*, 255-267.

27. Gao, Y.; Peng, X. Photogenerated Excitons in Plain Core CdSe Nanocrystals with Unity Radiative Decay in Single Channel: The Effects of Surface and Ligands. *J. Am. Chem. Soc.* **2015**, *137*, 4230-4235.

28. Underwood, D. F.; Kippeny, T.; Rosenthal, S. J. Ultrafast Carrier Dynamics in CdSe Nanocrystals Determined by Femtosecond Fluorescence Upconversion Spectroscopy. *J. Phys. Chem. B* **2001**, *105*, 436-443.

29. Murray, C. B.; Norris, D. J.; Bawendi, M. G. Synthesis and Characterization of Nearly Monodisperse CdE (E = Sulfur, Selenium, Tellurium) Semiconductor Nanocrystallites. *J. Am. Chem. Soc.* **1993**, *115*, 8706-8715.

30. Kalyuzhny, G.; Murray, R. W. Ligand Effects on Optical Properties of CdSe Nanocrystals. *J. Phys. Chem. B* **2005**, *109*, 7012-7021.

31. Munro, A. M.; Jen-La Plante, I.; Ng, M. S.; Ginger, D. S. Quantitative Study of the Effects of Surface Ligand Concentration on CdSe Nanocrystal Photoluminescence. *J. Phys. Chem. C* **2007**, *111*, 6220-6227.

32. Hines, M. A.; Guyot-Sionnest, P., Synthesis and Characterization of Strongly Luminescing ZnS-Capped CdSe Nanocrystals. *J. Phys. Chem.* **1996**, 100, 468-471.

33. Dabbousi, B. O.; Rodriguez-Viejo, J.; Mikulec, F. V.; Heine, J. R.; Mattoussi, H.; Ober, R.; Jensen, K. F.; Bawendi, M. G., (CdSe)ZnS Core−Shell Quantum Dots: Synthesis and Characterization of a Size Series of Highly Luminescent Nanocrystallites. *J. Phys. Chem. B* **1997**, 101, 9463-9475.

34. Talapin, D. V.; Rogach, A. L.; Kornowski, A.; Haase, M.; Weller, H. Highly Luminescent Monodisperse CdSe and CdSe/ZnS Nanocrystals Synthesized in a Hexadecylamine−Trioctylphosphine Oxide−Trioctylphospine Mixture. *Nano Lett.* **2001**, *1*, 207-211.

35. Battaglia, D.; Li, J. J.; Wang, Y.; Peng, X. Colloidal Two-Dimensional Systems: CdSe Quantum Shells and Wells. *Angew. Chem. Int. Ed.* **2003**, *42*, 5035-5039.

36. Zhong, X.; Xie, R.; Zhang, Y.; Basché, T.; Knoll, W. High-Quality Violet- to Red-Emitting ZnSe/CdSe Core/Shell Nanocrystals. *Chem. Mater.* **2005**, *17*, 4038-4042.

37. Battaglia, D.; Li, J. J.; Wang, Y.; Peng, X. Colloidal Two- Dimensional Systems: CdSe Quantum Shells and Wells. *Angew. Chem. Int. Ed.* **2003**, *42*, 5035-5039.

38. Saha, A.; Chellappan, K. V.; Narayan, K. S.; Ghatak, J.; Datta, R.; Viswanatha, R. Near-Unity Quantum Yield in Semiconducting Nanostructures: Structural Understanding Leading to Energy Efficient Applications. *J. Phys. Chem. Lett.* **2013**, *4*, 3544-3549.

39. Pedetti, S.; Ithurria, S.; Heuclin, H.; Patriarche, G.; Dubertret, B. Type-II CdSe/CdTe Core/Crown Semiconductor Nanoplatelets. *J. Am. Chem. Soc.* **2014**, *136*, 16430-16438.

40. Kim, S.; Fisher, B.; Eisler, H.-J.; Bawendi, M. Type-II Quantum Dots: CdTe/CdSe(Core/Shell) and CdSe/ZnTe(Core/Shell) Heterostructures. *J. Am. Chem. Soc.* **2003**, *125*, 11466-11467.

41. Wang, J.; Mora-Seró, I.; Pan, Z.; Zhao, K.; Zhang, H.; Feng, Y.; Yang, G.; Zhong, X.; Bisquert, J. Core/Shell Colloidal Quantum Dot Exciplex States for the Development of Highly Efficient Quantum-Dot-Sensitized Solar Cells. *J. Am. Chem. Soc.* **2013**, *135*, 15913-15922.

42. Xie, Y.; Tan, Q.; Zhang, Z.; Lu, K.; Li, M.; Xu, W.; Qin, D.; Zhang, Y.; Hou, L.; Wu, H. Improving Performance in CdTe/CdSe Nanocrystals Solar Cells by Using Bulk Nano-Heterojunctions. *J. Mater. Chem. C* **2016**, *4*, 6483-6491.

43. Schöps, O.; Le Thomas, N.; Woggon, U.; Artemyev, M. V. Recombination Dynamics of CdTe/CdS Core−Shell Nanocrystals. *J. Phys. Chem. B* **2006**, *110*, 2074-2079.

44. Chuang, C.-H.; Lo, S. S.; Scholes, G. D.; Burda, C. Charge Separation and Recombination in CdTe/CdSe Core/Shell Nanocrystals as a Function of Shell Coverage: Probing the Onset of the Quasi Type-II Regime. *J. Phys. Chem. Lett.* **2010**, *1*, 2530-2535.

45. Regulacio, M. D.; Han, M.-Y. Composition-Tunable Alloyed Semiconductor Nanocrystals. *Acc. Chem. Res.* **2010**, *43*, 621-630.

46. Swafford, L. A.; Weigand, L. A.; Bowers, M. J.; McBride, J. R.; Rapaport, J. L.; Watt, T. L.; Dixit, S. K.; Feldman, L. C.; Rosenthal, S. J. Homogeneously Alloyed CdS_xSe_{1-x} Nanocrystals: Synthesis, Characterization, and Composition/Size-Dependent Band Gap. *J. Am. Chem. Soc.* **2006**, *128*, 12299-12306.

47. Zhong, X.; Han, M.; Dong, Z.; White, T. J.; Knoll, W. Composition-Tunable $Zn_xCd_{1-x}Se$ Nanocrystals with High Luminescence and Stability. *J. Am. Chem. Soc.* **2003**, *125*, 8589-8594.

48. Zhong, X.; Zhang, Z.; Liu, S.; Han, M.; Knoll, W. Embryonic Nuclei-Induced Alloying Process for the Reproducible Synthesis of Blue-Emitting $Zn_xCd_{1-x}Se$ Nanocrystals with Long-Time Thermal Stability in Size Distribution and Emission Wavelength. *J. Phys. Chem. B* **2004**, *108*, 15552-15559.

49. Qian, H.; Dong, C.; Peng, J.; Qiu, X.; Xu, Y.; Ren, J. High-Quality and Water-Soluble Near-Infrared Photoluminescent CdHgTe/CdS Quantum Dots Prepared by Adjusting Size and Composition. *J. Phys. Chem. C* **2007**, *111*, 16852-16857.

50. Al-Salim, N.; Young, A. G.; Tilley, R. D.; McQuillan, A. J.; Xia, J. Synthesis of CdSeS Nanocrystals in Coordinating and Noncoordinating Solvents: Solvent's Role in Evolution of the Optical and Structural Properties. *Chem. Mater.* **2007**, *19*, 5185-5193.

51. Piven, N.; Susha, A. S.; Döblinger, M.; Rogach, A. L. Aqueous Synthesis of Alloyed $CdSe_xTe_{1-x}$ Nanocrystals. *J. Phys. Chem. C* **2008**, *112*, 15253-15259.

52. Chen, B.; Zhong, H.; Zhang, W.; Tan, Z. a.; Li, Y.; Yu, C.; Zhai, T.; Bando, Y.; Yang, S.; Zou, B. Highly Emissive and Color-Tunable $CuInS_2$-Based Colloidal Semiconductor Nanocrystals: Off-Stoichiometry Effects and Improved Electroluminescence Performance. *Adv. Funct. Mater.* **2012**, *22*, 2081-2088.

53. Zhang, J.; Xie, R.; Yang, W. A Simple Route for Highly Luminescent Quaternary Cu-Zn-In-S Nanocrystal Emitters. *Chem. Mater.* **2011**, *23*, 3357-3361.

54. Spangler, L. C.; Chu, R.; Lu, L.; Kiely, C. J.; Berger, B. W.; McIntosh, S. Enzymatic Biomineralization of Biocompatible $CuInS_2$, $(CuInZn)S_2$ and $CuInS_2$/ZnS Core/Shell Nanocrystals for Bioimaging. *Nanoscale* **2017**, *9*, 9340-9351.

55. Girma, W. M.; Fahmi, M. Z.; Permadi, A.; Abate, M. A.; Chang, J.-Y. Synthetic Strategies and Biomedical Applications of I-III-VI Ternary Quantum Dots. *J. Mater. Chem. B* **2017**, *5*, 6193-6216.

56. Li, L.; Pandey, A.; Werder, D. J.; Khanal, B. P.; Pietryga, J. M.; Klimov, V. I. Efficient Synthesis of Highly Luminescent Copper Indium Sulfide-Based Core/Shell Nanocrystals with Surprisingly Long-Lived Emission. *J. Am. Chem. Soc.* **2011**, *133*, 1176-1179.

57. Tan, Z.; Zhang, Y.; Xie, C.; Su, H.; Liu, J.; Zhang, C.; Dellas, N.; Mohney, S. E.; Wang, Y.; Wang, J.; Xu, J. Near- Band- Edge Electroluminescence from Heavy- Metal- Free Colloidal Quantum Dots. *Adv. Mater.* **2011**, *23*, 3553-3558.

58. Aldakov, D.; Lefrancois, A.; Reiss, P. Ternary and Quaternary Metal Chalcogenide Nanocrystals: Synthesis, Properties and Applications. *J. Mater. Chem. C* **2013**, *1*, 3756-3776.

59. Yarema, O.; Yarema, M.; Bozyigit, D.; Lin, W. M. M.; Wood, V. Independent Composition and Size Control for Highly Luminescent Indium-Rich Silver Indium Selenide Nanocrystals. *ACS Nano* **2015**, *9*, 11134-11142.

60. Chen, B.; Zhong, H.; Zhang, W.; Tan, Z. a.; Li, Y.; Yu, C.; Zhai, T.; Bando, Y.; Yang, S.; Zou, B. Highly Emissive and Color- Tunable $CuInS_2$- Based Colloidal Semiconductor

Nanocrystals: Off- Stoichiometry Effects and Improved Electroluminescence Performance. *Adv. Funct. Mater* **2012**, *22*, 2081-2088.

61. Dai, M.; Ogawa, S.; Kameyama, T.; Okazaki, K.-i.; Kudo, A.; Kuwabata, S.; Tsuboi, Y.; Torimoto, T. Tunable Photoluminescence from the Visible to Near-Infrared Wavelength Region of Non-Stoichiometric $AgInS_2$ Nanoparticles. *J. Mater. Chem.* **2012**, *22*, 12851-12858.

62. Torimoto, T.; Adachi, T.; Okazaki, K.-i.; Sakuraoka, M.; Shibayama, T.; Ohtani, B.; Kudo, A.; Kuwabata, S. Facile Synthesis of $ZnS{-}AgInS_2$ Solid Solution Nanoparticles for a Color-Adjustable Luminophore. *J. Am. Chem. Soc.* **2007**, *129*, 12388-12389.

63. Zhong, H.; Wang, Z.; Bovero, E.; Lu, Z.; van Veggel, F. C. J. M.; Scholes, G. D. Colloidal $CuInSe_2$ Nanocrystals in the Quantum Confinement Regime: Synthesis, Optical Properties, and Electroluminescence. *J. Phys. Chem. C* **2011**, *115*, 12396-12402.

64. Tan, Z., Zhang, Y., Xie, C., Su, H., Liu, J., Zhang, C., Dellas, N., Mohney, S. E., Wang, Y., Wang, J. and Xu, J. Near-Band-Edge Electroluminescence from Heavy-Metal-Free Colloidal Quantum Dots. *Adv. Mater* **2011**, 23 3553–3558.

65. Abdel-Galil, A.; Balboul, M. R.; Sharaf, A. Synthesis and Characterization of Mn-Doped ZnO Diluted Magnetic Semiconductors. *Physica B: Condensed Matter* **2015**, *477*, 20-28.

66. Muckel, F.; Yang, J.; Lorenz, S.; Baek, W.; Chang, H.; Hyeon, T.; Bacher, G.; Fainblat, R. Digital Doping in Magic-Sized CdSe Clusters. *ACS Nano* **2016**, *10*, 7135-7141.

67. Bhargava, R. N.; Gallagher, D.; Hong, X.; Nurmikko, A. Optical Properties of Manganese-Doped Nanocrystals of ZnS. *Phys. Rev. Lett.* **1994**, *72*, 416-419.

68. Santra, P. K.; Kamat, P. V. Mn-Doped Quantum Dot Sensitized Solar Cells: A Strategy to Boost Efficiency over 5%. *J. Am. Chem. Soc.* **2012**, *134*, 2508-2511.

69. Norris, D. J.; Efros, A. L.; Erwin, S. C. Doped Nanocrystals. *Science* **2008**, *319*, 1776-1779.

70. Rath, A. K.; Bhaumik, S.; Pal, A. J. Mn-doped Nanocrystals in Light-Emitting Diodes: Energy-Transfer to Obtain Electroluminescence from Quantum Dots. *Appl. Phys. Lett.* **2010**, *97*, 113502.

71. Sitbon, G.; Bouccara, S.; Tasso, M.; Francois, A.; Bezdetnaya, L.; Marchal, F.; Beaumont, M.; Pons, T. Multimodal Mn-Doped I-III-VI Quantum Dots for Near Infrared Fluorescence and Magnetic Resonance Imaging: from Synthesis to in Vivo Application. *Nanoscale* **2014**, *6*, 9264-9272.

72. Pradhan, N.; Sarma, D. D. Advances in Light-Emitting Doped Semiconductor Nanocrystals. *J. Phys. Chem. Lett.* **2011**, *2*, 2818-2826.

73. Sapra, S.; Prakash, A.; Ghangrekar, A.; Periasamy, N.; Sarma, D. D. Emission Properties of Manganese-Doped ZnS Nanocrystals. *J. Phys. Chem. B* **2005**, *109*, 1663-1668.

74. Cao, S.; Li, C.; Wang, L.; Shang, M.; Wei, G.; Zheng, J.; Yang, W. Long-Lived and Well-Resolved Mn^{2+} Ion Emissions in CuInS-ZnS Quantum Dots Sci. Rep. **2014**, *4*, 7510.

75. Wang, J.; Li, Y.; Shen, Q.; Izuishi, T.; Pan, Z.; Zhao, K.; Zhong, X. Mn Doped Quantum Dot Sensitized Solar Cells with Power Conversion Efficiency Exceeding 9%. *J. Mater. Chem. A* **2016**, *4*, 877-886.

76. Zhao, X.-G.; Yang, D.; Sun, Y.; Li, T.; Zhang, L.; Yu, L.; Zunger, A. Cu–In Halide Perovskite Solar Absorbers. *J. Am. Chem. Soc.* **2017**, *139*, 6718-6725.

77. Huang, D.; Persson, C. Photocatalyst $AgInS_2$ for Active Overall Water-Splitting: A First-Principles Study. *Chem. Phys. Lett.* **2014**, *591*, 189-192.

78. Oikkonen, L. E.; Ganchenkova, M. G.; Seitsonen, A. P.; Nieminen, R. M. Vacancies in $CuInSe_2$: New Insights from Hybrid-Functional Calculations. *J. Phys. Condens. Matter* **2011**, *23*, 422202.

79. Moon, S.; Kim, K.; Kim, Y.; Heo, J.; Lee, J. Highly Efficient Single-Junction GaAs Thin-Film Solar Cell on Flexible Substrate. *Sci. Rep.* **2016**, *6*, 30107.

80. Carey, G. H.; Abdelhady, A. L.; Ning, Z.; Thon, S. M.; Bakr, O. M.; Sargent, E. H. Colloidal Quantum Dot Solar Cells. *Chem. Rev.* **2015**, *115*, 12732-12763.

81. Ye, M.; Wen, X.; Wang, M.; Iocozzia, J.; Zhang, N.; Lin, C.; Lin, Z. Recent Advances in Dye-Sensitized Solar Cells: from Photoanodes, Sensitizers and Electrolytes to Counter Electrodes. *Mater. Today* **2015**, *18*, 155-162.

82. Kamat, P. V. Quantum Dot Solar Cells. The Next Big Thing in Photovoltaics. *J. Phys. Chem. Lett.* **2013**, *4*, 908-918.

83. NREL Solar Cell Efficiency Chart. https://www.nrel.gov/pv/assets/images/efficiency-chart.png

84. S. Siebentritt and U. Rau, *Wide-Gap Chalcopyrites*. Springer, 2006.

85. Torimoto, T.; Tada, M.; Dai, M.; Kameyama, T.; Suzuki, S.; Kuwabata, S. Tunable Photoelectrochemical Properties of Chalcopyrite $AgInS_2$ Nanoparticles Size-Controlled with a Photoetching Technique. *J. Phys. Chem. C* **2012**, *116*, 21895-21902.

86. Sharma, D. K.; Hirata, S.; Bujak, L.; Biju, V.; Kameyama, T.; Kishi, M.; Torimoto, T.; Vacha, M. Single-particle spectroscopy of I-III-VI semiconductor nanocrystals: spectral

diffusion and suppression of blinking by two-color excitation. *Nanoscale* **2016**, *8*, 13687-13694.

87. Peng, S.; Zhang, S.; Mhaisalkar, S. G.; Ramakrishna, S. Synthesis of $AgInS_2$ Nanocrystal Ink and Its Photoelectrical Application. *Phys. Chem. Chem. Phys.* **2012**, *14*, 8523-8529.

88. Kovalenko, M. V.; Scheele, M.; Talapin, D. V. Colloidal Nanocrystals with Molecular Metal Chalcogenide Surface Ligands. *Science* **2009**, *324*, 1417-1420.

89. Nag, A.; Kovalenko, M. V.; Lee, J.-S.; Liu, W.; Spokoyny, B.; Talapin, D. V. Metal-Free Inorganic Ligands for Colloidal Nanocrystals: S^{2-}, HS^-, Se^{2-}, HSe^-, Te^{2-}, HTe^-, TeS_3^{2-}, OH^-, and NH^{2-} as Surface Ligands. *J. Am. Chem. Soc.* **2011**, *133*, 10612-10620.

90. Fujishima, A.; Honda, K. Electrochemical Photolysis of Water at a Semiconductor Electrode. *Nature* **1972**, *238*, 37.

91. Dette, C.; Pérez-Osorio, M. A.; Kley, C. S.; Punke, P.; Patrick, C. E.; Jacobson, P.; Giustino, F.; Jung, S. J.; Kern, K. TiO_2 Anatase with a Bandgap in the Visible Region. *Nano Lett.* **2014**, *14*, 6533-6538.

92. Yang, J.; Yan, H.; Zong, X.; Wen, F.; Liu, M.; Li, C. Roles of Cocatalysts in Semiconductor-Based Photocatalytic Hydrogen Production. *Philos. Trans. Royal Soc. A* **2013**, *371*.

93. Zhong, H.; Bai, Z.; Zou, B. Tuning the Luminescence Properties of Colloidal I–III–VI Semiconductor Nanocrystals for Optoelectronics and Biotechnology Applications. *J. Phys. Chem. Lett.* **2012**, *3*, 3167-3175.

94. Du, Y.; Xu, B.; Fu, T.; Cai, M.; Li, F.; Zhang, Y.; Wang, Q. Near-Infrared Photoluminescent Ag_2S Quantum Dots from a Single Source Precursor. *J. Am. Chem. Soc.* **2010**, *132*, 1470-1471.

95. Bose, R.; Manna, G.; Jana, S.; Pradhan, N. Ag_2S-$AgInS_2$: p-n Junction Heteronanostructures with Quasi Type-II Band Alignment. *Chem. Commun.* **2014**, *50*, 3074-3077.

Chapter 2

Origin of Photoluminescence in $AgInS_2$ Nanocrystals

The following paper has been published based on the work presented in this chapter.

Rao, M. J.; Shibata, T.; Chattopadhyay, S.; Nag, A. Origin of Photoluminescence and XAFS Study of $(ZnS)_{1-x}(AgInS_2)_x$ Nanocrystals. *J. Phys. Chem. Lett.* **2014**, *5*, 167-173. Copy right permission has been taken from American Chemical Society for the entire paper.

Summary

Donor-Acceptor transition was previously suggested as mechanism for luminescence in $AgInS_2$ nanocrystals. Here we show the participation of delocalized valence/conduction band in the luminescence of $(ZnS)_{1-x}(AgInS_2)_x$ nanocrystal with x = 0.33 to 1 . Two emission pathways are observed: path-1 involves transition between a delocalized state and a localized state exhibiting higher energy and shorter lifetime (~25 ns), and path-2 (donor-acceptor) involves two localized defect states exhibiting lower emission energy and longer lifetime (>185 ns). Surprisingly, Path-1 dominates (82% for x = 0.33) for nanocrystals with lower x, in sharp difference with prior assignment. Luminescence peak blue-shift systematically by 0.57 eV with decreasing x, because of this large contribution from path-1. X-ray absorption fine structure (XAFS) study of $(ZnS)_{1-x}(AgInS_2)_x$ nanocrystals shows larger AgS_4 tetrahedra compared to InS_4 tetrahedra with Ag-S and In-S bond lengths 2.52 and 2.45 Å, respectively. Whereas Zn-S bond length is 2.33 Å along with the absence of 2nd nearest neighbor Zn-S-metal correlation.

Graphical abstract

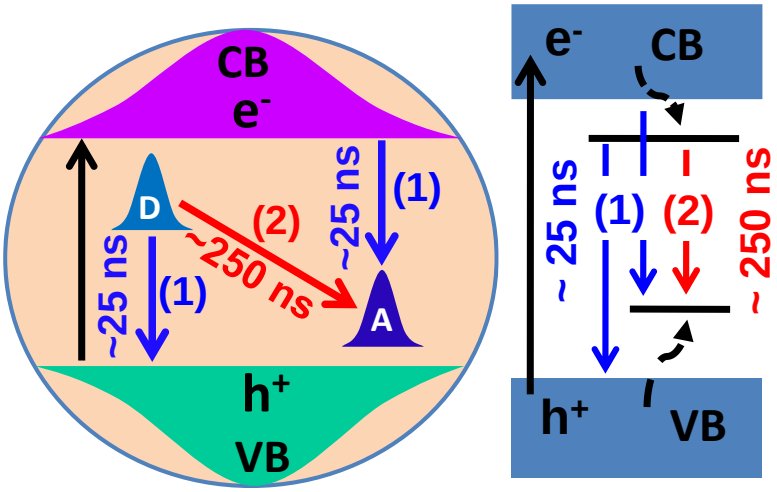

2.1 Introduction

The band gap of bulk $AgInS_2$ is 1.98 eV and 1.87 eV for orthorhombic and chalcopyrite crystal structure, respectively. The band gap of $AgInS_2$ nanocrystals (NCs) further can be tuned in the visible range of spectrum by making $(ZnS)_{1-x}(AgInS_2)_x$ solid solution therefore making them suitable for visible light driven optoelectronic and photocatalytic applications.[1] $(ZnS)_{1-x}(AgInS_2)_x$ NCs are being explored recently for various applications including photovoltaic,[2-4] photocatalysis,[5-6] photodetector[7] and luminescence[8-11]. Till date, luminescence of $(ZnS)_{1-x}(AgInS_2)_x$ appears to be most promising property for application.

Similar to band edge emission of cadmium chalcogenide based NCs,[12-15,16] photoluminescence (PL) of $(ZnS)_{1-x}(AgInS_2)_x$ NCs can be tuned over a wide range of wavelengths (500 to 750 nm), along with high quantum efficiency ~70%.[8, 17-19] However, $(ZnS)_{1-x}(AgInS_2)_x$ NCs exhibit some interesting and intrinsic differences from cadmium chalcogenide NCs: (i) $(ZnS)_{1-x}(AgInS_2)_x$ is non-toxic as opposed to cadmium chalcogenide, (ii) $(ZnS)_{1-x}(AgInS_2)_x$ NCs exhibit large Stokes shift between absorption and emission unlike band-edge emission of CdSe NCs, and therefore detrimental self-absorption and/or nonradiative Forster resonance energy transfer is less probable for $(ZnS)_{1-x}(AgInS_2)_x$ NCs, and (iii) $(ZnS)_{1-x}(AgInS_2)_x$ NCs exhibit poorer color purity with larger full width at half maxima (FWHM ~100 nm). Another kind of bright NC emitter are doped NCs, particularly Mn-doped NCs,[11, 20-21] that also exhibit large Stokes shift and large FWHM. However, unlike $(ZnS)_{1-x}(AgInS_2)_x$ NCs, ensembles of Mn-doped NCs typically show PL wavelength fixed around 580 nm, apart from a recent study[22] showing the PL of single (not ensemble) Mn-doped NCs tunable over a wide range. Furthermore, lifetime of Mn-related emission is close to a millisecond while that of $(ZnS)_{1-x}(AgInS_2)_x$ is around a few hundreds of nanosecond. Lower lifetime of $(ZnS)_{1-x}(AgInS_2)_x$ NCs is advantageous to produce high efficiency electroluminescence devices.[23]

Here we describe the origin of luminescence in $(ZnS)_{1-x}(AgInS_2)_x$ NCs with x = 0.33 to 1 and explore the local structure of these NCs using X-ray absorption fine structure (XAFS). The origin of PL in $(ZnS)_{1-x}(AgInS_2)_x$ NCs was previously described as donor-acceptor (D-A) transitions involving two localized defect states, where the emission energy can be tuned through change in the coulomb interaction due to change in the distance between the D-A pair.[5-6, 24-25] $(ZnS)_{1-x}(AgInS_2)_x$ NCs allow us to tune the band gap simply by varying the composition but without changing the size of NCs, and therefore not altering the D-A pair distance. Interestingly, the systematic blue-shift in band gap for decreasing x, leads to very

similar shift in PL peak, which cannot be explained by the D-A model. Furthermore, the PL shift of 0.57 eV by changing x from 1 to 0.33 is too large compared to D-A pair Coulomb energy. Our PL study shows that the luminescence has two components, (i) a faster (~25 ns) transition involving delocalized valence/conduction band and localized defects and (ii) a slower (>185 ns) transition involving localized D-A pair transition. The D-A pair contribution decreases drastically with decreasing x, and for x = 0.33, the other path, delocalized-localized transition dominates the PL.

The electronic and optical properties depend strongly on the structure and surface chemistry of the NC. These NCs are too small to undergo single-crystal x-ray diffraction (XRD) study, and even the powder XRD peaks broaden, sometimes making it difficult to distinguish between different crystal structures and compositions (homogeneous or heterogeneous).[26-27] In an effort to gain detailed insight about the local structure of $(ZnS)_{1-x}(AgInS_2)_x$ NCs we have performed XAFS study. Unlike XRD, XAFS does not rely on long-range ordering in a crystal. XAFS study on $(ZnS)_{1-x}(AgInS_2)_x$ NCs shows Ag-S, Zn-S and In-S bond lengths to be 2.52, 2.33 and 2.45 Å respectively, similar to those in bulk ZnS and $AgInS_2$ respectively. However, metal-metal 2nd nearest neighbor correlation is largely absent because of both small size of NCs and random occupation of the cation sites in the solid solution. To the best of our knowledge, XAFS study on $(ZnS)_{1-x}(AgInS_2)_x$ NCs for all x > 0 has not been reported before.

2.2 Experimental section

2.2.1 Synthesis of $(ZnS)_{1-x}(AgInS_2)_x$ NCs

$(ZnS)_{1-x}(AgInS_2)_x$ NCs were synthesized following ref.[28] by using single molecular precursor $(AgIn)_yZn_{2(1-y)}(S_2CN(C_2H_5)_2)_4$, where x = y/[y+2(1-y)]. Reactions with molecular precursor composition y = 1, 0.75, and 0.5 is expected to yield $(ZnS)_{1-x}(AgInS_2)_x$ NCs with x = 1, 0.6 and 0.33. The molecular precursor was prepared by mixing of a 50 mL aqueous solution of sodium diethyldithiocarbamate (DDTC) (0.05 mol/L) with 50 mL aqueous solution of 0.025 mol/L metal ions containing $AgNO_3$: $InNO_3$: $Zn(NO_3)_2$ = y : y : 2(1-y). The obtained precipitate was washed with water and methanol three times and dried under vacuum at room temperature. Oleylamine capped $(ZnS)_{1-x}(AgInS_2)_x$ NCs were prepared via decomposing the molecular precursor. 50 mg molecular precursor was heated at 180 ^oC for 30 min in a three neck round-bottom flask maintaining inert atmosphere yielding brown powder. 3 mL oleylamine was injected and the reaction was carried out for another 3min at 180 ^oC. The resulting suspension was centrifuged at 2000 rpm for 2 min and the supernatant was

extracted. $(ZnS)_{1-x}(AgInS_2)_x$NCs were precipitated from the supernatant using methanol as a non solvent and dispersed in toluene or chloroform for characterization.

2.2.2 Characterisation

UV-visible absorption and PL spectra of colloidal $(ZnS)_{1-x}(AgInS_2)_x$ NCs were recorded using a Perkin Elmer, Lambda-45 UV/Vis spectrometer and FluoroMax-4 spectrofluoremeter (HORIBA scientific), respectively. PL decay dynamics were measured using time correlated single photon counting (TCSPC) technique set up from Horiba Jobin Yvon at an excitation energy of 459 nm (2.70 eV). Powder XRD data were collected by using Bruker D8 Advance Powder XRD diffractometer using Cu Kα radiation (λ = 1.54Å). Transmission electron microscopy (TEM) data were obtained using a JEOL JEM 2100F microscope operated at 200 kV.

2.2.3 Extended X-ray absorption fine structure (EXAFS) and x-ray absorption near edge structure (XANES)

EXAFS and XANES are comes under x-ray absorption spectroscopy (XAS). In XAS synchrotron source is used for generating different high energy x-rays. The range of X-rays in XAS is 200-35,000 eV. XAS is the measurement of x-ray absorption coefficient (μ(E)) of a material as a function of energy(eV). These measurements have been done in Argonne National Laboratory by Tomohiro Shibata and Soma Chattopadhyay at Argonne, Illinois in United States

2.3. Results and discussion

2.3.1 Tuning of band gap by changing composition

Oleylamine capped colloidal $(ZnS)_{1-x}(AgInS_2)_x$ NCs were synthesized following ref.[29] UV-visible absorption spectra in Figure 2.1a-c show that the optical gap of NCs blue shifts systematically with increase in ZnS content, without exhibiting sharp excitonic feature similar to prior reports.[5, 29] The optical band gap of direct gap semiconductor can be obtained by using the equation $\alpha h\nu = P(h\nu - E_g)^{1/2}$, where, α is the absorption coefficient, hν is the photon energy, E_g is the optical band gap and P is a constant.[2, 30] We can replace α by absorbance A since optical path and concentration of sample are invariant here.[4] Figure 2.1a-c show plots of $(Ah\nu)^2$ vs. hν for NC samples with different compositions, x. E_g is obtained by extrapolating the linear portion of the plot at $(Ah\nu)^2 = 0$. Band gaps are found to be 2.07, 2.37 and 2.59 eV for NCs with x = 1, 0.6 and 0.33, respectively. Band gap of 2.07 eV for

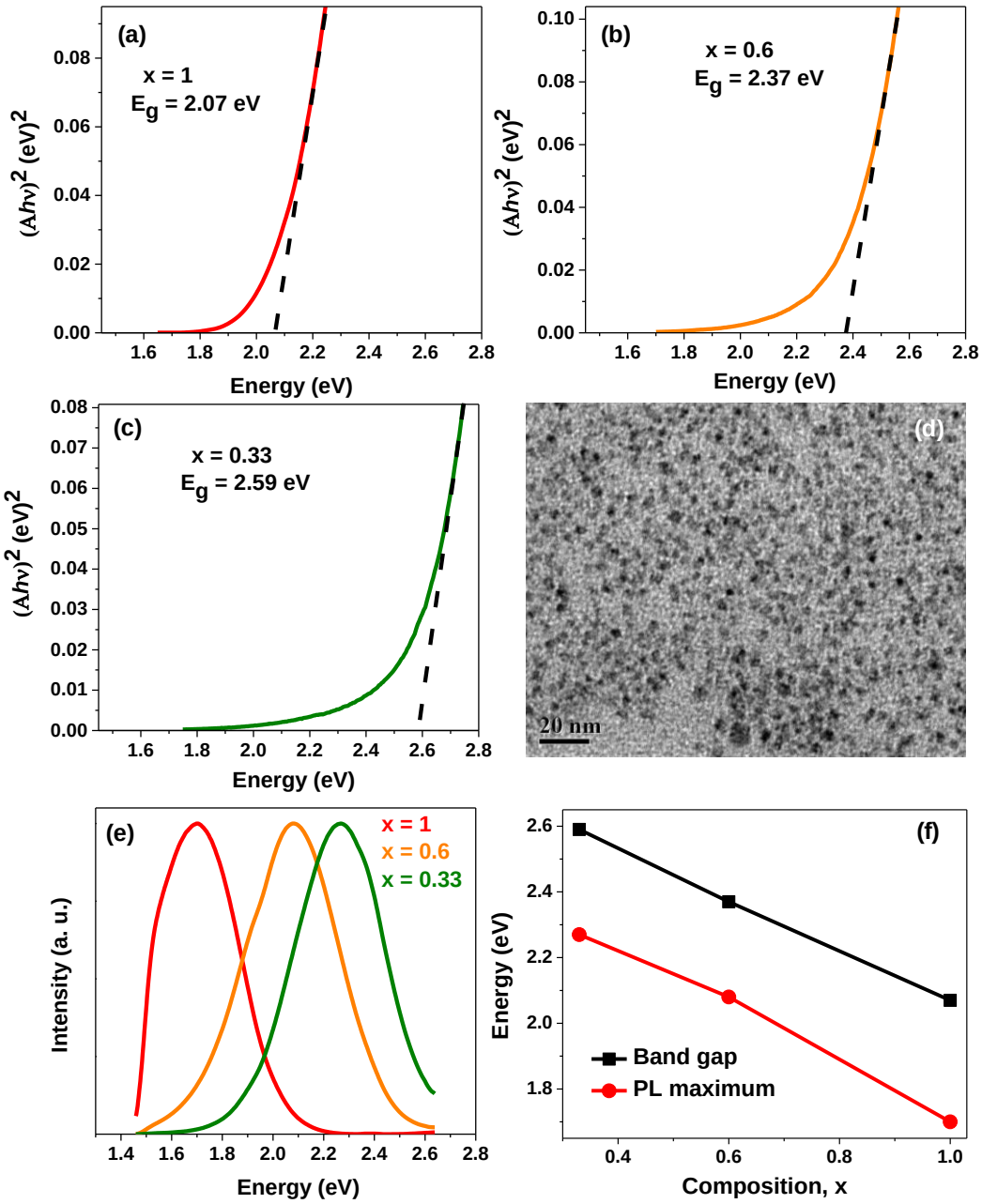

Figure 2.1:(a-c) UV-visible absorption data plotted as $(Ahv)^2$ versus energy for colloidal $(ZnS)_{1-x}(AgInS_2)_x$ NCs with different x. Black dash line shows the extrapolation of the linear portion of the plot to $(Ahv)^2 = 0$. (d) Transmission electron microscopy image of $AgInS_2$ NCs. (e) Photoluminescence (PL) data for colloidal $(ZnS)_{1-x}(AgInS_2)_x$ NCs with different x, after excitation at 2.76 eV (450 nm); all the spectra were normalized at their respective maximum intensity. (f) Compares variation in band gap and PL peak position with composition x of $(ZnS)_{1-x}(AgInS_2)_x$ NCs.

$AgInS_2$ (x = 1) NCs is slightly higher than that of bulk $AgInS_2$ (1.87 eV for chalcopyrite phase and 1.98 eV for orthorhombic phase)[31] suggesting quantum confinement effect in our NCs. Size of NCs obtained from TEM remain similar (~5 nm) for all the three NC as shown

in Figure 2.1d for x = 1, in accordance with ref.,[29] suggesting that the change in band gap is because of the change in composition of NCs.

PL spectra (Figure 2.1e) of colloidal $(ZnS)_{1-x}(AgInS_2)_x$ NCs exhibit a significant blue shift with increase of ZnS content, similar to absorption spectra. Figure 2.1f shows a similar trend in the change of band gap and PL peak position with composition of NCs. However, the origin of PL appears to be different than band edge emission, exhibiting a large Stokes shift compared to band gap and also a broad FWHM. In fact, the origin of PL in these solid solution NCs has previously been assigned[6, 24-25] to defect related D-A transitions which does not involve the valance band maximum and conduction band minimum. However, a similar shift in energy for both band gap and PL peak position is unexpected from D-A model.

2.3.2 Origin of photoluminescence in $(ZnS)_{1-x}(AgInS_2)_x$ NCs

Prior reports suggesting that the PL of $AgInS_2$ NCs arising from transitions between localized (D-A) states which lies in the mid-gap region. In $AgInS_2$ NCs, Ag, S interstial and Ag, S vacancies are responsible for mid-gap trap states. Ag interstial and S interstial act as donor and acceptor states, respectively. Unlike conduction band (CB) and valance band (VB), these mid-gap defects are point defects (localized in nature). Therefore, the probability of carriers in these states are mostly confined whereas VB and CB are delocalized in nature lead to the probability of charge carriers on the entire VB and/or CB, as shown in Figure 2.2a. Figure 2.2a-b show schematic presentation of possible emission mechanism in terms of space and energy, respectively. Two kinds of defect related emissions are possible giving large Stokes shift. The first one involves transition between a delocalized state (valence band maximum or conduction band minimum) and a localized defect state as indicated by path-1, and the second one involves D-A transition between two localized states indicated as path-2. The energy of the D-A pair emission is given by[23]

$$E = E_g - (E_A + E_D) + e^2/4\pi\varepsilon_o\varepsilon r$$

here E_A and E_D are ionization energies of acceptor and donor respectively, r is the distance between donor and acceptor, e is the electron charge, ε is the dielectric constant and ε_o is the permittivity of vacuum. The last term, $e^2/4\pi\varepsilon_o\varepsilon r$, accounts for the Coulomb interaction between the donor and acceptor, and smaller r results in higher emission energy. Coulomb interaction energy = $e^2/4\pi\varepsilon_o\varepsilon r$, for chalcopyrite $AgInS_2$ has been calculated by using $\varepsilon = 9.6$,[25] after incorporating the standard values of e and ε_o. The calculated values of Coulomb energies for some D-A distances are tabulated in Table 2.1. However, the observed shift in

PL peak position with composition in Figure 2.1d is 0.57 eV, which is too high to attribute to Coulomb energy for D-A pairs (~0.15 eV for r ~ 1 nm, see Table 2.1). Also a possible change in ε with change in composition of NCs will be too small to account for the change in PL energy using D-A pair mechanism.

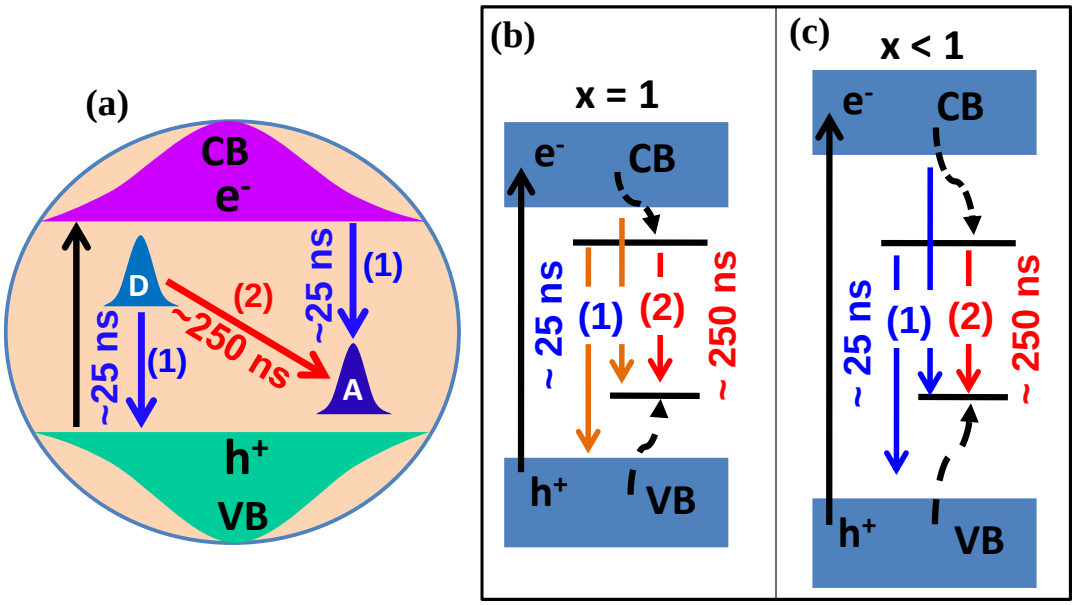

Figure 2.2: (a) Schematic diagram explaining the luminescence mechanism of $AgInS_2$ NCs in space where VB and CB are delocalized states and donor and acceptor states are localized states. (b-c) Schematic diagram explaining the luminescence mechanism of $(ZnS)_{1-x}(AgInS_2)_x$ NCs for (b) x = 1, and (c) x < 1. Valence band and conduction band systematically moves downward and upward respectively, with increase in ZnS content; deep mid-gap defect levels remain largely unaltered. This scenario leads to a systematic blue shift in emission path-1 depending upon the shift in valence/conduction band with decreasing x, but energy of path-2 remains unaltered for similar sized NCs.

Table 2.1: Expected Coulomb energies for different D-A pair distance in $AgInS_2$.

D-A distance, r (nm)	Coulomb energy, $e^2/4\pi\varepsilon_o\varepsilon r$ (meV)
1	151
2	76
3	50
4	38
5	30
6	25
7	22

In order to distinguish the contributions of two paths in Figure 2.2a-c, we prepared $(ZnS)_{1-x}(AgInS_2)_x$ solid solution NCs where valence/conduction band shift with composition, but the

size of NCs remains unchanged, therefore with not much change in the D-A pair distance. Figure 2.2c shows the schematic energy level diagram for $(ZnS)_{1-x}(AgInS_2)_x$ (x <1) solid solution NCs in comparison with Figure 2.2a,b for $AgInS_2$ (x = 1) NCs. There might be some spread in the energy level of defect states based on composition and local environment, however for simplicity we have not altered the defect state energies in both schematics in Figure 2.2b and 2.2c. Since both the size of the NC and hence distance between D-A pairs remains similar for all x, D-A pair transition (path-2) energy should not vary much with composition, as opposed to our observation in Figure 2.1d. Furthermore, the lifetime of path-2 is also expected to be similar for all compositions, since there is no systematic change in the wavefunction overlap of D-A pairs for similar sized NCs.

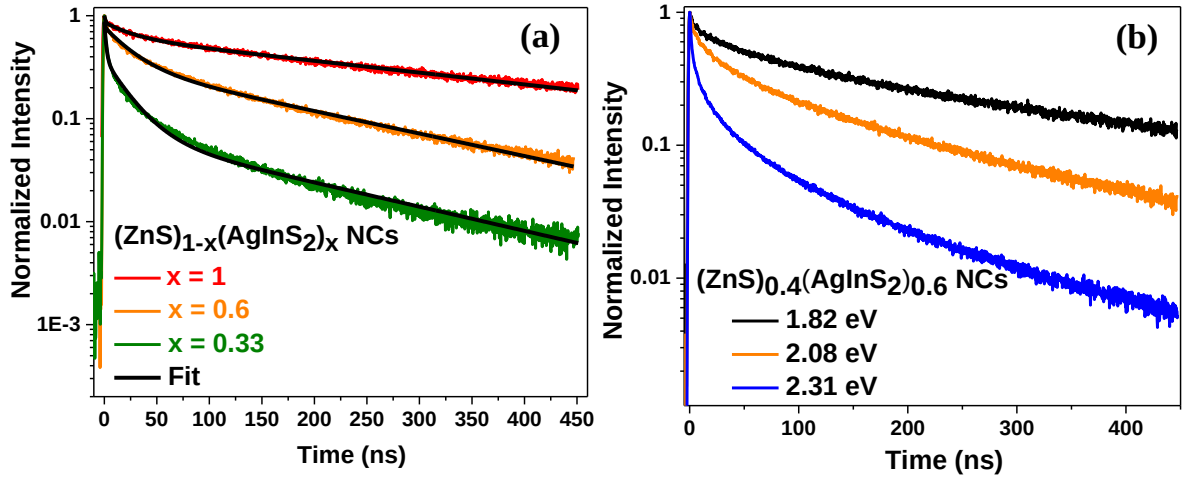

Figure 2.3: PL decay dynamics of colloidal $(ZnS)_{1-x}(AgInS_2)_x$ NCs for different x, after excitation at 2.7 eV (459 nm). Emission energies were fixed at the peak positions of corresponding steady state spectrum shown in Figure 2.1d. b) PL decay dynamics of colloidal $(ZnS)_{0.4}(AgInS_2)_{0.6}$ NCs at three different emission energies of the broad spectrum. Excitation was at 2.7 eV (459 nm) for all three spectrum. The steady state PL of the sample is given in Figure 2.1d of the manuscript.

Table 2.2: The best fit parameters of photoluminescence decay profiles of $(ZnS)_{1-x}(AgInS_2)_x$ solid solution NCs in Figure 2.3, using tri-exponential decay: $I(t) = a_1\exp(-t/\tau_1) + a_2\exp(-t/\tau_2) + a_3\exp(-t/\tau_3)$.

Composition x	Energy (eV)	a_0 (%)	τ_0 (ns)	a_1 (%)	τ_1 (ns)	a_2 (%)	τ_2 (ns)
1	1.70	16	0.9	24	27	60	380
0.6	2.08	11	0.9	52	26	37	199
0.33	2.27	55	1	37	23	8	185

Figure 2.3a shows the PL decay for $(ZnS)_{1-x}(AgInS_2)_x$ NCs with x = 1, 0.6 and 0.33. The emission energies were fixed at the corresponding emission maxima obtained from Figure 2.1d. Clearly, the decay becomes faster with decreasing x. These decays can be fitted with three exponentials, and the best fit parameters are given in Table 2.2. For all samples, two radiative channels are observed with lifetimes $\tau_1 \sim 25$ ns and $\tau_2 > 185$ ns, similar to previous studies[6, 10, 24]. We assign the faster (τ_1) decay to path-1 (delocalized-localized transitions) and slower (τ_2) decay to path-2 (localized-localized transition). A sub-nanosecond ($\tau_0 = \sim 0.9$ ns) decay that typically arises from nonradiative decay channels is also observed, which is more prominent for x = 0.33 composition. The amplitude, a_2 for τ_2 (path-2) sharply decreases with decreasing x. For x = 1, path-2 has 60% contribution in the overall PL decay which decreases systematically to only 8% for x = 0.33, suggesting a minor contribution of D-A transition in the PL for x = 0.33. Further, to compare the relative contributions only from radiative processes τ_1 and τ_2, excluding the non-radiative τ_0, %values for $a_1/(a_1+a_2)$ and $a_2/(a_1+a_2)$ have been extracted from Table 2.2. It shows that the relative radiative contribution for path-2, $a_2/(a_1+a_2)$ in %, systematically decreases from 81% for x = 1 to 41% and 18% for x = 0.6 and 0.33 respectively. In contrast, contribution from path-1 increases from 29% for x = 1 to 60% and 82% for x = 0.6 and 0.33 respectively. These data suggest the light emission for x = 0.33 (lower x) has very minor contribution from D-A pair transition, in sharp difference to prior reports[5-6, 24-25], and instead almost entirely governed by path-1. This large contribution from path-1 can explain the similar trend in the change in band gap and PL peak position with different compositions shown in Figure 2.1f. Interestingly, the steady state PL spectra (Figure 2.1e and ref[28]) with intermediate compositions x, having comparable contributions from both emission paths 1 and 2, also show the possibility of convolution of two broad emission features. It is to be noted that though majority of I-III-VI NCs reports suggest D-A pair transition as origin of PL,[19] some reports[18, 23, 32] also suggested path-1 type transitions in $CuInS_2$ and $CuInSe_2$ based NCs.

It has been commonly observed that for a given sample of $(ZnS)_{1-x}(AgInS_2)_x$ NCs, the PL decay at lower energy end of the spectrum is slower, as shown in Figure 2.3b for x=0.6 composition. Such inhomogeneous lifetimes at different energies of a given spectrum can also be explained within our model considering contributions from both path-1 and path-2 (D-A pair) in Figure 2.2. The blue shift in PL observed for $AgInS_2$ NCs with increasing excitation intensity shown in ref.[24] can also be explained within our model. Lower energy transition path-2 with longer lifetime saturates faster with increasing excitation intensity

compared to path-1 having a shorter lifetime, therefore, effectively increasing the higher energy path-1 contribution at higher excitation intensity. Next we discuss the structural aspect of $(ZnS)_{1-x}(AgInS_2)_x$ NCs.

2.3.3 Structural characterization of $(ZnS)_{1-x}(AgInS_2)_x$ NCs

XRD patterns in Figure 2.4 show a systematic shift of peak position towards higher 2θ values similar to previous report[29] indicating the contraction of the lattice parameters with incorporation of ZnS. The broad nature of XRD pattern makes it difficult to distinguish between chalcopyrite and zinc-blende structure of $(ZnS)_{1-x}(AgInS_2)_x$ NCs, which makes the application of Vegard's law[33] of alloy formation somewhat uncertain. This XRD shift is also accompanied with systematic blue shift in absorption spectra with incorporation of ZnS suggest the formation of $(ZnS)_{1-x}(AgInS_2)_x$ solid solution. However, the formation of smaller $AgInS_2$ core in $AgInS_2$/ZnS core/shell NCs with increase in ZnS precursor cannot be excluded completely.[34] Further, energy dispersive x-ray spectroscopy (EDS) data of these NCs found to be x = 1, 0.61 and 0.37, respectively for composition, x = 1, 0.6 and 0.33, also matches with precursor concentration.

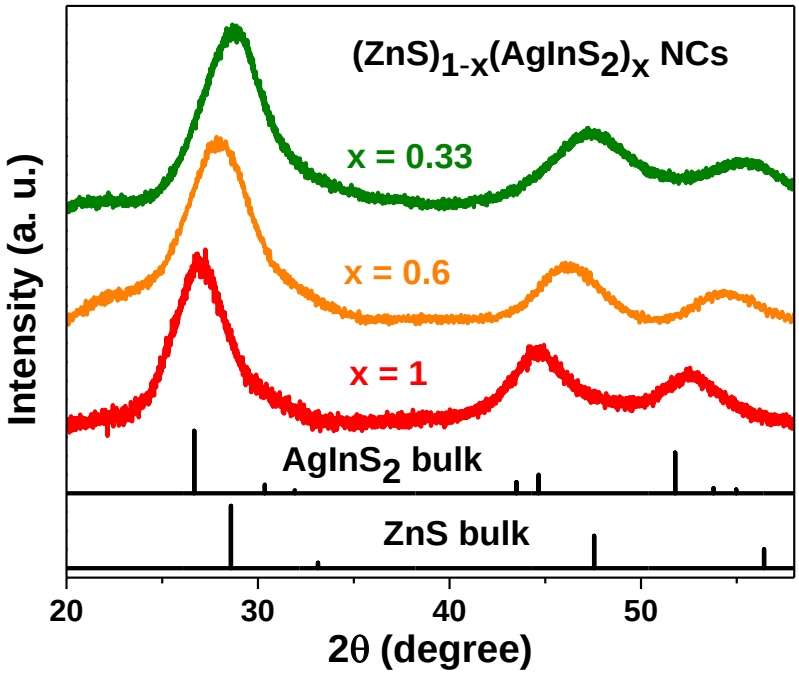

Figure 2.4: Powder XRD data for $(ZnS)_{1-x}(AgInS_2)_x$ NCs with different compositions x. Reference patterns for bulk ZnS and $AgInS_2$ are also given. The patterns are shifted vertically for a clear representation.

We carried out XAFS study on $(ZnS)_{1-x}(AgInS_2)_x$ NCs in order to elucidate the local structure. Zn K edge (9658 eV), Ag K edge (25514 eV), and In K edge (27940 eV) were

measured using high brilliance synchrotron radiation at 10ID in Advanced Photon Source, Argonne National Laboratory. The Extended x-ray absorption fine structure (EXAFS) data were processed using Athena,[35] by extracting the EXAFS oscillations χ(k) as a function of photoelectron wavenumber k following standard procedures.[36]

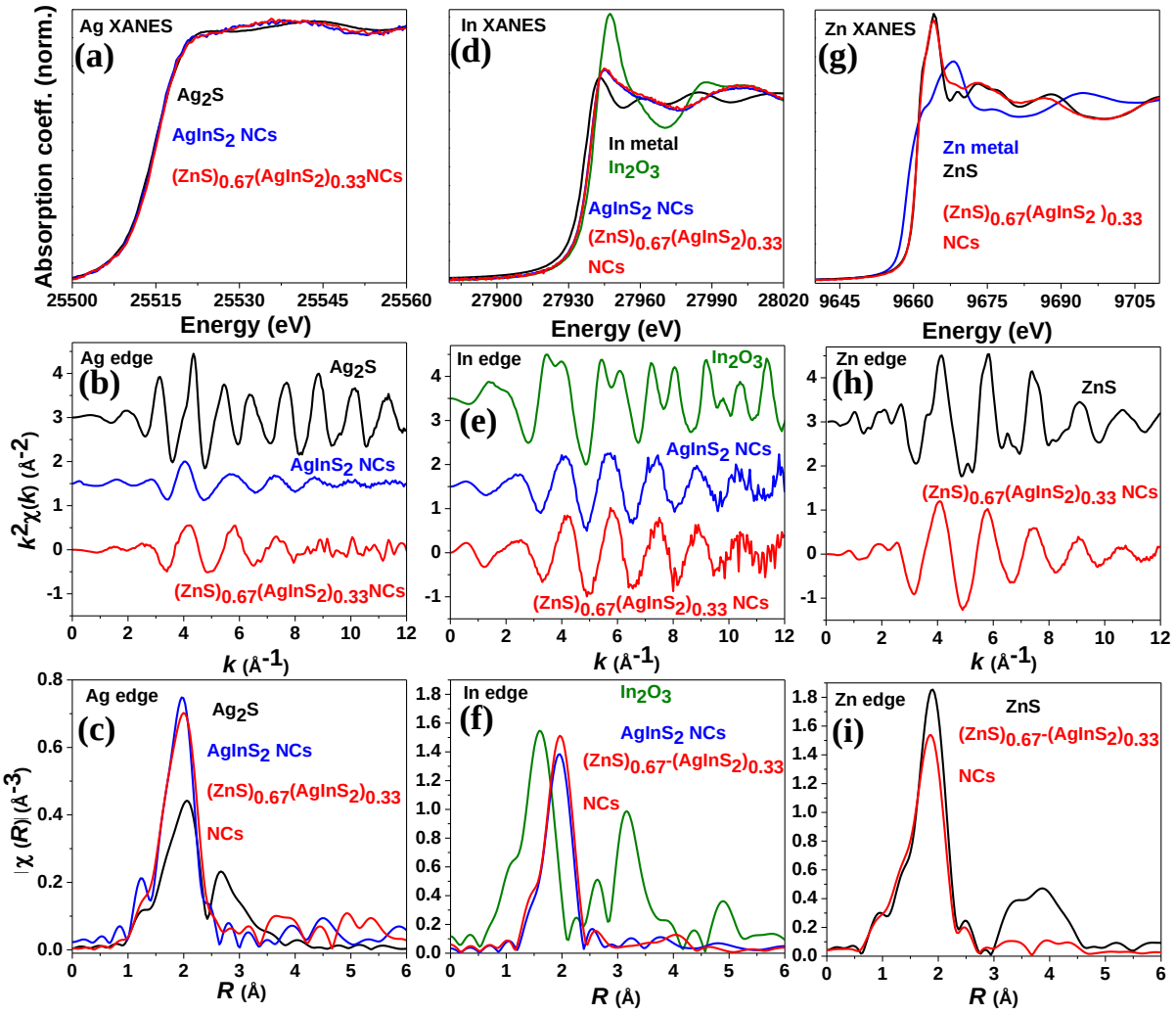

Figure 2.5: (a-c) Ag K edge data for bulk Ag_2S standard, $AgInS_2$ NCs and $(ZnS)_{0.67}(AgInS_2)_{0.33}$ NCs: (a) XANES, (b) k^2 weighted χ(k) data and (c) magnitude of Fourier transformed data in R-space. (d-f) In K-edge data: (d) XANES, (e) k^2 weighted χ(k) data and (f) magnitude of Fourier transformed data in R-space for NC samples and bulk standards. (g-i) Zn K-edge data for ZnS-$AgInS_2$ NCs and bulk standards: (g) XANES, (h) k^2 weighted χ(k) data and (i) magnitude of Fourier transformed data in R-space. k^2 weighted χ(k) data for $AgInS_2$ NCs in (b) and (e) have shifted vertically by 1.5 for a better representation. Likewise, data for Ag_2S, In_2O_3 and ZnS in (b), (e) and (h) have been shifted vertically by 3, 3.5 and 3 respectively.

The theoretical paths were generated using FEFF6 code implemented in Artemis fitting software.[35] The real (R) space data χ(R) were obtained by a Fourier transform of k^2 weighted

χ(*k*). XAFS data of Ag K-edge, In K-edge, and Zn K-edge for $(ZnS)_{1-x}(AgInS_2)_x$ NCs (x = 1 and 0.33) along with different bulk standards are shown in Figure 2.5a-c, Figure 2.5d-f, and Figure 2.5g-i respectively. Data for both (x = 1 and 0.33) NC samples were fitted and a representative fit for $(ZnS)_{0.67}(AgInS_2)_{0.33}$ NCs for all three edges are shown in Figure 2.6. The obtained best fit parameters for both NC samples are tabulated in Table 2.3.

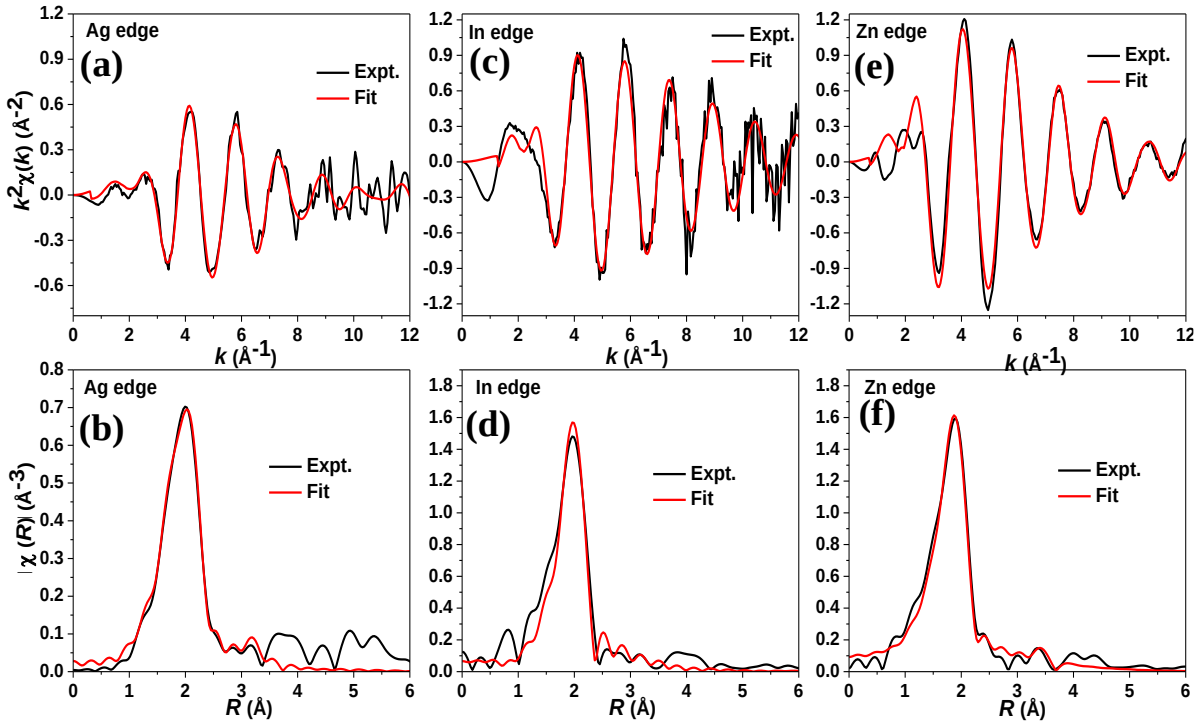

Figure 2.6: Fitting of k^2 weighted χ(k) data and magnitude of Fourier transformed data in R-space for Ag (a and b), In (c and d) and Zn (e and f) for $(ZnS)_{0.67}(AgInS_2)_{0.33}$ NCs. R space data $\tilde{\chi}(R)$ is obtained by Fourier transform of k^2 weighted χ(k) data where k = 2-11Å^{-1} was transformed. In both k space and R space data, most of the contributions are from the first neighbors, and features from the farther neighbors (faster oscillations in χ(k)) are very small. Thus the data were fitted only for the first nearest neighbor. Note that due to the photoelectron phase shift (φ_j) the Fourier peaks appear at shorter distance than the actual bond lengths.

Figure 2.5a shows that Ag K edge x-ray absorption near edge structure (XANES) of both $(ZnS)_{1-x}(AgInS_2)_x$ NC samples with x = 1 and 0.33 are similar to each other, and also the edge energy is similar to that of reference Ag_2S suggesting Ag is in 1+ oxidation state in our NCs. However, Ag_2S has somewhat different features compared to our NCs owing to different structural aspects.[37] χ(R) for Ag-edge in Figure 2.5c shows only one peak corresponding to one Ag-S bond length, clearly different from the standard Ag_2S which shows existence of different Ag-S bond lengths similar to previous report[37]. Fitting of k^2

weighted $\chi(k)$ and R-space data (Figure 2.6a and b; Table 3) show nearest neighbor Ag-S bond length for both $(ZnS)_{1-x}(AgInS_2)_x$ NCs is about 2.52 Å, similar to bulk[38] $AgInS_2$. The coordination number (CN) for Ag-S is slightly smaller than the ideal CN of 4 expected from chalcopyrite or orthorhombic structure both with tetrahedral coordination. This small decrease in CN is probably due to surface termination of NCs where the metal ions do not have MS_4 tetrahedron.[39] The 2nd nearest neighbor Ag-S-metal correlation is weak for both the NC samples.

Table 2.3: Best fit parameters for the first shell Ag-S, In-S and Zn-S for $(ZnS)_{1-x}$-$(AgInS_2)_x$ NCs with x = 1 and 0.33 by fitting R space data. The R space data were obtained by Fourier transform of k^2 weighted $\chi(k)$ data where k_{min} = 2 $Å^{-1}$, k_{max} = 11 $Å^{-1}$ are transformed. The goodness of the fit (r factor) are less than 0.01.

(N=Coordination Number, R=bond length, σ^2=mean square displacement of the distance between the atoms).

NC Sample	Bond	N	R (Å)	$\sigma^2(Å^2)$
$AgInS_2$	Ag-S	3.47 ±0.27	2.523±0.009	0.009± 0.001
	In-S	3.66 ±0.67	2.447±0.017	0.004± 0.002
$(ZnS)_{0.67}(AgInS_2)_{0.33}$	Zn-S	3.15±0.24	2.327±0.006	0.0075±0.0009
	Ag-S	3.48 ±0.36	2.504±0.009	0.010± 0.001
	In-S	3.86 ±0.59	2.452±0.017	0.004± 0.002

In-edge energies of XANES (Figure 2.5d) of NC samples are similar to that of In_2O_3 and different from In metal suggesting In is in 3+ oxidation state in our NCs. k^2 weighted $\chi(k)$ (Figure 2.5e) and R-space (Figure 2.5f) In-edge data are similar for both NC samples, and is clearly different from the standard In_2O_3. R-space data shows longer nearest neighbor In-S bond in NCs compared In-O bond lengths suggesting absence of any unwanted oxide formation, also 2nd nearest neighbor correlation is present in the standard In_2O_3 but absent in our NC samples. Fitting (Figure 2.6c and 2.d) of k^2 weighted $\chi(k)$ and R-space data show nearest neighbor In-S bond length for both $(ZnS)_{1-x}(AgInS_2)_x$ NC samples is about 2.45 Å, with CN slightly lower than the ideal tetrahedral coordination. The smaller InS_4 tetrahedra (In-S bond length 2.45 Å) compared to AgS_4 tetrahedra (Ag-S bond length 2.52 Å) is because of the smaller ionic radius of tetrahedral In^{3+} compared to tetrahedra Ag^+.[40] On the other hand S is expected to be surrounded by two Ag and two In, so the 2nd nearest neighbor metal-S-metal correlation is not expected to be prominent in the EXAFS of solid solution

nanocrystals. Further, the large surface/volume ratio of our NCs can contribute in the blurring of 2nd nearest neighbor correlation.

Zn-edge XANES data for $(ZnS)_{0.67}(AgInS_2)_{0.33}$ NCs in Figure 2.5g shows Zn is in 2+ oxidation state similar to reference ZnS. However, reference ZnS shows distinct feature at ~9668.7 eV which got blurred for $(ZnS)_{0.67}(AgInS_2)_{0.33}$ NCs. Similarly, R-space data (Figure 2.5i) for Zn-edge also shows the absence of Zn-S-Zn 2nd nearest neighbor correlation for $(ZnS)_{0.67}(AgInS_2)_{0.33}$ NCs ~4 Å, which is clearly visible for reference ZnS. Owing to small size, NC samples typically do not show second neighbor correlations, however, some NCs can show such correlations. Thus the complete absence of second nearest neighbor correlations in our $(ZnS)_{0.67}(AgInS_2)_{0.33}$ NCs may not be solely because of the size-effect, but also because of random occupation of second neighbor sites by Zn, Ag and In suggesting the formation of solid solution. Absence of this feature in our NC sample can be because of both formation of solid solution and small NC size. Fitting (Figure 2.6e and f) of k^2 weighted $\chi(k)$ and R-space data yields Zn-S bond length 2.33 Å similar to that of ZnS reference (2.35 Å) and is smaller than that of both Ag-S (2.52 Å) and In-S (2.45 Å). The similarity in nearest neighbor (Zn-S) bond length between the solid solution and the end-member ZnS is rather commonly observed fact.[41]

2.3.4 Photoluminescence vs structure

PL depends on very small concentration of defects. On the other end, structural investigations based on XRD, high resolution TEM and EXAFS can be insensitive to probe defects at such smaller concentrations. However, our EXAFS results, in combination with XRD and UV-visible data agrees with the formation of $(ZnS)_{1-x}(AgInS_2)_x$ solid solution NCs. Our detailed structural investigation showing no detectable phase separated products further builds the confidence of our PL analysis. In $AgInS_2$ NCs, defects can originate from different bonding nature of Ag-S and In-S and typical defects can be Ag vacancy/interstitial, sulfur vacancy/interstitial, In in the place of Ag or vice-versa. Unfortunately, so far, not much is known about the exact nature of defects in $AgInS_2$ NCs that is responsible for PL transitions. Incorporation of Zn in the lattice has been reported to reduce some of these defect densities,[10] which might reduce the contribution of path-2 with increasing ZnS content. Another possibility is that, as the energy difference between defects states and valence/conduction band increases with incorporation of ZnS, nonradiative relaxation of electron or hole to the

respective defect states can be slower requiring multiphonon processes,[42] thereby, reducing contribution from path-2.

2.4 Conclusions

In conclusion, $(ZnS)_{1-x}(AgInS_2)_x$ NCs allowed us to change the band gap simply by changing the composition but without changing the size of the NCs (~ 5 nm). Therefore, if the luminescence mechanism is D-A pair transition, as suggested previously, the D-A pair distance is expected to be same for all NC samples with different x, and are anticipated to exhibit similar emission energy and lifetime. In sharp contrast, we observe a systematic change in PL peak position that is quantitatively comparable with the change in band gap with composition x, and also the PL decay is significantly faster for smaller x. Furthermore, the PL peak blue-shifts by 0.57 eV which is too high to be explained by any change in D-A pair Coulomb interaction energy. Clearly, these experimental observations cannot be explained by previously assigned D-A pair transition, instead, we put forward a new light emission mechanism that has contributions from two paths.

Path-1 involves delocalized valence/conduction band and localized defect states exhibiting higher emission energy with smaller lifetime (~25 ns), and path-2 involves two localized donor and acceptor states with lower emission energy and longer lifetime (>185 ns). Contribution from path-1 increases systematically with decreasing x, and in fact for x = 0.33, the emission is mostly governed by path-1. This large contribution from path-1 can explain the large (0.57 eV) and systematic blue shift in PL spectra, similar to the change in band gap, with composition x. XANES and EXAFS results for Ag K-edge, In K-edge and Zn K-edge elucidates the local structure of $(ZnS)_{1-x}(AgInS_2)_x$ NCs for the first time for all x > 0. Nearest neighbor Ag-S and In-S bond lengths were found to be 2.52 and 2.45 Å respectively, for $AgInS_2$ (x = 1) NCs and solid solutions having tetrahedral coordination. Zn-S bond length is found to be 2.33 Å for $(ZnS)_{0.67}(AgInS_2)_{0.33}$ NCs, with no 2^{nd} nearest neighbor Zn-S-metal correlation.

References

1. Tsuji, I.; Kato, H.; Kobayashi, H.; Kudo, A. Photocatalytic H_2 Evolution Reaction from Aqueous Solutions over Band Structure-Controlled $(AgIn)_{(x)}Zn_{2(1-x)}S_2$ Solid Solution Photocatalysts with Visible-Light Response and Their Surface Nanostructures. *J. Am. Chem. Soc.* **2004**, *126,* 13406-13413.

2. Peng, S. J.; Zhang, S. Y.; Mhaisalkar, S. G.; Ramakrishna, S. Synthesis of $AgInS_2$ Nanocrystal Ink and Its Photoelectrical Application. *Phys. Chem. Chem. Phys.* **2012**, *14,* 8523-8529.

3. Sasamura, T.; Okazaki, K.; Kudo, A.; Kuwabata, S.; Torimoto, T. Photosensitization of ZnO Rod Electrodes with $AgInS_2$ Nanoparticles and ZnS-$AgInS_2$ Solid Solution Nanoparticles for Solar Cell Applications. *RSC Adv.* **2012**, *2,* 552-559.

4. Guchhait, A.; Pal, A. J. Copper-Diffused $AgInS_2$ Ternary Nanocrystals in Hybrid Bulk-Heterojunction Solar Cells: Near-Infrared Active Nanophotovoltaics. *ACS Appl. Mater. Interfaces* **2013**, *5,* 4181-4189.

5. Takahashi, T.; Kudo, A.; Kuwabata, S.; Ishikawa, A.; Ishihara, H.; Tsuboi, Y.; Torimoto, T. Plasmon-Enhanced Photoluminescence and Photocatalytic Activities of Visible-Light-Responsive ZnS-$AgInS_2$ Solid Solution Nanoparticles. *J. Phys. Chem. C* **2013**, *117,* 2511-2520.

6. Uematsu, T.; Doko, A.; Torimoto, T.; Oohora, K.; Hayashi, T.; Kuwabata, S. Photoinduced Electron Transfer of ZnS-$AgInS_2$ Solid-Solution Semiconductor Nanoparticles: Emission Quenching and Photocatalytic Reactions Controlled by Electrostatic Forces. *J. Phys. Chem. C* **2013**, *117,* 15667-15676.

7. Deng, M. J.; Shen, S. L.; Wang, X. W.; Zhang, Y. J.; Xu, H. R.; Zhang, T.; Wang, Q. B. Controlled Synthesis of $AgInS_2$ Nanocrystals and Their Application in Organic-Inorganic Hybrid Photodetectors. *CrystEngComm* **2013**, *15,* 6443-6447.

8. Torimoto, T.; Ogawa, S.; Adachi, T.; Kameyama, T.; Okazaki, K. I.; Shibayama, T.; Kudo, A.; Kuwabata, S. Remarkable Photoluminescence Enhancement of ZnS-$AgInS_2$ Solid Solution Nanoparticles by Post-Synthesis Treatment. *Chem. Commun.* **2010**, *46,* 2082-2084.

9. Chang, J. Y.; Wang, G. Q.; Cheng, C. Y.; Lin, W. X.; Hsu, J. C. Strategies for Photoluminescence Enhancement of $AgInS_2$ Quantum Dots and Their Application as Bioimaging Probes. *J. Mater. Chem.* **2012**, *22,* 10609-10618.

10. Tang, X. S.; Ho, W. B. A.; Xue, J. M. Synthesis of Zn-Doped $AgInS_2$ Nanocrystals and Their Fluorescence Properties. *J. Phys. Chem. C* **2012**, *116,* 9769-9773.

11. Manna, G.; Jana, S.; Bose, R.; Pradhan, N. Mn-Doped Multinary CIZS and AIZS Nanocrystals. *J. Phys. Chem. Lett.* **2012**, *3*, 2528-2534.

12. Murray, C. B.; Norris, D. J.; Bawendi, M. G. Synthesis and Characterization of Nearly Monodisperse CdE (E = S, Se, Te) Semiconductor Nanocrystallites. *J. Am. Chem. Soc.* **1993**, *115*, 8706-8715.

13. Talapin, D. V.; Nelson, J. H.; Shevchenko, E. V.; Aloni, S.; Sadtler, B.; Alivisatos, A. P. Seeded Growth of Highly Luminescent CdSe/CdS Nanoheterostructures with Rod and Tetrapod Morphologies. *Nano Lett.* **2007**, *7*, 2951-2959.

14. Dias, E. A.; Sewall, S. L.; Kambhampati, P. Light Harvesting and Carrier Transport in Core/Barrier/Shell Semiconductor Nanocrystals. *J. Phys. Chem. C* **2007**, *111*, 708-713.

15. Santra, P. K.; Kamat, P. V. Tandem-Layered Quantum Dot Solar Cells: Tuning the Photovoltaic Response with Luminescent Ternary Cadmium Chalcogenides. *J. Am. Chem. Soc.* **2013**, *135*, 877-885.

16. Saha, A.; Chellappan, K. V.; Narayan, K. S.; Ghatak, J.; Datta, R.;Viswanatha, R. Near-Unity Quantum Yield in Semiconducting Nanostructures: Structural Understanding Leading to Energy Efficient Applications. *J. Phys. Chem. Lett.* **2013**, 4, 3544−3549.

17. Xie, R. G.; Rutherford, M.; Peng, X. G. Formation of High-Quality I-III-VI Semiconductor Nanocrystals by Tuning Relative Reactivity of Cationic Precursors. *J. Am. Chem. Soc.* **2009**, *131*, 5691-5697.

18. Li, L. A.; Pandey, A.; Werder, D. J.; Khanal, B. P.; Pietryga, J. M.; Klimov, V. I. Efficient Synthesis of Highly Luminescent Copper Indium Sulfide-Based Core/Shell Nanocrystals with Surprisingly Long-Lived Emission. *J. Am. Chem. Soc.* **2011**, *133*, 1176-1179.

19. Zhong, H. Z.; Bai, Z. L.; Zou, B. S. Tuning the Luminescence Properties of Colloidal I-III-VI Semiconductor Nanocrystals for Optoelectronics and Biotechnology Applications. *J. Phys. Chem. Lett.* **2012**, *3*, 3167-3175.

20. Pradhan, N.; Goorskey, D.; Thessing, J.; Peng, X. G. An alternative of CdSe Nanocrystal Emitters: Pure and Tunable Impurity Emissions in ZnSe Nanocrystals. *J. Am. Chem. Soc.* **2005**, *127*, 17586-17587.

21. Nag, A.; Chakraborty, S.; Sarma, D. D. To dope Mn^{2+} in a semiconducting nanocrystal. *J. Am. Chem. Soc.* **2008**, *130*, 10605-10611.

22. Hazarika, A.; Layek, A.; De, S.; Nag, A.; Debnath, S.; Mahadevan, P.; Chowdhury, A.; Sarma, D. D. Ultranarrow and Widely Tunable Mn^{2+}-Induced Photoluminescence from Single Mn-Doped Nanocrystals of ZnS-CdS Alloys. *Phys. Rev. Lett.* **2013**, *110*.

23. Tan, Z. N.; Zhang, Y.; Xie, C.; Su, H. P.; Liu, J.; Zhang, C. F.; Dellas, N.; Mohney, S. E.; Wang, Y. Q.; Wang, J. K.; Xu, J. Near-Band-Edge Electroluminescence from Heavy-Metal-Free Colloidal Quantum Dots. *Adv. Mater* **2011**, *23*, 3553-3558.

24. Ogawa, T.; Kuzuya, T.; Hamanaka, Y.; Sumiyama, K. Synthesis of Ag-In binary sulfide nanoparticles-structural tuning and their photoluminescence properties. *J. Mater. Chem.* **2010**, *20*, 2226-2231.

25. Hamanaka, Y.; Ogawa, T.; Tsuzuki, M.; Kuzuya, T. Photoluminescence Properties and Its Origin of $AgInS_2$ Quantum Dots with Chalcopyrite Structure. *J. Phys. Chem. C* **2011**, *115*, 1786-1792.

26. Rockenberger, J.; Troger, L.; Kornowski, A.; Vossmeyer, T.; Eychmuller, A.; Feldhaus, J.; Weller, H. EXAFS Studies on the Size Dependence of Structural and Dynamic Properties of CdS Nanoparticles. *J. Phys. Chem. B* **1997**, *101*, 2691-2701.

27. Nag, A.; Kumar, A.; Kiran, P. P.; Chakraborty, S.; Kumar, G. R.; Sarma, D. D. Optically Bifunctional Heterostructured Nanocrystals. *J. Phys. Chem. C* **2008**, *112*, 8229-8233.

28. Torimoto, T.; Adachi, T.; Okazaki, K.-i.; Sakuraoka, M.; Shibayama, T.; Ohtani, B.; Kudo, A.; Kuwabata, S. Facile Synthesis of $ZnS{-}AgInS_2$ Solid Solution Nanoparticles for a Color-Adjustable Luminophore. *J. Am. Chem. Soc.* **2007**, *129*, 12388-12389.

29. Torimoto, T.; Adachi, T.; Okazaki, K.; Sakuraoka, M.; Shibayama, T.; Ohtani, B.; Kudo, A.; Kuwabata, S. Facile synthesis of ZnS-$AgInS_2$ solid solution nanoparticles for a color-adjustable luminophore. *J. Am. Chem. Soc.* **2007**, *129*, 12388-12389.

30. Mao, B. D.; Chuang, C. H.; Wang, J. W.; Burda, C. Synthesis and Photophysical Properties of Ternary I-III-VI $AgInS_2$ Nanocrystals: Intrinsic versus Surface States. *J. Phys. Chem. C* **2011**, *115*, 8945-8954.

31. Shay, J. L.; Tell, B.; Schiavon.Lm; Kasper, H. M.; Thiel, F. Energy-Bands of $AgInS_2$ in Chalcopyrite and Orthorhombic Structures. *Phys. Rev. B* **1974**, *9*, 1719-1723.

32. Nose, K.; Omata, T.; Otsuka-Yao-Matsuo, S. Colloidal Synthesis of Ternary Copper Indium Diselenide Quantum Dots and Their Optical Properties. *J. Phys. Chem. C* **2009**, *113*, 3455-3460.

33. Vegard, L. Die Konstitution der Mischkristalle und die Raumfüllung der Atome. *Z. Phys.* **1921**, *5*, 17.

34. Yang, X.; Tang, Y.; Tan, S. T.; Bosman, M.; Dong, Z.; Leck, K. S.; Ji, Y.; Demir, H. V.; Sun, X. W. Facile Synthesis of Luminescent $AgInS_2{-}ZnS$ Solid Solution Nanorods. *Small* **2013**, *9*, 2689–2695

35. Ravel, B.; Newville, M. J. ATHENA, ARTEMIS, HEPHAESTUS: Data Analysis For X-Ray Absorption Spectroscopy Using IFEFFIT. *Synchrot. Radiat* **2005**, *12*, 537−541.

36. *X-ray Absorption, Principles, Applications, Techniques of EXAFS, SEXAFS and XANES*; Korningsberger, D. C.,Prins, R., Eds.; JohnWiley & Sons: New York, 1988.

37. Kashida, S.; Watanabe, N.; Hasegawa, T.; Iida, H.; Mori, M.; Savrasov, S. Electronic Structure of Ag_2S, Band Calculation and Photoelectron Spectroscopy. *Solid State Ionics* **2003,** *158, 1*67-175.

38. Delgado, G.; Mora, A. J.; Pineda, C.; Tinoco, T. Simultaneous Rietveld refinement of three phases in the Ag-In-S semiconducting system from X-ray powder diffraction. *Mater. Res. Bull.* **2001,** *36, 2*507-2517.

39. Nag, A.; Chung, D. S.; Dolzhnikov, D. S.; Dimitrijevic, N. M.; Chattopadhyay, S.; Shibata, T.; Talapin, D. V. Effect of Metal Ions on Photoluminescence, Charge Transport, Magnetic and Catalytic Properties of All-Inorganic Colloidal Nanocrystals and Nanocrystal Solids. *J. Am. Chem. Soc.* **2012,** *134, 1*3604-13615.

40. Shannon, R. D. Revised Effective Ionic-Radii and Systematic Studies of Interatomic Distances in Halides and Chalcogenides. *Acta Crystallogr., Sect. A* **1976,** *32*, 751−767.

41. Santangelo, S. A.; Hinds, E. A.; Vlaskin, V. A.; Archer, P. I.; Gamelin, D. R. Bimodal Bond-length Distributions in Cobalt-Doped CdSe, ZnSe, and $Cd_{1-x}Zn_xSe$ Quantum Dots. *J. Am. Chem. Soc.* **2007,** *129, 3*973-3978.

42. Cooney, R. R.; Sewall, S. L.; Anderson, K. E. H.; Dias, E. A.; Kambhampati, P. Breaking the Phonon Bottleneck for Holes in Semiconductor Quantum Dots. *Phys. Rev. Lett.* **2007,** *98,* 177403.

Chapter 3

Synthesis of Organic- Free $AgInS_2$ and Other Metal Sulfide Nanocrystals for Solar Cell Applications

---

The following papers have been published based on the work presented in this chapter.

1. Rao, M. J.; Kadlag, K. P.; Nag, A. Ligand-Free, Colloidal, and Luminescent Metal Sulfide Nanocrystals. *J. Phys. Chem. Lett.* **2013**, *4*, 1676-1681. Copy right permission has been taken from American Chemical Society for the entire paper.

2. Kadlag, K. P.; Patil, P.; Jagadeeswara Rao, M.; Datta, S.; Nag, A. Luminescence and solar cell from ligand-free colloidal $AgInS_2$ nanocrystals. *CrystEngComm* **2014**, *16*, 3605-3612. Reproduced with permission from the Royal Society of Chemistry.

Summary

We report here a different kind of binary and ternary colloidal inorganic nanocrystals, where no organic capping ligand is used. Surface of these organic-free nanocrystals were designed to exhibit negative charges, and therefore, electrostatically repel each other, forming a colloidal dispersion in a polar solvent. Undoped and Mn-doped $Zn_xCd_{1-x}S$ nanocrystals were studied both in solution and close-packed films. While undoped samples exhibit poor luminescence because of surface defects, Mn-doped nanocrystals show strong luminescence both in solution (20% quantum efficiency) and film. Organic-free $AgInS_2$ nanocrystals display significant defect-related sub-band gap photo-absorption in addition to the excitonic absorption. The post-synthesis annealing of the nanocrystal dispersion at 150 °C reduces the intrinsic defect density, and also increases the nanocrystal size (5.8 nm) thereby reducing surface related defects. Organic-free $AgInS_2$ nanocrystals sensitized solar cell was fabricated which exhibit a maximum power conversion efficiency of 0.8% and an open circuit voltage of 0.45 V. The device performance is better compared to previous $AgInS_2$ nanocrystal based solar cells, due to both the use of the organic-free nanocrystals that improve the charge transport and the post-synthesis annealing which partially removes the mid-gap defect states.

Graphical abstract

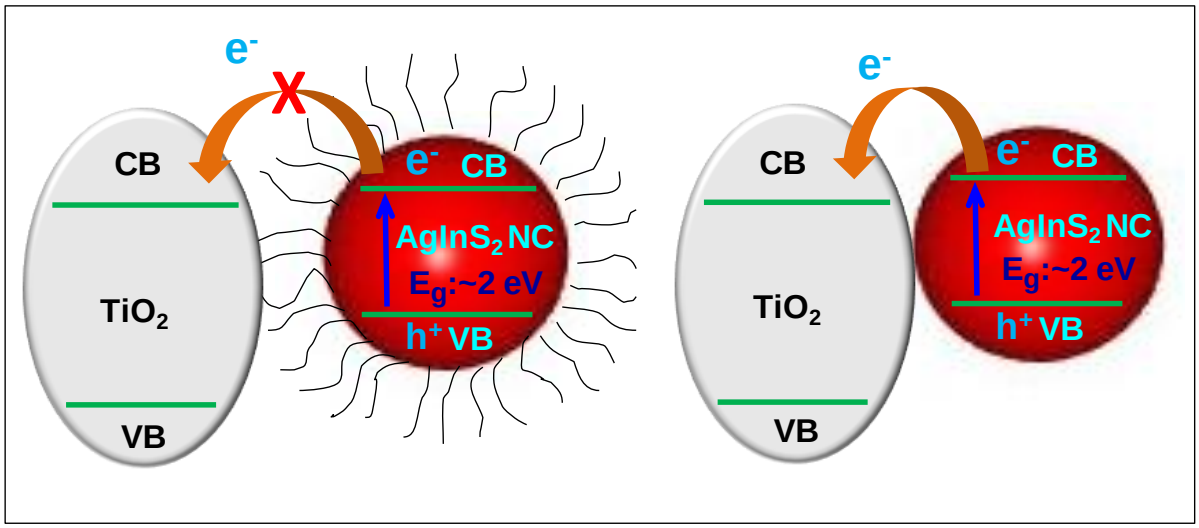

3.1 Introduction

Synthesis of colloidal semiconductor nanocrystals (NCs) has been reported since 1982.[1] Subsequently, different organic capping ligands, particularly short-chain thiols and reverse micelles were developed for aqueous (polar solvent) synthesis of group II-VI semiconductor NCs.[2-5] There are also few reports on non-generic synthesis of all-inorganic colloidal NCs,[6-10] for example,[6] $(NaPO_3)_6$ passivated CdS NCs. Development of hot-injection technique (200-360 ^oC) revolutionized the colloidal synthesis of NCs obtaining narrow size distribution, using long hydrocarbon chain organic capping.[11-12] These colloidal NCs typically have an inorganic/organic hybrid structure. While the property of an individual NC is mainly governed by the inorganic core, its interaction with surrounding environment is governed by the organic capping ligand.

Often, the organic ligands have long hydrocarbon chain (8-18 carbons), and are insulating in nature. Therefore, films of such hybrid NCs, irrespective of the nature (metallic or semiconductor) of the inorganic core, behaves like an insulator.[13] Consequently, a post-synthesis modification of NC surface is required in order to get rid of the insulating ligands, prior to their use in an electronic and optoelectronic device. Two major approaches have already been employed: in one, the surface modification is carried out after making the film of insulating organic capped NCs,[14-19] and in the other approach,[20-24] the modification is done in solution phase. There are some complications for film processing approach: (i) removal of organic ligands (~25 wt% loss) generates cracks in the film and tedious layer-by-layer film casting is required to obtain a crack-free film,[18] (ii) small molecules like hydrazine that replaces bulky organic ligands are volatile in nature making the device unstable,[16] and (iii) incomplete removal of organic species. Talapin *et al.* developed molecular metal chalcogenide (MCC)[20] and simple chalcogenide[22] ligands for modification of NC surface in the solution phase. Band-like electronic transport was observed from the film of $In_2Se_4^{2-}$ MCC capped CdSe NCs providing a very high electronic mobility of 16 $cm^2V^{-1}S^{-1}$ from a NC film.[25]

All the surface modification approaches discussed above involves at least two steps. In the first step, insulating organic capped NCs were prepared, followed by a post-synthesis ligand exchange/removal reaction in the second step. This requirement of multiple steps is because of the absence of a generic synthesis protocol to prepare organic-free colloidal all-inorganic NCs. Here we report a different, but simple and generic single-step synthesis protocol for colloidal, all-inroganic or organic-free NCs. Binary and ternary metal sulfide NCs of group

II-VI and I-III-VI semiconductors were prepared. To verify the effectiveness of our synthesis protocol, first we prepared and studied simpler II-VI NCs like organic-free CdS, ZnS, and their alloy. Then, organic-free Mn-doped $Zn_xCd_{1-x}S$ NCs were prepared, exhibiting strong luminescence from both solution and film. Finally non-toxic, organic-free $AgInS_2$ NCs were prepared and studied in detail. Organic-free $AgInS_2$ NCs display significant defect-related sub-band gap photo-absorption in addition to the excitonic absorption. The post-synthesis annealing of the nanocrystal dispersion at 150 °C reduces the intrinsic defect density, and also increases the NC size (5.8 nm) thereby reducing surface related defects. These organic-free $AgInS_2$ NCs used in preparing NC sensitized solar cell. 5.8 nm size, $AgInS_2$ NCs sensitized solar cell exhibits photo conversion efficiency 0.8% and open circuit voltage 0.45 V. To the best of our knowledge, the organic-free Mn-doped semiconductor NCs and organic-free $AgInS_2$ NCs were not reported previously, even with multiple-step post-synthesis surface modification.

3.2 Experimental Section

3.2.1 Synthesis of organic-free CdS nanocrystals (NCs)

In a typical reaction, $Cd(ClO_4)_2.H_2O$ (0.2 mmol, 0.0622 g) was dissolved in 10 mL formamide (FA) in a 50 ml three-neck RB flask. The flask was heated to 70 ^oC under N_2 flow, and degassed along with magnetic stirring for about 15 minutes. 100 μL $(NH_4)_2S$ solution (40-48% in water) was diluted by adding 1 mL FA and was injected drop by drop to this hot solution. CdS NCs forms immediately after the injection of S^{2-} precursor and the reaction was carried out for 15 minutes. The reaction mixture was then cooled to room temperature by removing the heat supply, followed by precipitation and washing of NCs using acetonitrile. These NCs can be dispersed in different polar solvents like N-methyl formamide (NMF, dielectric constant, ε = 186), FA (ε = 106), water (ε = 80), dimethylsulfoxide (DMSO, ε = 47) and dimethylformamide (DMF, ε = 36) for solution-based studies, and also can be dried under vacuum at room temperature for powder-based studies.

3.2.2 Synthesis of organic-free $Zn_xCd_{1-x}S$ NCs

Y mmol of $Zn(NO_3)_2.6H_20$ and (0.2 - Y) mmol of $Cd(ClO_4)_2.H_2O$ was used as a cationic precursor solution in 10 mL FA, such that total cationic precursor is 0.2 mmol. Rest of the synthesis procedures is similar to those of organic-free CdS NCs.

3.2.3 Synthesis of organic-free Mn-doped $Zn_xCd_{1-x}S$ NCs

Different amount of Manganese (II) nitrate hexahydrate (0.001, 0.002, 0.003, 0.004, 0.005, or 0.010 mmol) in the range of 0.5 to 5% of 0.2 mmol (Y mmol of $Zn(NO_3)_2.6H_20$ and (0.2 - y) mmol of $Cd(ClO_4)_2.H_2O$) host cationic precursor was added in 10 mL of FA to constitute the cationic solution. Rest of the synthesis procedures is similar to the synthesis of organic-free CdS NCs.

3.2.4 Synthesis of organic-free $AgInS_2$ NCs

A mixture of $AgNO_3$ (0.1 mmol, 0.0169 g) and $In(NO_3)_3.H_2O$ (0.1 mmol, 0.0300 g) were dissolved in 10 mL FA in a 50 ml three neck round bottom flask. The flask was heated up to 70 ^oC under N_2 flow, and degassed along with magnetic stirring for about 15 minutes. 100 µL $(NH_4)_2S$ solution (40-48 wt% in water) was diluted by adding 1 mL FA and was injected slowly to this hot cationic precursor solution. The reaction was carried out for 15 minutes and cooled to room temperature by removing the heat supply. The reaction mixture was then centrifuged at 5000 rpm for 5 minutes, and the supernatant liquid was collected after discarding the precipitate. Acetonitrile was added to the supernatant liquid leading to second precipitation, followed by centrifugation. The obtained second precipitate is the final $AgInS_2$ NC product discussed in this chapter.

3.2.5 Heat treatment of colloidal $AgInS_2$ NCs

The supernatant liquid obtained after 1st precipitation as discussed above was further diluted by two times by adding fresh FA. The dilute $AgInS_2$ NC dispersion is put in to a three-neck round bottom flask maintaining inert atmosphere and subsequently heated to a desired temperature (up to 150 ^oC) for 15 minutes.

3.2.6 Synthesis of oleic acid capped CdS NCs

The synthesis was carried following a reported recipe.[26] 0.0496 g CdO, 0.5 ml of oleic acid and 10 mL 1-Octadecene was degassed with nitrogen for at 120 ^oC for 30 minutes. The reaction mixture was heated up to 300 ^oC forming a clear solution. 0.016 g sulfur was dissolved in 1 mL 1-octadecene. The sulfur solution is then quickly injected to the Cd solution kept at 300 ^oC. The reaction was carried out for ~5 minutes. The solution was cooled down to room temperature, diluted with ~10 mL toluene and precipitated by adding excess of ethanol. The precipitate was redispersed in toluene and again precipitated with acetonitrile, a

process that was repeated thrice. The precipitate was dried under vacuum at room temperature.

3.2.7 Preparation of NC film

NC films are prepared by drop-casting a concentrated solution of NCs on a quartz substrate followed by drying at room temperature. Oleic acid capped NCs were dispersed in hexane, whereas organic-free NCs were dispersed acetonitrile.

3.2.8 Characterization

UV-visible absorption and photoluminescence (PL) spectra of NCs were recorded using a Perkin Elmer, Lambda-45 UV/Vis spectrometer and FluoroMax-4 spectrofluoremeter (HORIBA scientific), respectively. PL quantum efficiency of NCs were measured by using Rhodamine 6G (QE = 95%) in ethanol as a reference dye. Fourier-transform infrared (FTIR) spectra were acquired in the transmission mode using a NICOLET 6700 FTIR spectrometer (Thermo scientific). Thermogravimetric analysis (TGA) data were measured under inert atmosphere using Perkin Elmer STA 6000, simultaneous thermal analyser. ζ-potential were calculated from measured electrophoretic mobility employing Henry's equation in the Smoluchowski limit,[27] using a Zetasizer Nano series, Nano-ZS90 (Malvern Instruments, U.K.). Powder x-ray diffraction (XRD) data were collected by using Bruker D8 Advance Powder XRD diffractometer. Transmission electron microscopy (TEM) data were obtained using a JEOL JEM 2100F microscope operated at 200 kV.

3.3 Results and discussion

3.3.1 Synthesis and characterization of organic-free CdS NCs

Before synthesizing colloidal organic-free $AgInS_2$ NCs which is a complex system, first we illustrate the synthesis of colloidal organic-free CdS NCs, which is a simple and well understood system. Simple addition of Cd^{2+} and S^{2-} ions in a polar solvent like water leads to precipitation of CdS. In order to achieve colloidal CdS NCs, a non-stoichiometric NC surface was formed, for example, by having excess of sulfide (CdS_{1+x}) on the NC surface; schematic of such non-stoichiometric surface is shown in Figure 3.1a. This excess sulfide ion concentration gives rise to a negatively charged NC surface, which was experimentally configured by a negative zeta potential value of -40 mV (Figure 3.1b). The magnitude of this negative charge is large enough to resist agglomeration of NCs in a polar solvent like (FA, dielectric constant, $\varepsilon = 106$) *via* electrostatic repulsion between individual NCs.

The negatively charged NC surface was achieved simply by adding excess S^{2-} precursor compared to Cd^{2+} precursor. Equimolar concentration of Cd^{2+} and S^{2-} leads to the precipitation of CdS under identical reaction conditions. It is to be noted that the non-stoichiometric surface is required not only for the present organic-free colloidal NCs, but also for the traditional organic capped NCs, where the organic ligands are generally electron-rich, and thus bind to cation-rich NC surface.[22, 24] Figure 3.1c shows UV-visible absorption spectrum of the CdS NCs synthesized at 70 °C. A blue-shift in excitonic absorption shoulder compared to the band gap of bulk[28] CdS (2.42 eV, 513 nm) is observed as a result of quantum confinement in CdS NCs. The average size of CdS NCs is calculated[29] using this absorption

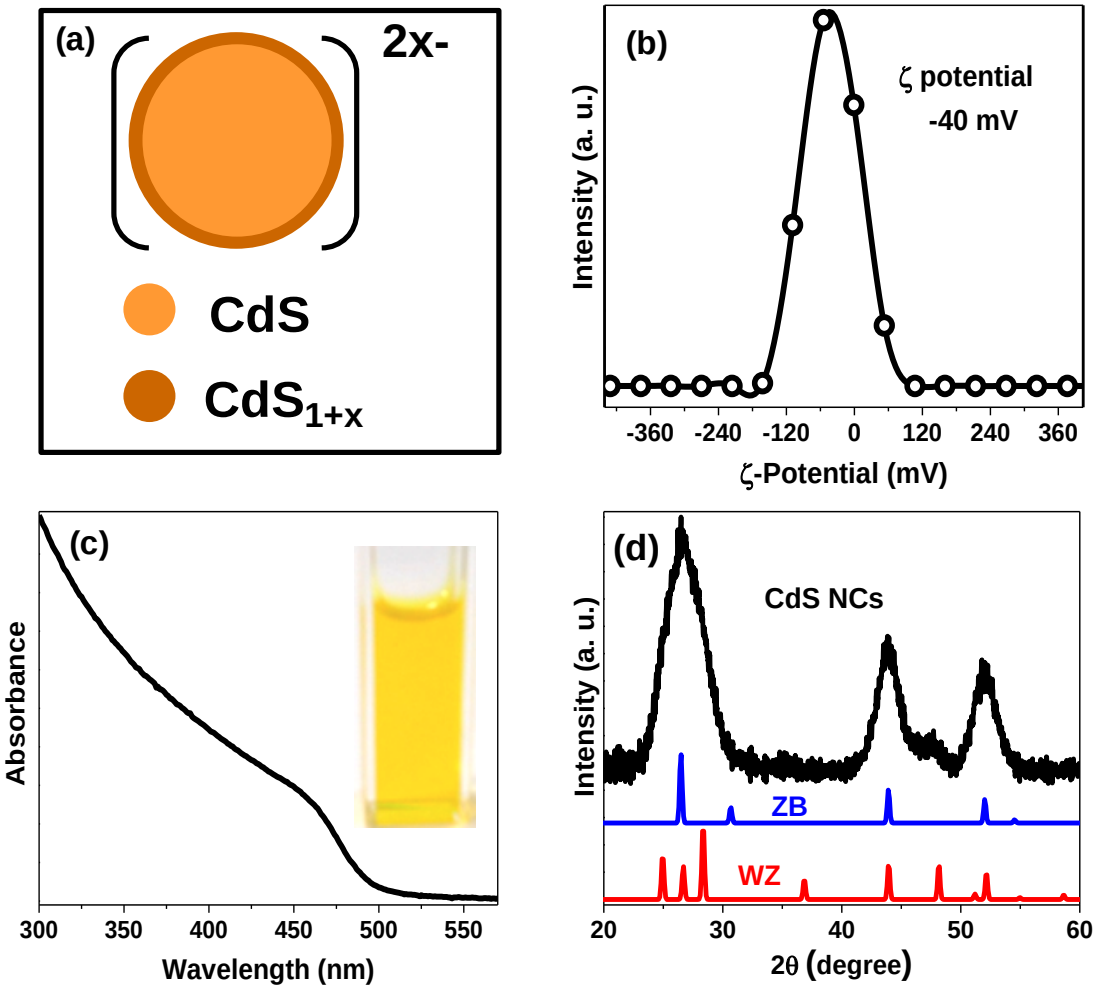

Figure 3.1: (a) Schematic diagram of a organic-free CdS NC with non-stoichiometric excess of S on the surface layer. (b) ζ-potential of organic-free CdS NCs dispersed in formamide. Open circles are experimental data, whereas solid line is a guide to eye. (c) UV-visible absorption spectrum of organic-free CdS NCs dispersed in formamide. Inset shows the photograph of a dispersion of ligand-free CdS NCs in formamide. (d) XRD pattern of ligand-free CdS NCs synthesized at 70 °C.

spectrum is 4.3 nm. Figure 3.1d shows powder x-ray diffraction (XRD) pattern of the CdS NCs corresponding to a predominant wurtzite phase of CdS NCs. Broadening of the XRD peaks owing to the small crystallite size makes the assignment of crystalline phase somewhat complicated.[25]

3.3.2 Surface characterization of organic-free CdS NCs

Thermogravimetric analysis (TGA) data in Figure 3.2a shows less than 4% weight loss upon heating the ligand-free CdS NC powder up to 550 ^{o}C. This weight loss is mainly because of the evaporation of residual FA solvents. However, decomposition of $(NH_4)_2S$ in to gaseous species might also contribute to the weight loss. On the other hand, oleic acid capped CdS NCs of similar size shows a weight loss of 24%, mainly due to the decomposition/evaporation of organic capping ligand. A comparison of FTIR data between organic-free and oleic acid capped CdS NCs in Figure 3.2b shows the absence of CH_2 stretching bands around 2853 and 2920 cm^{-1} for organic-free NCs. However, the FTIR spectrum for organic-free NCs shows features due to solvent (FA or water) molecules. The TGA and FTIR data reveal that our NCs are all-inorganic in nature. However, a small amount of the solvent is found in the NC powder, which can be either residual solvent and/or weakly bound solvent to the NC surface.

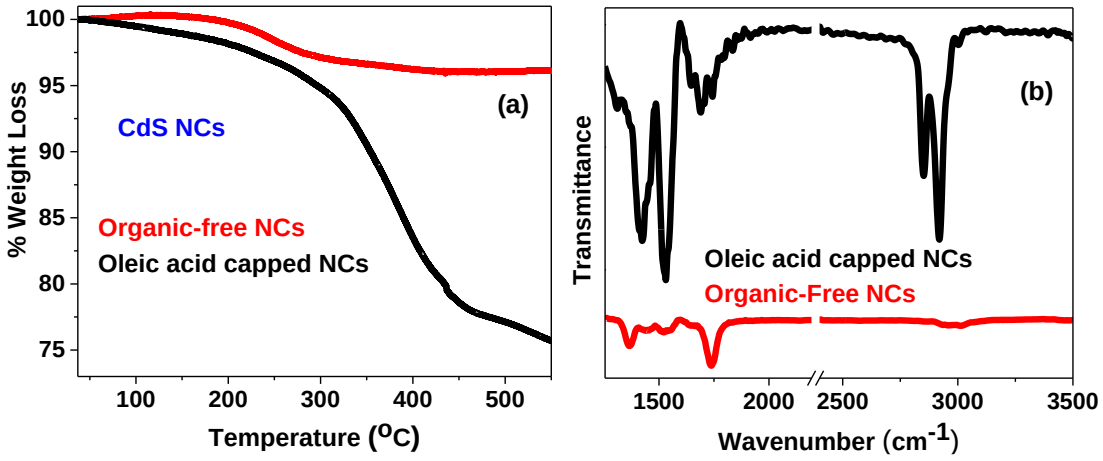

Figure 3.2: (a) Comparison of TGA data of ligand-free and oleic acid capped CdS NCs of similar size. (b) Comparison of FTIR spectra of ligand-free CdS NCs with oleic acid capped CdS NCs.

3.3.3 Phase-transfer reaction of negatively charged organic-free CdS NCs

To probe the surface chemistry further with the idea that if the surface of NCs is negatively charged then it should interact easily with suitable electron deficient molecule. In this regard, a phase transfer reaction was designed where the interacting molecule is dispersed in a non-

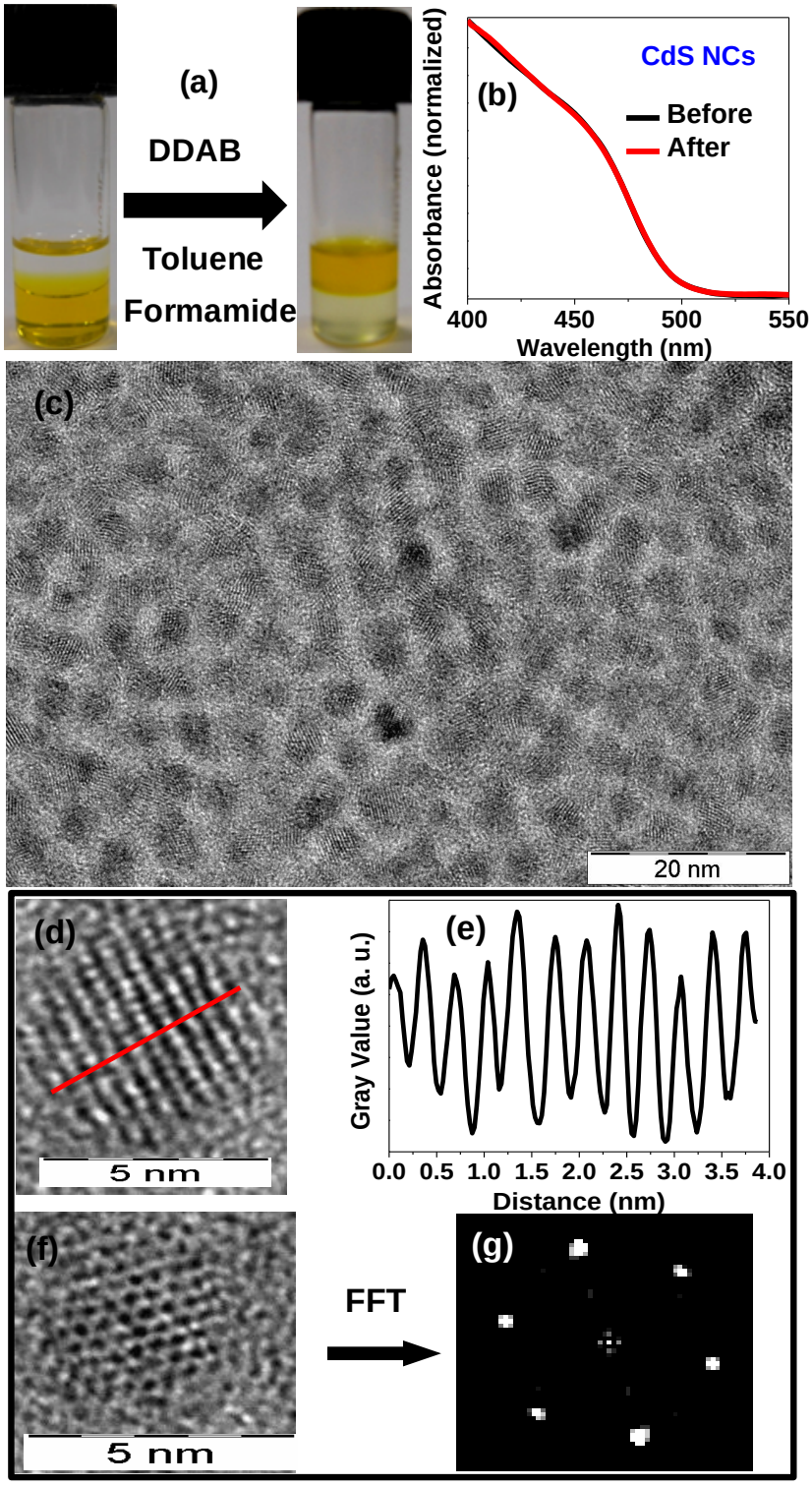

Figure 3.3: (a) Photograph of a phase-transfer reaction of negatively charged organic-free CdS NCs after interacting with didecyldimethylammonium bromide (DDAB). (b) Comparison of UV-visible absorption spectra of ligand-free CdS NCs before and after treating with DDAB. (c) TEM image of DDAB treated CdS NCs. (d) HRTEM image of a DDAB treated organic-free CdS NC. (e) Gray value intensity line profile of the bright and dark spots along a red line taken from Figure 3.3d. (f) HRTEM image of another NC taken from the same sample. (g) FFT pattern of the image shown in Figure 3.3f.

polar phase and the NCs are dispersed in a polar phase. If the interaction between the NC and molecule is strong enough, then the NCs are expected to be transferred from the polar to non-polar phase. S-rich CdS NCs with negatively charged bare surface bind readily with a positively charged quaternary ammonium salt, didecyldimethylammonium bromide (DDAB). S-rich CdS NCs are dispersed in FA, and is immiscible with the nonpolar solvent toluene (Figure 3.3a). However addition of DDAB quickly transfers the NCs in toluene phase because of the binding of DDAB on NC surface.[30] This was evident from the change in ζ-potential value of NCs from -40 mV in FA to ~0 mV in toluene.

The size of NCs remains unaltered during this phase transfer reaction as shown by the UV-visible absorption spectra in Figure 3.3b. TEM image S-rich CdS NCs after the phase transfer reaction with DDAB is shown in Figure 3.3c. NCs are spherical in shape with average diameter of 4.2 nm. The high resolution TEM (HRTEM) data in the inset of Figure 3.3d shows a single crystalline CdS NCs with (100) lattice planes of wurtzite phase with an interplanar distance of 3.52 Å. Figure 3.3e shows the gray-value intensity line profile along the red line as shown in the HRTEM image in Figure 3.3d. The bright and dark spots in Figure 3.3d correspond to the peak and dip in gray-value intensity respectively, in Figure 3.3e. The periodicity of the gray-value intensity throughout the NC indicates single crystalline nature of the organic-free CdS NC. HRTEM image of another NC from the same sample of S-rich CdS after phase transfer reaction with DDAB, along with its corresponding Fast Fourier Transform (FFT) pattern is shown in Figure 3.3f and 3.3g, respectively. FFT shows a hexagonal pattern. The obtained interplanar distance (3.52 Å) along with the hexagonal pattern correspond to (100) planes of wurtzite CdS NCs along the [001] zone axis.

Electron rich molecules like oleic acid and dodecanethiol do not bind on the negatively charged CdS NC surface. Conversely, electron rich oleic acid and dodecanethiol bind to Cd-rich CdS NCs, where electron deficient DDAB fails. We note that Cd-rich CdS NCs can be prepared by using excess of Cd^{2+} precursor, however, these NCs exhibit poor colloidal stability in FA

3.3.4 Structural characterization of organic-free $Zn_xCd_{1-x}S$ NCs and their optical properties

After establishing the synthesis of organic-free CdS NCs, we verified the protocol for the synthesis of other metal sulfide NCs. The protocol developed for the synthesis of organic-free S-rich CdS NCs can be easily extended for the synthesis of $Zn_xCd_{1-x}S$ NCs. The XRD

patterns (Figure 3.4a) of $Zn_xCd_{1-x}S$ NCs shifts systematically from ZnS to CdS with a change in composition. Figure 3.4b-d show that the interplanar distances shifts linearly with composition, x, following Vegard's law[31] of alloy formation.

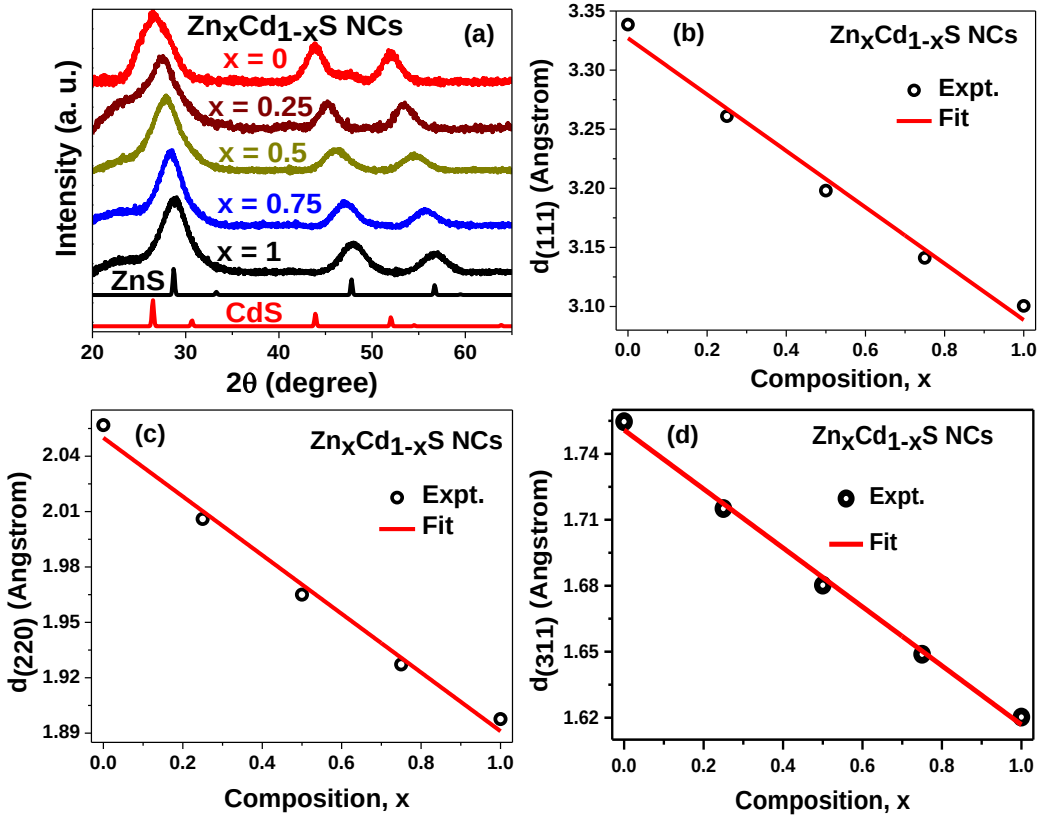

Figure 3.4: (a) XRD patterns of $Zn_xCd_{1-x}S$ NCs. (b) Variation of different interplanar distances (as indicated in the Y-axis label for each plot) with composition "x" for the zinc blende $Zn_xCd_{1-x}S$ NCs, calculated from their corresponding XRD patterns shown in Figure 3.4a. CdS (x = 0) NCs exhibit wurtzite structure, in difference with other compositions, and the interplanar distances for x = 0 is obtained from the standard zinc-blende pattern of bulk CdS.

Expectedly, $Zn_xCd_{1-x}S$ alloy NCs also show a systematic shift in the excitonic absorption energies with a change in composition as shown in Figure 3.5a. The optical band gap increases systematically as x in $Zn_xCd_{1-x}S$ NCs increases from 0 to 1. Figure 3.5b shows the PL data of organic-free $Zn_xCd_{1-x}S$ NCs which corresponds to weak surface-state emission. Often, the poor luminescence of NCs synthesized at a lower temperature (~100 ^oC) is attributed to a poor crystallinity of NCs resulting from the low-temperature reaction. However, certain highly luminescent NCs like CdTe NCs were earlier prepared using low-temperature aqueous synthesis,[32] suggesting that highly crystalline NCs can be achieved even at a lower reaction temperature. The poor luminescence of thiol-capped aqueous CdS and CdSe NCs is rather because of hole scavenging from the valence band of semiconductor NCs

by the ligands, which is energetically not favorable for the case of CdTe NCs.[33]Our results and previous results suggest that poor emission of organic capped $Zn_xCd_{1-x}S$ is probably because of the poor passivation of S-dangling bonds on the surface of NCs. Core of the NCs exhinbit good crystallinity as suggested by the HRTEM images in Figure 3.3. To check it further whether deects in core or surface of NCs is mainly quenching the PL efficiency, we prepare Mn-doped NCs.

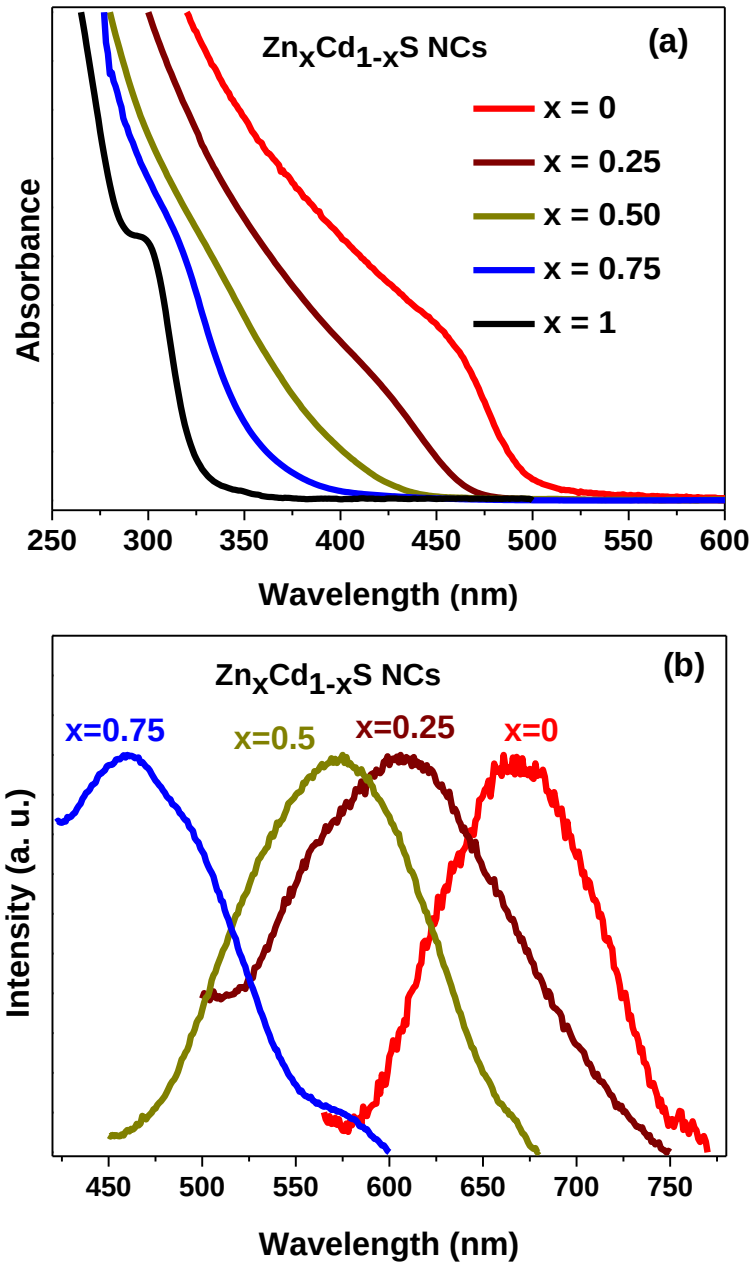

Figure 3.5: a) UV-visible absorption spectra of $Zn_xCd_{1-x}S$ NCs dispersed in formamide. All spectra were normalized at their corresponding maximum absorbance for a better comparison. (b) PL data of colloidal organic-free $Zn_xCd_{1-x}S$ NCs in formamide.

3.3.5 Mn doping in organic-free $Zn_xCd_{1-x}S$ NCs

In order to explore the possibility of strong luminescence from organic-free NCs, we have doped the lattice of $Zn_xCd_{1-x}S$ NCs with Mn^{2+} ion. Mn^{2+} ion in a tetrahedral coordination exhibit an atomic-like inner-core d-d transition ($^4T_1$ to $^6A_1$),[34] emitting light. These d-electrons are largely localized in the Mn^{2+} ion and do not spread over the entire NC. Thus emission coming from a Mn^{2+} ion doped inside the core of a NC is expected to be less susceptible to the surface trap states compared to the excitonic and surface state emission of

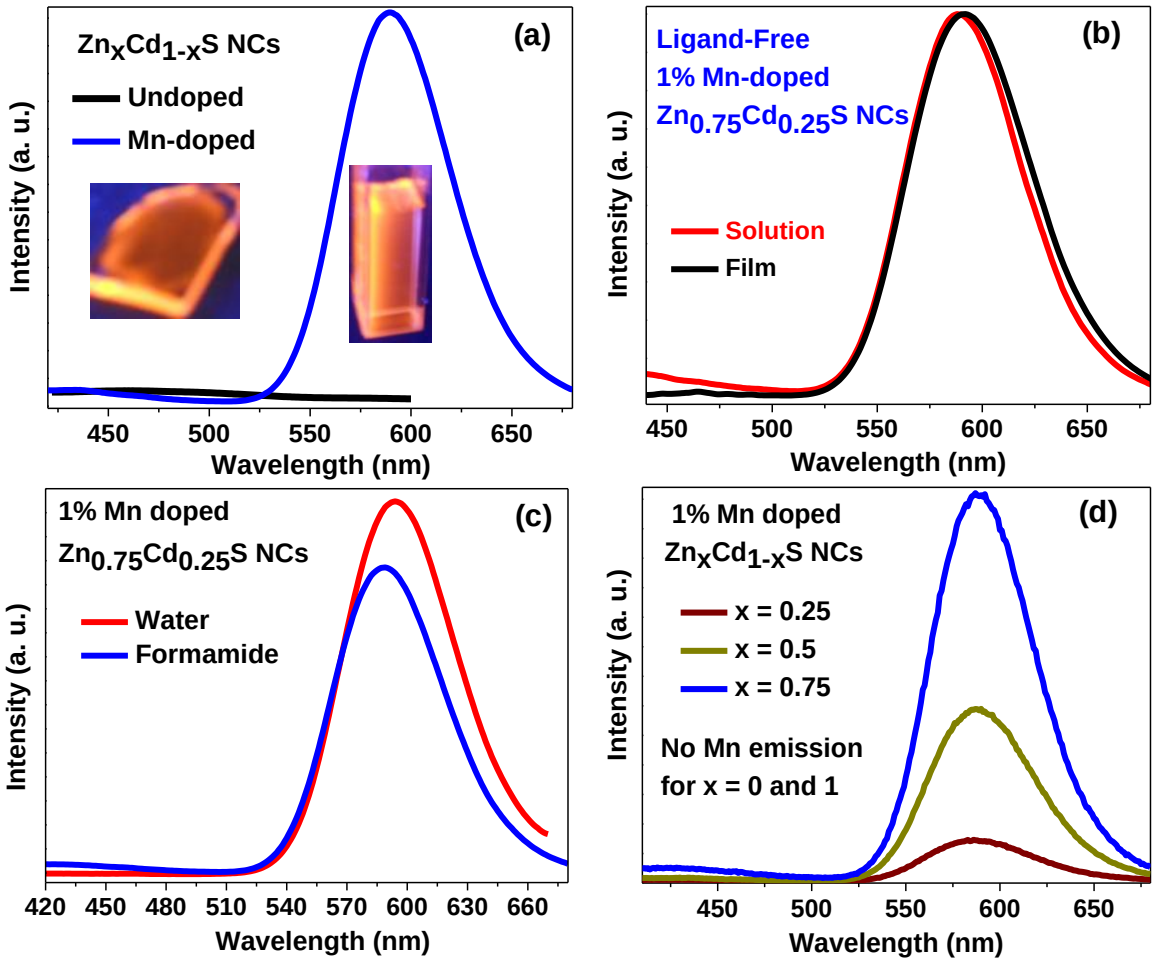

Figure 3.6: (a) PL data of undoped and 1% Mn-doped $Zn_{0.75}Cd_{0.25}S$ NCs dispersed in formamide. Insets show photographs of luminescence from 1% Mn-doped $Zn_{0.75}Cd_{0.25}S$ NCs in formamide solution and after casting a film on a quartz substrate. 365 nm UV light was used to excite the NCs, which is slightly smaller than the optical gap and falls in the tail of absorption spectra. (b) Comparison of PL spectra of ligand-free 1% Mn doped $Zn_{0.75}Cd_{0.25}S$ NCs dispersed in formamide with that of NC film on quartz substrate. (c) Comparison of PL spectra of 1% Mn doped $Zn_{0.75}Cd_{0.25}S$ NCs dispersed in formamide and water. (d) Comparison of PL data of 1% Mn-doped $Zn_xCd_{1-x}S$ NCs with different host compositions. PL intensities for all samples were normalized by their corresponding absorbance at the excitation wavelength.

the host. Figure 3.6a compares the PL spectra of undoped and 1% Mn-doped $Zn_{0.75}Cd_{0.25}S$ NCs after normalizing the spectra with corresponding absorbance at their excitation wavelength of 350 nm. Clearly, a strong emission peak is observed with a maximum at 588 nm for Mn doped sample.[35-36] The best sample shows a quantum efficiency of 20%, when measured using Rhodamine 6G as a reference dye. Insets of Figure 3.6a show photographs of luminescence from both solution and film of the Mn-doped NCs after excitation with 365 nm UV light. PL spectra for both solution and film are similar as shown in Figure 3.6b. Interestingly, the NC precipitate obtained after synthesis in FA, can be re-dispersed in water (which is an essential solvent for biomedical applications), without decreasing the Mn^{2+} emission intensity as shown in Figure 3.6c.

Figure 3.6d shows that Mn^{2+} emission intensity is the highest emission intensity for x = 0.75. This highest emission intensity 1% Mn doped $Zn_{0.75}Cd_{0.25}S$ NCs is not because of different extent of Mn doping in different hosts. Instead, because of higher energy of the surface state emission for x = 0.75 (Figure 3.5b) compared to the energy of Mn d emission, that allows energy transfer from surface states to Mn d states. Such an energy transfer process populates excited Mn d states, which then de-excited by emitting light. Surface state energies red-shift with decreasing x, and can even have lower energies compared to the Mn d emission energy, where energy transfer from surface states to Mn d states is suppressed. However, the excitonic energy transfer from host to Mn is possible for all three hosts with x = 0.25, 0.5, 0.75. It is to be noted that, for a given composition of the host (x = 0.25 or 0.5 or 0.75), maximum PL intensity is observed for about 1% Mn doping, when the doping level is varied step-wise between 0.5 to 5%. Similar results were obtained previously for organic capped NCs as well, thereby, suggesting that the non-interacting Mn^{2+} ions are the most luminescent ones.[37] The % of Mn mentioned here are the precursor concentrations of Mn.

3.3.6 Electronically coupled NC films

Measuring the electron (hole) mobility by making a filed effect transistor (FET) is one of the popular method to quantitatively measure electronic communication in NC films.[25] Here we present preliminary qualitative data on possible electronic coupling between adjacent NCs by measuring excitonic absorption of NCs in their dilute dispersion and in close-packed film.[20] Figure 3.7a shows that UV-visible absorption spectra of oleic acid capped CdS NCs are similar for both dilute dispersion and film. However, a red-shift is observed in absorption spectrum of film of organic-free CdS NCs compared to their dispersion in FA (Figure 3.7b). Dispersion of organic-free NCs exhibits an optical gap of 478 nm (2.59 eV), whereas the film

exhibit a gap of 487 nm (2.54 eV). Interestingly, re-dispersing the NC film in FA, reversibly change the absorption spectrum back to the original one with 478 nm optical gap. This reversible red-shift in absorption spectrum of the film of organic-free NCs suggests possible electronic coupling between adjacent NCs in their film.[20] In a close packed film of organic-free NCs, the tail of electronic wavefunctions can spread over multiple adjacent NCs, and consequently, exhibit a red-shift in excitonic absorption. No such red-shift is observed for the film of oleic acid capped NCs because of insulating organic ligand that inhibit spreading of electronic wavefunctions between adjacent NCs. Thus, organic-free NCs can be promising candidates for solar cell applications. We reemphasize that our results only suggest a possible electronic coupling between organic-free NCs, however, transport measurements are required in order to draw an unambiguous conclusion.

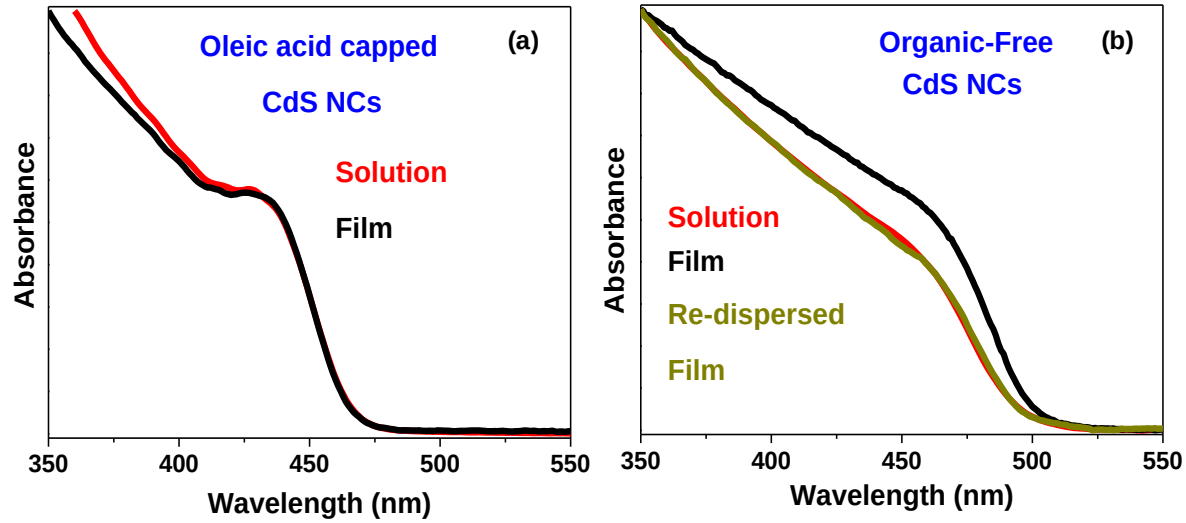

Figure 3.7: (a) Comparison of UV-visible absorption spectrum of oleic acid capped CdS NCs dispersed in toluene with that of NC film on quartz substrate. (b) Comparison of UV-visible absorption spectra of ligand-free NCs in different forms: formamide solution, film on a quartz substrate, and after redispersing the NC film in formamide.

3.3.7 Synthesis of organic-free $AgInS_2$ NCs

However, organic-free CdS NCs with optical band gap ~ 450 nm is not sufficient enough to absorb good amount of sun-light. On the other hand, $AgInS_2$ exhibits direct band gaps of 1.87 and 1.98 eV correspond to chalcopyrite and orthorhombic crystal phases, respectively, at room temperature.[38] The band gap is suitable for absorption and emission of visible light, and thus $AgInS_2$ is an interesting alternative for both photovoltaic, light emitting and other optoelectronic applications.[39-45] Importantly, $AgInS_2$ is non-toxic as opposed to cadmium chalcogenides. Therefore, we have extended the organic-free synthesis further to group I-III-

VI based semiconductor NCs. Organic-free $AgInS_2$ NCs were prepared by reacting a solution of Ag^+ and In^{3+} with excess of S^{2-} in a polar solvent like FA at 70 °C. Figure 3.8a shows the XRD pattern for organic-free colloidal $AgInS_2$ NCs which corresponds to the orthorhombic-phase $AgInS_2$ (JCPDS 025-1328) NCs. Figure 3.8b shows TEM image of organic-free $AgInS_2$ NCs and size of NCs is 2.5 nm. Figure 3.8c shows selected area electron diffraction (SAED) pattern which also shows the formation of orthorhombic phase of $AgInS_2$ NCs. These NCs exhibit a negative ζ-potential of -39 mV shown by Figure 3.9d. Hence, similar to previously discussed II-VI semiconductor NCs, $AgInS_2$ NCs form colloidal dispersion in a polar solvent via electrostatic repulsions between NCs.

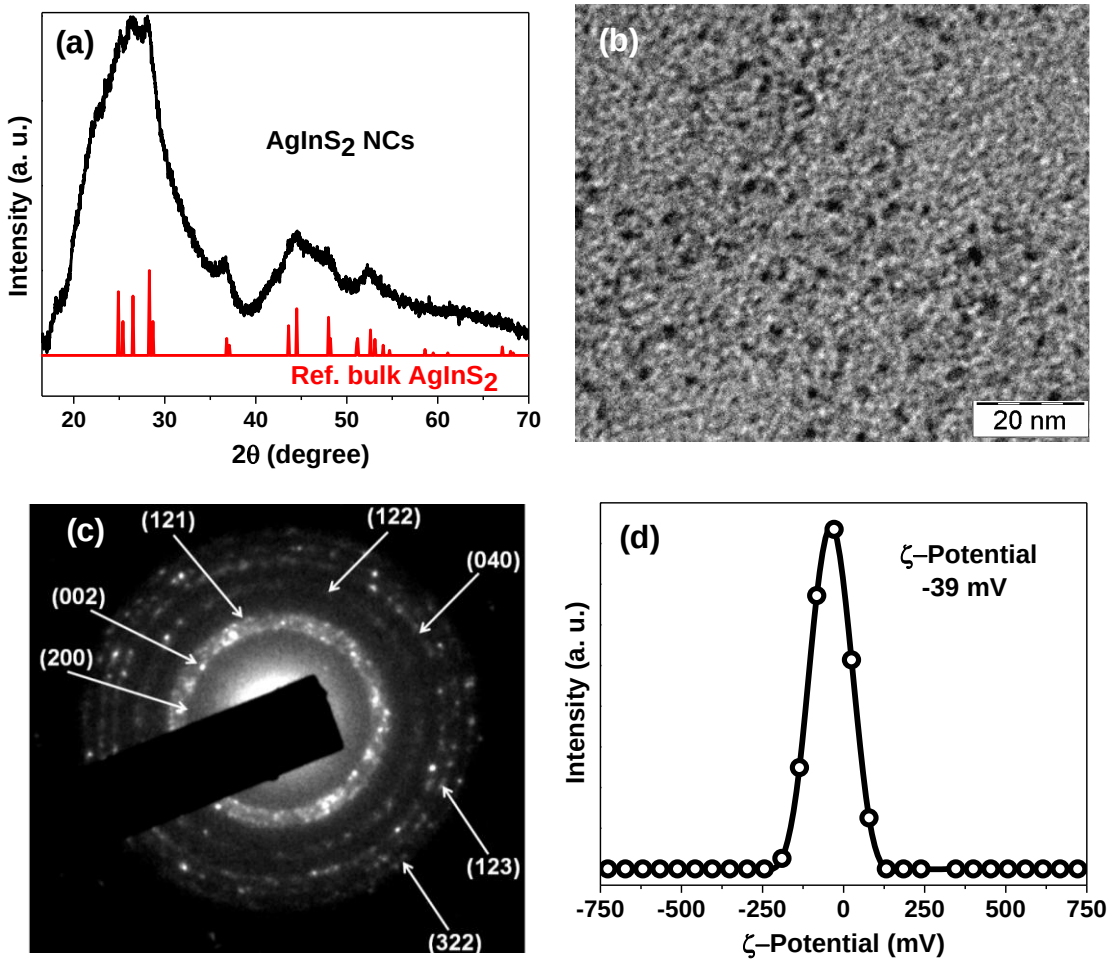

Figure 3.8: (a) XRD pattern, and (b) TEM image of organic-free $AgInS_2$ NCs. (c) Selected area electron diffraction pattern of organic-free $AgInS_2$ NCs showing planes corresponding to orthorhombic phase. (d) ζ-potential of organic-free $AgInS_2$ NCs dispersed in formamide; open circles are experimental data, whereas solid line is a guide to eye.

3.3.8 Surface characterization of organic-free $AgInS_2$ NCs

The FTIR spectrum in Figure 3.9a shows that the NCs are largely organic-free, with negligible contributions from CH_2 stretching bands around 2853 and 2920 cm^{-1}, however, the

signature of the FA solvent molecules is present. However, the FTIR spectrum for organic-free $AgInS_2$ NCs shows features due to solvent (FA or water) molecules. The TGA plot in Figure 3.9b shows ~4% weight loss upon heating the ligand-free $AgInS_2$ NC powder up to 500 °C, and the weight loss is mainly due to the evaporation of the residual FA solvents. This weight loss is significantly small compared to the ~25% weight loss that typically arises from organic capped NCs of a similar size. These negatively charged surface of $AgInS_2$ NCs binds readily with DDAB molecules similar to Figure 3.3a. These results confirm that formation of organic-free $AgInS_2$ NCs.

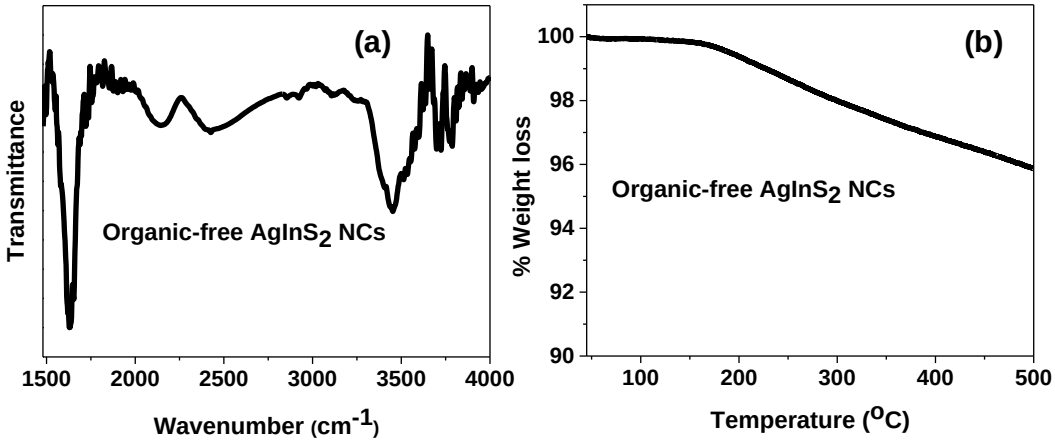

Figure 3.9: (a) FTIR, and (b) TGA data of organic-free $AgInS_2$ NCs synthesized at 70 °C.

3.3.9 Light absorption of organic-free $AgInS_2$ NCs

UV-visible absorption spectrum (Figure 3.10a) of $AgInS_2$ NCs shows a broad featureless spectrum. Unlike II-VI semiconductor NCs, $AgInS_2$ NCs rarely exhibit sharp excitonic features.[39, 42, 45-47] Absence of sharp excitonic features might be because of both broad particle size distribution and/or large density of defect states in the mid-gap region. PL spectrum in Figure 3.10a shows a peak at about 570 nm with full width at half maximum (FWHM) of 110 nm. Such broad emission of $AgInS_2$ NCs was attributed to two kinds of transitions: i) transition between at least one delocalized state (either CB or VB) and localized state, and ii) Transition between two localized states (donor-acceptor type transition) as discussed in the chapter 2. Compared to CdSe NC based emitters, $AgInS_2$ NCs are non-toxic, however, the obtained PL efficiency is <5% when measured using Rhodamine 6G as a reference dye suggesting that many non-radiative defects are present within the band gap of as prepared $AgInS_2$ NCs.

The broad absorption feature can typically arise from NCs with a very broad size distribution. However, in the present case, a significant absorption is observed at energies even below the

band gap of bulk of $AgInS_2$, which cannot be explained by a broader size distribution. Also, the NCs forms a stable colloidal solution even after centrifuging at 7000 rpm for 10 minutes, suggesting the lower energy absorption tail is not arising from scattering of light by agglomerated NCs. Interestingly, when we anneal the colloidal NCs at a higher temperatures such as 125 ^oC and 150 ^oC for 15 minutes each, the absorbance of the tail below bulk band gap decrease, appearing to be a blue shift in the absorption onset shown in Figure 3.10b. $AgInS_2$ NCs heated at 150 ^oC shows appearance of excitonic absorption feature around 2.1 eV, which is higher than the band gaps of both orthorhombic and chalcopyrite $AgInS_2$, suggesting confinement of charge carries in our NCs.

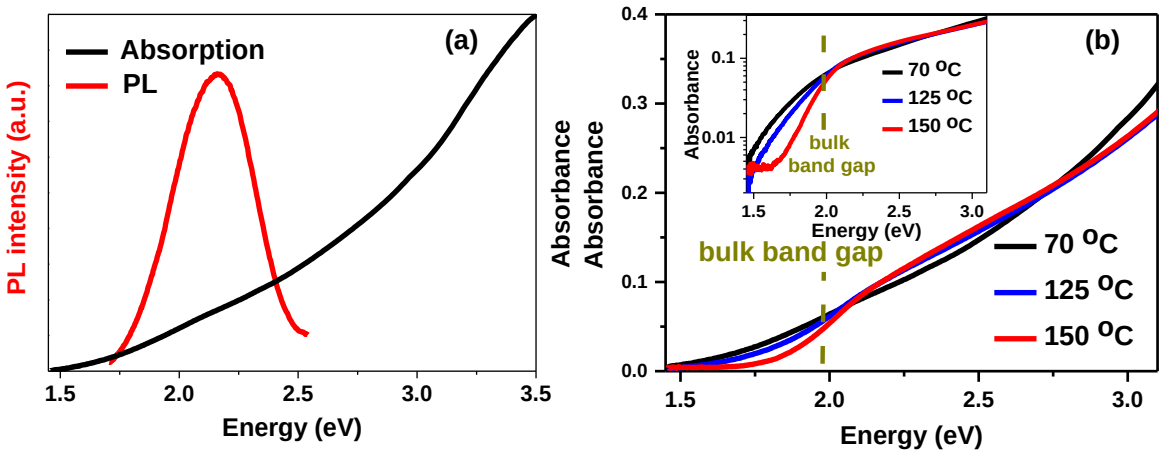

Figure 3.10: (a) UV-visible absorption and PL (excitation at 400 nm) spectra of organic-free colloidal $AgInS_2$ NCs dispersed in formamide. (b) The UV-visible absorption spectra of the colloidal $AgInS_2$ NCs annealed at different temperatures. The NCs were dispersed in a formamide solvent. The inset shows the same absorption spectra but the Y-axis is plotted in a logarithmic scale.

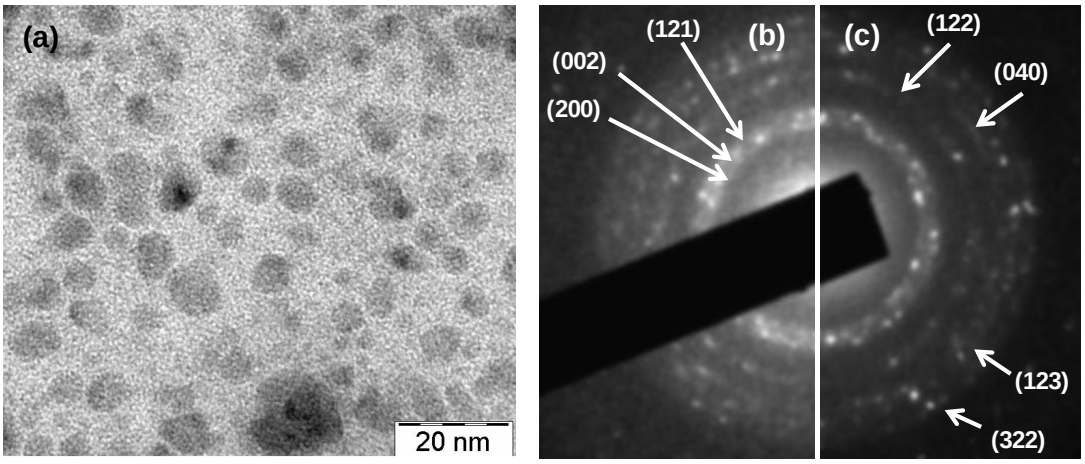

3.11: (a) TEM images of $AgInS_2$ NCs after annealing at 150 ^oC. (b,c) SAED patterns of $AgInS_2$ NCs synthesized at 70 ^oC and after annealing at 150 ^oC, respectively.

Figure 3.11a shows TEM image of $AgInS_2$ NCs after annealing at 150 ^oC. The average diameter of the NCs is 5.8 nm which is larger in size than the NCs prepared at 70 ^oC (2.5 nm). Therefore, the blue-shift in absorption onset in Figure 3.10b is not because of decrease in NC size with increasing processing temperature, in contrast, NC size increased with temperature. SAED patterns in Figures 3.11b and 3.11c show that the crystal structures of NCs remains the same orthorhombic phase during the heat treatment. Therefore, there is no possibility of different crystal structure modifying the band gap during the heat treatment.

The absorption tail at energies lower than the band gap has been observed previously in doped/disordered semiconductors, and is often termed as Urbach tail.[48,49] The absorption coefficient $\alpha(h\nu) \sim \exp(h\nu/E_u)$ over some energy ranges below the band gap, where E_u has been termed as Urbach energy. Plots (inset to Figure 3.10b) of absorbance in logarithmic scale vs photon energy show somewhat linear regions below bulk band gap suggesting the possibility of Urbach tail in our $AgInS_2$ NCs. However, conclusive assignment is not possible from these data since the typical UV-visible absorption spectrometer cannot measure absorbance over several orders of magnitude, which is required to study Urbach tail. Such a tail arises from light absorption involving localized states in the mid gap region. Ag-S and In-S bonds have different strengths, and are known to generate various defects like interstitial Ag, Ag vacancy, S vacancy and interstitial S in bulk $AgInS_2$ crystal.[50-51] These defect states are localized states with poor overlap of electronic wave-functions and typically have a poor absorption coefficient. However, for 2.5 nm $AgInS_2$ NCs, a larger part of the crystal is constituted by surface and sub-surface region having higher defect density. The high defect density, and consequently, closer proximity of defect states, both owing to small NC size, lead to measurable defect-state related absorption in our NCs. In fact, the possibility of Urbach tail from surface defects have been discussed even in the absorption spectrum binary CdSe NC film, where intrinsic defects inside the crystal is minimal, unlike the case of ternary $AgInS_2$ NCs.[52] As the processing temperature of NCs is increased, a systematic decrease is observed in the absorption tail. Increase in processing temperature can (i) improve the crystallinity reducing intrinsic defects, and (ii) increase the NC size reducing surface related defects. In addition to the reduction of defect density resulting lesser number transitions responsible for light absorption, larger size and lesser defect density can increase the spatial separation between defect sites, which reduces the absorption coefficient. Consequently, the final NCs annealed at 150 ^oC show a small increment in the PL intensity.

3.3.10 $AgInS_2$ NCs sensitized solar cell

Having band gap in visible range with high absorption coefficient values and reasonable QY $AgInS_2$ NCs can be promising material in solar cell application. In addition to this, organic-free $AgInS_2$ NCs are expected to allow the charge carrier injection (extraction) from (to) NC to TiO_2 with reasonably good efficiency. We have fabricated sensitized solar cell using organic-free $AgInS_2$ NCs as photo absorber. Figure 3.12a shows the working principle of NC sensitized solar cell. Photo anode made by coating organic-free $AgInS_2$ NCs on top of the

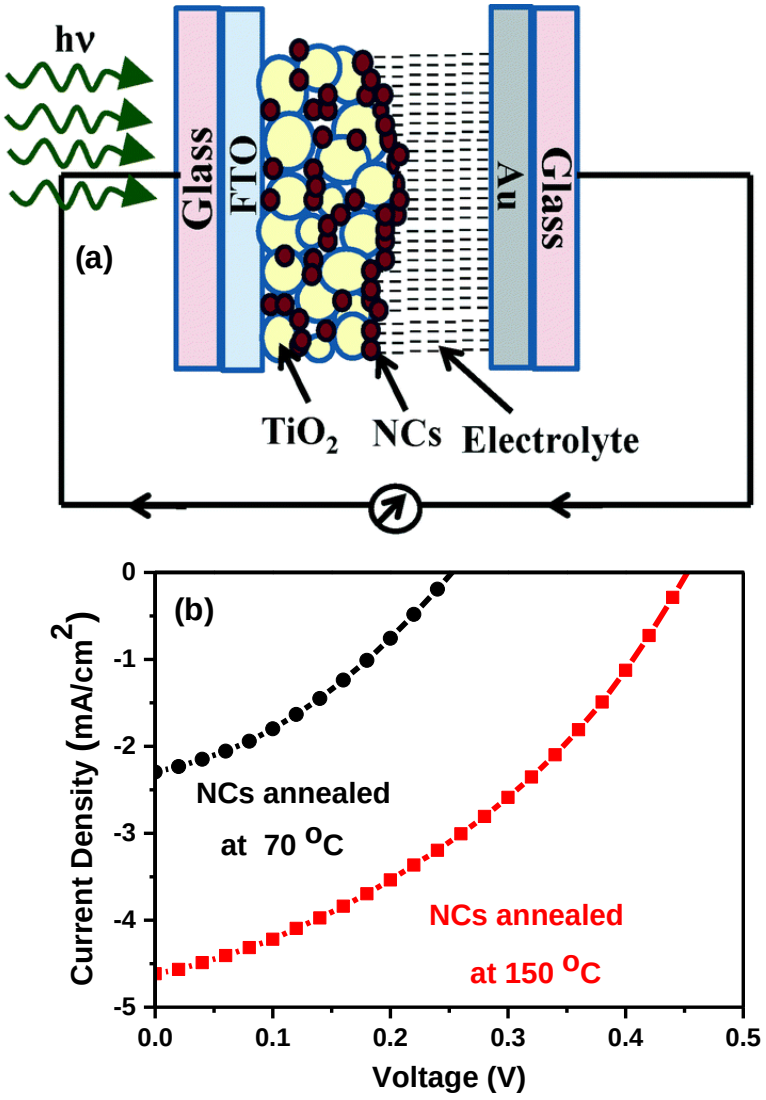

Figure 3.12: a) A schematic diagram representing the working principle of a quantum dot sensitized solar cell (QDSSC). (b) The J–V characteristics of QDSSCs fabricated using two differently processed organic-free $AgInS_2$ NCs: colloidal NCs prepared at 70 °C and annealed at 150 °C. The effective area is 0.16 cm^2 for both cells.

Note: Solar cell device fabrication was carried out by Dr. Padmashri Patil, in the laboratory of Dr. Souvik Datta from Physics Department of IISER-Pune. The complete details can be found in her Ph.D thesis.

TiO_2 film (TiO_2 film made by coating TiO_2 nanoprticals on top of the conducting glass). Poly sulfide was used as an electrolyte and Au electrode (deposited on cleaned FTO glass by dc sputtering) was used as counter electrode. The cell was tested by assembling photo anode and counter electrode using a 50 micron thick scotch tape spacer along with a 10 micro-liter polysulfide electrolyte under Xe-lamp.

Figure 3.12b shows the current density-voltage (J-V) plot for organic-free $AgInS_2$ NCs processed at 70 ^oC and 150 ^oC. Table 3.1 shows the corresponding solar cell parameters such as short circuit current density (J_{sc}), open circuit voltage (V_{oc}), fill factor (FF) and photo conversion efficiency (PCE). The PCE values clearly indicating that $AgInS_2$ NCs annealed at 150 ^oC shows better performance than NCs synthesized at 70 ^oC. This trend in the PCE values can be explained by defect density present in the mid gap region as shown by the Figure 3.10b. NCs having more mid gap defects exhibit low PCE due to mid gap defects act as non-radiative trap states do not allow the separation of charge carriers. As a result, the performance of solar cell is poor for $AgInS_2$ NCs annealed at 70 ^oC.

Table 3.1: The solar cell parameters obtained from the J–V characteristics of respective cells in Figure 3.12b.

NC annealing temperature/size	J_{sc} (mA/cm^2)	V_{oc} (V)	FF	PCE (η %)
70 ^oC/2.5 nm	2.3	0.26	0.32	0.2
150 ^oC/5.8 nm	4.62	0.45	0.39	0.8

As expected our organic-free $AgInS_2$ NCs show superior performance than previously reported organic capped $AgInS_2$ NCs. For example in ref. 43, authors made NC sensitized solar cell using organic capped $AgInS_2$ NCs which shows low J_{sc} = 0.91 mA/cm^2 due to the insulating nature of organic capping on the surface of the NC. Lower J_{sc} effects other solar cell parameters resulting into very low PCE of 0.06%. However, the PCE values obtained for best samples of organic-free $AgInS_2$ NCs (0.8%) is still lower than group II-VI (CdS) based semiconductor NCs due to high density of defects in our $AgInS_2$ NCs. The defect density was decreased by annealing colloidal NCs at 150 ^oC, but further decrease in defect density is required to improve the solar cell efficiency. cannot be done by simple annealing at higher temperatures (>150 ^oC) because of limitation of boiling point of solvent (FA) which was used it for annealing of NCs.

3.4 Conclusions

We have shown a generic synthesis protocol for organic-free, all-inorganic metal sulfide NCs that forms a colloidal dispersion in a polar solvent. The surface of these NCs is designed to have excess sulfide ions compared to the cationic species, therefore, providing a negatively charged NC surface. These negatively charged NCs electrostatically repel each other providing colloidal stability in a polar solvent like FA. Different NC systems, namely, CdS, ZnS, $Zn_xCd_{1-x}S$ alloys, Mn-doped $Zn_xCd_{1-x}S$ and $AgInS_2$ have been synthesized. Organic-free Mn-doped $Zn_xCd_{1-x}S$ NCs, both in solution and film exhibit strong luminescence, whereas corresponding undoped samples show poor luminescence. The strong Mn emission (d-d transition) is attributed to the localization of d-electrons largely within the Mn^{2+} ions and thus interact less with the non-radiative decay channels on the surface of NCs. organic-free $AgInS_2$ NCs show significant defect-related photoabsorption at energies below the bulk band gap, probably leading to an Urbach tail. Defects in the $AgInS_2$ NCs can arise from both surface termination and intrinsic defects within the crystal because of the difference in the Ag–S and In–S bonds. The low-energy absorption tail decreases systematically as the annealing temperature is increased from 70 to 150 °C, which is also accompanied by an increase in the NC size from 2.5 nm to 5.8 nm. A higher annealing temperature reduces the intrinsic defects, and at the same time the formation of larger NCs reduces the surface defect contribution. Organic-free $AgInS_2$ NCs exhibit broad luminescence similar to prior reports. NC sensitized solar cell prepared using $AgInS_2$ NC dispersion after annealing at 150 °C show higher values of PCE (0.8%), V_{OC} (0.45 V) and J_{SC} (4.62 mA cm^{-2}) as a consequence of the partial removal of the defect states compared to NCs annealed at 70 °C (0.2%, 0.26 V and 2.3 mA cm^{-2}). The obtained solar cell parameters are superior than the previous reports of $AgInS_2$ NC based solar cells, owing to the organic-free nature of our NCs facilitating charge transport, and the partial removal of defect states following post-synthesis annealing. However, further improvement of device performance is essential for practical use, and the major step would be synthesizing intrinsic defect-free $AgInS_2$ NCs.

References

1. Henglein, A. Photo-Degradation and Fluorescence of Colloidal-Cadmium Sulfide in Aqueous-Solution. Ber. Bunsen-Ges. *Phys. Chem.Chem. Phys*. **1982**, *86*, 301−305.

2. Rossetti, R.; Nakahara, S.; Brus, L. E. Quantum Size Effects in the Redox Potentials, Resonance Raman-Spectra, and Electronic-Spectra of CdS Crystallites in Aqueous-Solution. *J. Chem. Phys.* **1983**, *79*, 1086−1088.

3. Ramsden, J. J.; Gratzel, M. Photoluminescence of Small Cadmium-Sulfide Particles. *J. Chem. Soc., Faraday Trans.* **1984**, *80*, 919.

4. Petit, C.; Lixon, P.; Pileni, M. P. Synthesis of Cadmium-Sulfide In Situ in Reverse Micelles. 2. Influence of the Interface on the Growth of the Particles. *J. Phys. Chem.* **1990**, *94*, 1598−1603.

5. Ben-Moshe, A.; Govorov, A. O.; Markovich, G. Enantioselective Synthesis of Intrinsically Chiral Mercury Sulfide Nanocrystals. *Angew. Chem. Int. Ed.* **2013**, *52*, 1275-1279.

6. Nozik, A. J.; Williams, F.; Nenadovic, M. T.; Rajh, T.; Micic, O. I. Size Quantization in Small Semiconductor Particles. *J. Phys. Chem.* **1985**, *89*, 397-399.

7. Micic, O. I.; Nenadovic, M. T.; Peterson, M. W.; Nozik, A. J. Size Quantization in Layered Semiconductor Colloids with Tetrahedral Bonding - HgI_2. *J. Phys. Chem.* **1987**, *91*, 1295-1297.

8. Van Hyning, D. L.; Zukoski, C. F. Formation Mechanisms and Aggregation Behavior of Borohydride Reduced Silver Particles. *Langmuir* **1998**, *14*, 7034-7046.

9. Zhao, Y. X.; Hernandez-Pagan, E. A.; Vargas-Barbosa, N. M.; Dysart, J. L.; Mallouk, T. E. A High Yield Synthesis of Ligand-Free Iridium Oxide Nanoparticles with High Electrocatalytic Activity. *J. Phys. Chem. Lett.* **2011**, *2*, 402-406.

10. Holman, Z. C.; Kortshagen, U. R. Nanocrystal Inks without Ligands: Stable Colloids of Bare Germanium Nanocrystals. *Nano Lett.* **2011**, *11*, 2133-2136.

11. Murray, C. B.; Norris, D. J.; Bawendi, M. G. Characterization of Nearly Monodisperse CdE (E = S, Se, Te) Semiconductor Nanocrystallites. *J. Am. Chem. Soc.* **1993**, *115*, 8706−8715.

12. Peng, Z. A.; Peng, X. G. Formation of High-Quality CdTe, CdSe, and CdS Nanocrystals Using CdO as Precursor. *J. Am. Chem. Soc.* **2001**, *123*, 183-184.

13. Talapin, D. V.; Lee, J. S.; Kovalenko, M. V.; Shevchenko, E. V. Prospects of Colloidal Nanocrystals for Electronic and Optoelectronic Applications. *Chem. Rev.* **2010**, *110*, 389-458.

14. Yu, D.; Wang, C. J.; Guyot-Sionnest, P. n-Type Conducting CdSe Nanocrystal Solids. *Science* **2003**, *300,* 1277-1280.

15. Jarosz, M. V.; Porter, V. J.; Fisher, B. R.; Kastner, M. A.; Bawendi, M. G. Photoconductivity Studies of Treated CdSe Quantum Dot Films Exhibiting Increased Exciton Ionization Efficiency. *Phys. Rev. B* **2004**, *70,* 195327.

16. Talapin, D. V.; Murray, C. B. PbSe Nanocrystal Solids for n- and p-Channel Thin Film Field-Effect Transistors. *Science* **2005**, *310,* 86-89.

17. Law, M.; Luther, J. M.; Song, O.; Hughes, B. K.; Perkins, C. L.; Nozik, A. J. Structural, Optical, and Electrical Properties of PbSe Nanocrystal Solids Treated Thermally or with Simple Amines. J. *Am. Chem. Soc.* **2008**, *130,* 5974-5985.

18. Kang, M. S.; Sahu, A.; Norris, D. J.; Frisbie, C. D. Size-Dependent Electrical Transport in CdSe Nanocrystal Thin Films. *Nano Lett.* **2010**, *10,* 3727-3732.

19. Tang, J.; Kemp, K. W.; Hoogland, S.; Jeong, K. S.; Liu, H.; Levina, L.; Furukawa, M.; Wang, X. H.; Debnath, R.; Cha, D. K.; et al. Colloidal-Quantum-Dot Photovoltaics Using Atomic-Ligand Passivation. *Nat. Mater.* **2011,** *10,* 765−771.

20. Kovalenko, M. V.; Scheele, M.; Talapin, D. V. Colloidal Nanocrystals with Molecular Metal Chalcogenide Surface Ligands. *Science* **2009**, *324,* 1417-1420.

21. Dong, A. G.; Ye, X. C.; Chen, J.; Kang, Y. J.; Gordon, T.; Kikkawa, J. M.; Murray, C. B. A Generalized Ligand-Exchange Strategy Enabling Sequential Surface Functionalization of Colloidal Nanocrystals. *J. Am. Chem. Soc.* **2010**, *133,* 998-1006.

22. Nag, A.; Kovalenko, M. V.; Lee, J. S.; Liu, W. Y.; Spokoyny, B.; Talapin, D. V. Metal-Free Inorganic Ligands for Colloidal Nanocrystals: S^{2-}, HS^{-}, Se^{2-}, HSe^{-}, Te^{2-}, HTe^{-}, TeS_3^{2-}, OH^{-}, and NH_2^{-} as Surface Ligands. *J. Am. Chem. Soc.* **2011,** *133,* 10612−10620.

23. Fafarman, A. T.; Koh, W. K.; Diroll, B. T.; Kim, D. K.; Ko, D. K.; Oh, S. J.; Ye, X. C.; Doan-Nguyen, V.; Crump, M. R.; Reifsnyder, D. C.; Murray, C. B.; Kagan, C. R. Thiocyanate-Capped Nanocrystal Colloids: Vibrational Reporter of Surface Chemistry and Solution-Based Route to Enhanced Coupling in Nanocrystal Solids. *J. Am. Chem. Soc.* **2011,** *133,* 15753-15761.

24. Rosen, E. L.; Buonsanti, R.; Llordes, A.; Sawvel, A. M.; Milliron,D. J.; Helms, B. A. Exceptionally Mild Reactive Stripping of Native Ligands from Nanocrystal Surfaces by Using Meerwein's Salt. *Angew. Chem. Int. Ed.* **2012,** *51,* 684−689.

25. Lee, J. S.; Kovalenko, M. V.; Huang, J.; Chung, D. S.; Talapin, D. V. Band-Like Transport, High Electron Mobility and High Photoconductivity in All-Inorganic Nanocrystal Arrays. *Nat. Nanotechnol.* **2011,** *6,* 348−352.

26. Nag, A.; Chakraborty, S.; Sarma, D. D. To Dope Mn^{2+} in a Semiconducting Nanocrystal. *J. Am. Chem. Soc.* **2008**, *130,* 10605-10611.

27. Pons, T.; Uyeda, H. T.; Medintz, I. L.; Mattoussi, H. Hydrodynamic Dimensions, Electrophoretic Mobility, and Stability of Hydrophilic Quantum Dots. *J. Phys. Chem. B* **2006**, *110,* 20308-20316.

28. Kittel, C. *Introduction to Solid State Physics*, 7th ed.; John Wiley & Sons: New York; 2007.

29. Sapra, S.; Sarma, D. D. Evolution of the Electronic Structure with Size in II-VI Semiconductor Nanocrystals. *Phys. Rev. B* **2004**, *69,* 125304.

30. Kovalenko, M. V.; Bodnarchuk, M. I.; Talapin, D. V. Nanocrystal Superlattices with Thermally Degradable Hybrid Inorganic-Organic Capping Ligands. *J. Am. Chem. Soc.* **2010**, *132,* 15124-15126.

31. Denton, A. R.; Ashcroft, N. W. Vegard Law. Phys. Rev. A **1991**, *43,* 3161-3164.

32. Rogach, A. L.; Franzl, T.; Klar, T. A.; Feldmann, J.; Gaponik, N.; Lesnyak, V.; Shavel, A.; Eychmuller, A.; Rakovich, Y. P.; Donegan, J. F. Aqueous Synthesis of Thiol-Capped CdTe Nanocrystals: State-of-the-Art. *J. Phys. Chem. C* **2007**, *111*, 14628-14637.

33. Wuister, S. F.; Donega, C. D.; Meijerink, A. Influence of Thiol Capping on the Exciton Luminescence and Decay Kinetics of CdTe and CdSe Quantum Dots. *J. Phys. Chem. B* **2004**, *108,* 17393-17397.

34. Beaulac, R.; Archer, P. I.; Gamelin, D. R. Luminescence in Colloidal Mn^{2+}-Doped Semiconductor Nanocrystals. *J. Solid State Chem.* **2008**, *181,* 1582-1589.

35. Pradhan, N.; Sarma, D. D. Advances in Light-Emitting Doped Semiconductor Nanocrystals. *J. Phys. Chem. Lett*. **2011,** *2,* 2818-2826.

36. Srivastava, B. B.; Jana, S.; Karan, N. S.; Paria, S.; Jana, N. R.; Sarma, D. D.; Pradhan, N. Highly Luminescent Mn-Doped ZnS Nanocrystals: Gram-Scale Synthesis. J. Phys. Chem. Lett. **2010**, *1,* 1454-1458.

37. Suyver, J. F.; Wuister, S. F.; Kelly, J. J.; Meijerink, A. Luminescence of Nanocrystalline ZnSe : Mn^{2+}. *Phys. Chem. Chem. Phys.* **2000**, *2,* 5445-5448.

38. Shay, J. L.; Tell, B.; Schiavon.Lm; Kasper, H. M.; Thiel, F. Energy-Bands of $AgInS_2$ Iin Chalcopyrite and Othorhombic Structures. *Phys. Rev. B* **1974**, *9,* 1719-1723.

39. Torimoto, T.; Adachi, T.; Okazaki, K.; Sakuraoka, M.; Shibayama, T.; Ohtani, B.; Kudo, A.; Kuwabata, S. Facile Synthesis of ZnS-$AgInS_2$ Solid Solution Nanoparticles for a Color-Adjustable Luminophore. *J. Am. Chem. Soc.* **2007**, *129,* 12388-12389.

40. Xie, R. G.; Rutherford, M.; Peng, X. G. Formation of High-Quality I-III-VI Semiconductor Nanocrystals by Tuning Relative Reactivity of Cationic Precursors. *J. Am. Chem. Soc.* **2009**, *131*, 5691-5697.

41. Santra, P. K.; Nair, P. V.; Thomas, K. G.; Kamat, P. V. $CuInS_2$-Sensitized Quantum Dot Solar Cell. Electrophoretic Deposition, Excited-State Dynamics, and Photovoltaic Performance. *J. Phys. Chem. Lett.* **2013**, *4*, 722-729.

42. Peng, S. J.; Zhang, S. Y.; Mhaisalkar, S. G.; Ramakrishna, S. Synthesis of $AgInS_2$ Nanocrystal Ink and Its Photoelectrical Application. *Phys. Chem. Chem. Phys.* **2012**, *14*, 8523-8529.

43. Tian, L.; Elim, H. I.; Ji, W.; Vittal, J. J. One-Pot Synthesis and Third-Order Nonlinear Optical Properties of $AgInS_2$ Nanocrystals. *Chem. Commun.* **2006**, 4276-4278.

44. Du, W. M.; Qian, X. F.; Yin, J.; Gong, Q. Shape- and Phase-Controlled Synthesis of Monodisperse, Single-Crystalline Ternary Chalcogenide Colloids Through a Convenient Solution Synthesis Strategy. *Chem.-Eur. J.* **2007**, *13*, 8840-8846.

45. Tang, X. S.; Ho, W. B. A.; Xue, J. M. Synthesis of Zn-Doped $AgInS_2$ Nanocrystals and Their Fluorescence Properties. *J. Phys. Chem. C* **2012**, *116*, 9769-9773.

46. Torimoto, T.; Ogawa, S.; Adachi, T.; Kameyama, T.; Okazaki, K. I.; Shibayama, T.; Kudo, A.; Kuwabata, S. Remarkable Photoluminescence Enhancement of ZnS-$AgInS_2$ Solid Solution Nanoparticles by Post-Synthesis Treatment. *Chem. Commun.* **2010**, *46*, 2082-2084.

47. Mao, B. D.; Chuang, C. H.; Wang, J. W.; Burda, C. Synthesis and Photophysical Properties of Ternary I-III-VI $AgInS_2$ Nanocrystals: Intrinsic versus Surface States. *J. Phys. Chem. C* **2011**, *115*, 8945-8954.

48**.** Urbach, F. The Long-Wavelength Edge of Photographic Sensitivity and of the Electronic Absorption pf Solids *Phys. Rev.* **1953,** *92*, 1324

49. Cody, G. D.; Tiedje, T.; Abeles, B.; Brooks, B.; Goldstein, Y. Disorder and the Optical-Absorption Edge of Hydrogenated Amorphous-Silicon. *Phys. Rev. Lett.* **1981**, *47*, 1480-1483.

50. Krustok, J.; Raudoja, J.; Krunks, M.; Mandar, H.; Collan, H. Nature of the Native Deep Localized Defect Recombination Centers in the Chalcopyrite and Orthorhombic $AgInS_2$. *J. Appl. Phys.* **2000**, *88*, 205-209.

51. Hattori, K.; Akamatsu, K.; Kamegashira, N. Electrical-Properties of Polycrystalline Chalcopyrite $AgInS_2$ Films. *J. Appl. Phys.* **1992**, *71*, 3414-3418.

52. Guyot-Sionnest, P.; Lhuillier, E.; Liu, H. A Mirage Study of CdSe Colloidal Quantum Dot Films, Urbach Tail, and Surface States. *J. Chem. Phys.* **2012**, *137*, 154704.

Chapter 4

Photoluminescence and Solar Cell from Ag_2S-$AgInS_2$ Hetero Dimer Nanocrystals

---

The following paper has been published based on the work presented in this chapter.

Jagadeeswararao, M.; Swarnkar, A.; Markad, G. B.; Nag, A. Defect-Mediated Electron–Hole Separation in Colloidal Ag_2S–$AgInS_2$ Hetero Dimer Nanocrystals Tailoring Luminescence and Solar Cell Properties. *J. Phys. Chem. C* **2016**, *120*, 19461-19469.Copy right permission has been taken from American Chemical Society for entire manuscript.

Summary

Nanoscale heterojunctions with type-II band alignment can efficiently separate photogenerated electron-hole pair, and therefore find applications in solar cells and photocatalysis. Here we prepare a nano-junction in the form of Ag_2S-$AgInS_2$ hetero dimer nanocrystal that does not contain toxic Cd and Pb. A combination of photophysics, cyclic voltammetry and nanocrystal sensitized solar cell properties show that the junction/interface has a type-I band alignment, but still electron-hole separation takes place with efficacy across the interface because of defect states. The electron gets localized in a defect state within $AgInS_2$ part and the hole resides in the Ag_2S part of the hetero dimer nanocrystal. This type-II-like defect mediated electron-hole separation, irrespective of the nature interfacial band alignment, is an interesting phenomenon, and can be utilized to tune optoelectronic properties of heterostructured nanocrystals. For example, very long (13 μS) photoluminescence lifetime has been observed for Ag_2S-$AgInS_2$ hetero dimer nanocrystals because of this defect-mediated spatial separation of electron and hole wavefunctions, which in turn improve the solar cell efficiency by more than three times compared to $AgInS_2$ nanocrystals.

Graphical abstract

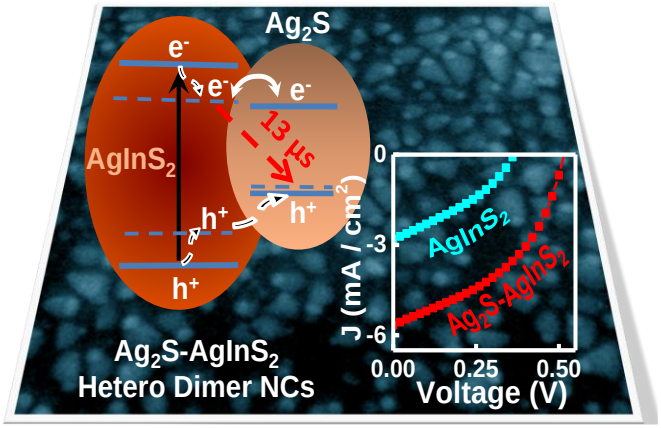

4.1 Introduction

Heterostructure nanocrystals (NCs) have at least two chemically distinct compositions separated by an interface within a single NC. Such interfaces control electronic, optical and optoelectronic properties of a semiconductor heterostructured NC.[1-5] For example, (i) type-I alignment across the interface of CdSe/ZnS core/shell NCs gives superior PL efficiency compared to both CdSe and ZnS NCs,[6-7] (ii) type-II band alignment across CdTe/CdSe NCs can create a nanoscale p-n junction improving efficiency for charge separation,[8-9] which is essential for applications such as photovoltaics and photocatalysis. In most heterostructured NCs, the nature of interface is controlled by the band offsets at the interface, i.e. the energy difference between valence and conduction band edges of both component semiconductors. Here we present an interesting example of Ag_2S-$AgInS_2$ hetero dimer NCs (HDNCs) where band offsets suggest type-I interface (not favoured for charge separation), but the intrinsic defects leads to a type-II like properties exhibiting efficacy for charge separation.

Environmentally benign colloidal I-III-VI semiconductor NCs namely $CuInE_2$, and $AgInE_2$ (E = S, Se, and Te) are being studied extensible because of their interesting optical and optoelectronic properties in the visible and near infrared (NIR) region.[10-17] Orthorhombic $AgInS_2$ and monoclinic Ag_2S NCs exhibit band gaps of 1.98 and 1.1 eV respectively.[18-19] High luminescence efficiency of $AgInS_2$ was tuned throughout the visible region forming alloy with ZnS,[20-21] and is a potential candidate for light emitting diodes. Various other applications such as photovoltaic,[22] and visible-light driven photocatalytic H_2 production,[23-24] are now being explored using $AgInS_2$ based NCs which do not contain toxic Cd and Pb. On the other hand, luminescence of Ag_2S NCs was tuned in the NIR region by tuning the size of NCs.[25-26] Such NIR emitting Ag_2S NCs are presently being investigated for application as a biocompatible fluorescence probe.[27-28] Also, Mn-doping in Ag_2S-ZnS heterostructured NCs exhibit their optical properties from visible to NIR range.[29] These successes have motivated researchers to prepare heterostructured Ag_2S-$AgInS_2$ HDNCs.[30] Pradhan et al recently showed the interface in Ag_2S-$AgInS_2$ HDNCs can form a p-n junction exhibiting 0.56 % photo conversion efficiency.[31] However, the nature of the interface is far from being sufficiently understood.

In this chapter we prepared colloidal Ag_2S-$AgInS_2$ HDNCs employing a single-step reaction using single molecular precursors. Mechanistic studies show that Ag_2S NCs forms first followed by nucleation and growth of $AgInS_2$ phase. Cyclic voltammetry (CV) results show a

type-I band alignment across the interface of Ag_2S-$AgInS_2$ HDNCs. Interestingly, we observed defect-related NIR photoluminescence (PL) from HDNCs for the first time, and exhibit a long PL lifetime of 13 μS. This combination of CV results and long PL lifetime suggest localization of charge carriers into two different components of the HDNC because of defect mediated separation of electron and hole. Such electron-hole separation typically happens in an interface with type-II band alignment, however we observe here a relatively new phenomena where defects lead to electron-hole separation across the interface in spite of having type-I band alignment. The efficacy of this defect mediated electron-hole separation was also demonstrated by increases the efficiency of Ag_2S-$AgInS_2$ HDNC sensitized solar cells to 1.3% compared to 0.4 % efficiency of $AgInS_2$ NC sensitized solar cells. This possibility of achieving type-II like electron-hole separation behaviour through defect states will be useful to design future materials.

4.2 Experimental section

4.2.1 Preparation of molecular precursor

The molecular precursor powder was prepared by following prior literature[20] where mixing 50 mL aqueous solution of sodium diethyldithiocarbamate (DDTC) (0.05 mol/L) with 50 mL aqueous solution of 0.025 mol/L metal ions. For synthesis of Ag_2S and In_2S_3 NCs, the metal ion solution was made of $AgNO_3$ and $InNO_3$, and the obtained molecular precursors are termed here as Ag(DDTC) and $In(DDTC)_3$ respectively. Whereas, for the synthesis of $AgInS_2$ NCs and Ag_2S-$AgInS_2$ HDNCs, the metal ion solution contained a mixture of 0.0125 mol/L $AgNO_3$ and 0.0125 mol/L $InNO_3$, and the obtained precursor was termed as $AgIn(DDTC)_4$. The precipitate obtained after mixing DDTC and metal ion solution was washed with water and methanol three times, and dried under vacuum at room temperature.

4.2.2 Synthesis of $AgInS_2$ NCs

$AgInS_2$ NCs have been prepared by following ref[20]. 50 mg $AgIn(DDTC)_4$ precursor powder was transferred into a three-neck round bottom (RB) flask and heated at 180 ^oC for 30 minutes in the N_2 atmosphere. 3 mL oleylammine was added to the above heated powder and the reaction was continued for 3 minutes at 180 ^oC. The reaction mixture was allowed to cool naturally and then supernatant was extracted from the suspension after removing the larger particles. Methanol was added as non-solvent to the above obtained supernatant followed by centrifugation. This washing was repeated twice, and the obtained NCs were re-dispersed in chloroform for characterization and solar cell fabrication.

4.2.3 Single-step synthesis of Ag_2S-$AgInS_2$ HDNCs

40 mg $AgIn(DDTC)_4$ powder was mixed with 2.0 mL of oleylamine. Vacuum was applied to this mixture for 15 minutes followed by flow of N_2 gas for 5 minutes with vigorous stirring at room temperature. The mixture was then injected into the three-neck RB flask containing 10 mL 1-octadecene (ODE) at 250 ^oC with stirring under N_2 atmosphere. The reaction was carried out for 1 hour, and then allowed to cool naturally to ~100 ^oC, followed by injection of toluene (10 mL) and subsequent cooling to room temperature. The product Ag_2S-$AgInS_2$ HDNCs were precipitated by adding ethanol as a non-solvent, and re-dispersed in chloroform. This NC dispersion was centrifuged at 5000 RPM for 5 minutes precipitating out the larger NCs, and the obtained filtrate was used for further measurements and solar cell fabrication.

4.2.4 Synthesis of Ag_2S NCs and subsequent two-step synthesis of Ag_2S-$AgInS_2$ HDNCs

This two step process was employed only to understand underlying mechanism behind the formation of Ag_2S-$AgInS_2$ HDNC following the above mentioned single-step reaction. Ag_2S NCs were prepared following a synthetic protocol similar to that of $AgInS_2$ NCs, but with only difference in precursor powder. Ag(DDTC) was used for the synthesis of Ag_2S NCs. The obtained Ag_2S NCs were re-dispersed in 2 mL toluene, and was used for the two-step synthesis of Ag_2S-$AgInS_2$ HDNCs. The above Ag_2S NC dispersion was transferred to 50 mL RB containing 10 mL ODE. Vacuum was applied at 120 ^oC to get rid of the toluene from the reaction mixture then the temperature was raised up to 250 ^oC under N_2 atmosphere. 50 mg $In(DDTC)_3$ precursor powder in 2 mL of oleylamine was added drop wise to the above mixture (*ca.* 5 minutes was taken for addition), then the reaction was continued for another 15 minutes. The obtained HDNCs were washed with same procedure as mentioned above for single-step synthesis of Ag_2S-$AgInS_2$ HDNCs.

4.2.5 Electrochemical measurements

CV measurements were performed with the help of PAR Potentiostat/Galvanostat (model PARSTAT 2273). A commercial Pt disk electrode (CHI Instruments, USA, 2-mm diameter), Ag wire, and Pt-wire loop were used as working, quasi reference, and counter electrodes, respectively. Prior to use, the working electrode was polished over 0.5 μm alumina powder and rinsed with milli-Q water. Further it was pre-treated electrochemically with 0.5 M H_2SO_4

by cycling the potential for several times between 1.2 V and -0.55 V (scan rate of 1 V s^{-1}).[32] Typically 3 µL sample dispersion was drop casted on the Pt working electrode surface and dried under the vacuum, this drop casted Pt electrode was used as working electrode.[33-34] Blank measurements were recorded without drop casting the sample. After fixing all the electrodes to the cell, 0.171 g of tetrabutyl ammonium perchlorate (TBAP) was transferred and cell was air tight inside the glove-box. The cell was then taken out, and TBAP was vacuum dried at 80 ˚C. The cell was allowed to cool down to room temperature naturally and vacuum was then relived through high purity N_2 gas. 5 mL anhydrous acetonitrile was injected into the cell. All the electrochemical measurements were performed under a slight positive pressure of N_2 gas. Oxidation and reduction peak potentials were used to calculate the energy of valance band maximum (VBM) and conduction band minimum (CBM) respectively and difference between oxidation and reduction peak potential has been consider as electrochemical band gap.[35] At the end of each set of experiments, the potentials were calibrated with respect to the normal hydrogen electrode (NHE), using ferrocene as an internal standard.[36]

4.2.6 Porous TiO_2 electrode preparation

F-doped SnO_2 (FTO) coated glass with resistance 7 Ω/Sq was cleaned sequentially with soap solution water, distil water and ethanol (each wash for 30 minutes) using ultra sonication bath followed by heating at 450 ^oC for 10 minutes in order to get rid of the organic contaminants. The compact layer of TiO_2 was made on the top of the conducting surface of FTO coated glass by treating with 0.04 M $TiCl_4$ aqueous solution at 80 ^oC for 30 minutes then cleaned with distil water and ethanol. The mesoporous TiO_2 active layer prepared on the compact layer by using commercial TiO_2 paste (Dyesol DSL-18NR-T, diameter ~20 nm) through doctor blading technique followed by sintering at 450 ^oC. The resultant thickness of the active layer was ~10 µm, measured by scanning electron microscopy (SEM). Over this active layer a scattering layer of TiO_2 (Dyesol WER2-O, diameter 150-250 nm) was doctor bladed followed by sintering at 450 ^oC. The thickness of the scattering layer was ~ 5 µm measured by using SEM, which is shown in the Figure 4.1. Thus obtained films were again treated with aqueous solution of 0.04 M $TiCl_4$ and then sintered at 450 ^oC for 30 minutes to get rid of the pin holes and cracks formed in the film.

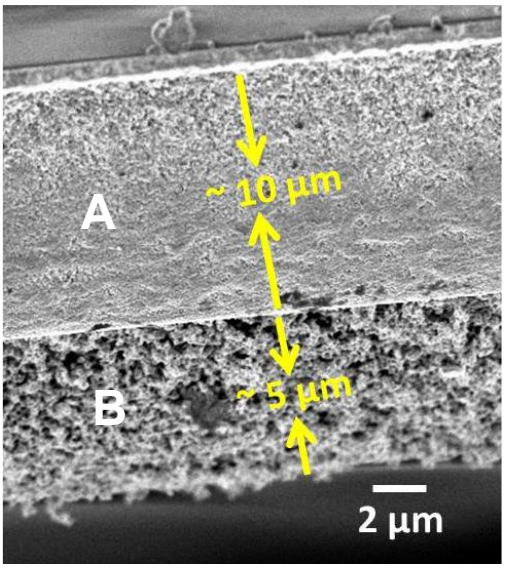

Figure 4.1: Cross section SEM image of TiO_2 electrode where regions A and B are representing the active layer and scattering layer respectively.

4.2.7 Fabrication of $AgInS_2$ NC and Ag_2S-$AgInS_2$ HDNC sensitized solar cell

Porous TiO_2 electrodes were made following prior literature[37] and the details are given in the above paragraph. For sensitization, hot TiO_2 electrode (at 60 ^oC) was dipped into oleylamine capped Ag_2S-$AgInS_2$ HDNCs (or $AgInS_2$ NCs) dispersed in $CHCl_3$ and kept in dark for 72 hours at room temperature. For better charge transport, the oleylamine capped NCs sensitized TiO_2 electrode was allowed to stay in S^{2-} solution (0.8 M Na_2S in 1:1 v/v methanol: water solution) for 48 hours at room temperature in dark.[24, 38] The final photoanode was cleaned with water then ethanol and dried at 80 ^oC under N_2 environment for 30 min.

NC sensitized solar cells were assembled by sandwiching the photoanode with Pt counter electrode, spatially separated (~80 µm) by parafilm spacer and electrically connected through 10 µL sulphide/polysulfide electrolyte. Sulfide/polysulfide electrolyte used in our work was prepared by following ref[39], where Na_2S (0.5 M), sulfur (2 M), KCl (0.2 M) and NaOH (0.5 M) were mixed in mixture of methanol : water in 7 : 3 v/v. Current-voltage (I-V) measurements were performed using Keithly 2611 source meter. Xe lamp 150 W fitted with AM 1.5 filter was used for illumination in all the solar cell measurements. Intensity of the lamp was adjusted to 1 sun (100 mW/cm^2) by using NREL-calibrated silicon solar cell. The active area of the solar cell measurement was 0.16 cm^2.

4.2.8 Characterization

UV-visible-NIR absorption spectra were recorded using a lambda-45 UV/vis spectrometer. Steady state photoluminescence (PL) and PL decay dynamics (time correlated single photon counting (TCSPC)) were measured using FLS 980 (EDINBURGH Instruments). Powder x-ray diffraction (XRD) data were recorded using a Bruker D8 Advance X-ray diffractometer using Cu Kα radiation (1.54 Å). Transmission electron microscopy (TEM) and scanning transmission electron microscope - annular dark-field (STEM - ADF) imaging were carried out using a JEOL, JEM 2100 F, Field Emission TEM. Field emission scanning electron microscopy (FESEM) was carried out using a Zeiss Ultra Plus scanning electron microscope. External quantum efficiency (EQE) was measured using Newport IPCE system over the range of 350- 1000 nm.

4.3 Results and discussion

4.3.1 Synthesis and characterization of Ag_2S-$AgInS_2$ HDNCs

We have prepared colloidal Ag_2S-$AgInS_2$ HDNCs by thermal decomposition of single molecular precursor $AgIn(DDTC)_4$ in the presence of oleylamine and ODE at 250 ^oC. TEM and STEM images in Figure 4.2a-b show each single NC contains two parts with different contrast. This contrast difference suggest two different compositions, phase separated within a single NC. High resolution TEM (HRTEM) image in Figure 4.2c shows two different interplanar distances, suggesting both composition phases are highly crystalline. The obtained interplanar distances (*d*) 0.33 nm and 0.24 nm correspond to (200) plane of orthorombic $AgInS_2$ and (121) plane of monoclinic α-Ag_2S respectively. This finding also explain the contrast difference in Figure 4.2a, where smaller and darker part of a NC corresponds to Ag_2S and larger part of the NC with less contrast is assigned to $AgInS_2$. Ag_2S is known to exhibit more contrast in TEM image because of higher electron density compared to $AgInS_2$.[31]

Microscopic data suggest the formation of Ag_2S-$AgInS_2$ HDNCs following our single-step reaction. Though there are inhomogeniety in size and shape of these HDNCs, the size-distribution plots in Figure 4.2d-e shows that the Ag_2S part has a diameter 4 ± 0.8 nm and $AgInS_2$ part exhibit a diameter 7.9 ± 2.8 nm, considering distorted spherical particles. Further structural characterization of the sample using XRD patterns (Figure 4.2f) exhibiting intense peaks for orthorhombic $AgInS_2$, along with less intense additional peaks for monoclinic α-Ag_2S. In order to assign the less intense additional peaks, inset to Figure 4.2f compares a

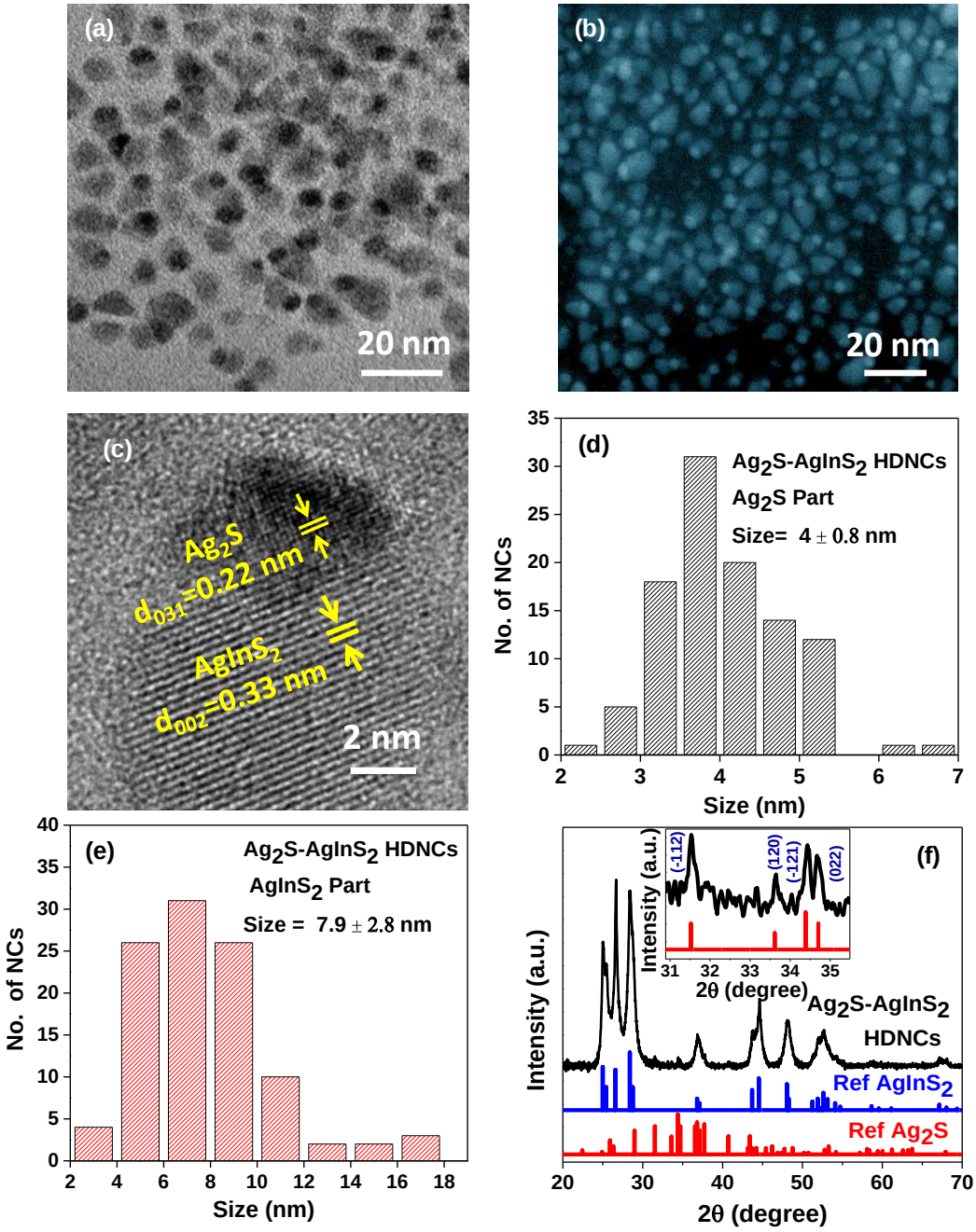

Figure 4.2: (a) TEM, (b) STEM – ADF (colour image shown for better presentation), and (c) HRTEM micrographs of Ag_2S-$AgInS_2$ HDNCs. (d, e) Size distribution plots for Ag_2S and $AgInS_2$ parts of Ag_2S-$AgInS_2$ HDNCs, respectively. There are irregularity in NC shape, so we measured the length of each NC in two perpendicular directions, and the average length has been considered here as diameter of the distorted spherical (non-spherical) NCs. (f) Comparison of XRD pattern of Ag_2S-$AgInS_2$ HDNCs with bulk references of orthorhombic $AgInS_2$ (JCPDS No: 25-1328) and monoclinic α-Ag_2S (JCPDS No: 14-0072). Inset shows the magnified view in the 2θ range 31-35 degree.

magnified view of the XRD pattern of the NC sample in the range 2θ = 31- 35 degree, with that of reference bulk monoclinic α-Ag_2S. This comparison shows that the less intense XRD

peaks originates from Ag_2S component of the NCs. These two different crystalline phases, along with their intensity ratios in XRD peaks agrees with the HRTEM data in Figure 4.2c, where smaller Ag_2S phase contributes less in the XRD intensities compared to the larger $AgInS_2$ phase.

4.3.2 Mechanistic insights on the formation of Ag_2S-$AgInS_2$ HDNCs

4.3.2.1 Single-step reaction of Ag_2S-$AgInS_2$ HDNCs

The molecular precursor $AgIn(DDTC)_4$ used in the synthesis has pre-bonded Ag-S and In-S moieties, which can lead to the nucleation of Ag_2S and In_2S_3 NCs. Depending on the rates of nucleation and growth of these two components along with their lattice strain, homogeneous alloy like $AgInS_2$, or hetero-structures like onion type core/shells and dimers, or a mixture of two different NCs can form. In this sub-section, we will discuss about why Ag_2S-$AgInS_2$ HDNCs are selectively formed within our reaction conditions, excluding other possibilities.

To start with, control reaction using only $In(DDTC)_3$ molecular precursor do not form In_2S_3 NCs. On the other hand, Ag_2S NCs forms easily when only Ag(DDTC) molecular precursor was used, keeping all other reaction conditions identical. These observations give a preliminary indication that when $AgIn(DDTC)_4$ precursor was used for the synthesis of Ag_2S-$AgInS_2$ HDNCs, Ag_2S nucleates first, and subsequently activates the nucleation of In-S or Ag-In-S moieties on its surface. This possibility has been verified below using different sets of experimental data.

Figure 4.3a shows UV-vis-NIR absorption spectra of aliquots taken from reaction mixture of Ag_2S-$AgInS_2$ HDNCs, at different time intervals during the reaction. Inset of Figure 4.3a shows the NIR region of these spectra. All aliquots, starting from 20 sec reaction time exhibit NIR absorption probably because of the formation of Ag_2S NCs, since the band gap of bulk monoclinic α-Ag_2S is 1127 nm (1.1 ev).[19] A shoulder appears at ~ 600 nm as early as 20 sec of reaction, and can be attributed to $AgInS_2$. As the reaction time increases to 60 min, the absorbance contribution from this shoulder increases, without exhibiting any considerable change in the optical gap. These results are tempting to be interpreted as (i) size of $AgInS_2$ component remains constant during the reaction period, and/or (ii) contribution from $AgInS_2$ component increases with reaction time. However, such interpretation is not straightforward for $AgIn_2S$ and $CuInS_2$ NCs, which are notoriously known for contribution of mid-gap defect states complicating the absorption spectrum.[40] For example, defect related absorption can overlap with excitonic transition blurring the excitonic peak/shoulder, and the excitonic

feature can become more prominent with reaction time simply because of the decrease in defect concentration with annealing time.[41] XRD patterns (Figure 4.3b) of samples prepared at 20 sec and 60 min show peaks correspond to both Ag_2S and $AgInS_2$. However, contribution from $AgInS_2$ peaks relative to that of Ag_2S is more for sample obtained after 60 min. These UV-vis-NIR absorption and XRD results taken during the progress of reaction are not conclusive enough, but still agrees with the idea that Ag_2S NCs forms first, followed by the formation of $AgInS_2$ on its surface.

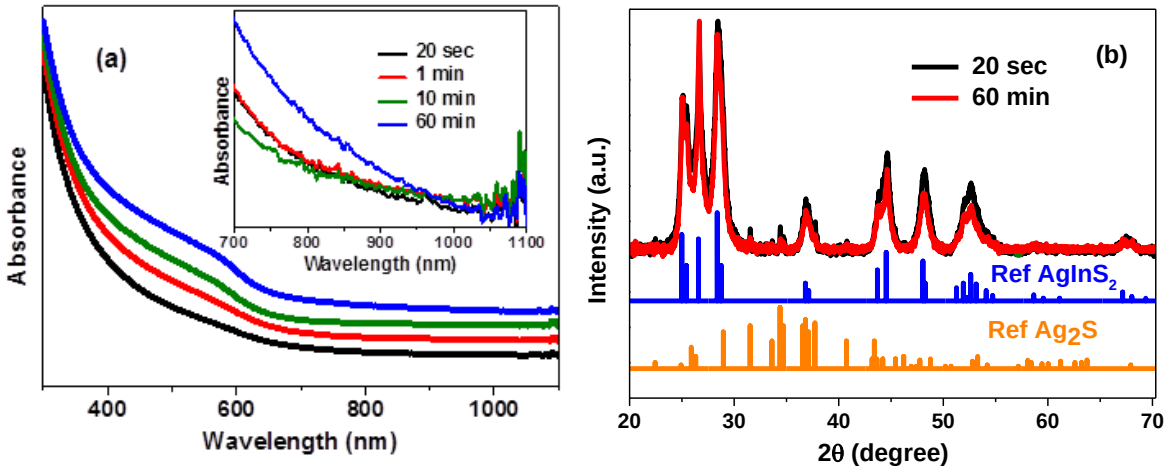

Figure 4.3: (a-b) Ag_2S-$AgInS_2$ HDNCs prepared in a single-step reaction; (a) UV-Vis-NIR absorption spectrum of Ag_2S-$AgInS_2$ HDNCs, at different intervals of time. Inset in the figure (a) is enlarged version of HDNCs in the range of 700 to 1100 nm as in figure (a) without vertical shift in the absorption which represents the absorption corresponds to Ag_2S. (b) XRD pattern of Ag_2S-$AgInS_2$ HDNCs at 20 sec and 60 min along with reference data corresponds to Ag_2S and $AgInS_2$.

4.3.2.2 Confirmation of initial formation of Ag_2S followed by $AgInS_2$/ Ag_2S-$AgInS_2$ HDNCs by a two-step synthesis

In order to verify this idea in a different way, we employed a two-step synthesis where Ag_2S NCs were prepared first using Ag(DDTC) precursor, and subsequently $In(DDTC)_3$ precursor were reacted with the already formed Ag_2S NCs. XRD pattern in Figure 4.4a shows the formation of Ag_2S NCs in the first step, and after adding $In(DDTC)_3$ precursor to the Ag_2S NCs in the second step, the sample shows contributions from both $AgInS_2$ and Ag_2S as shown in Figure 4.4b. TEM image of this sample obtained after second step indeed suggest the formation of Ag_2S-$AgInS_2$ HDNCs as shown in Figure 4.4c with ~6 nm Ag_2S part and ~13 nm $AgInS_2$ part as shown in Figure 4.4d. These results suggest that Ag_2S NCs promotes the nucleation and growth of $AgInS_2$ phase similar to the findings reported in ref[30].

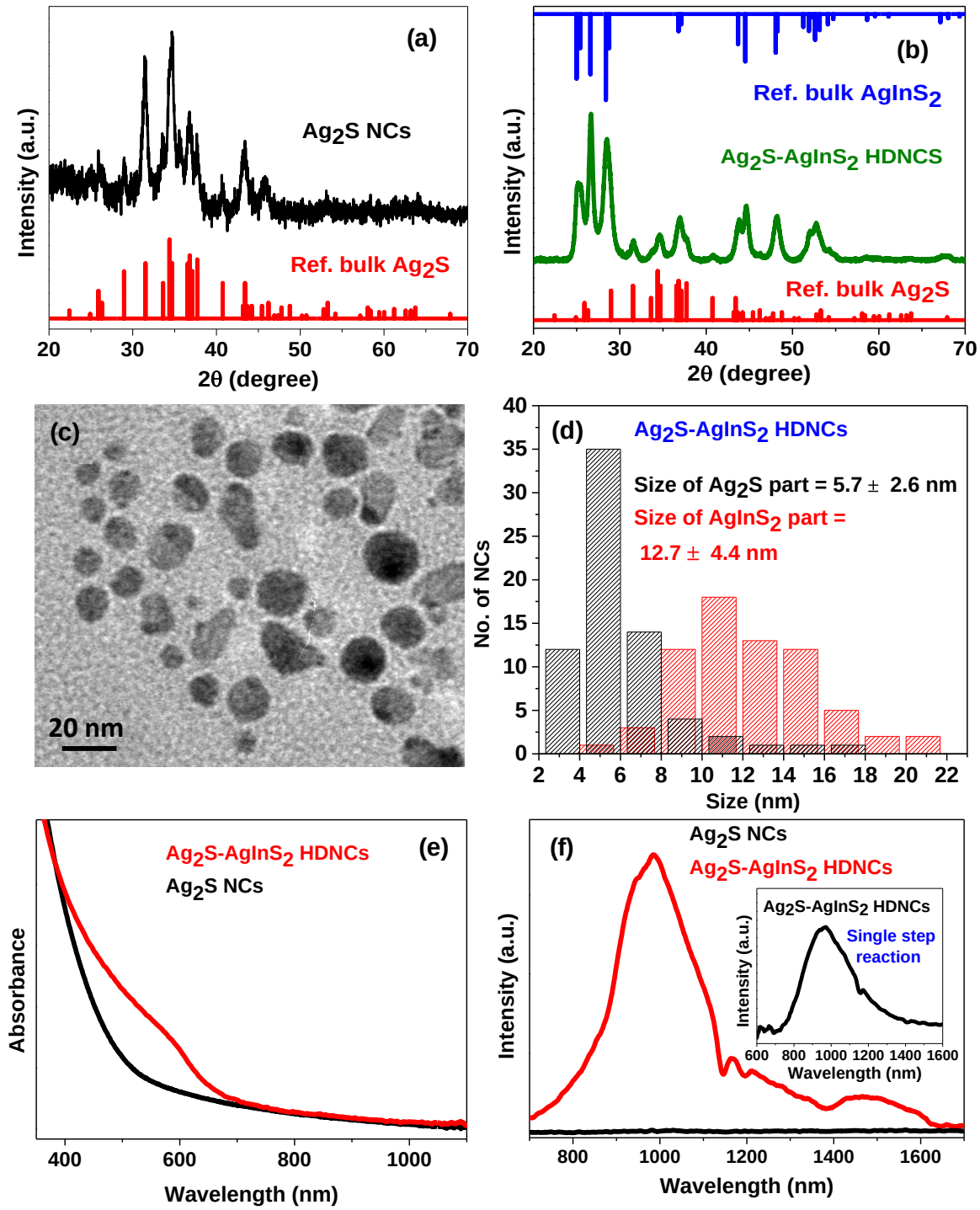

Figure 4.4: (a) XRD pattern of Ag_2S NCs. (b) XRD pattern of Ag_2S-$AgInS_2$ HDNCs formed upon addition of $In(DDTC)_3$ to Ag_2S NCs. (c) TEM image of Ag_2S-$AgInS_2$ HDNCs prepared in two-step reaction. (d) Size distribution plots for Ag_2S-$AgInS_2$ HDNCs prepared. We measured the length of each NC in two perpendicular directions, and the average length has been considered as diameter of the distorted spherical NCs (e) UV-Vis-NIR absorption spectrum, and (f) PL spectrum of Ag_2S NCs and Ag_2S-$AgInS_2$ HDNCs, respectively. Here, Ag_2S-$AgInS_2$ HDNCs have been prepared using a two-step reaction. Inset in Figure (f) shows PL corresponds to Ag_2S-$AgInS_2$ HDNCs formed in single-step.

Furthermore, the evidence for Ag_2S-$AgInS_2$ HDNCs formation can be shown by optical properties as well. For example, in Figure 4.4e Ag_2S NCs show featureless absorption spectrum from UV-vis to NIR region with negligible PL as shown in Figure 4.4f. But, after addition of $In(DDTC)_3$ precursor to the Ag_2S NCs, an excitonic peak is obtained at ~600 nm along with broad absorption in UV-vis-NIR spectral window (similar to Figure 4.3a) suggest that the formation Ag_2S-$AgInS_2$ HDNCs. Interestingly, these obtained Ag_2S-$AgInS_2$ HDNCs show PL peak in NIR region as shown in Figure 4.4f, which is similar to PL of Ag_2S-$AgInS_2$ HDNCs prepared by single-step reaction as shown in the inset of Figure 4.4f. However, the PL intensity of resultant Ag_2S-$AgInS_2$ HDNCs is less than ten times of magnitude compared with that of Ag_2S-$AgInS_2$ HDNCs obtained by single-step. On the other hand, Ag_2S NCs exhibit a featureless absorption spectrum without any measurable PL. These results of (i) two-step reaction (Figure 4.4a-f), (ii) change in the NC characteristic during the reaction time in single-step reaction (Figure 4.3a-b), and (iii) absence of any crystalline product for a control reaction with only $In(DDTC)_3$ precursor, suggest that in the single-step reaction using $AgIn(DDTC)_4$ precurssor, Ag_2S forms first promoting the nucleation of $AgInS_2$ phase on Ag_2S NCs, yielding the Ag_2S-$AgInS_2$ HDNCs as the final product.

4.3.3 Band alignment using electrochemical measurements

Electronic, optical and optoelectronic properties of Ag_2S-$AgInS_2$ HDNCs, will strongly depend upon the alignment of VBM and CBM at the interface of Ag_2S and $AgInS_2$. We have elucidated the band alignment by performing CV measurements on the Ag_2S NCs, $AgInS_2$ NCs and Ag_2S-$AgInS_2$ HDNCs as shown in Figure 4.5a. In case of Ag_2S and $AgInS_2$ while scanning the potential from 0 V to more positive side one anodic peak (A_1) is observed, similarly on reversal of cycle, one cathodic peak (C_1) is observed. These anodic and cathodic peaks were assigned to the electron transfer between NCs and working electrode via VBM and CBM respectively.[35, 42] The obtained CBM for $AgInS_2$ NCs is about 0.22 eV higher in energy compared to that of Ag_2S NCs, and the VBM of $AgInS_2$ is 0.67 eV lower in energy compared to that of Ag_2S NCs. These results suggest that if $AgInS_2$ and Ag_2S share an interface, a type-I band alignment will be obtained, with a small barrier for electron transfer across the interface, and therefore can be even termed as pseudo type-II band alignment.[31]

In the case of our Ag_2S-$AgInS_2$ HDNCs, while scanning the potential from 0 V to more positive side two anodic peaks (A_1 and A_2), and on reversal of cycle, two cathodic peaks (C_1 and C_2) were observed. Comparing with cyclic voltammograms of Ag_2S and $AgInS_2$, A_1 and

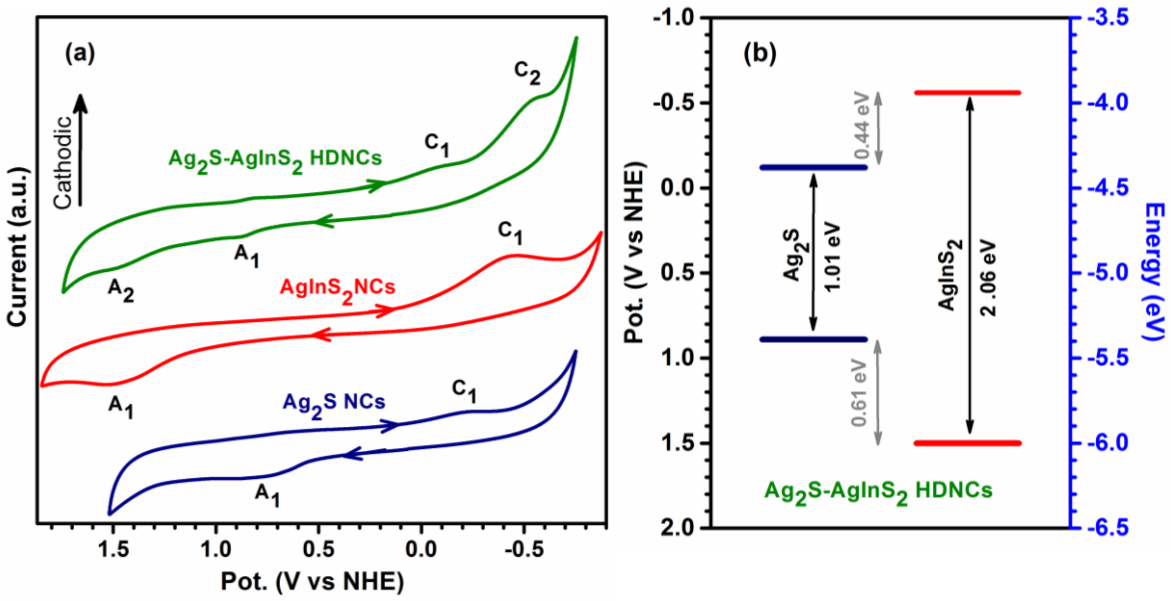

Figure 4.5: (a) Cyclic voltammograms recorded on Ag_2S NCs, $AgInS_2$ NCs and Ag_2S-$AgInS_2$ HDNCs. Scan rate used is 50 mV/s for all samples. Cathodic current direction shown in the figure by upward arrow. (b) Band alignment diagram in Ag_2S-$AgInS_2$ HDNCs constructed on the basis of CV data.

C_1 in HDNCs correspond to VBM and CBM of Ag_2S component, whereas, A_2 and C_2 correspond to VBM and CBM of $AgInS_2$ component. These assignments of CV response lead to Figure 4.5b showing band alignment diagram of Ag_2S-$AgInS_2$ HDNCs. A type-I band alignment was observed at the interface, with a small barrier for electron transfer. The band gap (2.04 eV) obtained from CV for the $AgInS_2$ component of the HDNCs, agrees with optical bandgap (~2.06 eV) in Figure 4.3a. Likewise, inset of Figure 4.3a suggests an optical gap of ~1000 nm (~1.24 eV) for Ag_2S component of the HDNCs, which also agrees with the CV band gap of 1.01 eV, keeping in mind the experimental uncertainties and differences in methodologies of both measurement techniques. It is to be noted that though CV shows the type-I (or close to pseudo type-II) band alignment at the interface of Ag_2S-$AgInS_2$ HDNCs, the spatial separation and/or recombination of electron-hole pair will depend strongly on the presence of mid-gap trap states.

4.3.4 Luminescence of Ag_2S-$AgInS_2$ HDNCs

To the best of our knowledge, luminescence from Ag_2S-$AgInS_2$ HDNCs are reported here for the first time, which in turn provided insights about mid-gap trap states that are crucial for optoelectronic applications. Figure 4.6a compares PL spectra of Ag_2S-$AgInS_2$ HDNCs with that of $AgInS_2$ NCs, whereas, Ag_2S NCs prepared in this method do not exhibit measurable PL. PL intensity of both samples were normalized by the corresponding absorbance at the

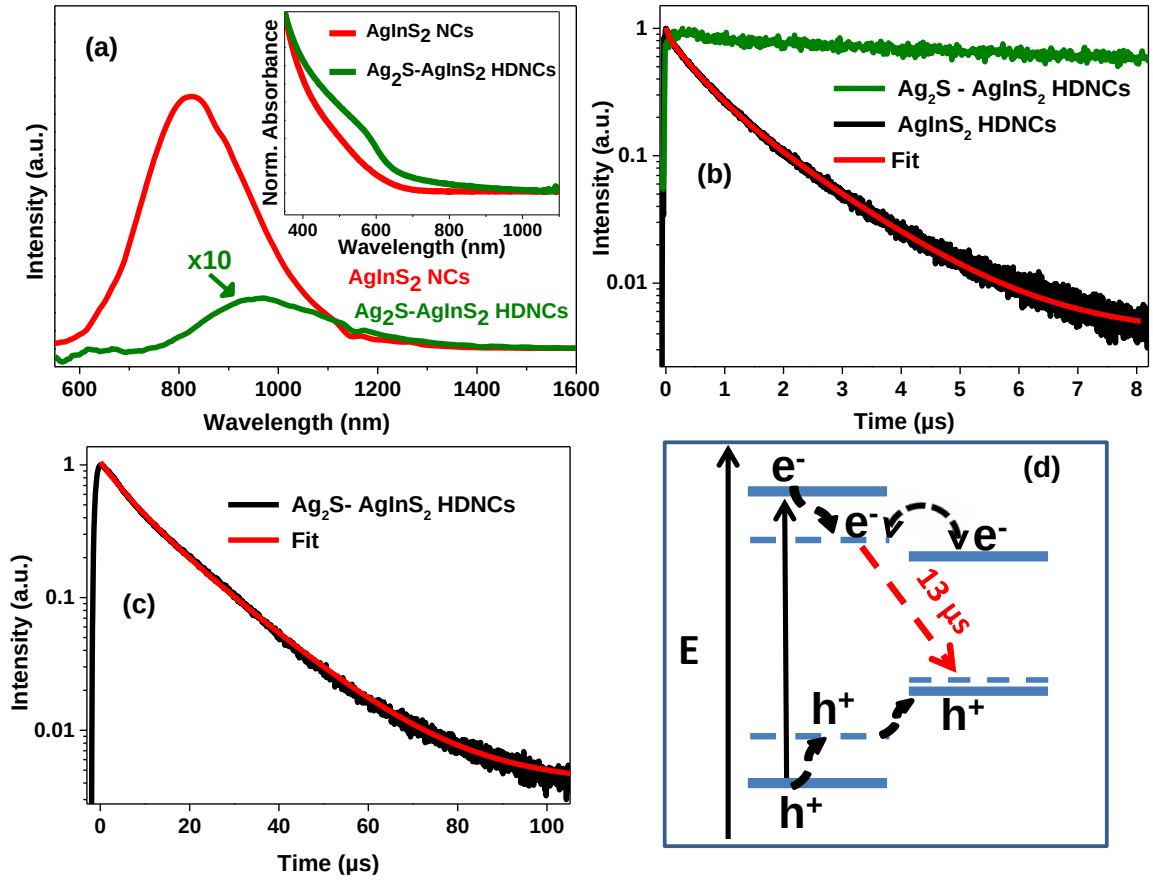

Figure 4.6: (a) PL spectra of $AgInS_2$ NCs and Ag_2S-$AgInS_2$ HDNCs. Intensity of PL spectrum for Ag_2S-$AgInS_2$ HDNCs has been multiplied by 10 times for a better representation. Inset shows UV-visible-NIR spectra of $AgInS_2$ NCs and Ag_2S-$AgInS_2$ HDNCs. (b-c) PL decay profile of $AgInS_2$ NCs and Ag_2S-$AgInS_2$ HDNCs was collected at their PL peak position 825 nm and 970 nm respectively, after excitation with 405 nm using (b) nanosecond LASER source and (c) microsecond flash lamp. (d) Schematic diagram explaining the mechanism of luminescence in Ag_2S-$AgInS_2$ HDNC.

excitation wavelength 450 nm. Inset of Figure 4.5a shows UV-vis-NIR spectra for Ag_2S-$AgInS_2$ HDNCs and $AgInS_2$ NCs. Broad PL spectrum, shifted towards lower energy (longer wavelength) compared optical gap is observed for $AgInS_2$ NCs, which is characteristic defect related emissions in I-III-VI NCs, as discussed in prior literature.[20-21, 43-44] Interestingly, Ag_2S-$AgInS_2$ HDNCs also exhibit a similar broad PL spectrum, but with lower intensity. To understand the mechanism of electron-hole recombination, we have studied PL decay dynamics (Figure 4.6b) keeping emission wavelength fixed at the peak positions 825 nm and 970 nm for $AgInS_2$ NCs and Ag_2S-$AgInS_2$ HDNCs, respectively. The decay profile for $AgInS_2$ NCs was fitted using a tri-exponential decay with lifetimes 54±20 ns (14±1.1% contribution), 520±70 ns (46±6% contribution), and 1.37±0.11 µs (40±7.5%). As suggested in ref[21], long lifetimes over many hundreds of ns can be attributed to donor-acceptor kind of

transitions involving localized traps within the bandgap, and tens of ns lifetime is observed for transitions involving one delocalized state (VBM or CBM) and a localized trap state of $AgInS_2$ NCs.On the other hand PL decay profile (Figure 4.6b) for Ag_2S-$AgInS_2$ HDNCs, is orders of magnitude slower with minimal decrease in intensity till 8 μs. Consequently, we used microsecond flash lamp for collecting the complete decay using multichannel scaling technique, where the time scales was measured up to sub-milliseconds as shown in Figure 4.6c. This PL decay of HDNCs was fitted using a bi-exponential decay curve with lifetimes 5.1±0.5 μS (30±5% contribution) and 14.67±0.5 μS (70±5% contribution), yielding an average lifetime of 13 μs. Please note that the time resolutions of the PL decays in Figures 4.6b-c is not small enough to probe the sub-nanosecond (non-radiative) decay channels. This μs long lifetime clearly signifies that the PL of HDNCs does not arise from band-edge transitions of both $AgInS_2$ and Ag_2S components, since band edge (or excitonic) transition from these systems has lifetime in the range of few tens of ns.[26] So the PL cannot be directly explained by the type-I band alignment of Ag_2S-$AgInS_2$ HDNCs, as suggested by the CV results (Figure 4.5b). Another possibility is since the band offset for CBM is smaller at the interface, electron can be delocalized over the entire HDNC, but the hole is localized only in the Ag_2S component, resulting into a pseudo type-II band alignment. Prior reports on similar pseudo type-II systems such as CdSe/CdS core shell NCs shows an increase in lifetime from 20 to over 100 ns because of decrease in overlap of electron and hole wavefunctions.[45-46] Furthermore, in a typical type-II alignment, for example in the case of CdTe/CdSe and CdS/ZnSe NCs also the lifetime is <100 ns.[47-48] Therefore, the observed average lifetime of 13 μs for our Ag_2S-$AgInS_2$ HDNCs cannot be explained by transitions involving CBM and VBM of two components, irrespective of the type of interfacial band alignment.

These results indicate that the PL involves mid-gap trap states. Lifetime of PL involving such localized mid-gap states in $AgInS_2$ are orders of magnitude smaller (Figure 4.6b) compared to lifetimes of Ag_2S-$AgInS_2$ HDNCs. On the other hand, the PL peak energy of HDNCs appears to be little higher or comparable to the optical gap for Ag_2S component, and also prior literature[26] suggest ~11 ns lifetime for excitonic PL from Ag_2S NCs. Therefore, the longer lifetime of 13 μs indicates that the PL of Ag_2S-$AgInS_2$ HDNCs is very much different from that of the individual components $AgInS_2$ and Ag_2S NCs. We attribute this 13 μs long lifetime of Ag_2S-$AgInS_2$ HDNCs to spatial separation of the defect-related electron and hole wavefunctions, where one of the defect-bound carrier is localized in the $AgInS_2$ part and the other one is in the Ag_2S part. Please note that these spatial separation of electron is not

because of type-II band alignment, but because of defect-mediated charge trapping which is possible even within the type-I alignment of Ag_2S-$AgInS_2$ HDNCs, as suggested by our CV data.

Ref[31] reported scanning tunnelling spectroscopy (STS) data of Ag_2S-$AgInS_2$ HDNCs showing Fermi level of $AgInS_2$ component slightly moves towards its CBM, whereas the Fermi level of Ag_2S part moves significantly closer to the VBM. These results can be explained by the formation of a deep electron donor states in the $AgInS_2$ component, and shallow electron acceptor states in the Ag_2S components of Ag_2S-$AgInS_2$ HDNCs. However further experimental studies are needed to know the location of donor and acceptor defect states. After combining this information with our PL results, a schematic showing plausible mechanism for PL in HDNCs is shown in Figure 4.6d. After excitation of a HDNC, an electron can get trapped to a localized defect state in $AgInS_2$, whereas the hole resides either in a shallow trap (or VBM) of Ag_2S. Radiative recombination of these spatially separated electron and hole gives rise to PL with 13 μs long lifetime.

4.3.5 $AgInS_2$ NCs and Ag_2S-$AgInS_2$ HDNCs sensitized solar cell

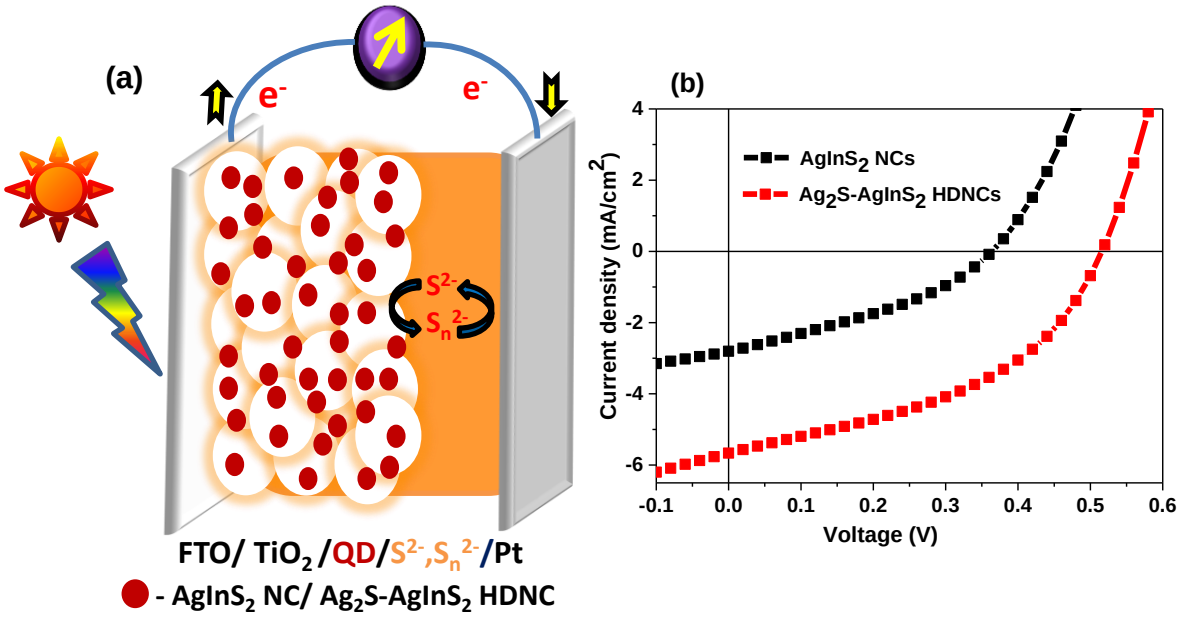

Figure 4.7: (a) Schematic of typical mesoporous-TiO_2 based nanocrystal sensitized solar cell. (b) J-V characteristics of $AgInS_2$ NCs and Ag_2S-$AgInS_2$ HDNCs measured by Xe lamp at standard conditions AM 1.5 G. The active area of the solar cell was 0.16 cm^2.

It is well understood that electron-hole separation by type-II band alignment across the interface of two materials is beneficial for solar cell application. Our Ag_2S-$AgInS_2$ HDNC represents a unique situation, where defect-mediated spatial separation of electron and hole

occurs, in spite of having a type-I band alignment. Importantly, PL lifetime of HDNCs is long (13 μS), and it has been recently reported that the long PL lifetime of Mn^{2+} doped CdSe based NCs suppress charge recombination improving solar cell efficiencies.[49-51] To investigate the influence of defect-mediated electron-hole separation, we prepared NC sensitized solar cells using both $AgInS_2$ NCs and Ag_2S-$AgInS_2$ HDNCs, the typical solar cell device is shown by the schematic figure 4.7a. Figure 4.7b shows the corresponding current density (J) - voltage (V) plots for un-optimized champion cells. The obtained solar cell parameters short circuit current density (J_{sc}), fill factor (FF), and open circuit voltage (V_{oc}), resulting into the overall power conversion efficiency (PCE, η), are given in the Table 4.1.

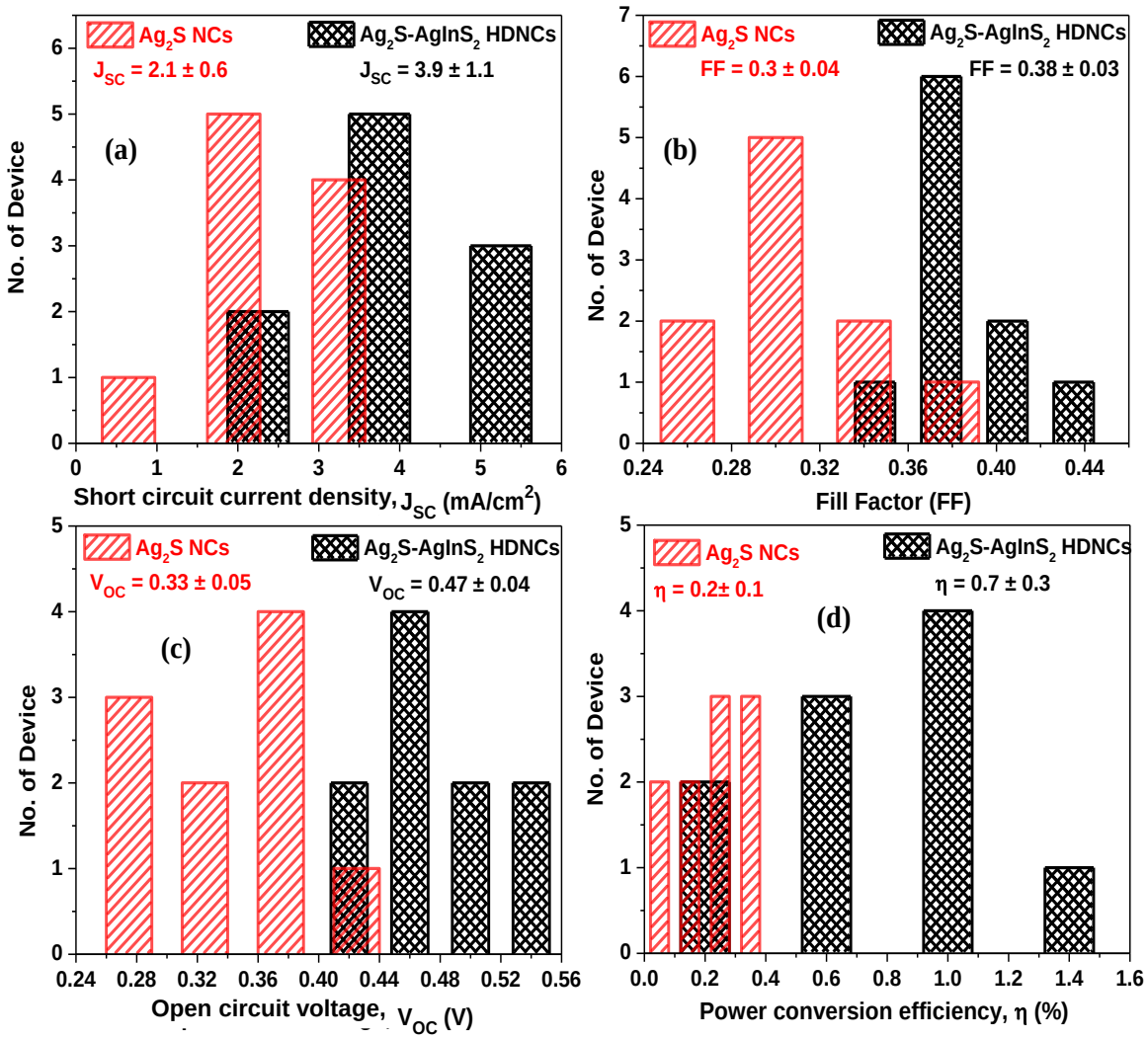

Figure 4.8: Comparison of solar cell parameters: (a) short circuit current density (J_{sc}), (b) fill factor (FF), (c) open circuit voltage (V_{oc}), and (d) power conversion efficiency, between $AgInS_2$ NC and Ag_2S-$AgInS_2$ HDNC sensitized solar cells. Histograms were made based on performance of 20 cells.

Table 4.1: Solar cell parameters obtained for champion cells from J-V plots shown in Figure 4.6. The statistics of solar cell parameters are shown in the parenthesis.

Sample	J_{sc} (mA/cm^2)	Fill Factor (FF)	V_{oc} (V)	η (%)
$AgInS_2$ NCs	2.8 (2.1±0.6)	0.35 (0.3±0.04)	0.37 (0.33±0.05)	0.4 (0.2±0.1)
Ag_2S-$AgInS_2$ HDNCs	5.7(3.9±1.1)	0.43 (0.38±0.03)	0.52 (0.47±0.04)	1.3 (0.7±0.3)

Interestingly, all these solar cell parameters are significantly superior for the champion Ag_2S-$AgInS_2$ HDNC sensitized solar cells compared to the champion $AgInS_2$ NC sensitized cells. For a more reliable comparison of the solar cell parameters (J_{sc}, FF, V_{oc}, and η), statistics on 20 such solar cells have been presented using bar diagrams in Figure 4.8 and the final statistic values have been given in the parenthesis of Table 4.1.[52] This statistics clearly show that Ag_2S-$AgInS_2$ HDNCs perform better for solar cell with mean η = 0.7 ± 0.3 and mean V_{oc} = 0.47 ± 0.04, which are significantly larger than the parameters for $AgInS_2$ NC sensitized solar cell (mean η = 0.2 ± 0.1 and mean V_{oc} = 0.33 ± 0.05).

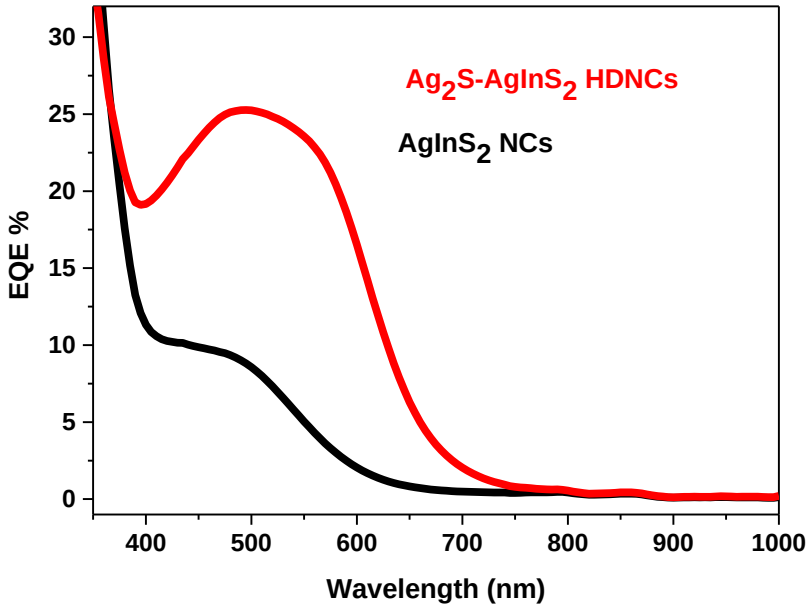

Figure 4.9: External quantum efficiency (EQE %) spectra of Ag_2S-$AgInS_2$ HDNCs and $AgInS_2$ NCs.

Figure 4.9 shows that the EQE for the HDNCs (25%) is also higher compared to $AgInS_2$ NCs (~10%) at 500 nm. EQE data shows that photocurrent of HDNCs is dominated by photo-

absorption because of the $AgInS_2$ component with little contribution in the NIR absorption by Ag_2S. This data agrees with the fact that UV-vis-NIR spectrum of HDNCs is also dominated by the $AgInS_2$ components, and furthermore, Ag_2S NCs prepared under similar conditions do not exhibit any PL suggesting faster (sub-ns) non-radiative electron-hole recombination in Ag_2S part of the HDNCs, and therefore, exhibit inefficient generation of photocurrent.

The improvement in solar cell parameters for Ag_2S-$AgInS_2$ HDNCs compared to $AgInS_2$ NCs can also be explained by the schematic energy level diagram shown in Figure 4.6d. The excited electrons located in $AgInS_2$ part transfers to TiO_2 electrode, whereas, the hole residing in Ag_2S part transfers to the redox couple S^{2-}/S_n^{2-}. This spatial separation of electron and hole, yielding longer PL lifetime, is known to increase J_{sc}, which in turn increases V_{oc}, since V_{oc} is proportional to the logarithm of $J_{sc.}$ Eventually, the PCE for Ag_2S-$AgInS_2$ HDNCs is 1.3 %, which is 3 times higher compared to that of $AgInS_2$ NC sensitized solar cell. To the best of our knowledge, this 1.3% PCE is the high reported value so far for NC sensitized solar cell fabricated using both Ag_2S NCs, and $AgInS_2$ NCs.[26, 41] Further optimization of device fabrication, with better selections of electrolytes and electrodes is expected to improve the efficiency of Ag_2S-$AgInS_2$ HDNC based solar cell.

4.4 Conclusions

Colloidal Ag_2S-$AgInS_2$ HDNCs have been prepared in a single-step reaction using $(AgIn)(DDTC)_4$ precursor at 250 ^oC in presence of oleylamine. Though the precursors were added in a single-step, the formation of Ag_2S-$AgInS_2$ HDNCs involved multiple steps, where Ag_2S nucleates first, which then promote the nucleation and growth of $AgInS_2$ part. CV shows the interface has a type-I band alignment with CBM of $AgInS_2$ component is 0.44 eV higher in energy than that of Ag_2S component, and VBM of $AgInS_2$ exhibit 0.61 eV lower energy compared to that of Ag_2S component. This type-I alignment suggest both electron and hole will reside in the Ag_2S component, and expected to recombine fast. But in the contrary, a very long PL lifetime (13 μS) was observed for Ag_2S-$AgInS_2$ HDNCs. To the best of our knowledge, PL has been observed from Ag_2S-$AgInS_2$ HDNCs for the first time, and the observed lifetimes are orders of magnitude higher than the PL from both $AgInS_2$ NCs and Ag_2S NCs. This long PL lifetime along with observed type-I band alignment suggest defect-mediated charge separation across the interface of the HDNCs, where the photo-excited electron gets trapped by a defect state inside the $AgInS_2$ component, and the hole resides either in VBM or shallow defect states of Ag_2S component. The efficacy of such defect

mediated electron-hole separation was also tested by fabricated NC sensitized solar cell where the photo conversion efficiency (1.3%) of Ag_2S-$AgInS_2$ HDNCs is more than three times higher than that of $AgInS_2$ NCs (0.4%). This possibility of achieving type-II like electron-hole separation via defect states, irrespective of the nature of band offsets at the interface, can lead to new ways to tailor material properties by employing controlled doping strategies manipulating the defect states.

References

1. Choi, C. L.; Alivisatos, A. P. From Artificial Atoms to Nanocrystal Molecules: Preparation and Properties of More Complex Nanostructures. *Annu. Rev. Phys. Chem.* **2010**,*61*, 369-389

2. Sarma, D. D.; Santra, P. K.; Mukherjee, S.; Nag, A. X-Ray Photoelectron Spectroscopy: A Unique Tool to Determine the Internal Heterostructure of Nanoparticles. *Chem. Mater.* **2013**, *25*, 1222-1232.

3. Patra, B. K.; Guria, A. K.; Dutta, A.; Shit, A.; Pradhan, N. Au-SnS Hetero Nanostructures: Size of Au Matters. *Chem. Mater.* **2014**, *26*, 7194-7200.

4. Choi, H.; Radich, J. G.; Kamat, P. V. Sequentially Layered CdSe/CdS Nanowire Architecture for Improved Nanowire Solar Cell Performance. *J. Phys. Chem. C* **2014,** *118*, 206-213.

5. Xu, S.; Shen, H.; Zhou, C.; Yuan, H.; Liu, C.; Wang, H.; Ma, L.; Li, L. S. Effect of Shell Thickness on the Optical Properties in CdSe/CdS/$Zn_{0.5}Cd_{0.5}S$/ZnS and CdSe/CdS/$Zn_xCd_{1-x}S$/ZnS Core/Multishell Nanocrystals. *J. Phys. Chem. C* **2011**, *115*, 20876−20881.

6. Hines, M. A.; Guyot-Sionnest, P. Synthesis and Characterization of Strongly Luminescing ZnS-Capped CdSe Nanocrystals. *J. Phys. Chem.* **1996**, *100*, 468-471.

7. Dabbousi, B. O.; RodriguezViejo, J.; Mikulec, F. V.; Heine, J. R.; Mattoussi, H.; Ober, R.; Jensen, K. F.; Bawendi, M. G. (CdSe)ZnS Core-Shell Quantum Dots: Synthesis and Characterization of a Size Series of Highly Luminescent Nanocrystallites. *J. Phys. Chem. B* **1997**, *101*, 9463-9475.

8. Reiss, P.; Protiere, M.; Li, L. Core/Shell Semiconductor Nanocrystals. *Small* **2009**, *5*, 154-168.

9. Sahasrabudhe, A.; Bhattacharyya, S. Dual Sensitization Strategy for High-Performance Core/Shell/Quasi-Shell Quantum Dot Solar Cells. *Chem. Mater.* **2015**, *27*, 4848-4859.

10. Choi, S. H.; Kim, E. G.; Hyeon, T. One-Pot Synthesis of Copper-Indium Sulfide Nanocrystal Heterostructures with Acorn, Bottle, and Larva Shapes. *J. Am. Chem. Soc.* **2006**, *128*, 2520-2521.

11. Li, L.; Daou, T. J.; Texier, I.; Tran, T. K. C.; Nguyen, Q. L.; Reiss, P. Highly Luminescent $CuInS_2$/ZnS Core/Shell Nanocrystals: Cadmium-Free Quantum Dots for in Vivo Imaging. *Chem. Mater.* **2009**, *21*, 2422-2429.

12. McDaniel, H.; Koposov, A. Y.; Draguta, S.; Makarov, N. S.; Pietryga, J. M.; Klimov, V. I. Simple Yet Versatile Synthesis of $CuInSe_xS_{2-x}$ Quantum Dots for Sunlight Harvesting. *J. Phys. Chem. C* **2014**, *118*, 16987−16994.

13. Zhong, H. Z.; Bai, Z. L.; Zou, B. S. Tuning the Luminescence Properties of Colloidal I-III-VI Semiconductor Nanocrystals for Optoelectronics and Biotechnology Applications. *J. Phys. Chem. Lett.* **2012**, *3*, 3167-3175.

14. Kang, X., Huang, L., Yang, Y., Pan, D. Scaling up the Aqueous Synthesis of Visible Light Emitting Multinary $AgInS_2$/ZnS Core/Shell Quantum Dots. *J. Phys. Chem. C* **2015**, *119*, 7933-7940.

15. Kameyama, T.; Takahashi, T.; Machida, T.; Kamiya, Y.; Yamamoto, T.; Kuwabata, S.; Torimoto, T. Controlling the Electronic Energy Structure of ZnS−$AgInS_2$ Solid Solution Nanocrystals for Photoluminescence and Photocatalytic Hydrogen Evolution. *J. Phys. Chem. C* **2015**, *119*, 24740−24749.

16. Panthani, M. G.; Stolle, C. J.; Reid, D. K.; Rhee, D. J.; Harvey, T. B.; Akhavan, V. A.; Yu, Y. X.; Korgel, B. A. $CuInSe_2$ Quantum Dot Solar Cells with High Open-Circuit Voltage. *J. Phys. Chem. Lett.* **2013**, *4*, 2030-2034.

17. Panthani, M. G.; Khan, T. A.; Reid, D. K.; Hellebusch, D. J.; Rasch, M. R.; Maynard, J. A.; Korgel, B. A., In Vivo Whole Animal Fluorescence Imaging of a Microparticle-Based Oral Vaccine Containing ($CuInSe_xS_{2-X}$)/ZnS Core/Shell Quantum Dots. *Nano Lett.* **2013**, *13*, 4294-4298.

18. Huang, D.; Persson, C. Photocatalyst $AgInS_2$ for Active Overall Water-Splitting: A First-Principles Study. *Chem. Phys. Lett.* **2014**, *591*, 189-192.

19. Du, Y.; Xu, B.; Fu, T.; Cai, M.; Li, F.; Zhang, Y.; Wang, Q. Near-Infrared Photoluminescent Ag_2S Quantum Dots from a Single Source Precursor. *J. Am. Chem. Soc.* **2010**, *132*, 1470-1471.

20. Torimoto, T.; Adachi, T.; Okazaki, K.; Sakuraoka, M.; Shibayama, T.; Ohtani, B.; Kudo, A.; Kuwabata, S. Facile Synthesis of ZnS-$AgInS_2$ Solid Solution Nanoparticles for a Color-Adjustable Luminophore. *J. Am. Chem. Soc.* **2007**, *129*, 12388-12389.

21. Rao, M. J.; Shibata, T.; Chattopadhyay, S.; Nag, A. Origin of Photoluminescence and XAFS Study of $(ZnS)_{(1-X)}(AgInS_2)_{(X)}$ Nanocrystals. *J. Phys. Chem. Lett.* **2014**, *5*, 167-173.

22. Guchhait, A.; Pal, A. J. Copper-Diffused $AgInS_2$ Ternary Nanocrystals in Hybrid Bulk-Heterojunction Solar Cells: Near-Infrared Active Nanophotovoltaics. *ACS Appl. Mater. Interfaces* **2013**, *5*, 4181-4189.

23. Tsuji, I.; Kato, H.; Kobayashi, H.; Kudo, A. Photocatalytic H_2 Evolution Reaction from Aqueous Solutions over Band Structure-Controlled $(AgIn)_{(X)}Zn_{2(1-X)}S_2$ Solid Solution Photocatalysts with Visible-Light Response and Their Surface Nanostructures. *J. Am. Chem. Soc.* **2004**, *126*, 13406-13413.

24. Jagadeeswararao, M.; Dey, S.; Nag, A.; Rao, C. N. R. Visible Light-Induced Hydrogen Generation Using Colloidal $(ZnS)_{(0.4)}(AgInS_2)_{(0.6)}$ Nanocrystals Capped by S^{2-} Ions. *J. Mater. Chem. A* **2015**, *3*, 8276-8279.

25. Zhang, Y. J.; Liu, Y. S.; Li, C. Y.; Chen, X. Y.; Wang, Q. B. Controlled Synthesis of Ag_2S Quantum Dots and Experimental Determination of the Exciton Bohr Radius. *J. Phys. Chem. C* **2014**, *118*, 4918-4923.

26. Mir, W. J.; Swarnkar, A.; Sharma, R.; Katti, A.; Adarsh, K. V.; Nag, A. Origin of Unusual Excitonic Absorption and Emission from Colloidal Ag_2S Nanocrystals: Ultrafast Photophysics and Solar Cell. *J. Phys. Chem. Lett.* **2015**, *6*, 3915-3922.

27. Zhang, Y.; Hong, G. S.; Zhang, Y. J.; Chen, G. C.; Li, F.; Dai, H. J.; Wang, Q. B. Ag_2S Quantum Dot: A Bright and Biocompatible Fluorescent Nanoprobe in the Second near-Infrared Window. *ACS Nano* **2012**, *6*, 3695-3702.

28. Tang, R.; Xue, J.; Xu, B.; Shen, D.; Sudlow, G. P.; Achilefu, S. Tunable Ultrasmall Visible-to-Extended near-Infrared Emitting Silver Sulfide Quantum Dots for Integrin-Targeted Cancer Imaging. *ACS Nano* **2015**, *9*, 220-230.

29. Shen, S.; Zhang, Y.; Liu, Y.; Peng, L.; Chen, X.; Wang, Q. Manganese-Doped Ag_2S-ZnS Heteronanostructures. *Chem. Mater.* **2012**, *24*, 2407-2413.

30. Zhu, G. X.; Xu, Z. Controllable Growth of Semiconductor Heterostructures Mediated by Bifunctional Ag_2S Nanocrystals as Catalyst or Source-Host. *J. Am. Chem. Soc.* **2011**, *133*, 148-157.

31. Bose, R.; Manna, G.; Jana, S.; Pradhan, N. Ag_2S-$AgInS_2$: p-n Junction Heteronanostructures with Quasi Type-II Band Alignment. *Chem. Commun.* **2014**, *50*, 3074-3077.

32. Bard, A. J.; Faulkner, L. R. *Electrochemical Methods: Fundamentals and Applications*; Wiley, 2000.

33. Poznyak, S. K.; Osipovich, N. P.; Shavel, A.; Talapin, D. V.; Gao, M. Y.; Eychmuller, A.; Gaponik, N. Size-Dependent Electrochemical Behavior of Thiol-Capped CdTe Nanocrystals in Aqueous Solution. *J. Phys. Chem. B* **2005**, *109*, 1094-1100.

34. de la Cueva, L.; Lauwaet, K.; Otero, R.; Gallego, J. M.; Alonso, C.; Juarez, B. H. Effect of Chloride Ligands on CdSe Nanocrystals by Cyclic Voltammetry and X-Ray Photoelectron Spectroscopy. *J. Phys. Chem. C* **2014**, *118*, 4998-5004.

35. Haram, S. K.; Quinn, B. M.; Bard, A. J. Electrochemistry of CdS Nanoparticles: A Correlation between Optical and Electrochemical Band Gaps. *J. Am. Chem. Soc.* **2001**, *123*, 8860-8861.

36. Zoski, C. *Handbook of Electrochemistry*; Elsevier: New Mexico, USA, 2007.

37. Choi, H.; Nicolaescu, R.; Paek, S.; Ko, J.; Kamat, P. V. Supersensitization of CdS Quantum Dots with a Near-Infrared Organic Dye: Toward the Design of Panchromatic Hybrid-Sensitized Solar Cells. *ACS Nano* **2011**, *5*, 9238-9245.

38. Nag, A.; Kovalenko, M. V.; Lee, J. S.; Liu, W. Y.; Spokoyny, B.; Talapin, D. V. Metal-Free Inorganic Ligands for Colloidal Nanocrystals: S^{2-}, HS^-, Se^{2-}, HSe^-, Te^{2-}, HTe^-, TeS_3^{2-}, OH^- and NH_2^- as Surface Ligands. *J. Am. Chem. Soc.* **2011**, *133*, 10612-10620.

39. Wu, J. J.; Chang, R. C.; Chen, D. W.; Wu, C. T. Visible to Near-Infrared Light Harvesting in Ag_2S Nanoparticles/ZnO Nanowire Array Photoanodes. *Nanoscale* **2012**, *4*, 1368-1372.

40. Jara, D. H.; Stamplecoskie, K. G.; Kamat, P. V. Two Distinct Transitions in Cu_xInS_2 Quantum Dots. Bandgap versus Sub-Bandgap Excitations in Copper-Deficient Structures *J. Phys. Chem. Lett.* **2016**, *7*, 1452–1459

41. Kadlag, K. P.; Patil, P.; Rao, M. J.; Datta, S.; Nag, A. Luminescence and Solar Cell from Ligand-Free Colloidal $AgInS_2$ Nanocrystals. *CrystEngComm* **2014**, *16*, 3605-3612.

42. Ma, X. D.; Mews, A.; Kipp, T. Determination of Electronic Energy Levels in Type-II CdTe-Core/CdSe-Shell and CdSe-Core/CdTe-Shell Nanocrystals by Cyclic Voltammetry and Optical Spectroscopy. *J. Phys. Chem. C* **2013**, *117*, 16698-16708.

43. Li, L. A.; Pandey, A.; Werder, D. J.; Khanal, B. P.; Pietryga, J. M.; Klimov, V. I. Efficient Synthesis of Highly Luminescent Copper Indium Sulfide-Based Core/Shell Nanocrystals with Surprisingly Long-Lived Emission. *J. Am. Chem. Soc.* **2011**, *133*, 1176-1179.

44. Leach, A. D. P.; Shen, X.; Faust, A.; Cleveland, M. C.; La Croix, A. D.; Banin, U.; Pantelides, S. T.; Macdonald, J. E. Defect Luminescence from Wurtzite $CuInS_2$ Nanocrystals: Combined Experimental and Theoretical Analysis. *J. Phys. Chem. C* **2016**, *120*, 5207-5212.

45. Christodoulou, S.; Vaccaro, G.; Pinchetti, V.; Donato, F. De ; Grim, J. Q.; Casu, A.; Genovese, A.; Vicidomini, G.; Diaspro, A.; Brovelli, S.; et al. Synthesis of Highly

Luminescent Wurtzite CdSe/CdS Giant-Shell Nanocrystals Using a Fast Continuous Injection Route. *J. Mater. Chem. C* **2014**, *2*, 3439-3447.

46. Brovelli, S.; Schaller, R. D.; Crooker, S. A.; Garcia-Santamaria, F.; Chen, Y.; Viswanatha, R.; Hollingsworth, J. A.; Htoon, H.; Klimov, V. I. Nano-Engineered Electron-Hole Exchange Interaction Controls Exciton Dynamics in Core-Shell Semiconductor Nanocrystals. *Nat. Commun.* **2011**, *2*.

47. Kim, S.; Fisher, B.; Eisler, H. J.; Bawendi, M. Type-II Quantum Dots: CdTe/CdSe(Core/Shell) and CdSe/ZnTe(Core/Shell) Heterostructures. *J. Am. Chem. Soc.* **2003**, *125*, 11466-11467.

48. Verma, S.; Kaniyankandy, S.; Ghosh, H. N. Charge Separation by Indirect Bandgap Transitions in CdS/ZnSe Type-II Core/Shell Quantum Dots. *J. Phys. Chem. C* **2013**, *117*, 10901-10908.

49. Santra, P. K.; Kamat, P. V. Mn-Doped Quantum Dot Sensitized Solar Cells: A Strategy to Boost Efficiency over 5%. *J. Am. Chem. Soc.* **2012**, *134*, 2508-2511.

50. Debnath, T.; Maity, P.; Maiti, S.; Ghosh, H. N. Electron Trap to Electron Storage Center in Specially Aligned Mn-Doped CdSe d-Dot: A Step Forward in the Design of Higher Efficient Quantum-Dot Solar Cell. *J. Phys. Chem. Lett.* **2014**, *5*, 2836-2842.

51. Wang, J.; Li, Y.; Shen, Q.; Izuishi, T.; Pan, Z.; Zhao, K.; Zhong, X. Mn Doped Quantum Dot Sensitized Solar Cells with Power Conversion Efficiency Exceeding 9%. *J. Mater. Chem. A* **2016**, *4*, 877-886.

52. Luber, E. J.; Buriak, J. M. Reporting Performance in Organic Photovoltaic Devices. *ACS Nano* **2013**, *7*, 4708-4714.

Chapter 5

Colloidal $CuInSe_2$ Based Nanocrystals for Solar Cell

Summary

Optical band gap of $CuInSe_2$ NCs is 1.3 eV, which is sufficient to absorb solar-light from visible to near-infra red (NIR) region. Also, energy of conduction band minimum (CBM) of $CuInSe_2$ NCs is just higher than that of TiO_2, so that it can be fine tuned for efficient electron transfer from $CuInSe_2$ to TiO_2. In addition, $CuInSe_2$ is environmentally benign. With these properties in mind, we prepared colloidal $(Zn)_x(CuIn)_{1-x}Se_2$ (x = 0, 0.24, 0.42) NCs, and studied their photophysical properties. Incorporation of Zn in the $CuInSe_2$ lattice tunes the band gap, shifts the CBM to somewhat higher energies, and modifies defect densities both in the core and on the surface of NCs. $(Zn)_{0.24}(CuIn)_{0.76}Se_2$ NCs exhibit the highest PL intensity among the all three aforementioned compositions, and exhibit a band gap of 1.5 eV, which is suitable for quantum dot sensitized solar cell (QDSSC). Therefore, $(Zn)_{0.24}(CuIn)_{0.76}Se_2$ NCs were used to fabricate QDSSC device. Photoconversion efficiency (PCE) obtained from $(Zn)_{0.24}(CuIn)_{0.76}Se_2$ NCs is 0.8%, which is low suggesting that too many electron-hole recombination centres are there in these NCs. In order to improve the PCE from these NCs, we have coated ZnS on $(Zn)_{0.24}(CuIn)_{0.76}Se_2$ NCs sensitised TiO_2 electrode by employing successive ionic layer adsorption and reaction (SILAR) technique. Eventually, ZnS coated photoanode shows the PCE of 3.6% under AM 1.5G one sun illumination, confirming that ZnS coating reduces the unwanted recombination processes.

Graphical abstract

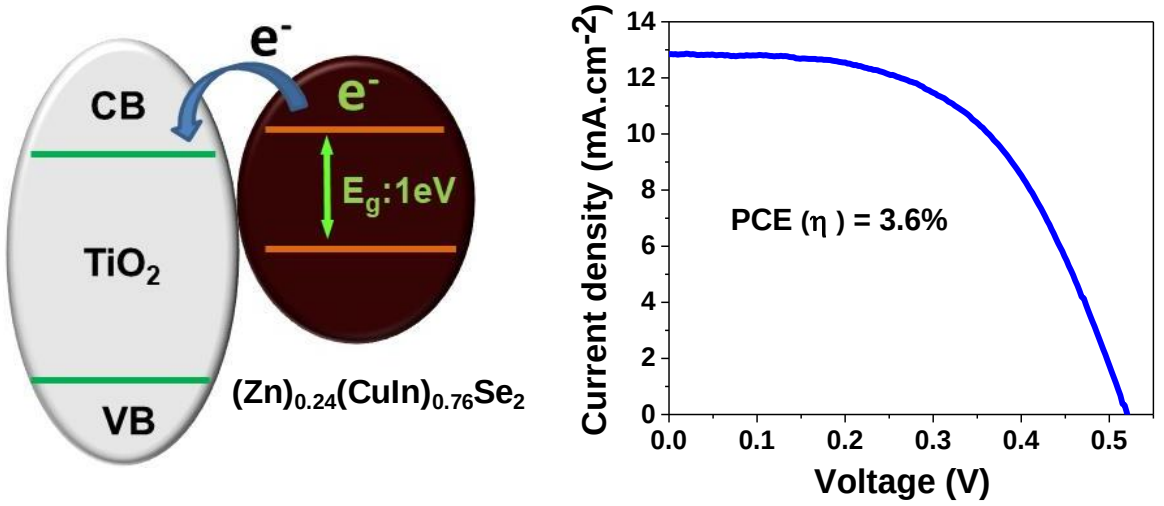

5.1 Introduction

Colloidal semiconductor nanocrystals (NCs) or quantum dots (QDs) are one of the interesting, efficient and low-cost materials for solar cell applications. QDs exhibit size-tunable band gaps, high absorption cross section, and high photoluminescence quantum yield (PL QY).[1-4] Furthermore, QDs exhibit multiple exciton generation (MEG) process and slow hot electron cooling time, which lead to the theoretical photo conversion efficiency (PCE) values more than the Schokley-Quassier limit.[5-7] Therefore, one of the promising way to generate electricity from solar energy is using quantum dot sensitized solar cell (QDSSC). In this regard, Cd-based and Pb-based QDSSC are well studied, and the PCE values have been significantly improved from less than 1% to 11%.[8-13]

This improvement in PCE can be attributed to minimization of unwanted losses in QDSSC at each part of the QDSSC right from photoabsorber, to photoanode, to counter electrode. Let us first discuss the case of photoabsorber. The preparation of highly crystalline NCs at higher reaction temperatures leads to reduction of crystal defects that trap charge carriers. Dangling bonds on the surface of NC act as another source of non-radiative trap states. In order to passivate these dangling bonds, often a thin shell with higher band gap material coated.[14] Such treatments decrease the non-radiative trap states. But, care should be taken in the design of these treatments such that the efficiency of charge injection (or extraction) process to (from) NCs are not significantly reduced. The efficiency of charge separation can be enhanced by making hetero structured NCs like hetero dimer NCs with type-II band alignment. In addition to these strategies, doping of Mn^{2+} ion in NCs also helps in enhancing the carriers state lifetimes of carriers.[15-17] Thus, enhancing the probability of extraction of charge carriers from these NCs.

To make an efficient photoanode, we need to load more NCs on TiO_2 and improve the electron transfer rate from NCs to TiO_2. To achieve both these functionalities, organic ligands with long hydrocarbon chain are replaced from the surface of NCs with smaller organic ligands (for example; 3-mercaptopropionic acid, MPA) and/or inorganic ligands such as $S_2O_3^{2-}$ and S^{2-} by post synthesis modification.[18-19] These surface modifications offer the dispersion of NCs in polar solvents leading to both better loading of NCs onto the polar surface of TiO_2 electrode,[20] and enhanced electron transfer rate from NCs to TiO_2.[21] However, post synthesis surface modifications sometimes result in creating new mid-gap trap states, which hinder the transport and transfer of charge carriers.[1] In order to overcome this issue, often TiO_2 electrode sensitized by QDs (photoanode) are treated with wide band gap

materials such as ZnS and CdS by successive ionic layer adsorption and reaction (SILAR) process including coating of few amorphous layers of SiO_2 and TiO_2.[11-12] Such treatment reduces interfacial recombination and increases charge collection efficiency by passivating the surface of both NCs and uncovered TiO_2 portions.[12]

Now, we discuss about the role of counter electrodes in governing PCE values. Initially Pt was used in QDSSC as counter electrode. Though Pt exhibit high conductivity and catalytic activity, polysulfide electrolytes get chemically adsorbed and corrode Pt counter electrode. These reasons led to the usage of Au counter electrode in QDSSC. However, the solar cell performance was not so high using Au counter electrode. Also, noble metals like Au and Pt are expensive. Later, metal sulphide were studied as possible inexpensive and stable counter electrodes for QDSSC.[22-23] Other inexpensive systems like carbon derivatives,[24] and polymers[25] are also being used as counter electrodes. Recently, Ti mesh supported mesoporous carbon has been used as counter electrode in QDSSC and reported one of the highest PCE values of 11.16% for QDSSC by Du et al.[13] Many of the aforementioned studies were carried out for toxic Cd and Pb based NCs. Group I (Cu, Ag)-III (In, Ga)-VI (S, Se) semiconductor NCs are emerging as environment friendly NCs for QDSSC.[26]

Bulk $CuInSe_2$ exhibit a narrow direct band gap of 1.04 eV,[26] which can absorb light starting from 1200 nm to visible range with high (10^5 cm^{-1}) absorption coefficient values.[27] The larger exciton Bohr diameter (~20 nm) of $CuInSe_2$ compared with other I-III-VI semiconductors allows the shifting of conduction band minimum (CBM) of $CuInSe_2$ NCs to higher energies by decreasing the size of NCs. Increase in the energy of CBM of $CuInSe_2$ compared to that of TiO_2 enhances the efficiency of electron injection from $CuInSe_2$ to TiO_2.[28] It has been shown that $CuInSe_2$ NCs exhibit MEG with external quantum efficiency (EQE) above 120%.[5] Often, PL of I-III-VI based NCs involves localized (donor-acceptor) states along with delocalized states. In $CuInSe_2$ Oikkonen et al reported that there is no deep levels in the mid-gap region corresponding to vacancies of Cu and In. However, acceptor level corresponding to Se vacancy lie in the mid-gap region.[29] The smaller band gap of $CuInSe_2$ is also advantageous for not having deep defect states. Thus, $CuInSe_2$ is relatively more defect tolerant compared to other I-III-VI materials. These properties motivated us to use $CuInSe_2$ QDs for solar cell applications. Moreover, the elements are environmentally benign for real life applications.

In this work, we have synthesized chalcopyrite structure of oleylamine capped $CuInSe_2$ NCs with size ~ 6 nm at a reaction temperature of 180 ^oC. A small amount of diphenyl phosphine (0.6 ml diphenyl phosphine (DPP) in 10% of hexane) was used for dissolution of Se. $CuInSe_2$

NCs exhibit band gap 1.3 eV showing quantum confinement effect. PL from $CuInSe_2$ NCs exhibit defect related luminescence with ~ 300 nm full width at half maximum (FWHM). To optimize energy of CBM and PL efficiency, we have prepared alloy of $Zn_{0.24}(CuIn)_{0.76}Se_2$ and $Zn_{0.42}(CuIn)_{0.58}Se_2$ NCs. The composition of $Zn_{0.24}(CuIn)_{0.76}Se_2$ NCs show relatively more PL intensity and less (~ 180 nm) FWHM than other two compositions along with a suitable band gap (1.5 eV) for QDSSC. Subsequently, we have modified the surface of the oleylamine capped $Zn_{0.24}(CuIn)_{0.76}Se_2$ NCs to MPA capped NCs, which allows redispersion of NCs in water. The optical properties remains similar after the surface modification. We have used these MPA capped $Zn_{0.24}(CuIn)_{0.76}Se_2$ NCs in QDSSC. ZnS treatment has been done for QD sensitized TiO_2 electrode. The PCE for $Zn_{0.24}(CuIn)_{0.76}Se_2$ QDs using Cu_2S as counter electrode with polysulfide electrolyte is 3.63%.

5.2 Experimental section

5.2.1 Synthesis of $CuInSe_2$ NCs

0.01 mmol (19.2 mg) copper iodide (CuI), and 0.01 mmol (30 mg) indium acetate $In(OAc)_3$ were taken in a three neck round bottom flask (RB) containing a mixture of 2 mL octadecene (ODE) and 2 mL oleylamine. The above reaction mixture was kept under vacuum and then the temperature was increased from room temperature to 100 ^oC. Vacuum was continued for another 20 mininutes at 100 ^oC. Then the temperature of reaction mixture was increased to180 ^oC under N_2 atmosphere. Selinium (Se) precursor was prepared by mixing of ~23 mg Se powder with 0.3 mL oleylamine and 0.6 ml DPP in 10% hexane inside a N_2 filled glove box. The colourless solution of Se was injected into the RB drop-wise at 180 ^oC and the reaction was continued for 15 minutes. After that, the reaction was quenched by removing the heat supply, and the temperature was quickly reduced to 90 ^oC by using ice bath. At this temperature 10 mL hexane was injected into the solution followed by cooling down the reaction mixture to room temperature. The obtained NCs were precipitated by adding mixture containing equal volume of ethanol and acetone, followed by centrifugation at 5000 rpm for 5 minutes. The supernatant liquid was discarded and the obtained precipitate was re-dispersed in 5 mL chloroform ($CHCl_3$). To the above solution, 10 mL methanol was added and centrifuged again at 5000 rpm for 5 minutes. The precipitate obtained after discarding the supernatant liquid is $CuInSe_2$ NCs which were re-dispersed in $CHCl_3$ for optical studies.

5.2.2. Synthesis of $(Zn)_{0.24}(CuIn)_{0.76}Se_2$ NCs

To prepare $(Zn)_{0.24}(CuIn)_{0.76}Se_2$ NCs, 0.08 mmol (50 mg) zinc stearate ($Zn(C_{18}H_{35}O_2)_2$), 0.06 mmol (11.9 mg) CuI and 0.06 mmol (18.1 mg) $In(OAc)_3$ were taken in three neck RB which contains 4 mL ODE and 2.5 mL oleylamine. Se concentration and other experimental procedures were same as $CuInSe_2$ NCs synthesis.

5.2.3 Synthesis of $(Zn)_{0.42}(CuIn)_{0.58}Se_2$ NCs

To prepare $(Zn)_{0.42}(CuIn)_{0.58}Se_2$ NCs, 0.12 mmol (75 mg) zinc stearate ($Zn(C_{18}H_{35}O_2)_2$), 0.04 mmol (7.3 mg) CuI and 0.04 mmol (11.6 mg) of $(In(OAc)_2$ were taken in three neck RB which contains 4 mL ODE and 2.5 mL oleylamine. Remaining experimental procedures were same as $CuInSe_2$ NCs synthesis.

5.2.4 Phase transfer reaction of oleylamine capped NCs

$(Zn)_{0.24}(CuIn)_{0.76}Se_2$ NCs were dispersed in 5 mL $CHCl_3$ solution. To this dispersion, 1 mL methanol, 0.3 mL deionized water and 0.5 mL MPA (pH of MPA was maintained at ~ 12 by adding 10% NaOH solution) were added and stirred for 1 hour. NCs transfer from organic phase to aqueous phase leaving oleylamine in $CHCl_3$. Colourless organic part was removed. 5 mL acetone was added to the remaining aqueous solution, and was centrifuged at 5000 rpm for 5 min. The obtained precipitate was redispersed in deionized water. 120 µL MPA (maintaining pH ~12) was added to the NCs in water medium and this solution was used for sensitization of NCs on TiO_2 electrode.

5.2.5 Preparation of Cu_2S counter electrodes

Figure 5.1: (a) Photograph of brass plate. (b) Plates after treating wih HCl at 80 °C. (c) Photograph of Cu_2S coated brass plates obtained by drop casting Na_2S/S solution on treated brass plates shown in Figure (b).

2 × 1.5 cm^2 brass plates as shown Figure 5.1a were rubbed with sand paper for 15 minutes followed by heating the brass plates in 35% HCl at 80 °C for 30 min. In this process, the light yellowish colour of brass transformed to brown colour as shown Figure 5.1b, indicating the removal of Zn from top of brass plates. The obtained brown colour plates were sonicated in

deionized water for 2-3 minutes in order to remove the residuals of acid. Then 50 µL polysulfide solution was drop casted on brown coloured plates. The plates now become black in colour, indicating the formation of Cu_2S films on top of treated brass plates,[30] as shown in Figure 5.1c.

5.2.6 Fabrication of $Zn_{0.24}(CuIn)_{0.76}Se_2$ NC sensitized solar cell

Mesoporous TiO_2 electrode were prepared following reported procedure,[31] discussed in chapter 4. These electrodes were heated at 80 ^oC for 10 min and dipped in MPA capped $Zn_{0.24}(CuIn)_{0.76}Se_2$ QD solution for 48 hours. The colourless TiO_2 electrode turned into dark brown indicating the sensitization of QDs. After sensitization, the electrodes were washed with water and ethanol and dried at 110^o C for 10 mins. Then, ZnS coating was done on the electrodes by following successive ionic layer adsorption and reaction (SILAR) method by alternatively dipping (1 min/dip) the electrode in solutions of Zn^{2+} and S^{2-} ions. Solution for Zn^{2+} was prepared by dissolving 0.1mmol $Zn(OAc)_2$ in methanol, whereas S^{2-} solution was prepared by dissolving 0.1 mmol $Na_2S.9H_2O$ in 1:1 volume mixture of methanol and water. 8 cycles of ZnS coating were carried out following ref.[32] After the SILAR coating of ZnS, electrodes were washed with deionised water and methanol respectively.

QDSSCs were assembled by sandwiching the photoanode with Cu_2S counter electrode, spatially separated (~80 µm) by cello tape spacer and electrically connected through 20 µL polysulfide electrolyte. Polysulfide electrolyte used in our work was prepared by following ref[33], where Na_2S (1 M), sulfur (1 M), KCl (0.1 M) were mixed in mixture of methanol : water in 7 : 3 v/v. Current-voltage (I-V) measurements were carried out using Keithly 2611 source meter. 150 W, Xe lamp fitted with AM 1.5 filter was used for illumination in all of the solar cell measurements. Intensity of the Xe lamp was adjusted to 1 sun (100 mW/cm^2) by using NREL-calibrated silicon solar cell. The active area of the solar cell measurement was 0.25-0.3 cm^2.

5.2.7 Characterization

UV-visible-NIR absorption spectra were measured using a lambda-45 UV/vis spectrometer. Steady state PL and PL decay dynamics (time correlated single photon counting (TCSPC)) were recorded using FLS 980 EDINBURGH Instruments. Powder x-ray diffraction (XRD) data were recorded using a Bruker D8 Advance X-ray diffractometer using Cu Kα radiation (1.54 Å). Transmission electron microscopy (TEM) was carried out using a JEOL, JEM 2100

F, Field Emission TEM. Field emission scanning electron microscopy (FESEM) was carried out using a Zeiss Ultra Plus scanning electron microscope.

5.3. Results and Discussion

5.3.1. Synthesis and structural characterization of $Zn_x(CuIn)_{1-x}Se_2$ NCs

Oleylamine capped $Zn_x(CuIn)_{1-x}Se_2$ NCs have been prepared with x = 0, 0.24 and 0.76 compositions. $CuInSe_2$ with x = 0 composition was prepared by following ref.[28] Other compositions, x = 0.24 and 0.42 were prepared after modifying the procedure for x = 0 composition. Table 5.1 shows elemental analysis of product NCs using energy dispersive X-ray spectroscopy (EDS). Increasing the amount of Zn from x = 0, 0.4, and 0.6 in the precursor solution result into forming $CuInSe_2$, $(Zn)_{0.24}(CuIn)_{0.76}Se_2$, and $(Zn)_{0.42}(CuIn)_{0.58}Se_2$ NCs, respectively.

Table 5.1: EDS results comparing the elemental ratio Zn : (Cu + In) in precursor solution and final nanocrystal. Note that the ratio of Cu : In remains ~ 1 for precursor and product NCs for all the samples.

Precursor concentration		EDS for product	
Zn	Cu + In	Zn	Cu + In
0	1	0	1
0.4	0.6	0.24	0.76
0.6	0.4	0.42	0.58

Figure 5.2a shows the XRD patterns of $Zn_x(CuIn)_{1-x}Se_2$ NCs for all three compositions. The broadness of XRD peaks corresponds to smaller size of NCs. XRD pattern of $CuInSe_2$ (x = 0) NCs is matches with that of bulk $CuInSe_2$ showing chalcopyrite crystal structure. An increase in x, shifts the XRD patterns towards higher 2θ values, suggesting a decrease in lattice parameters. This shift in 2θ indicates the formation of $Zn_x(CuIn)_{1-x}Se_2$ alloy NCs. An increase in Zn content systematically reduces the volume of unit cell causing the shift in 2θ. This shift in XRD patterns in Figure 5.2a also agrees with EDS of $Zn_x(CuIn)_{1-x}Se_2$ NCs given in Table 5.1. Figure 5.2b shows TEM image for x = 0.24 composition in $Zn_x(CuIn)_{1-x}Se_2$ NCs. Distorted spherical shape of NCs are observed. Figure 5.2c shows the size distribution plot for $Zn_{0.24}(CuIn)_{0.76}Se_2$ NCs. Diameter of the NCs calculated to be 6.4 ± 1.3 nm. Sizes of the NCs for other two compositions are also similar to that of x = 0.24 (data not shown).

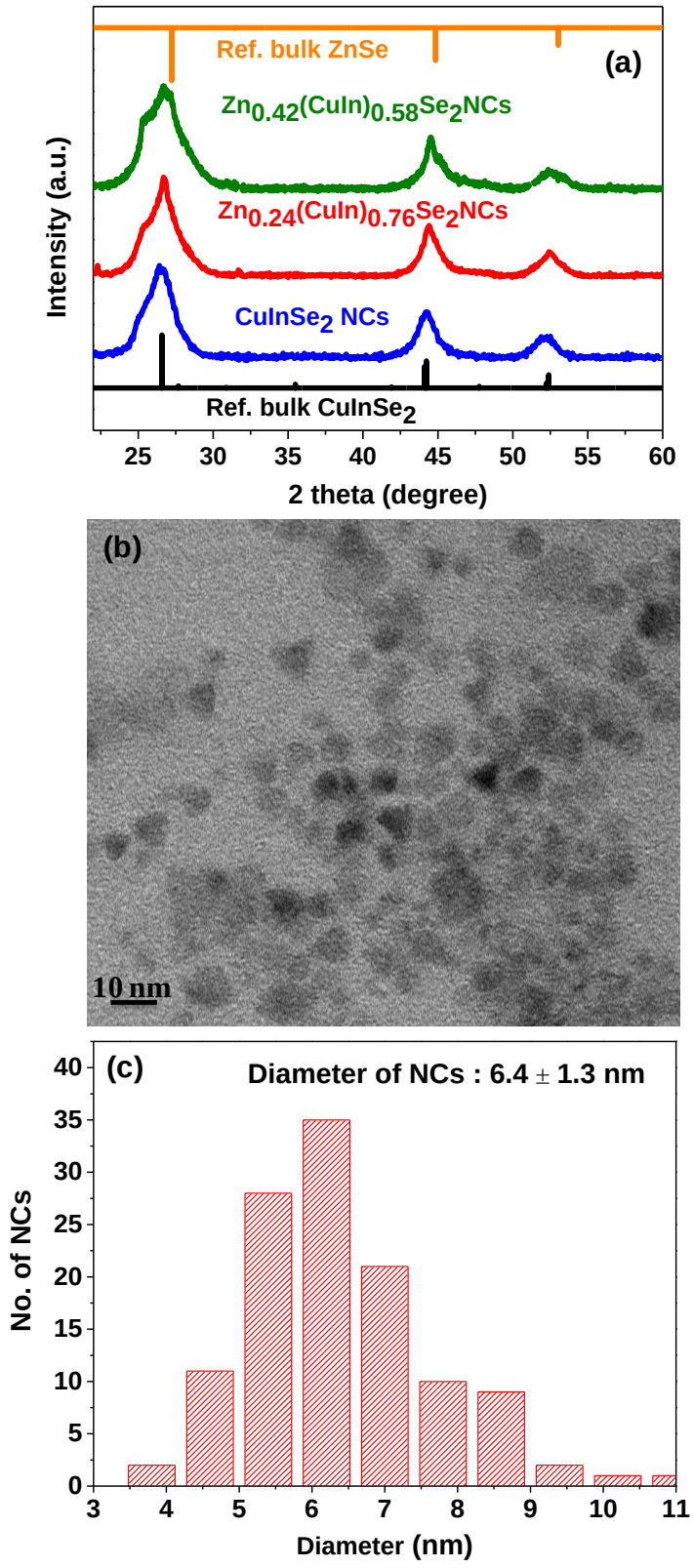

Figure 5.2: (a) XRD patterns of $Zn_x(CuIn)_{1-x}Se_2$ NCs with x = 0, 0.4 and 0.6 compositions. (b) TEM image of oleylamine capped $Zn_{0.4}(CuIn)_{0.6}Se_2$ NCs. (c) Size distribution plot for $Zn_{0.4}(CuIn)_{0.6}Se_2$ NCs.

5.3.2 Absorption and photoluminescence from $Zn_x(CuIn)_{1-x}Se_2$ NCs

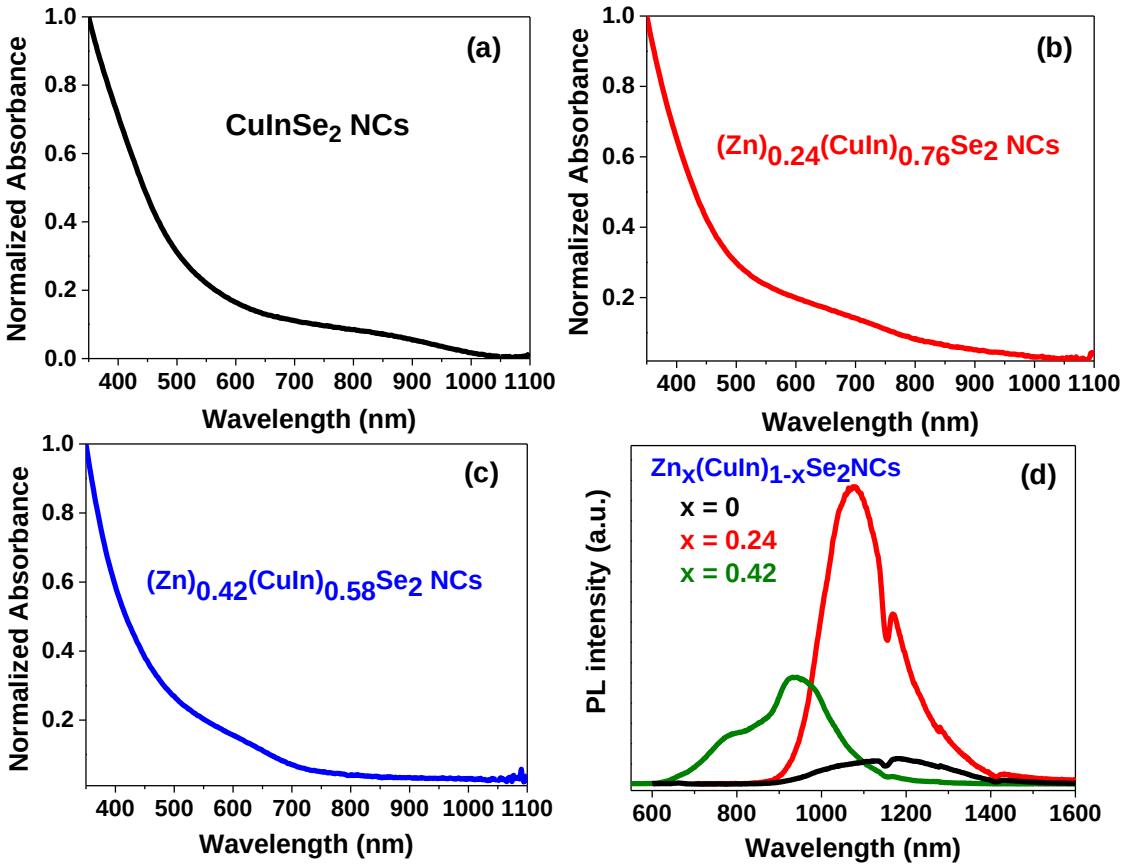

Figure 5.3: (a-c) UV-visible absorption data for colloidal $(Zn)_x(CuIn)_{1-x}Se_2$ NCs for compositions, x = 0, 0.24, and 0.42, respectively. (d) Photoluminescence (PL) data for colloidal $(Zn)_x(CuIn)_{1-x}Se_2$ NCs for all the three compositions after excitation at 2.48 eV (500 nm). PL spectra were normalized by the absorbance at their excitation wavelength.

Figure 5.3a-c show the UV-visible-near infrared (NIR) absorption spectra for colloidal $(Zn)_x(CuIn)_{1-x}Se_2$ NCs for three different compositions, x = 0, 0.24, and 0.42. The absorption spectra of these NCs blue shifts systematically with increase in x owing to the formation of alloy NCs, as suggested by EDS and XRD patterns. Figure 5.3d shows PL spectra of colloidal $Zn_x(CuIn)_{1-x}Se_2$ NCs exhibiting a significant blue shift in peak position with increase in Zn content. Absence of sharp band edge transition in the absorption spectra makes it difficult to estimate the band gap. The optical band gap of $Zn_x(CuIn)_{1-x}Se_2$ semiconductor NCs can be obtained by Tauc plot with some uncertainty, by using the equation $\alpha h\nu = C(h\nu - Eg)^{1/2}$, where, α is the absorption coefficient, $h\nu$ is the photon energy, E_g is the optical band gap and C is a constant.[34-35] We can replace α by absorbance A since optical path and concentration of sample are invariant here.[36] Figure 5.4a-c show the plots of $(Ah\nu)^2$ *vs* $h\nu$ where E_g is obtained

by extrapolating the linear portion of the plot at $(Ahv)^2 = 0$. Optical band gaps are found to be 1.3, 1.5 and 1.7 eV for NCs with x = 0, 0.24 and 0.42, respectively, as shown in Figure 5.4d.

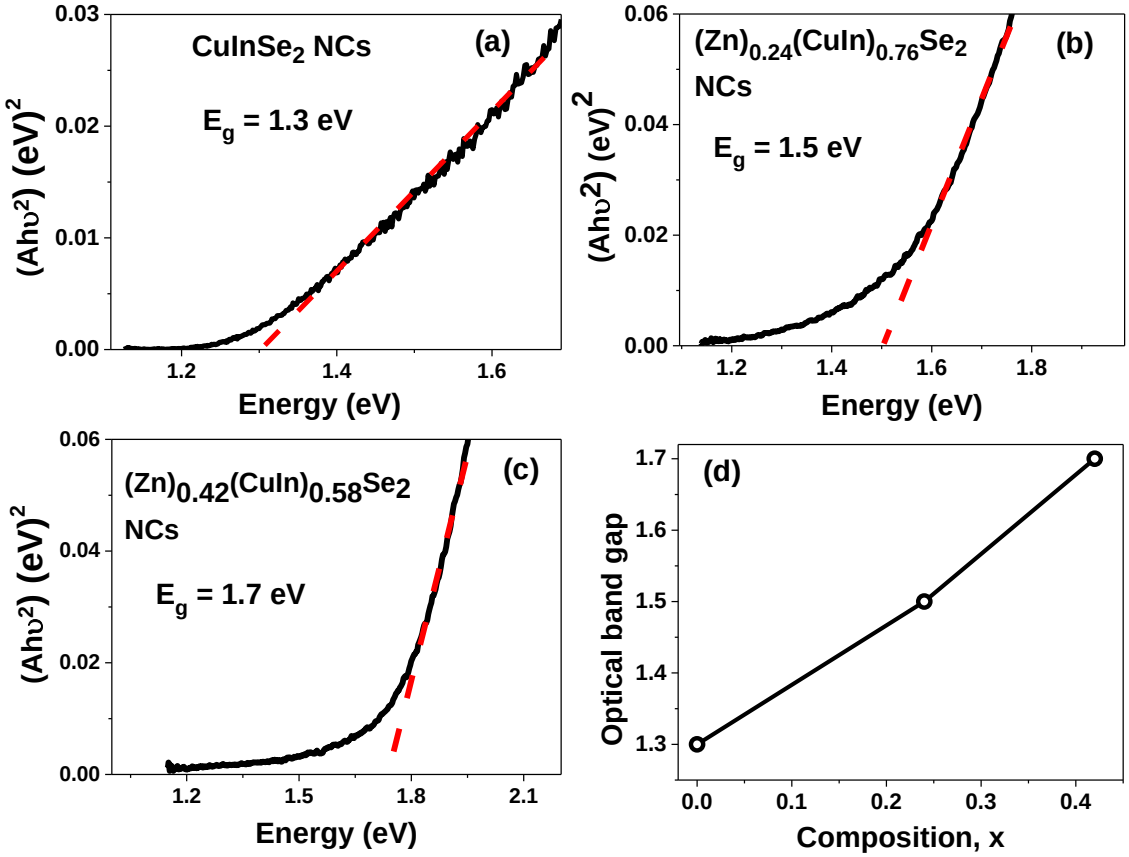

Figure 5.4:(a-c) UV-visible absorption data plotted as $(Ahv)^2$ versus energy for colloidal $(Zn)_x(CuIn)_{1-x}Se_2$ NCs with compositions, x = 0, 0.24, and 0.42. Red colour dashed lines show the extrapolation of the linear portion of the plot to $(Ahv)^2 = 0$. (d) Optical band gap of $(Zn)_x(CuIn)_{1-x}Se_2$ NCs with x = 0, 0.24, and 0.42. Circles show data points whereas line is just a guide to eye.

Optical band gap of 1.3 eV for $CuInSe_2$ (x = 0) NCs is higher than that of bulk $CuInSe_2$ (1.01 eV for chalcopyrite crystal phase)[26] suggesting quantum confinement effect in our NCs. Size of NCs obtained from TEM remain similar (~6 nm) for all the three compositions. Therefore, the change in optical band gap with composition of NCs is because of the alloy formation without much contribution from size induced quantum confinement. $Zn_x(CuIn)_{1-x}Se_2$ NCs exhibit broad PL with large Stoke's shift compared to band gap similar to prior reports suggesting the involvement of both delocalized states and localized states in PL.[37-38] $Zn_x(CuIn)_{1-x}Se_2$ NCs with x = 0.24 composition shows highest PL intensity among all three compositions, suggesting lower density of non-radative traps in $Zn_{0.24}(CuIn)_{0.76}Se_2$ NCs. Having suitable band gap of 1.5 eV with less trap states, we have chosen $Zn_{0.24}(CuIn)_{0.76}Se_2$ NCs for fabricating QDSSC.

5.3.3 Surface modification of oleylamine capped $Zn_{0.24}(CuIn)_{0.76}Se_2$ NCs

Prior to the use of $Zn_{0.24}(CuIn)_{0.76}Se_2$ NCs in QDSSC one need to remove the long hydrocarbon chain oleylamine ligand from the surface of NCs for better transport of charge carriers.[39] In order to do this, oleylamine capped $Zn_{0.24}(CuIn)_{0.76}Se_2$ NCs were first dispersed in nonpolar solvent such as $CHCl_3$. To this colloidal solution, a mixture of MPA, water and methanol was added. Here, pH of MPA was maintained at ~12. These mixture was stirred for 1 hour resulting into the transfer of NCs to aqueous medium. The phase transfer of NCs is shown in the Figure 5.5. –SH group of MPA is known to bind with NC surface, while the $–COO^-$ end of MPA interact with polar water molecules.[10] These colloidal NCs are stable for few months. This surface modification process was done by following reported procedure.[10]

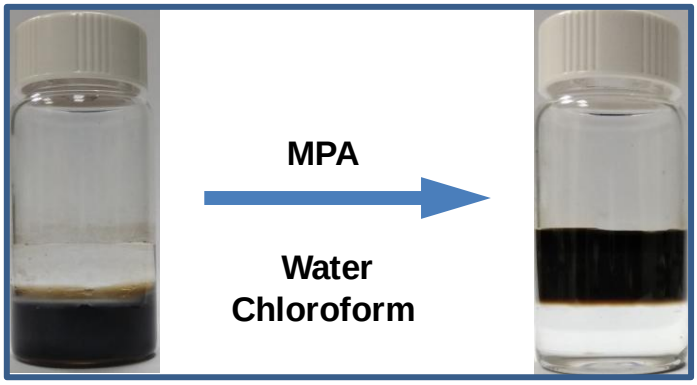

Figure 5.5: Photographs showing the phase transfer reaction of oleylamine capped $Zn_{0.24}(CuIn)_{0.76}Se_2$ NCs dispersed $CHCl_3$ to MPA capped $Zn_{0.24}(CuIn)_{0.76}Se_2$ NCs dispersed in aqueous medium.

In order to check the change in the optical properties after replacing the ligand on the surface of the NC, absorption and PL spectra of these NCs were measured. Figure 5.6a shows UV-visible-NIR absorption spectra for both oleylamine and MPA capped $Zn_{0.24}(CuIn)_{0.76}Se_2$ NCs. From the spectra it is clear that there is not much change in the optical band gap with surface modification. PL peak positions are also similar for both types of NCs but with a small decrease in PL intensity for MPA capped $Zn_{0.24}(CuIn)_{0.76}Se_2$ NCs. This small decrease in PL intensity is common in such phase transfer reactions and it can be attributed to some of the trap states that might get introduced during the phase transfer reaction which quenches the PL.

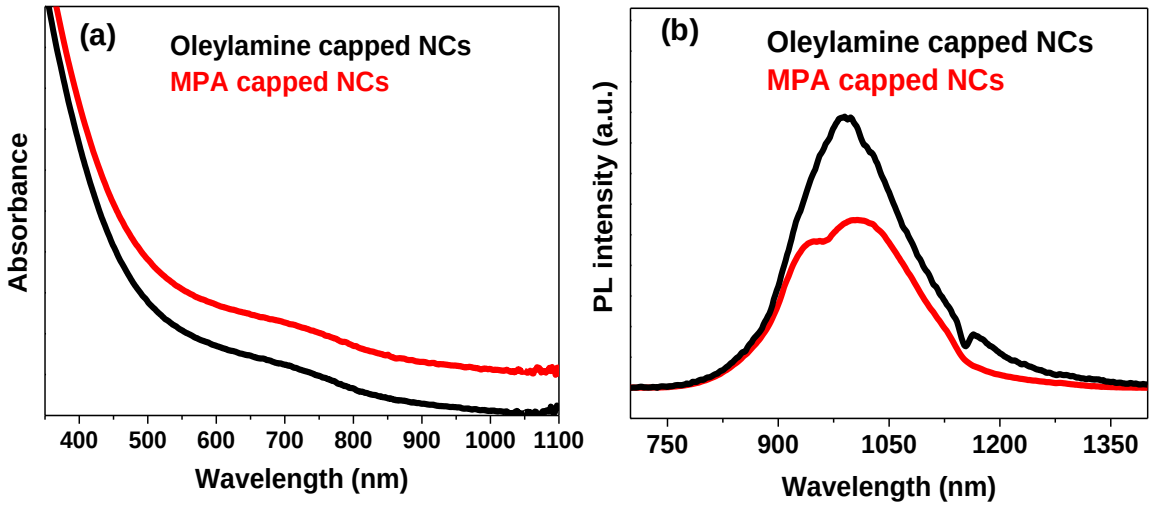

Figure 5.6: (a) UV-visible-NIR absorption spectra of oleylamine and MPA capped $Zn_{0.24}(CuIn)_{0.76}Se_2$ NCs. Spectrum for MPA capped NCs has been shifted vertically up for better representation. (b) The corresponding PL spectra of both oleylamine and MPA capped NCs.

5.3.4 Immobilisation of NCs onto TiO_2 surface

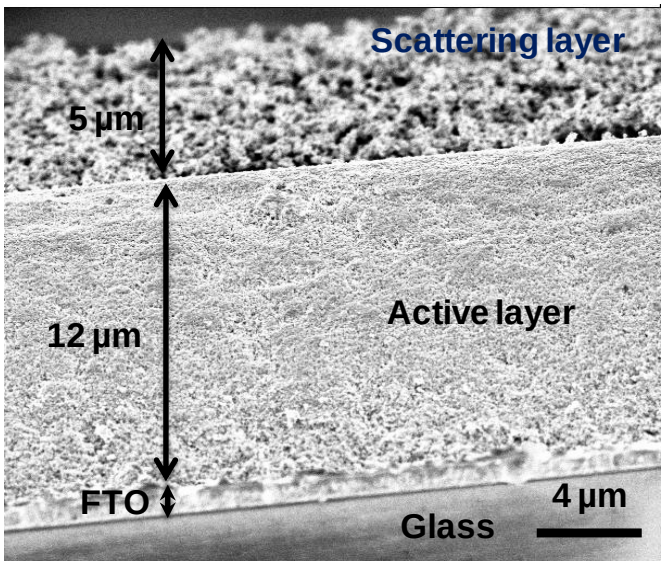

Figure 5.7: Cross section SEM image of TiO_2 electrode consists of two layers. One is active layer and other is scattering layer with thickness of 12 µm and 5 µm, respectively.

Mesoporous TiO_2 electrode was prepared using standard protocol (similar to 4th chapter). Figure 5.7 shows the cross section image of TiO_2 electrode on FTO substrate where Thickness of active layer of TiO_2 is 12 µm. Such thick layer can allow high loading of NCs on the pores of TiO_2. On top of the active layer, 5 µm thick TiO_2 scattering layer has been coated in order to trap sun-light.

In order to sensitize the NCs onto mesoporous TiO_2 electrode, these electrodes were dipped in MPA capped $Zn_{0.24}(CuIn)_{0.76}Se_2$ NCs solution for 2 days. NCs go through the pores and get adsorbed on TiO_2 particles in active layer. Such NCs transfer process onto TiO_2 is become faster and efficient due the strong affinity of $–COO^-$ group towards TiO_2.[40-41] as shown in Figure 5.8. Length of the alkyl chain is limited to two carbon atoms in MPA. This short chain lead to efficient charge carrier injection from NC to TiO_2. Thus, MPA capping allows both more loading of NCs on TiO_2, and better charge transfer at NC – TiO_2 interface. NC sensitised TiO_2 electrode is called photoanode.

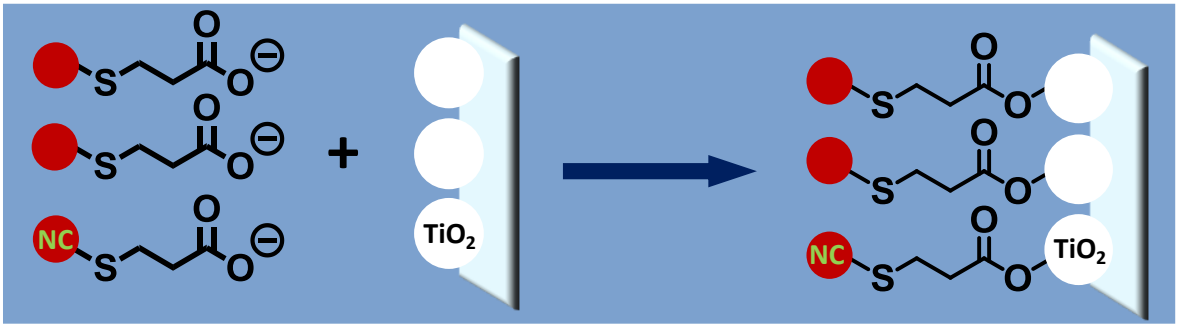

Figure 5.8: Schematic representation showing the immobilisation of MPA capped $Zn_{0.24}(CuIn)_{0.76}Se_2$ NCs to TiO_2 nanoparticals. Figure has been drawn following ref.[41]

5.3.5 $Zn_{0.24}(CuIn)_{0.76}Se_2$ NCs sensitized solar cell

Solar cells were made by assembling photoanode and Cu_2S counter electrode in a sandwich approach as shown in Figure 5.9a. J-V measurements were carried out by irradiating the cell with Xe lamp. Figure 5.9b shows J-V plot for MPA capped $Zn_{0.24}(CuIn)_{0.76}Se_2$ NCs. The obtained solar cell parameters, namely short circuit current density (J_{sc}), open circuit voltage (V_{oc}), fill factor (FF) and power conversion efficiency (PCE, η), are given in the Table 5.1.

$Zn_{0.24}(CuIn)_{0.76}Se_2$ NCs have suitable band gap, band alignment, and short chain ligand on the NC surface. But still the obtained PCE is low (0.8%). It suggests that less separation of charge carriers in the device. In other words more numbers of carrier recombinations at different interfaces as shown by the schematic in Figure 5.10a. In solar cell device, upon irradiation with Xe lamp electron-hole pair formation takes place in NCs. Then, some of the electrons transfer to TiO_2 whereas holes in the VB are regenerated by oxidising electrolyte. However, electrons from TiO_2 may recombine with oxidised electrolyte or with holes in VB of NC. In addition to this, electrons from NC may recombine with oxidised electrolyte instead of going to TiO_2. Of cource, the recombination within the NC cannot be excluded. All these recombination processes are detrimental for the solar cell performance.

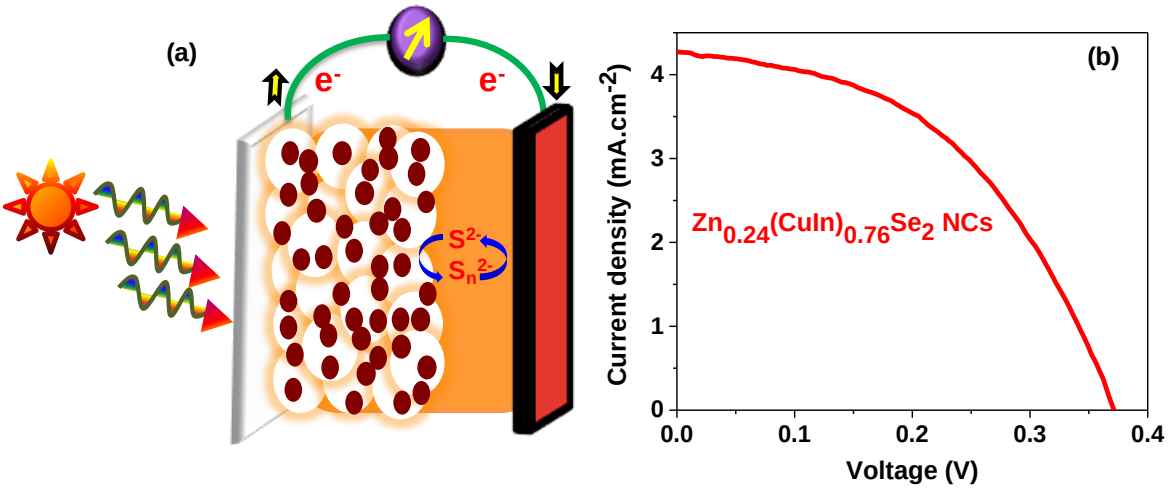

Figure 5.9: (a) Schematic of a NC sensitized solar cell, where Cu_2S is used as counter electrode. (b) J-V characteristics of $Zn_{0.24}(CuIn)_{0.76}Se_2$ NCs measured by using Xe lamp at standard conditions AM 1.5 G.

Table 5.1: Solar cell parameters obtained for champion cells from J-V plots shown in Figure 5.9.

Sample	J_{sc} (mA/cm^2)	V_{oc} (V)	FF	PCE (η %)
$Zn_{0.24}(CuIn)_{0.76}Se_2$ NCs	4.26	0.37	0.47	0.8

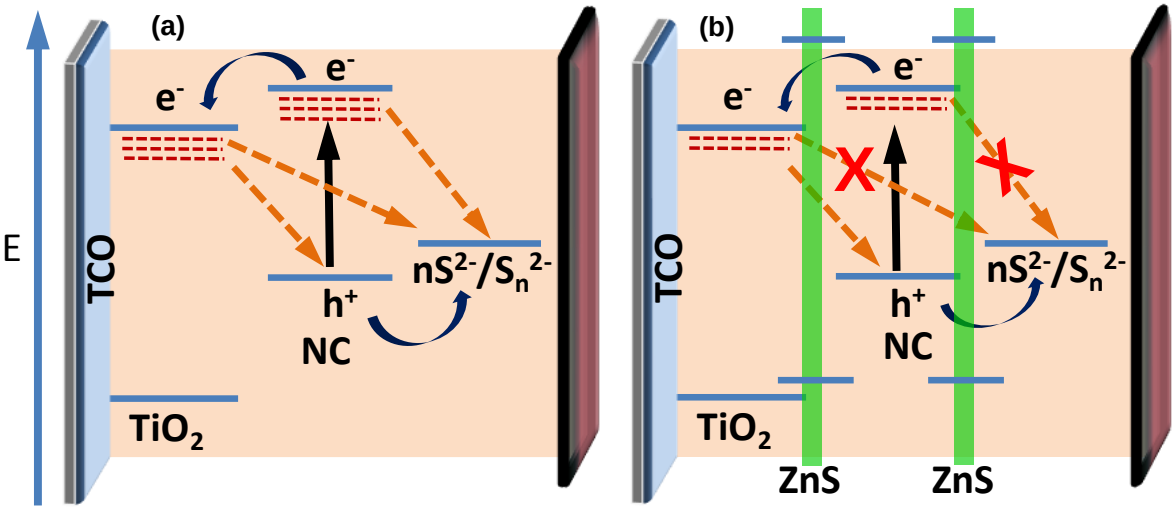

Figure 5.10: (a) Schematic showing recombinations of electron and hole in quantum dot sensitized solar cell upon irradiating by Xe lamp. (b) Schematic showing the control of recombinations of electron and hole after ZnS coating on photoanode. Figure (b) adapted from ref.[42]

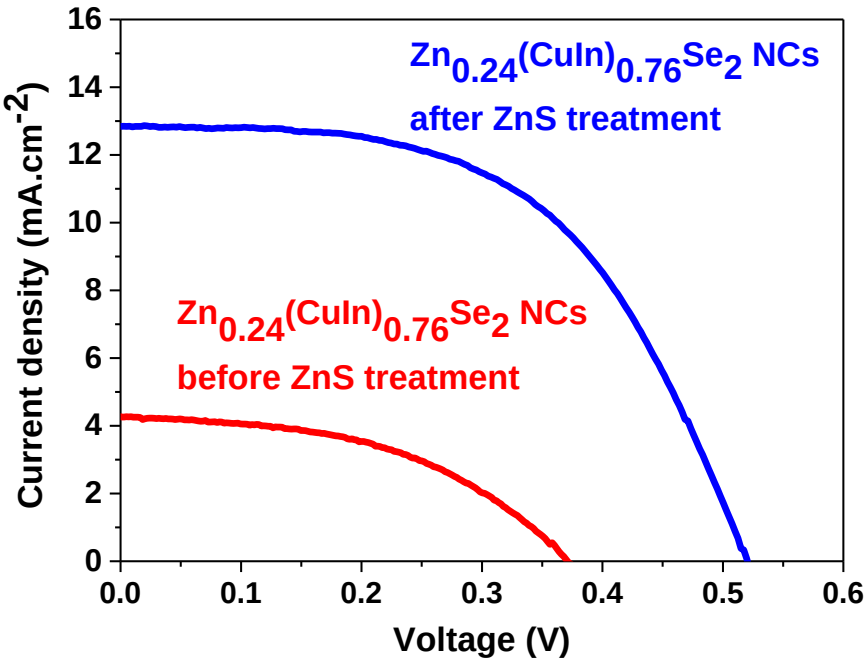

Figure 5.11: Current density-Voltage (J-V) characteristics of $Zn_{0.24}(CuIn)_{0.76}Se_2$ NCs before and after ZnS treatment.

These recombination process taking place at different interfaces can be reduced and the charge carrier collection efficiency can be increased by ZnS SILAR treatment. ZnS treatment helps in reducing the recombination at interfaces of NC and TiO_2 by creating high energy barrier as shown by schematic in Figure 5.10b. Moreover, ZnS treatment reduces the surface contribution of both TiO_2 and NC. Thus, ZnS treatment helps in reducing recombinations and increasing the charge carrier separation efficiency. We have coated 8 ZnS cycles on photoanode following prior report and tested these ZnS treated photoanode in solar cell device.[32] Figure 5.11 comparess the J-V plots for $Zn_{0.24}(CuIn)_{0.76}Se_2$ NCs before and after ZnS treatment. Indeed, the plots show a significant increase in J_{sc} and V_{oc} after ZnS treatment. Table 5.2 compares the solar cell parameters such as J_{sc}, V_{oc} and FF before and after ZnS treatment. The increase in the three solar cell parameters lead to increase in the overall PCE of $Zn_{0.24}(CuIn)_{0.76}Se_2$ NCs to 3.6%. Figure 5.12 shows statistics of J_{sc}, $V_{oc,}$ FF, and η obtained from 15 solar cells treated by ZnS. However, the obtained PCE from $CuInSe_2$ based NCs is still lower than recent report by Zhong et al,[28] where they have achieved PCE of 11.6% using $CuInSe_2$ based NCs where Ti mesh supported mesoporous carbon was used as counter electrode. This Ti/C counter electrode is a robust carbon film and provides better electrical conductivity than our Cu_2S counter electrode.[28] However such Ti/C electrode is highly expensive. Further work of improving PCE using cost-effective counter electrodes is in progress.

Table 5.2: Solar cell parameters obtained for champion cells from J-V plot shown in Figure 5.11.

$Zn_{0.24}(CuIn)_{0.76}Se_2$ NCs	J_{sc} (mA/cm^2)	V_{oc} (V)	FF	PCE (η %)
Before ZnS treatment	4.26	0.37	0.47	0.8
After ZnS treatment	12.84	0.52	0.543	3.6

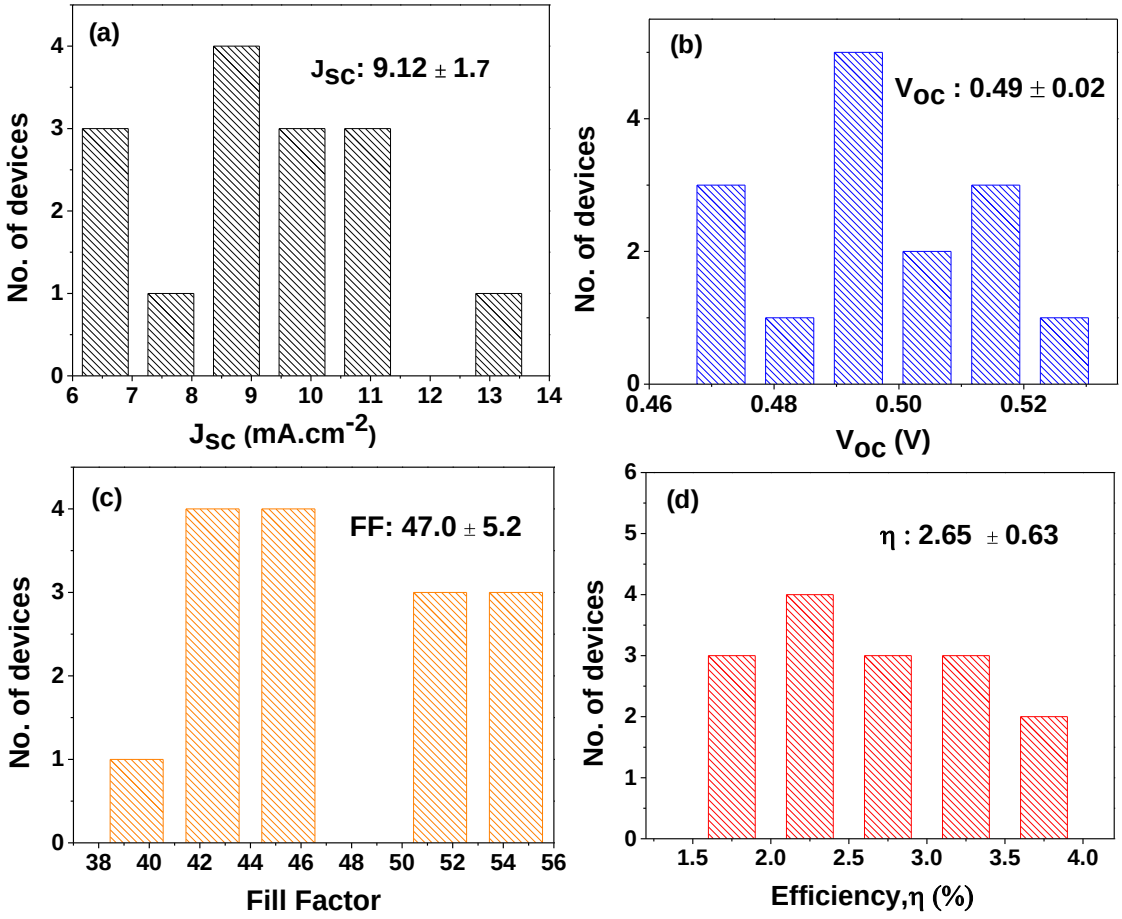

Figure 5.12: Statistics of solar cell parameters: (a) short circuit current density (J_{sc}), (b) open circuit voltage (V_{oc}), (c) fill factor (FF), and (d) power conversion efficiency, of $Zn_{0.24}(CuIn)_{0.76}Se_2$ NC sensitized solar cells after ZnS treatment. Histograms were made based on performance of 15 cells.

In this chapter using $CuInSe_2$ based NCs of QDSSC we have obtained PCE up to 3.6%. We have overcome a few problems which have been raised in earlier chapters for $AgInS_2$ QDSSC. Light absorption was limited to visible range for $AgInS_2$ NCs. The optical band gap of $AgInS_2$ is too high to absorb NIR part of solar spectrum, as discussed in chapter 3. In order to absorb NIR light along with visible-light we synthesized Ag_2S-$AgInS_2$ hetero dimer NCs in chapter 4, where Ag_2S is responsible for absorption of NIR light. Interestingly, defects in Ag_2S-$AgInS_2$ hetero dimer NCs lead to type-II band alignment with PCE of 1.3%. However,

CBM of Ag_2S part is lying below the CBM of TiO_2. Therefore, contribution to photocurrent from Ag_2S is not significant. $CuInSe_2$ based NCs with optical band gap 1.3 eV overcome both issues of poor NIR absorption, and charge transfer across NC – TiO_2 interface. Prior reports suggested that CBM of $CuInSe_2$ NCs is higher in energy than CBM of TiO_2. Incorporation of Zn in $CuInSe_2$ lattice shift the CBM to even further higher energy, which helps in efficient injection of electrons.

5.4 Conclusions

We have prepared colloidal oleylamine capped $(Zn)_x(CuIn)_{1-x}Se_2$ (x = 0, 0.24, 0.42) NCs and studied their optical properties. The obtained size of NCs is ~ 6 nm with chalcopyrite crystal structure for all compositions. $(Zn)_{0.24}(CuIn)_{0.76}Se_2$ NCs shows a optical band gap of 1.5 eV, which is suitable for solar cell applications. Also, shows the highest PL efficiency among all the three compositions. Therefore, we use $(Zn)_{0.24}(CuIn)_{0.76}Se_2$ NCs for QDSSC. In order to extract the charge carrier from NCs and increase in the NC loading onto mesoporous TiO_2 electrode, post-synthesis surface modification of NCs was carried out using MPA. Oleylamine ligands were replaced from the surface of NCs by MPA ligands maintained at pH ~ 12. Absorption spectrum of MPA capped NCs is similar to that of oleylamine capped NCs but a small decrease in PL intensity is observed after MPA capping. MPA capping also result into good NC loading into mesopores of TiO_2 electrode. As prepared photoanode was tested in a sandwich fashion using Cu_2S counter electrode and polysulphide electrolyte. The obtained PCE from these QDSSC is 0.8%. This low value of PCE is attributed to efficient recombinations of electrons and holes at the different interfaces. In order to suppress such unwanted recombinations, we have coated ZnS on photoelectrodes. ZnS treated solar cell shows improvement in the PCE of 3.63% under AM 1.5 G one sun illumination.

References

1. Carey, G. H.; Abdelhady, A. L.; Ning, Z.; Thon, S. M.; Bakr, O. M.; Sargent, E. H. Colloidal Quantum Dot Solar Cells. *Chem. Rev.* **2015**, *115*, 12732-12763.

2. Tyrrell, E. J.; Smith, J. M. Effective Mass Modeling of Excitons in Type-II Quantum Dot Heterostructures. *Phys. Rev. B* **2011**, *84*, 165328.

3. Talapin, D. V.; Koeppe, R.; Götzinger, S.; Kornowski, A.; Lupton, J. M.; Rogach, A. L.; Benson, O.; Feldmann, J.; Weller, H. Highly Emissive Colloidal CdSe/CdS Heterostructures of Mixed Dimensionality. *Nano Lett.* **2003**, *3*, 1677-1681.

4. Kim, S.; Fisher, B.; Eisler, H.-J.; Bawendi, M. Type-II Quantum Dots: CdTe/CdSe(Core/Shell) and CdSe/ZnTe(Core/Shell) Heterostructures. *J. Am. Chem. Soc.* **2003**, *125*, 11466-11467.

5. Stolle, C. J.; Harvey, T. B.; Pernik, D. R.; Hibbert, J. I.; Du, J.; Rhee, D. J.; Akhavan, V. A.; Schaller, R. D.; Korgel, B. A. Multiexciton Solar Cells of $CuInSe_2$ Nanocrystals. *J. Phys. Chem. Lett.* **2014**, *5*, 304-309.

6. Beard, M. C. Multiple Exciton Generation in Semiconductor Quantum Dots. *J. Phys. Chem. Lett.* **2011**, *2*, 1282-1288.

7. Hanna, M. C.; Nozik, A. J. Solar Conversion Efficiency of Photovoltaic and Photoelectrolysis Cells with Carrier Multiplication Absorbers. *J. Appl. Phys.* **2006**, *100*, 074510.

8. Baker, D. R.; Kamat, P. V. Photosensitization of TiO_2 Nanostructures with CdS Quantum Dots: Particulate versus Tubular Support Architectures. *Adv. Funct. Mater.* **2009**, *19*, 805-811.

9. Gonzalez-Pedro, V.; Sima, C.; Marzari, G.; Boix, P. P.; Gimenez, S.; Shen, Q.; Dittrich, T.; Mora-Sero, I. High Performance PbS Quantum Dot Sensitized Solar Cells exceeding 4% Efficiency: the Role of Metal Precursors in the Electron Injection and Charge Separation. *Phys. Chem. Chem. Phys.* **2013**, *15*, 13835-13843.

10. Zhang, H.; Cheng, K.; Hou, Y. M.; Fang, Z.; Pan, Z. X.; Wu, W. J.; Hua, J. L.; Zhong, X. H. Efficient CdSe Quantum Dot-Sensitized Solar Cells Prepared by a Postsynthesis Assembly Approach. *Chem. Commun.* **2012**, *48*, 11235-11237.

11. Zhao, K.; Pan, Z.; Mora-Seró, I.; Cánovas, E.; Wang, H.; Song, Y.; Gong, X.; Wang, J.; Bonn, M.; Bisquert, J.; Zhong, X. Boosting Power Conversion Efficiencies of Quantum-Dot-Sensitized Solar Cells Beyond 8% by Recombination Control. *J. Am. Chem. Soc.* **2015**, *137*, 5602-5609.

12. Ren, Z.; Wang, J.; Pan, Z.; Zhao, K.; Zhang, H.; Li, Y.; Zhao, Y.; Mora-Sero, I.; Bisquert, J.; Zhong, X. Amorphous TiO_2 Buffer Layer Boosts Efficiency of Quantum Dot Sensitized Solar Cells to over 9%. *Chem. Mater.* **2015**, *27*, 8398-8405.

13. Du, Z.; Pan, Z.; Fabregat-Santiago, F.; Zhao, K.; Long, D.; Zhang, H.; Zhao, Y.; Zhong, X.; Yu, J.-S.; Bisquert, J. Carbon Counter-Electrode-Based Quantum-Dot-Sensitized Solar Cells with Certified Efficiency Exceeding 11%. *J. Phys. Chem. Lett.* **2016**, *7*, 3103-3111.

14. McDaniel, H.; Fuke, N.; Makarov, N. S.; Pietryga, J. M.; Klimov, V. I. An Integrated Approach to Realizing High-Performance Liquid-Junction Quantum Dot Sensitized Solar Cells. *Nat. Commun.* **2013**, *4*, 2887.

15. Santra, P. K.; Kamat, P. V. Mn-Doped Quantum Dot Sensitized Solar Cells: A Strategy to Boost Efficiency over 5%. *J. Am. Chem. Soc.* **2012**, *134*, 2508-2511.

16. Tian, J.; Lv, L.; Fei, C.; Wang, Y.; Liu, X.; Cao, G. A Highly Efficient (>6%) $Cd_{1-x}Mn_xSe$ Quantum Qot Sensitized Solar Cell. *J. Mater. Chem. A* **2014**, *2*, 19653-19659.

17. Wang, J.; Li, Y.; Shen, Q.; Izuishi, T.; Pan, Z.; Zhao, K.; Zhong, X. Mn Doped Quantum Dot Sensitized Solar Cells with Power Conversion Efficiency Exceeding 9%. *J. Mater. Chem. A* **2016**, *4*, 877-886.

18. Stolle, C. J.; Panthani, M. G.; Harvey, T. B.; Akhavan, V. A.; Korgel, B. A. Comparison of the Photovoltaic Response of Oleylamine and Inorganic Ligand-Capped $CuInSe_2$ Nanocrystals. *ACS Appl. Mater. Interfaces* **2012**, *4*, 2757-2761.

19. Ren, Z.; Yu, J.; Pan, Z.; Wang, J.; Zhong, X. Inorganic Ligand Thiosulfate-Capped Quantum Dots for Efficient Quantum Dot Sensitized Solar Cells. *ACS Appl. Mater. Interfaces* **2017**, *9*, 18936-18944.

20. Guijarro, N.; Lana-Villarreal, T.; Mora-Seró, I.; Bisquert, J.; Gómez, R. CdSe Quantum Dot-Sensitized TiO_2 Electrodes: Effect of Quantum Dot Coverage and Mode of Attachment. *J. Phys. Chem. C* **2009**, *113*, 4208-4214.

21. Hines, D. A.; Forrest, R. P.; Corcelli, S. A.; Kamat, P. V. Predicting the Rate Constant of Electron Tunneling Reactions at the CdSe–TiO_2 Interface. *J. Phys. Chem. B* **2015**, *119*, 7439-7446.

22. Yuan, H.; Lu, J.; Xu, X.; Huang, D.; Chen, W.; Shen, Y.; Wang, M. Electrochemically Deposited CoS Films as Counter Electrodes for Efficient Quantum Dot-Sensitized Solar Cells. *J. Electrochem. Soc.* **2013**, *160*, H624-H629.

23. Yang, Z.; Chen, C.-Y.; Liu, C.-W.; Li, C.-L.; Chang, H.-T. Quantum Dot–Sensitized Solar Cells Featuring CuS/CoS Electrodes Provide 4.1% Efficiency. *Adv. Energy Mater.* **2011**, *1*, 259-264.

24. Youn, D. H.; Seol, M.; Kim, J. Y.; Jang, J.-W.; Choi, Y.; Yong, K.; Lee, J. S. TiN Nanoparticles on CNT–Graphene Hybrid Support as Noble-Metal-Free Counter Electrode for Quantum-Dot-Sensitized Solar Cells. *ChemSusChem* **2013**, *6*, 261-267.

25. AbdulAlmohsin, S.; Armstrong, J.; Cui, J. B. CdS Nanocrystal-Sensitized Solar Cells with Polyaniline as Counter Electrode. *J. Renew. Sustain. Energy* **2012**, *4*, 043108.

26. Zhong, H.; Bai, Z.; Zou, B. Tuning the Luminescence Properties of Colloidal I–III–VI Semiconductor Nanocrystals for Optoelectronics and Biotechnology Applications. *J. Phys. Chem. Lett.* **2012**, *3*, 3167-3175.

27. Allen, P. M.; Bawendi, M. G. Ternary I−III−VI Quantum Dots Luminescent in the Red to Near-Infrared. *J. Am. Chem. Soc.* **2008**, *130*, 9240-9241.

28. Du, J.; Du, Z.; Hu, J.-S.; Pan, Z.; Shen, Q.; Sun, J.; Long, D.; Dong, H.; Sun, L.; Zhong, X.; Wan, L.-J. Zn–Cu–In–Se Quantum Dot Solar Cells with a Certified Power Conversion Efficiency of 11.6%. *J. Am. Chem. Soc.* **2016**, *138*, 4201-4209.

29. Oikkonen, L. E.; Ganchenkova, M. G.; Seitsonen, A. P.; Nieminen, R. M. Vacancies in $CuInSe_2$: New Insights from Hybrid-Functional Calculations. *J. Phys. Condens. Matter* **2011**, *23*, 422202.

30. Hwang, I.; Yong, K. Counter Electrodes for Quantum-Dot-Sensitized Solar Cells. *ChemElectroChem* **2015**, *2*, 634-653.

31. Choi, H.; Nicolaescu, R.; Paek, S.; Ko, J.; Kamat, P. V. Supersensitization of CdS Quantum Dots with a Near-Infrared Organic Dye: Toward the Design of Panchromatic Hybrid-Sensitized Solar Cells. *ACS Nano* **2011**, *5*, 9238-9245.

32. Kim, J.-Y.; Yang, J.; Yu, J. H.; Baek, W.; Lee, C.-H.; Son, H. J.; Hyeon, T.; Ko, M. J. Highly Efficient Copper–Indium–Selenide Quantum Dot Solar Cells: Suppression of Carrier Recombination by Controlled ZnS Overlayers. *ACS Nano* **2015**, *9*, 11286-11295.

33. Wu, J. J.; Chang, R. C.; Chen, D. W.; Wu, C. T. Visible to Near-Infrared Light Harvesting in Ag_2S Nanoparticles/ZnO Nanowire Array Photoanodes. *Nanoscale* **2012**, *4*, 1368-1372.

34. Mao, B. D.; Chuang, C. H.; Wang, J. W.; Burda, C. Synthesis and Photophysical Properties of Ternary I-III-VI $AgInS_2$ Nanocrystals: Intrinsic versus Surface States. *J. Phys. Chem. C* **2011**, *115*, 8945-8954.

35. Peng, S. J.; Zhang, S. Y.; Mhaisalkar, S. G.; Ramakrishna, S. Synthesis of $AgInS_2$ Nanocrystal Ink and Its Photoelectrical Application. *Phys. Chem. Chem. Phys.* **2012**, *14*, 8523-8529.

36. Guchhait, A.; Pal, A. J. Copper-Diffused $AgInS_2$ Ternary Nanocrystals in Hybrid Bulk-Heterojunction Solar Cells: Near-Infrared Active Nanophotovoltaics. *ACS Appl. Mater. Interfaces* **2013**, *5,* 4181-4189.

37. Nose, K.; Omata, T.; Otsuka-Yao-Matsuo, S. Colloidal Synthesis of Ternary Copper Indium Diselenide Quantum Dots and Their Optical Properties. *J. Phys. Chem. C* **2009**, *113,* 3455-3460.

38. Tan, Z.; Zhang, Y.; Xie, C.; Su, H.; Liu, J.; Zhang, C.; Dellas, N.; Mohney, S. E.; Wang, Y.; Wang, J.; Xu, J. Near-Band-Edge Electroluminescence from Heavy-Metal-Free Colloidal Quantum Dots. *Adv. Mater.* **2011**, *23,* 3553-3558.

39. Li, W.; Zhong, X. Capping Ligand-Induced Self-Assembly for Quantum Dot Sensitized Solar Cells. *J. Phys. Chem. Lett.* **2015**, *6,* 796-806.

40. Cheng, K.-C.; Law, W.-C.; Yong, K.-T.; Nevins, J. S.; Watson, D. F.; Ho, H.-P.; Prasad, P. N. Synthesis of Near-Infrared Silver-Indium-Sulfide ($AgInS_2$) Quantum Dots as Heavy-Metal Free Photosensitizer for Solar Cell Applications. *Chem. Phys. Lett.* **2011**, *515,* 254-257.

41. Robel, I.; Subramanian, V.; Kuno, M.; Kamat, P. V. Quantum Dot Solar Cells. Harvesting Light Energy with CdSe Nanocrystals Molecularly Linked to Mesoscopic TiO_2 Films. *J. Am. Chem. Soc.* **2006**, *128,* 2385-2393.

42. Kokal, R. K.; Deepa, M.; Kalluri, A.; Singh, S.; Macwan, I.; Patra, P. K.; Gilarde, J. Solar Cells with PbS Quantum Dot Sensitized TiO_2-Multiwalled Carbon Nanotube Composites, Sulfide-Titania Gel and Tin Sulfide Coated C-Fabric. *Phys. Chem. Chem. Phys.* **2017**, *19,* 26330-26345.

Appendix

Visible Light-Induced Hydrogen Generation Using Colloidal $(ZnS)_{0.4}(AgInS_2)_{0.6}$ Nanocrystals Capped by S^{2-} Ions

---

The following paper has been published based on the work presented in this appendix.

Jagadeeswararao, M.; Dey, S.; Nag, A.; Rao, C. N. R. Visible Light-Induced Hydrogen Generation Using Colloidal $(ZnS)_{0.4}(AgInS_2)_{0.6}$ Nanocrystals Capped by S^{2-} ions. *J. Mater. Chem. A* **2015,** *3*, 8276-8279. Reproduced with permission from the Royal Society of Chemistry

Declaration: Photocatalytic H_2 evolution study (Figure A.3, A.4 and A.5) was carried out by Dr. Sunita Dey in the laboratory of Prof. C. N. R. Rao, at JNCASR Bangalore.

Summary

In chapter 2, we discussed about synthesis and optical properties of oleylamine capped $(ZnS)_{1-x}(AgInS_2)_x$ nanocrystals (NCs). Among various compositions, $(ZnS)_{0.4}(AgInS_2)_{0.6}$ NCs exhibit the appropriate band gap and band alignment for visible-light driven photocatalytic H_2 evolution. Here we replaced the oleylamine ligand with S^{2-} ions. S^{2-} ions helps the NCs to be dispersed in aqueous medium and better charge extraction and injection required for reduction of H^+ to H_2. A high activity of 5.0 mmol $g^{-1}h^{-1}$ is achieved using non-toxic $(ZnS)_{0.4}(AgInS_2)_{0.6}$ NCs as photocatalysts without the need of a noble metal co-catalyst.

Graphical abstract

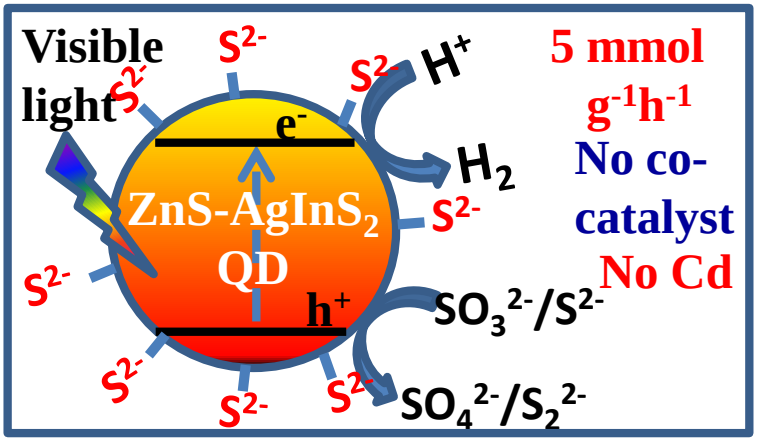

A.1 Introduction

Production of H_2 is important since it provides clean and renewable energy, particularly for use in fuel cells. The best possible scenario will be to produce H_2 using sunlight and water, both of which are available in plenty. [1-6] In this regard, semiconductors that absorb sunlight producing electrons in the conduction-band (CB) and holes in the valence-band (VB), have emerged as photocatalysts for the reduction of H^+ to H_2 via donation of the CB electrons. The thermodynamic requirement of such photocatalyst is that the CB minimum is more negative than the reduction potential of H^+/H_2 (0 V vs NHE). Good performance of a catalyst also depends upon other factors such as efficient exciton dissociation, migration of electrons to the surface of NCs and active surface sites where the H^+ ions can be reduced. Oxides such as TiO_2 can be used as catalysts, but they do not absorb visible sunlight. Similar high band gap (>3 eV) catalysts absorb UV-light, and are not suitable for sunlight driven photocatalysis since sunlight mainly consists of visible and infrared light along with only 5% of UV-light. Doping foreign elements in to an active high band gap catalyst provides levels at the mid-gap region, thereby absorbing visible light. However, such mid-gap states can also trap the photogenerated electrons.[7-9] Another strategy is to make a solid solution, for example, $(ZnS)_x(AgInS_2)_{1-x}$ where the band gap can be tuned between the high bandgap of ZnS (3.68 eV) and the low bandgap of $AgInS_2$ (1.87 eV) by controlling the composition.[10]

We have employed S^{2-} capped $(ZnS)_x(AgInS_2)_{1-x}$ nanocrystals (NCs) visible-light catalysis. The S^{2-}-capped NCs optimizes, (i) size and composition dependent bandgap, (ii) high surface area, (iii) $S^{2-\ (\delta-)}$ rich surface that can facilitate H^+ adsorption, and (iv) water solubility resulting into a non-toxic, efficient visible-light for H_2 evolution catalyst in the absence of a co-catalyst.

A.2 Experimental section

A.2.1 Synthesis of oleylamine capped $(ZnS)_{0.4}(AgInS_2)_{0.6}$ nanocrystals (NCs)

$(ZnS)_{0.4}(AgInS2)_{0.6}$ NCs were synthesized by following ref[11] using single molecular precursor $(AgIn)_xZn_{2(1-x)}(S_2CN(C2H5)_2)_4$, where x = 0.75. The molecular precursor was prepared by mixing 50 mL aqueous solution of 0.025 mol/L metal ions ($AgNO_3$: $InNO_3$: $Zn(NO_3)_2$ = x : x : 2(1-x)) with 50 mL aqueous solution of sodium diethyl dithiocarbamate trihydrate (0.05 mol/L). The resultant precipitate was washed several times with methanol

and water mixture and dried under vacuum at room temperature. 50 mg of precursor powder was taken in a three neck round bottom flask and was heated at 180 ^oC under Ar atmosphere for 30 minutes followed by injection of 3.0 mL of oleylamine and the reaction was continued for another 3 minutes. The obtained suspension was centrifuged at 2000 rpm for 2 minutes and the supernatant was collected by removing the larger particles. Sufficient amount of methanol was added to the supernatant containing NCs followed by centrifugation at the speed of 5000 rpm for 5 min. The obtained NC precipitate was redispersed in non-polar solvents like toluene and chloroform for further processing.

A.2.2 Ligand exchange of oleylamine capped $(ZnS)_{0.4}(AgInS_2)_{0.6}$ NCs using $(NH_4)_2S$

Ligand exchange reaction was carried out under ambient conditions. Oleylamine capped $(ZnS)_{0.4}(AgInS2)_{0.6}$ NCs were dispersed in 3 mL toluene in a glass vial. 3 mL formamide (FA) and 130-150 µL aqueous $(NH_4)_2S$ were added to the NC dispersion and magnetically stirred for 5 min. NCs were transferred into FA phase leaving a colorless toluene phase. The toluene phase was removed, followed by addition of pure toluene and stirring. The pure toluene removes any remaining organic molecules in FA phase, and this washing was repeated thrice. The resultant NCs in FA phase were precipitated by centrifugation after adding acetonitrile as a non-solvent. The obtained precipitate could be redispersed in FA or water for studying different properties.

A.2.3 Characterization

UV-visible absorption and photoluminescence (PL) spectra of $(ZnS)_{0.4}(AgInS_2)_{0.6}$ NCs were recorded using a Perkin Elmer, Lambda-45 UV/Vis spectrometer and FluoroMax-4 spectrofluoremeter (HORIBA scientific), respectively. PL decay dynamics were measured using time correlated single photon counting (TCSPC) technique set-up from Horiba JobinYvon at an excitation energy of 459 nm (2.70 eV). Fourier-transform infrared (FTIR) spectra were acquired in the transmission mode using a NICOLET 6700 FTIR spectrometer (Thermo scientific). Powder X-ray diffraction (XRD) data were collected by using Bruker D8 Advance Powder XRD diffractometer using Cu Kα radiation (λ = 1.54Å). Transmission electron microscopy (TEM) images were obtained by using a JEOL JEM 2100F microscope operated at 200 kV.

A.3 Results and discussion

A.3.1 Synthesis of oleylamine capped $(ZnS)_{0.4}(AgInS_2)_{0.6}$ solid solution NCs

Colloidal oleylamine capped $(ZnS)_{0.4}(AgInS_2)_{0.6}$ solid solution NCs were prepared following ref.[11] This specific composition was selected in order to have appropriate optical band gap that absorbs both visible light and exhibit suitable band alignment for photocatalytic H_2 evolution from aqueous solution. XRD patterns in Figure A.1a show the lattice parameters of the NCs to be in between those of ZnS and $AgInS_2$ suggesting the formation of solid solution NCs, similar to prior reports.[11-12] TEM image in Figure A.1b shows the average particle size to be 4.5 nm.

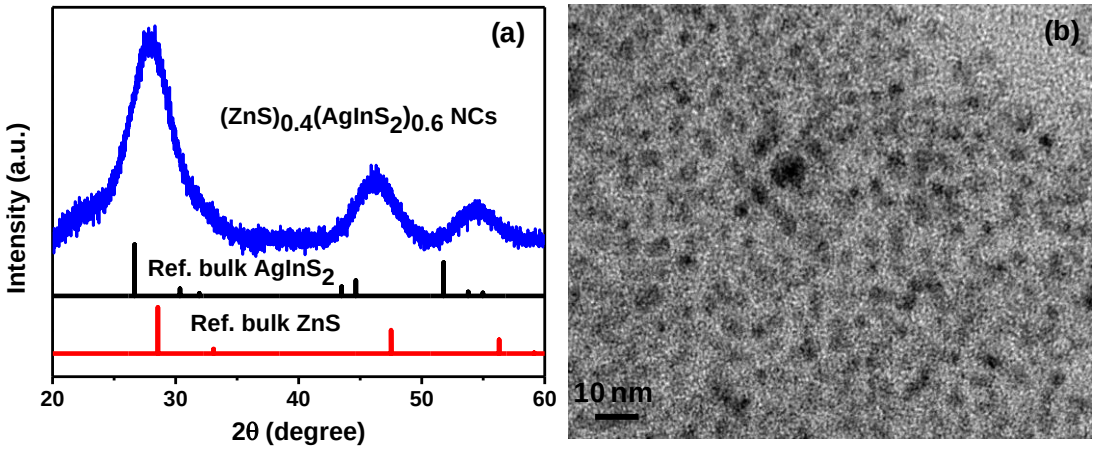

Figure A.1: (a) Powder XRD pattern of $(ZnS)_{0.4}(AgInS_2)_{0.6}$ NCs along with standard patterns for bulk $AgInS_2$ and ZnS. (b) TEM image of colloidal $(ZnS)_{0.4}(AgInS_2)_{0.6}$ NCs.

A.3.2 Surface modification of oleylamine capped $(ZnS)_{0.4}(AgInS_2)_{0.6}$ NCs

These oleylamine capped NCs are not miscible with aqueous solution, and more importantly, the long hydrocarbon chain in oleylamine is insulating in nature. Therefore, extraction (injection) of charge carriers from (into) the NC surface is inhibited. Photocatalytic H_2 evolution require injection/extraction of charge carriers to/from NCs, and therefore, we replaced the insulating oleylamine from NC surface with electronically transparent S^{2-} ions.[13] A.3.The ligand exchange reaction is simple and is carried out under ambient conditions. Figure A.2a shows oleylamine capped NCs dispersed in non-polar toluene phase showing the color of NCs, and the formamide (FA) phase is colorless suggesting the NCs are immiscible

to the polar FA solvent. However, the NCs transfer to the FA phase within 5 minutes after addition of $(NH_4)_2S$ solution. The NCs in the FA phase were washed, precipitated and used for different measurements.

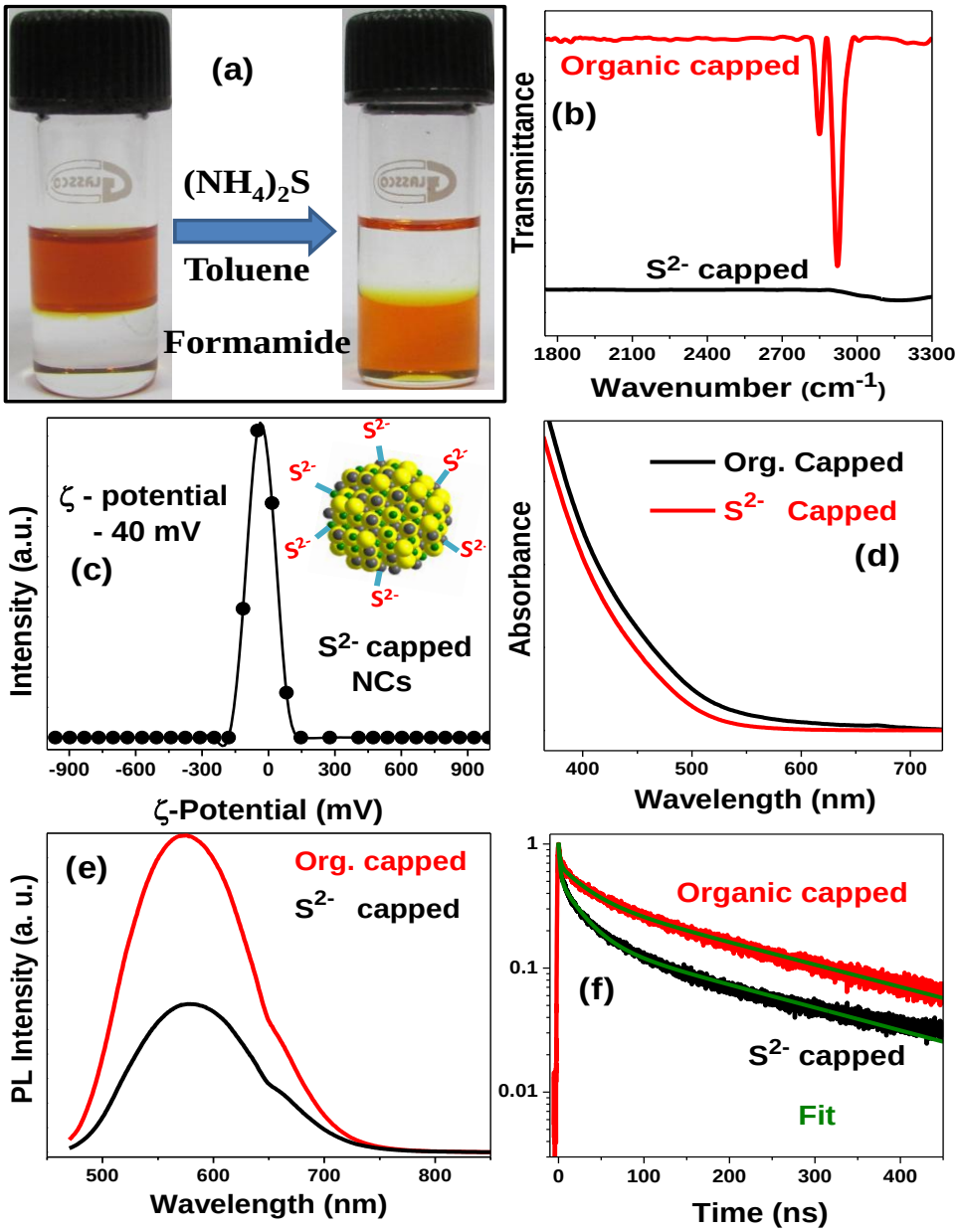

Figure A.2: (a) Yellow-orange colloidal $(ZnS)_{0.4}(AgInS_2)_{0.6}$ NCs undergo the phase transfer from toluene to formamide (FA) after replacing the original oleylamine ligands on the NC surface with S^{2-} ligands. (b) Comparison of the Fourier-transform infrared (FTIR) spectra of oleylamine and S^{2-} capped $(ZnS)_{0.4}(AgInS_2)_{0.6}$ NCs. (c) ζ-potential of S^{2-} capped $(ZnS)_{0.4}(AgInS_2)_{0.6}$ NCs dispersed in FA. Inset shows schematic of S^{2-} capped NCs. Comparison of (d) UV-visible absorption, (e) photoluminescence (PL) and (f) PL decay dynamics of oleylamine and S^{2-} capped $(ZnS)_{0.4}(AgInS_2)_{0.6}$ NCs.

FTIR spectra in Figure A.2b show strong doublet features at 2852 and 2925 cm^{-1} for oleylamine capped NCs corresponding to C-H stretching. However, the C-H stretching features vanish after the ligand-exchange reaction, suggesting a near complete removal of the native oleylamine ligand from the NC surface. This ligand exchange reaction using $(NH_4)_2S$ is expected to replace oleylamine with S^{2-} (or $S^{\delta-}$) on the NC surface, as shown by the schematic model in the inset of Figure A.2c. Indeed, ζ-potential data in Figure A.2c show that the NCs possess a negative charge on the surface, agreeing with the schematic in the inset. The negative charge on NC surface provide colloidal stability of S^{2-} capped NCs in a polar solvent like FA and water via electrostatic repulsion among NCs.

UV-vis absorption spectra (Figure A.2d) of $(ZnS)_{0.4}(AgInS_2)_{0.6}$ NCs before and after the ligand exchange reaction are similar suggesting that the size and composition of the NCs are intact during the ligand exchange reaction. The S^{2-} capped NCs exhibit an optical gap of 520 nm (2.39 eV) (Figure A.2d), therefore exhibiting a significant absorption of visible light. PL spectra in Figure A.2e show a decrease in PL intensity for the S^{2-} capped NCs without altering the emission energy. PL decay curves in Figure A.2f show increased contribution from faster decay for S^{2-} capped NCs compared to oleylamine capped NCs. PL decay plots were fitted using tri-exponential decay model and best-fit parameters are given in Table A.1. Fitting results are similar to ref 12 (chapter 2) with two radiative lifetimes (~30 ns and 240 ns) and along with faster (~1 ns) non-radiative lifetime. The origin of different PL lifetimes resulting in to broad and intense PL from $(ZnS)_x(AgInS_2)_{1-x}$ NCs has been discussed earlier in ref[12]. Though the faster decay and lower intensity suggest the formation of new non-radiative decay channels after the ligand exchange (surface modification) reaction, still the retention of intense PL for S^{2-} capped NCs suggest less abundance of trap states that can be detrimental for photocatalytic reactions.

Table A.1: Best-Fit parameters of PL decay profiles of $(ZnS)_{0.4}(AgInS_2)_{0.6}$ NCs capped with different ligands for the corresponding data shown in Figure A.2f of the main manuscript. A tri-exponential decay, $I(t) = a_1 \exp(-t/\tau_1) + a_2 \exp(-t/\tau_2) + a_3 \exp(-t/\tau_3)$ was used where τ_i correspond to i^{th} lifetime component, and a_i is contribution of i^{th} lifetime.

Capping ligand	τ_1 (ns)	a_1 (%)	τ_2 (ns)	a_2 (%)	τ_3 (ns)	a_3 (%)
Organic Capped	1.7	32	32	32	242	37
S^{2-} Capped	1.8	49	27	34	236	17

A.3.3 Photocatalytic H_2 evolution from S^{2-} capped $(ZnS)_{0.4}(AgInS_2)_{0.6}$ NCs

We have investigated photocatalytic H_2 evolution of S^{2-} capped $(ZnS)_{0.4}(AgInS_2)_{0.6}$ NCs under visible light irradiation. Photocatalytic H_2 evolution experiments were conducted in a stoppered quartz vessel. Schematic of the experimental setup is shown in Figure A.3. The catalyst (10 mg) was dispersed in 50 ml aqueous solution along with 0.25 (M) Na_2SO_3 and 0.35 (M) Na_2S. Samples were irradiated under 400 W Xe lamp (Newport 6280) equipped with water filter for IR removal and a 400 nm cut-off filter blocking UV lights. H_2 evolved was quantified using gas chromatography (Perkin Elmer, Clarus 580 GC) equipped with GC-TCD detector by manually injecting 1 ml of evolved gases from headspace of the quartz vessel over a constant period of time. Turn over frequency (TOF), turn over number (TON) and apparent quantum yield (AQY) were calculated by the equations given A.1-A.3.

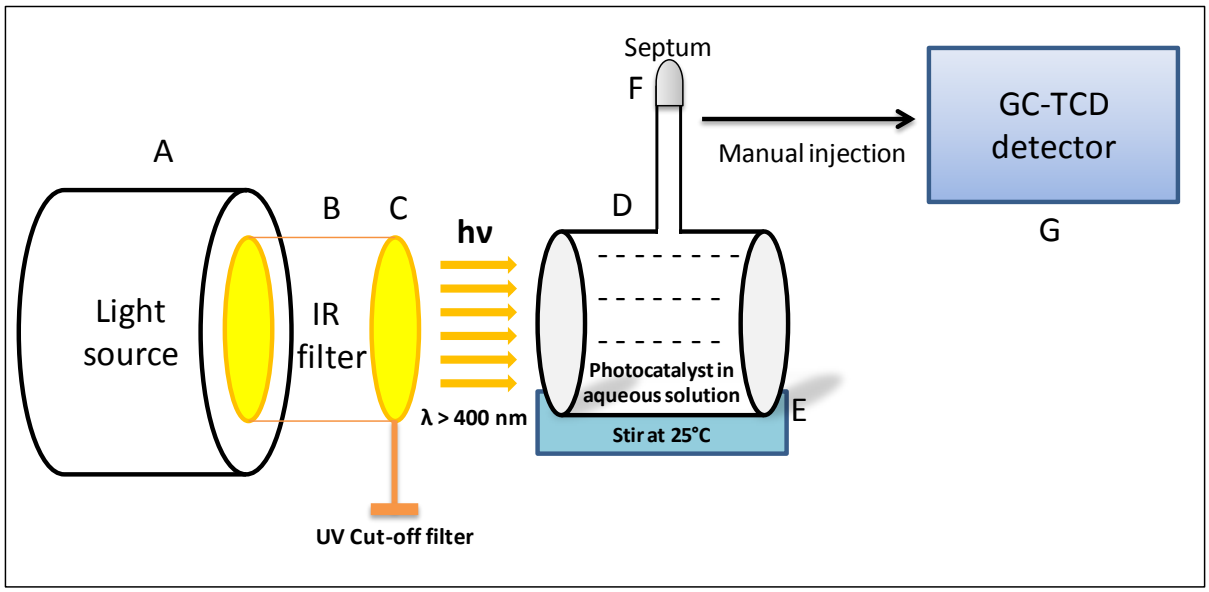

Figure A.3: Schematic representation of experimental setup for photocatalytic H_2 evolution from water. A: Xe lamp (working at 400 W); B: IR cut-off filter; C: UV cut-off filter (Newport) to allow $\lambda >$ 400 nm; D: reaction vessel containing aqueous solution of photocatalyst; E: stirring at room temperature; F: Septum to keep the reaction vessel air-tight; G: GC equipped with TCD. Distance between C and the exposed face of reaction vessel is maintained at 15 cm.

$$\text{TOF } (h^{-1}) = \frac{\text{moles of } H_2 \text{ evolved per hour}}{\text{moles of active catalysed used}} \qquad \text{(A.1)}$$

$$\text{TON } (h^{-1}) = \frac{\text{moles of hydrogen evolved (fixed time)}}{\text{moles of active catalysed used}} \qquad \text{(A.2)}$$

Apparent quantum yield (AQY) is defined by the following equation,

$$\text{AQY } (\%) = \frac{\text{The number of evolved } H_2 \text{ molecules} \times 2}{\text{The number of incident photons}} \times 100 \qquad \text{(A.3)}$$

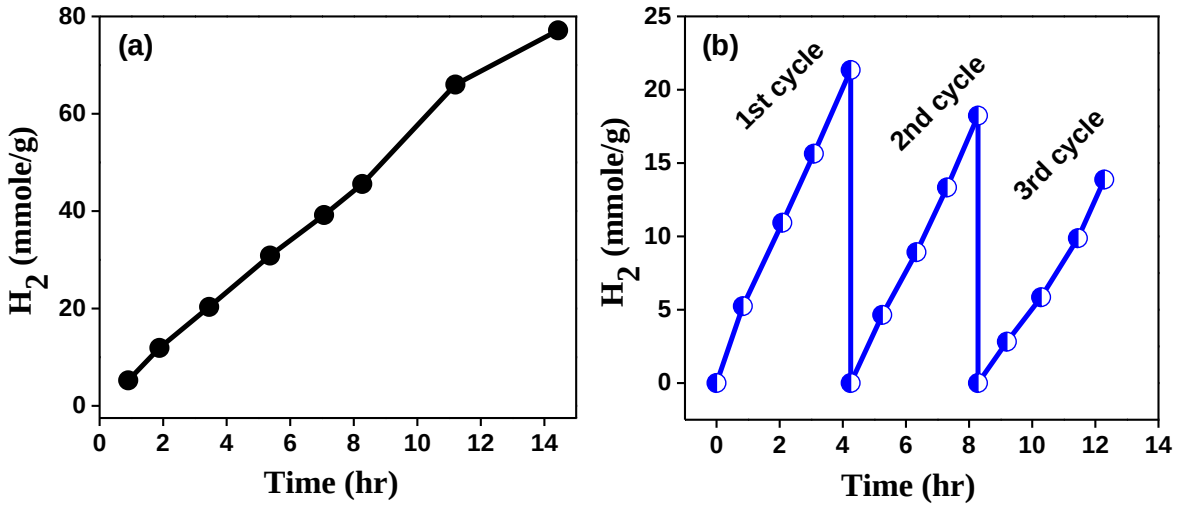

Figure A.4: (a) H_2 production as a function of time using $(ZnS)_{0.4}(AgInS_2)_{0.6}$ NC photocatalyst under the irradiation of visible light ($\lambda > 400$ nm). 0.35 (M) Na_2S and 0.25 (M) Na_2SO_3 were added as sacrificial electron donors. (b) Recyclability test of the same photocatalyst under identical reaction conditions. Symbols are data, and solid lines are just guides to eye.

Figure A.4a shows the H_2 evolution profile of an aqueous solution of S^{2-} capped $(ZnS)_{0.4}(AgInS_2)_{0.6}$ NCs. The activity is around 5.0 mmol/g/h. TON defines the amount of H_2 evolved in the expense of molar quantity of $(ZnS)_{0.4}(AgInS_2)_{0.6}$ used, is around 16 at the end of 14 hrs of reaction and shows a steady nature even after long reaction hours. Present study shows the photocatalytic H_2 evolution activity obtained with $(ZnS)_{0.4}(AgInS_2)_{0.6}$ NCs is better than most of such catalysts reported in the literature (Table A.2). Importantly, $(ZnS)_{0.4}(AgInS_2)_{0.6}$ NCs show superior activity even without the loading of any co-catalyst or noble metal. It is to be noted that $AgInS_2$ and ZnS NCs are not active under visible light exposure, however, the solid solution optimizes the band gap yielding an efficient visible light photocatalyst. AQY is estimated to be 9% and is quite significant considering the absence of both toxic Cd and expensive co-catalyst like Pt. Na_2SO_3 and Na_2S together act as electron donor, and playing an important role in the present photocatalytic study. Photogenerated electrons are accepted by H_2O reducing H^+ to H_2 whereas the holes oxidize SO_3^{2-} and S^{2-} as given by equations A.4-A.9.

Table A.2: Comparison of visible-light catalytic H_2 evolution data of the present study with the similar systems reported in literature.

Photcatalyst	Activity ($mmolg^{-1}h^{-1}$)	TOF (h^{-1})	Reaction Condition and Reference
$(ZnS)_{0.4}(AgInS_2)_{0.6}$ NCs	5.0	1.05	10 mg,[a] 400W,[b] $\lambda \geq 400$ nm, [c] $Na_2S + Na_2SO_3$,[d] Present work
$(AgIn)_{0.22}Zn_{1.56}S_2$	1.1	0.24	0.3 g,[a] 300W,[b] $\lambda \geq 420$ nm,[c] $Na_2S + K_2SO_3$,[d] ref[10]
$(AgIn)_{0.22}Zn_{1.56}S_2$ + 3 wt% Pt	3.2	0.69	0.3 g,[a] 300W,[b] $\lambda \geq 420$ nm,[c] $Na_2S + K_2SO_3$,[d] ref[10]
$(CuAg)_{0.15}In_{0.3}Zn_{1.4}S_2$ + 1.0 wt% Pt	1.1	0.24	0.3 g,[a] 300W,[b] $\lambda \geq 420$ nm,[c] $Na_2S + K_2SO_3$,[d] ref[14]
$(CuIn)_{0.09}Zn_{1.82}S_2$ + 0.5 wt% Pt	2.3	0.46	0.3 g,[a] 300W, [b] $\lambda \geq 420$ nm,[c]$Na_2S + K_2SO_3$,[d] ref[15]
CdS + 3 wt% Pt	1.2	0.17	0.3 g,[a] 300W,[b] $\lambda \geq 420$ nm,[c] $Na_2S + K_2SO_3$,[d] ref[10]
$Cd_{0.8}Zn_{0.2}S$	0.9	0.15	0.1 g,[a] 500W,[b] $\lambda \geq 420$ nm,[c] $Na_2S + Na_2SO_3$,[d] ref[16]
CdS NCs	trace	----	1.4 mg,[a] 300W,[b] $\lambda \geq 420$ nm,[c] $Na_2S + Na_2SO_3$,[d] ref[17]
CdS Nanosheets	41.1	5.93	1.4 mg,[a] 300W,[b] $\lambda \geq 420$ nm,[c] $Na_2S + Na_2SO_3$,[d] ref[17]
Cu_2ZnSnS_4	0.06	0.03	40 mg,[a] 300W,[b] $\lambda \geq 420$ nm,[c] $Na_2S + Na_2SO_3$,[d] ref[18]

a: weight of catalyst, b: power of light source, c: wavelength (λ) of light, d: electrolyte.

$$photocatalyst + h\nu \rightarrow e^-(CB) + h^+(VB) \quad \text{(A.4)}$$

$$2H_2O + 2e^- \rightarrow H_2 + 2OH^- \quad \text{(A.5)}$$

$$SO_3^{2-} + H_2O + 2h^+ \rightarrow SO_4^{2-} + 2H^+ \quad \text{(A.6)}$$

$$2S^{2-} + 2h^+ \rightarrow S_2^{2-} \quad \text{(A.7)}$$

$$S_2^{2-} + SO_3^{2-} \rightarrow S_2O_3^{2-} + S^{2-} \quad \text{(A.8)}$$

$$SO_3^{2-} + S^{2-} + 2h^+ \rightarrow S_2O_3^{2-} \quad \text{(A.9)}$$

We have investigated recyclability of activity and irradiation stability of the $(ZnS)_{0.4}(AgInS_2)_{0.6}$ NC photocatalyst over a fixed period of time under the identical reaction conditions, > 400 nm light irradiation using Na_2SO_3 and Na_2S hole scavenger (Figure A.3b). It illustrates the recyclability of present catalyst in H_2 evolution. A gradual decrease in H_2 production activity and TOF is observed in successive runs (Table S2 in ESI). However, decomposition of the hole scavenger and photo corrosion of the catalyst seem to be possible reasons for lowering it activity.

Table A.3: Activity of H_2 evolution and Turn over frequency (TOF) obtained during three successive cycles for $(ZnS)_{0.4}(AgInS_2)_{0.6}$ NC photocatalyst.

Cycles	Activity(mmol/g/h)	TOF (h^{-1})
1	4.99	1.05
2	4.23	0.89
3	3.14	0.66

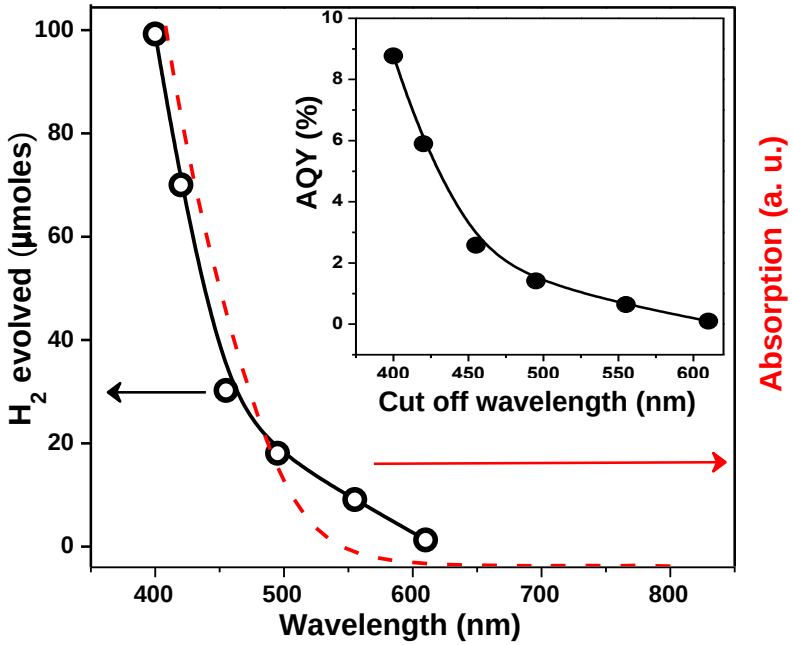

Figure A.5: Action spectrum of H_2 evolution for $(ZnS)_{0.4}(AgInS_2)_{0.6}$ NC photocatalyst. Comparison of UV-visible absorption spectrum (dashed line) with µmoles of H_2 evolved (open circles, solid line is just a guide to eye) by 10 mg photocatalyst under illumination for 2 hrs. Inset shows the variation of apparent quantum yield (AQY) with cut-off wavelength.

Figure A.5 presents the action spectrum of $(ZnS)_{0.4}(AgInS_2)_{0.6}$ NC catalyst corresponding to the H_2 evolution upon irradiating using various cut-off wavelengths by use of filters. The action spectrum shows maximum H_2 evolution due to the absorption at 400-425 nm region followed by a sharp decrease in the tail region (450-550 nm). This wavelength dependence of the action spectrum resembles that of the visible light absorption spectrum of the photocatalyst, confirming that the inter-band excitonic transition leads to the photoactivity of the $(ZnS)_{0.4}(AgInS_2)_{0.6}$ NC catalyst. The variation of AQY with the cut-off wavelength is presented in the inset of Figure 3 and supporting our conclusion. It is to be noted that the AQY of ~9% using a 400 nm cut-off filter is significantly high considering the fact that the irradiations with wavelengths longer than 550 nm do not lead to significant H_2 production. We note that XRD pattern shown in Figure A.6 and band gap of NC catalyst remained unchanged after the H_2 evolution reaction suggesting good stability of our catalyst.

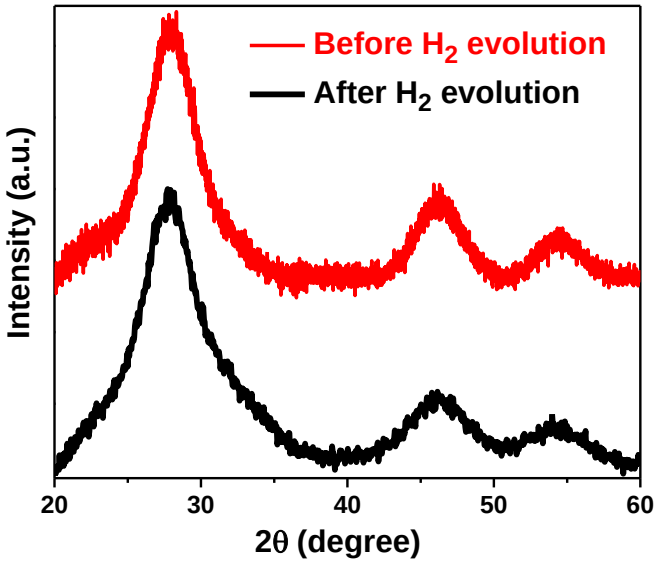

Figure A.6: Comparison of powder XRD pattern of as synthesized oleylamine capped $(ZnS)_{0.4}(AgInS_2)_{0.6}$ NCs with that of S^{2-} capped NCs after photocatalytic H_2 evolution reaction. These XRD patterns show that the structure and composition of NCs remain intact after both surface modification and catalysis reaction.

The photocatalytic activity of $(ZnS)_{0.4}(AgInS_2)_{0.6}$ NCs (5.0 mmol $g^{-1}h^{-1}$) is significantly higher compared to its bulk counterpart[10] (1.1 mmol $g^{-1}h^{-1}$). This increased activity for NCs is because of (i) increase in active sites resulting from both high specific surface area, and large fraction of under-coordinated surface atoms, (ii) easy transport of photo-generated charge carriers from NC core to the active surface because of both small distance between core and surface of a NC, and also, lattice defects that trap charge carriers can be easily removed,[19] and (iii) improved water solubility of NC catalysts compared to bulk catalysts along with

reduced scattering of visible light. Also, 4.5 nm $(ZnS)_x(AgInS_2)_{1-x}$ NCs exhibit quantum confinement of charge carriers.[12] Therefore, the absorption coefficient for NCs might be higher compared to the bulk sample. Furthermore, since electrons with lower effective mass typically feels the confinement effect more strictly compared to heavier holes, the conduction band minimum is expected to preferentially shift towards more negative potential providing the driving force for photocatalytic reduction of H^+. We note that the discussed possibility of enhancing photocatalytic activity of our NCs using quantum confinement effect is just an assumption at present.

A.4 Conclusions

S^{2-} capped $(ZnS)_{0.4}(AgInS_2)_{0.6}$ NCs are shown to be efficient visible-light catalysts for the generation of H_2 from water with Na_2SO_3 and Na_2S as sacrificial hole scavengers. The specific composition of the solid solution NC leads to a suitable electronic band structure for both absorption of visible light and sufficiently negative conduction band minimum for reduction of H^+ to H_2. On the other hand, S^{2-} ion is one of the smallest capping ligand possible for such NCs, and helps the extraction of photogenrated charge carriers from nanocrystals, which is utilized for reduction of H^+ to H_2. Photocatalytic activity for these NCs is 5.0 mmol $g^{-1}h^{-1}$ which is significantly higher than its bulk counterpart (1.1 mmol $g^{-1}h^{-1}$). The higher activity of NCs results mainly from (i) increased density of surface active sites, (ii) easier transport of photo-generated charge carriers from core to the surface of NCs, and (iii) improved water solubility along with reduced visible light scattering. Table-1 shows that our S^{2-} capped $(ZnS)_{0.4}(AgInS_2)_{0.6}$ NC is one of the best visible-light catalyst for H_2 evolution, particularly, for a catalyst that is free from both toxic Cd-compounds and expensive noble metal co-catalyst.

References

1. Zou, Z. G.; Ye, J. H.; Sayama, K.; Arakawa, H. Direct Splitting of Water under Visible Light Irradiation with an Oxide Semiconductor Photocatalyst. *Nature* **2001**, *414*, 625-627.

2. Li, Q.; Guo, B. D.; Yu, J. G.; Ran, J. R.; Zhang, B. H.; Yan, H. J.; Gong, J. R. Highly Efficient Visible-Light-Driven Photocatalytic Hydrogen Production of CdS-Cluster-Decorated Graphene Nanosheets. *J. Am. Chem. Soc*. **2011**, *133,* 10878-10884.

3. Lingampalli, S. R.; Gautam, U. K.; Rao, C. N. R. Highly Efficient Photocatalytic Hydrogen Generation by Solution-Processed ZnO/Pt/CdS, ZnO/Pt/$Cd_{1-x}Zn_xS$ and ZnO/Pt/$CdS_{1-x}Se_x$ Hybrid Nanostructures. *Energy Environ. Sci*. **2013**, *6,* 3589-3594.

4. Wang, J. R.; Osterloh, F. E. Limiting Factors for Photochemical Charge Separation in $BiVO_4/Co_3O_4$, a Highly Active Photocatalyst for Water Oxidation in Sunlight. *J. Mater. Chem. A* **2014**, *2,* 9405-9411.

5. Wu, P.; Wang, J. R.; Zhao, J.; Guo, L. J.; Osterloh, F. E. Structure Defects in g-C_3N_4 Limit Visible Light driven Hydrogen Evolution and Photovoltage. *J. Mater. Chem. A* **2014**, *2,* 20338-20344.

6. Lin, R.; Shen, L. J.; Ren, Z. Y.; Wu, W. M.; Tan, Y. X.; Fu, H. R.; Zhang, J.; Wu, L. Enhanced Photocatalytic Hydrogen Production Activity via Dual Modification of MOF and Reduced Graphene Oxide on CdS. *Chem. Commun.* **2014**, *50,* 8533-8535.

7. Choi, W. Y.; Termin, A.; Hoffmann, M. R. The Role of Metal-Ion Dopants in Quantum-Sized TIO_2 - Correlation Between Photoreactivity and Charge-Carrier Recombination Dynamics. *J. Phys. Chem.* **1994**, *98,* 13669-13679.

8. Kudo, A.; Sekizawa, M. Photocatalytic H_2 Evolution under Visible Light Irradiation on Ni-doped ZnS Photocatalyst. *Chem. Commun.* **2000**, 1371-1372.

9. Kumar, N.; Maitra, U.; Hegde, V. I.; Waghmare, U. V.; Sundaresan, A.; Rao, C. N. R. Synthesis, Characterization, Photocatalysis, and Varied Properties of TiO_2 Cosubstituted with Nitrogen and Fluorine. *Inorg. Chem.* **2013**, *52,* 10512-10519.

10. Tsuji, I.; Kato, H.; Kobayashi, H.; Kudo, A. Photocatalytic H_2 Evolution Reaction from Aqueous Solutions over Band Structure-Controlled $(AgIn)_{(x)}Zn_{2(1-x)}S_2$ Solid Solution Photocatalysts with Visible-Light Response and their Surface Nanostructures. *J. Am. Chem. Soc. **2004**, 126, 13406-13413.*

11. Torimoto, T.; Adachi, T.; Okazaki, K.; Sakuraoka, M.; Shibayama, T.; Ohtani, B.; Kudo, A.; Kuwabata, S. Facile Synthesis of ZnS-$AgInS_2$ Solid Solution Nanoparticles for a Color-Adjustable Luminophore. *J. Am. Chem. Soc.* **2007**, *129,* 12388-12389.

12. Rao, M. J.; Shibata, T.; Chattopadhyay, S.; Nag, A. Origin of Photoluminescence and XAFS Study of $(ZnS)_{(1-x)}(AgInS_2)_{(x)}$ Nanocrystals. *J. Phys. Chem. Lett.* **2014**, *5*, 167-173.

13. Nag, A.; Kovalenko, M. V.; Lee, J. S.; Liu, W. Y.; Spokoyny, B.; Talapin, D. V. Metal-Free Inorganic Ligands for Colloidal Nanocrystals: S^{2-}, HS^-, Se^{2-}, HSe^-, Te^{2-}, HTe^-, TeS_3^{2-}, OH^-, and NH_{2-} as Surface Ligands. *J. Am. Chem. Soc.* **2011,** *133*, 10612−10620.

14. Tsuji, I.; Kato, H.; Kudo, A. Photocatalytic Hydrogen Evolution on ZnS-$CuInS_2$-$AgInS_2$ Solid Solution Photocatalysts with Wide Visible Light Absorption Bands. *Chem. Mat.* **2006**, *18*, 1969-1975.

15. Tsuji, I.; Kato, H.; Kobayashi, H.; Kudo, A. Photocatalytic H_2 Evolution Under Visible-Light Irradiation over Band-Structure-Controlled $(CuIn)_{(x)}Zn_{2(1-x)}S_2$ Solid Solutions. *J. Phys. Chem. B* **2005**, *109*, 7323-7329.

16. Wang, L.; Wang, W.; Shang, M.; Yin, W.; Sun, S.; Zhang, L. Enhanced Photocatalytic Hydrogen Evolution Under Visible Light over $Cd_{1-x}Zn_xS$ Solid Solution with Cubic Zinc Blend Phase. *Int. J. Hydrogen Energy* **2010**, *35*, 19-25.

17. Xu, Y.; Zhao, W. W.; Xu, R.; Shi, Y. M.; Zhang, B. Synthesis of Ultrathin CdS Nanosheets as Efficient Visible-Light-Driven Water Splitting Photocatalysts for Hydrogen Evolution. *Chem. Commun*. **2013**, *49*, 9803-9805.

18. Chang, Z. X.; Zhou, W. H.; Kou, D. X.; Zhoua, Z. J.; Wu, S. X. Phase-Dependent Photocatalytic H_2 Evolution of Copper Zinc Tin Sulfide Under Visible Light. *Chem. Commun.* **2014**, *50*, 12726-12729.

19. Chan, T. L.; Zayak, A. T.; Dalpian, G. M.; Chelikowsky, J. R. Role of Confinement on Diffusion Barriers in Semiconductor Nanocrystals. *Phys. Rev. Lett.* **2009**, *102*.

Report on Thesis,
Outlook and Future Direction

Research content

Group II-VI vs I-III-VI semiconductor nanocrystals (NCs)

Group II-VI based colloidal semiconductor nanocrystals (NCs) are well established system for various applications. However, there are concerns about the toxicity of Cd. In order to surpass this issue, alternatives to II-VI system come into the picture, for example, by replacing two group II cations by one group I cation and group III cation. Such a replacement leads to the formation of I-III-VI type system which exhibit band gap and effective masses of charge carrier similar to that of II-VI semiconductors. I-III-VI type semiconductors are non-toxic in nature. These two types (II-VI and I-III-VI) of NCs exhibit similar PL intensities in polar and non-polar solvents. In difference with II-VI semiconductor NCs, I-III-VI semiconductor NCs exhibit broad photoluminescence (PL) (full width at half maximum (FWHM) ~100 nm) with large (200-300 meV) Stoke's shift and long PL lifetimes. Such large Stoke's shift helps in avoiding non-radiative processes like self-absorption and Forster resonance energy transfer (FRET), which are detrimental for opto-electronic applications.

Opto-electronic properties of Ag and Cu based I-III-VI NCs

In my thesis, we work mainly on Ag based I-III-VI semiconductor NCs which are less explored compared to Cu based semiconductor NCs. Ag based I-III-VI semiconductors exhibit higher band gap than relatively more studied I-III-VI $CuInS_2$ and $CuInSe_2$ semiconductors. For example, bulk $AgInS_2$ exhibit band gap of ~2 eV[1] whereas band gap of bulk $CuInS_2$ and $CuInSe_2$ is 1.5 eV and 1.05 eV, respectively.[2] Therefore, NCs of $AgInS_2$ and alloy of $(ZnS)_x(AgInS_2)_{1-x}$ shows further blue shift in optical band gap with high PL intensity. These NCs can be promising for white light generation and visible light driven photocatalytic water splitting. Therefore, understanding and optimization of photophysics of the colloidal Ag based NCs is essential. However, $AgInS_2$ NCs alone cannot be appropriate for solar cell applications because of its limited absorption of sun light up to ~600 nm and the involvement of mid-gap localized (donor-acceptor (D-A)) states in PL, which may acts as traps for charge carriers.[3] On the other hand, $CuInSe_2$ based NCs can be promising material for sensitized solar cell, though the PL of $CuInSe_2$ NCs is also mediated by the mid-gap localized states along with involvement of delocalized states.[4] In this regard, Oikkonen et al, calculated the energetics of vacancies of Cu and In from hybrid functional calculations and showed that these levels are not located in the mid-gap region apart from one deep acceptor level corresponding to Se vacancy.[5] Other reason for less deep defects is the band gap of bulk

$CuInSe_2$ is small. Thus, $CuInSe_2$ can be a potential material for solar cell. Furthermore, by controlling the stoichiometry of these NCs one can prepare either p-type or n-type materials.[6] The combination of wide band gap Ag based NCs and narrow band gap Cu based NCs might be useful for tandem solar cells for harvesting broad range of light energy.[7]

Methodology development

In order to address the better charge transport from $AgInS_2$ NCs we have prepared organic-free $AgInS_2$ NCs in a direct synthesis. The key point in the synthesis of organic-free $AgInS_2$ NCs is the excess sulphur on the surface of NCs and gives rise to negative charge on the surface, which can provide colloidal stability to these NCs in a polar solvent due to repulsion among negatively charged NCs. Details are given in the 3rd chapter.

In order to absorb wide range of light along with efficient charge separation, we have synthesized Ag_2S-$AgInS_2$ hetero dimer nanocrystals (HDNCs) in a single step using single molecular precursor containing Ag-S, In-S moieties in presence oleylamine. In this reaction condition, Ag_2S nucleates first which allow further the formation of Ag_2S-$AgInS_2$ HDNCs. Details are given in the 4th chapter.

$CuInSe_2$, $(Zn)_{0.24}(CuIn)_{0.76}Se_2$ and $(Zn)_{0.42}(CuIn)_{0.58}Se_2$ NCs have been prepared with a modified procedure which was reported in the prior literature.[8] Details are given in the 5th chapter.

Relevance of the results

In this thesis, we have understood the origin of PL of $AgInS_2$ NCs wherein along with localized D-A states involvement, at least one delocalized state (CB or VB) is also involving in the PL mechanism. Here, our finding is the involvement of delocalized states in the PL of $AgInS_2$ NCs. Such understanding helps the transfer of charge carriers from the I-III-VI NCs to TiO_2 at the interface and which can be responsible for attaining high PCE values in I-III-VI semiconductor NCs based quantum dot sensitized solar cell (QDSSC). First time, we have reported the synthesis of organic-free $AgInS_2$ NCs. QDSSC prepared using organic-free $AgInS_2$ NCs. The lack of organic capping on the surface of the NC improves the charge transfer from NCs to TiO_2. This results in increase of photo conversion efficiency (PCE) values more than 10 times compared with organic capped $AgInS_2$ NCs. Though the synthesis of organic-free $AgInS_2$ NCs was successful, but our lower temperature synthesis leads to significant mid-gap defects in the obtained organic-free $AgInS_2$ NCs. Wide band gap and large defect density of organic-free $AgInS_2$ NCs result in lower PCE values. In order to push

PCE values further high we have prepared Ag_2S-$AgInS_2$ HDNCs in a single step expecting broad absorption of light and efficient charge separation (p-n junction or type-II band alignment at the interface). From CV measurements, the band alignment at the interface is found to be type-I. Interestingly, for the first time we have observed defect related PL having long 13 μs PL lifetime following type-II band alignment from our HDNCs. This long PL lifetime is not arising because of the type-II band alignment at the junction of Ag_2S and $AgInS_2$ rather mid-gap defects are mediating in the separation of electron and hole. Interestingly, this defect mediated electron-hole separation also showed improvement in the PCE of 1.3% from our HDNCs, which is the high value from Ag_2S-$AgInS_2$ HDNCs in the literature. It suggests that defects can help in designing materials with type-II like electron hole separation for solar cell applications. However, still the obtained PCE values from HDNCs are lower due to no photocurrent observed from Ag_2S component of Ag_2S-$AgInS_2$ HDNC. This is due to the conduction band minimum (CBM) of Ag_2S is below than that of CBM of TiO_2. Therefore, we prepared $CuInSe_2$ based NCs with suitable band gap and band alignment for QDSSC. Finally, we have achieved PCE of 3.6% using $(Zn)_{0.24}(CuIn)_{0.76}Se_2$ NCs and low cost Cu_2S as a photo-absorber and counter electrode, respectively. However, the highest PCE of ~11% using $CuInSe_2$ based NCs with expensive Ti mesh supported mesoporous carbon counter electrode has been reported.[8] This thesis deals with the relevance of mid-gap defect states in optical and solar cell applications of colloidal I-III-VI semiconductor NCs.

Future direction

Applications of I-III-VI semiconductor NCs in luminescent solar concentrators

So far the most prominent property from colloidal semiconductor NCs is luminescence. In order to consume more amount of sun-light, large area photovoltaic module is needed. If it is Si based cell then along with large area, thicker films are also required owing to the indirect band gap of Si. Instead of making large area and/or thicker films, one can increase the photovoltaic efficiency with small area photovoltaic cell using luminescent solar concentrators (LSCs) which can reduce the cost of solar energy conversion to electricity.[9] LSC can be obtained by incorporation of luminescent NCs in a polymer or glass wave guide. These NCs collect solar energy by absorption of incident photons. Then, NCs will emit light in wave guide and which directs the light to the edges of wave guide. On these top of the

edges solar cell will be fixed as shown in Figure 1. Due to the high PL intensity with large Stoke's shift, I-III-VI semiconductor NCs such as $AgInS_2$ and $CuInS_2$ based NCs in wave guide can concentrate the emission at the edges of wave guide with less loss in intensity of emitted light. On the other hand, losses are more for II-VI semiconductor NCs because of small Stoke's shift between emission and absorption leading to efficient self-absorption and FRET. It has been shown by Gamelin et al that the incorporation of $CuInS_2$ NCs results into better performance in LSCs than that of CdSe/CdS core/shell NCs.[10]

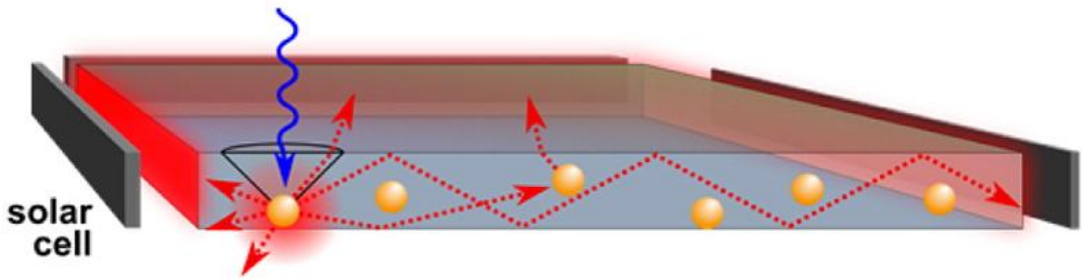

Figure 1: A typical planar LSC configuration in which a luminophore (yellow spheres) is incorporated into a waveguide material surrounded on all edges by solar cells. Figure has been adopted from ref.[11] Copyright 2015, American Chemical Society.

Effect of defects on opto-electronic applications

Emission of I-III-VI NCs at lower energy than optical band gap suggests that involvement of mid-gap defect states in PL decay dynamics. However, these defect states can be either deep or shallow. If defect states are shallow then the effect of such states are less on the performance of opto-electronic properties. But if the defects are deep localized states, then it traps the charge carriers, hindering optoelectronic processes. For example, if in NCs excited electrons are delocalized in CB but holes are getting trapped by deep localized traps, then, access to such holes by an electrolyte is not allowed. As a result holes cannot be refilled by an electrolyte, which leads to decrease in V_{oc} in QDSSC.[12-13] But, the radiative recombination of charge carriers via localized and delocalized states is somewhat good for luminescence based applications. Therefore, it is important to understand the nature of defects. The knowledge of how defects control the optical and opto-electronic properties is crucial to develop efficient devices.

The control over these defect states of I-III-VI semiconductor NCs is still in its infancy. Difference in bond strengths of Ag-S and In-S is believed to form Ag interstitial, Ag vacancy, S vacancy and S interstitial defects. These defects may act as localized trap states and can be located at random positions inside NCs. As a result PL spectrum from the ensemble of these

NCs is broad. One way of reducing the defect density is by controlling the reactivity of Ag (group I metal ion) and In (group III metal ion) towards S^{2-} anion. A better insight about the energies of these defect states can be experimentally obtained by a combination of cyclic voltammetry and single NC spectroscopy of $AgInS_2$ NCs. Of course, computational work is needed to understand the experimental observations.[14] The understanding and control of defects in colloidal I-III-VI semiconductor NCs is the key to achieve efficient optical and opto-electronic applications using these environmentally benign NCs.

References

1. Torimoto, T.; Adachi, T.; Okazaki, K.-i.; Sakuraoka, M.; Shibayama, T.; Ohtani, B.; Kudo, A.; Kuwabata, S. Facile Synthesis of ZnS−$AgInS_2$ Solid Solution Nanoparticles for a Color-Adjustable Luminophore. *J. Am. Chem. Soc.* **2007**, *129*, 12388-12389.

2. Castro, S. L.; Bailey, S. G.; Raffaelle, R. P.; Banger, K. K.; Hepp, A. F. Synthesis and Characterization of Colloidal $CuInS_2$ Nanoparticles from a Molecular Single-Source Precursor. *J. Phys. Chem. B* **2004**, *108*, 12429-12435.

3. Rao, M. J.; Shibata, T.; Chattopadhyay, S.; Nag, A. Origin of Photoluminescence and XAFS Study of $(ZnS)_{1-x}(AgInS_2)_x$ Nanocrystals. *J. Phys. Chem. Lett.* **2014**, *5*, 167-173.

4. Tan, Z.; Zhang, Y.; Xie, C.; Su, H.; Liu, J.; Zhang, C.; Dellas, N.; Mohney, S. E.; Wang, Y.; Wang, J.; Xu, J. Near-Band-Edge Electroluminescence from Heavy-Metal-Free Colloidal Quantum Dots. *Adv. Mater* **2011**, *23*, 3553-3558.

5. Oikkonen, L. E.; Ganchenkova, M. G.; Seitsonen, A. P.; Nieminen, R. M. Vacancies in CuInSe 2 : new insights from hybrid-functional calculations. *J. Phys. Condens. Matter* **2011**, *23*, 422202.

6. Chen, B.; Zhong, H.; Zhang, W.; Tan, Z. a.; Li, Y.; Yu, C.; Zhai, T.; Bando, Y.; Yang, S.; Zou, B. Highly Emissive and Color-Tunable $CuInS_2$-Based Colloidal Semiconductor Nanocrystals: Off-Stoichiometry Effects and Improved Electroluminescence Performance. *Adv. Funct. Mater* **2012**, *22*, 2081-2088.

7. Santra, P. K.; Kamat, P. V. Tandem-Layered Quantum Dot Solar Cells: Tuning the Photovoltaic Response with Luminescent Ternary Cadmium Chalcogenides. *J. Am. Chem. Soc.* **2013**, *135*, 877-885.

8. Du, Z.; Pan, Z.; Fabregat-Santiago, F.; Zhao, K.; Long, D.; Zhang, H.; Zhao, Y.; Zhong, X.; Yu, J.-S.; Bisquert, J. Carbon Counter-Electrode-Based Quantum-Dot-Sensitized Solar Cells with Certified Efficiency Exceeding 11%. *J. Phys. Chem. Lett.* **2016**, *7*, 3103-3111.

9. Erickson, C. S.; Bradshaw, L. R.; McDowall, S.; Gilbertson, J. D.; Gamelin, D. R.; Patrick, D. L. Zero-Reabsorption Doped-Nanocrystal Luminescent Solar Concentrators. *ACS Nano* **2014**, *8*, 3461-3467.

10. Knowles, K. E.; Kilburn, T. B.; Alzate, D. G.; McDowall, S.; Gamelin, D. R. Bright $CuInS_2$/CdS Nanocrystal Phosphors for High-Gain Full-Spectrum Luminescent Solar Concentrators. *Chem. Commun.* **2015**, *51*, 9129-9132.

11. Bradshaw, L. R.; Knowles, K. E.; McDowall, S.; Gamelin, D. R. Nanocrystals for Luminescent Solar Concentrators. *Nano Lett.* **2015**, *15*, 1315-1323.

12. Abdellah, M.; Marschan, R.; Žídek, K.; Messing, M. E.; Abdelwahab, A.; Chábera, P.; Zheng, K.; Pullerits, T. Hole Trapping: The Critical Factor for Quantum Dot Sensitized Solar Cell Performance. *J. Phys. Chem. C* **2014**, *118*, 25802-25808.

13. Zheng, K.; Žídek, K.; Abdellah, M.; Zhang, W.; Chábera, P.; Lenngren, N.; Yartsev, A.; Pullerits, T. Ultrafast Charge Transfer from CdSe Quantum Dots to p-Type NiO: Hole Injection vs Hole Trapping. *J. Phys. Chem. C* **2014**, *118*, 18462-18471.

14. Sandroni, M.; Wegner, K. D.; Aldakov, D.; Reiss, P. Prospects of Chalcopyrite-Type Nanocrystals for Energy Applications. *ACS Energy Lett.* **2017**, *2*, 1076-1088.

List of Publications

Included in thesis

1. **Rao, M. J.**; Shibata, T.; Chattopadhyay, S.; Nag, A. Origin of Photoluminescence and XAFS Study of $(ZnS)_{1-x}(AgInS_2)_x$ Nanocrystals. *J. Phys. Chem. Lett.* **2014,** *5*, 167-173.
2. **Rao, M. J.**; Kadlag, K. P.; Nag, A. Ligand-Free, Colloidal, and Luminescent Metal Sulfide Nanocrystals. *J. Phys. Chem. Lett.* **2013,** *4*, 1676-1681.
3. Kadlag, K. P.; Patil, P.; **Rao, M. J.**; Datta, S.; Nag, A. Luminescence and Solar Cell from Ligand-Free Colloidal $AgInS_2$ Nanocrystals. *CrystEngComm.* **2014,** *16* , 3605-3612.
4. **Jagadeeswararao, M.**; Swarnakar, A.; Markad, G.B.; Nag, A. Defect-Mediated Electron Hole Separation in Colloidal Ag_2S-$AgInS_2$ Hetero Dimer Nanocrystals Tailoring Luminescence and Solar Cell Properties. *J. phys. Chem. C*, **2016**, *120*, 19461-19469.
5. **Jagadeeswararao, M.**; Dey, S.; Nag, A.; Rao, C. N. R. Visible Light-Induced Hydrogen Generation using Colloidal $(ZnS)_{0.4}(AgInS_2)_{0.6}$ Nanocrystals Capped by S^{2-} ions. *J. Mater.Chem. A* **2015,** *3*, 8276-8279.

Not included in thesis

6. **Jagadeeswararao, M.**;Pal, S.; Nag, A.; Sarma, D.D. Electrical and Plasmonic Properties of Ligand-Free Sn^{4+}-Doped In_2O_3 (ITO) Nanocrystals. *ChemPhysChem* **2016**, *17*, 710.
7. Mir, W. J.; **Jagadeeswararao, M.**; Das, S.; Nag, A.; Colloidal Mn-Doped Cesium Lead Halide Perovskite Nanoplatelets. *ACS Energy Lett*. **2017**, 2, 537-543.
8. Shanker G. S.; Markad, G. B.; **Jagadeeswararao, M.**; Bansode, U.; Nag, A.; Colloidal Nanocomposite TiN and N-doped Few-Layer Graphene for Plasmonics and Electrocatalysis. *ACS Energy Lett.*, 2017, *2*, 2251–2256.

Title: Semiconductor Nanocrystals: Structure, Properties, and Band Gap Engineering

Author: Andrew M. Smith, Shuming Nie

Publication: Accounts of Chemical Research

Publisher: American Chemical Society

Date: Feb 1, 2010

PERMISSION/LICENSE IS GRANTED FOR YOUR ORDER AT NO CHARGE

This type of permission/license, instead of the standard Terms & Conditions, is sent to you because no fee is being charged for your order. Please note the following:

- Permission is granted for your request in both print and electronic formats, and translations.
- If figures and/or tables were requested, they may be adapted or used in part.
- Please print this page for your records and send a copy of it to your publisher/graduate school.
- Appropriate credit for the requested material should be given as follows: "Reprinted (adapted) with permission from (COMPLETE REFERENCE CITATION). Copyright (YEAR) American Chemical Society." Insert appropriate information in place of the capitalized words.
- One-time permission is granted only for the use specified in your request. No additional uses are granted (such as derivative works or other editions). For any other uses, please submit a new request.

If credit is given to another source for the material you requested, permission must be obtained from that source.

Title: Composition-Tunable Alloyed Semiconductor Nanocrystals

Author: Michelle D. Regulacio, Ming-Yong Han

Publication: Accounts of Chemical Research

Publisher: American Chemical Society

Date: May 1, 2010

PERMISSION/LICENSE IS GRANTED FOR YOUR ORDER AT NO CHARGE

This type of permission/license, instead of the standard Terms & Conditions, is sent to you because no fee is being charged for your order. Please note the following:

- Permission is granted for your request in both print and electronic formats, and translations.
- If figures and/or tables were requested, they may be adapted or used in part.
- Please print this page for your records and send a copy of it to your publisher/graduate school.
- Appropriate credit for the requested material should be given as follows: "Reprinted (adapted) with permission from (COMPLETE REFERENCE CITATION). Copyright (YEAR) American Chemical Society." Insert appropriate information in place of the capitalized words.
- One-time permission is granted only for the use specified in your request. No additional uses are granted (such as derivative works or other editions). For any other uses, please submit a new request.

If credit is given to another source for the material you requested, permission must be obtained from that source.

Title: Composition-Tunable ZnxCd1-xSe Nanocrystals with High Luminescence and Stability

Author: Xinhua Zhong, Mingyong Han, Zhili Dong, et al

Publication: Journal of the American Chemical Society

Publisher: American Chemical Society

Date: Jul 1, 2003

PERMISSION/LICENSE IS GRANTED FOR YOUR ORDER AT NO CHARGE

This type of permission/license, instead of the standard Terms & Conditions, is sent to you because no fee is being charged for your order. Please note the following:

- Permission is granted for your request in both print and electronic formats, and translations.
- If figures and/or tables were requested, they may be adapted or used in part.
- Please print this page for your records and send a copy of it to your publisher/graduate school.
- Appropriate credit for the requested material should be given as follows: "Reprinted (adapted) with permission from (COMPLETE REFERENCE CITATION). Copyright (YEAR) American Chemical Society." Insert appropriate information in place of the capitalized words.
- One-time permission is granted only for the use specified in your request. No additional uses are granted (such as derivative works or other editions). For any other uses, please submit a new request.

If credit is given to another source for the material you requested, permission must be obtained from that source.

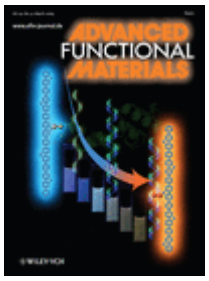

Title:	Highly Emissive and Color-Tunable CuInS2-Based Colloidal Semiconductor Nanocrystals: Off-Stoichiometry Effects and Improved Electroluminescence Performance
Author:	Bingkun Chen,Haizheng Zhong,Wenqing Zhang,Zhan\'ao Tan,Yongfang Li,Cairan Yu,Tianyou Zhai,Yoshio Bando,Shengyi Yang,Bingsuo Zou
Publication:	Advanced Functional Materials
Publisher:	John Wiley and Sons
Date:	Mar 2, 2012

Order Completed

Thank you for your order.

This Agreement between Jagadeeswararao Metikoti ("You") and John Wiley and Sons ("John Wiley and Sons") consists of your license details and the terms and conditions provided by John Wiley and Sons and Copyright Clearance Center.

Your confirmation email will contain your order number for future reference.

Printable details.

License Number	4175780799053
License date	Aug 25, 2017
Licensed Content Publisher	John Wiley and Sons
Licensed Content Publication	Advanced Functional Materials
Licensed Content Title	Highly Emissive and Color-Tunable CuInS2-Based Colloidal Semiconductor Nanocrystals: Off-Stoichiometry Effects and Improved Electroluminescence Performance
Licensed Content Author	Bingkun Chen,Haizheng Zhong,Wenqing Zhang,Zhan\'ao Tan,Yongfang Li,Cairan Yu,Tianyou Zhai,Yoshio Bando,Shengyi Yang,Bingsuo Zou
Licensed Content Date	Mar 2, 2012
Licensed Content Pages	8
Type of use	Dissertation/Thesis
Requestor type	University/Academic
Format	Print and electronic
Portion	Figure/table
Number of figures/tables	1
Original Wiley figure/table number(s)	1
Will you be translating?	Yes, including English rights
Number of languages	1
Languages	English
Title of your thesis / dissertation	Defect Manipulation in I-III-VI Metal Chalcogenide Semiconductor Nanocrystals for Luminescence and Solar Energy Applications
Expected completion date	Jan 2018
Expected size (number of pages)	120
Requestor Location	Jagadeeswararao Metikoti IISER Pune Pashan New hostel-2 Pune, 411008

	India Attn: Jagadeeswararao Metikoti
Publisher Tax ID	EU826007151
Billing Type	Invoice
Billing address	Jagadeeswararao Metikoti IISER Pune Pashan New hostel-2 Pune, India 411008 Attn: Jagadeeswararao Metikoti
Total	0.00 USD

Would you like to purchase the full text of this article? If so, please continue on to the content ordering system located here: Purchase PDF

If you click on the buttons below or close this window, you will not be able to return to the content ordering system.

ORDER MORE CLOSE WINDOW

Title: A Simple Route for Highly Luminescent Quaternary Cu-Zn-In-S Nanocrystal Emitters

Author: Jie Zhang, Renguo Xie, Wensheng Yang

Publication: Chemistry of Materials

Publisher: American Chemical Society

Date: Jul 1, 2011

PERMISSION/LICENSE IS GRANTED FOR YOUR ORDER AT NO CHARGE

This type of permission/license, instead of the standard Terms & Conditions, is sent to you because no fee is being charged for your order. Please note the following:

- Permission is granted for your request in both print and electronic formats, and translations.
- If figures and/or tables were requested, they may be adapted or used in part.
- Please print this page for your records and send a copy of it to your publisher/graduate school.
- Appropriate credit for the requested material should be given as follows: "Reprinted (adapted) with permission from (COMPLETE REFERENCE CITATION). Copyright (YEAR) American Chemical Society." Insert appropriate information in place of the capitalized words.
- One-time permission is granted only for the use specified in your request. No additional uses are granted (such as derivative works or other editions). For any other uses, please submit a new request.

If credit is given to another source for the material you requested, permission must be obtained from that source.

Title: Advances in Light-Emitting Doped Semiconductor Nanocrystals

Author: Narayan Pradhan, D. D. Sarma

Publication: Journal of Physical Chemistry Letters

Publisher: American Chemical Society

Date: Nov 1, 2011

PERMISSION/LICENSE IS GRANTED FOR YOUR ORDER AT NO CHARGE

This type of permission/license, instead of the standard Terms & Conditions, is sent to you because no fee is being charged for your order. Please note the following:

- Permission is granted for your request in both print and electronic formats, and translations.
- If figures and/or tables were requested, they may be adapted or used in part.
- Please print this page for your records and send a copy of it to your publisher/graduate school.
- Appropriate credit for the requested material should be given as follows: "Reprinted (adapted) with permission from (COMPLETE REFERENCE CITATION). Copyright (YEAR) American Chemical Society." Insert appropriate information in place of the capitalized words.
- One-time permission is granted only for the use specified in your request. No additional uses are granted (such as derivative works or other editions). For any other uses, please submit a new request.

If credit is given to another source for the material you requested, permission must be obtained from that source.

Title: Cu–In Halide Perovskite Solar Absorbers

Author: Xin-Gang Zhao, Dongwen Yang, Yuanhui Sun, et al

Publication: Journal of the American Chemical Society

Publisher: American Chemical Society

Date: May 1, 2017

PERMISSION/LICENSE IS GRANTED FOR YOUR ORDER AT NO CHARGE

This type of permission/license, instead of the standard Terms & Conditions, is sent to you because no fee is being charged for your order. Please note the following:

- Permission is granted for your request in both print and electronic formats, and translations.
- If figures and/or tables were requested, they may be adapted or used in part.
- Please print this page for your records and send a copy of it to your publisher/graduate school.
- Appropriate credit for the requested material should be given as follows: "Reprinted (adapted) with permission from (COMPLETE REFERENCE CITATION). Copyright (YEAR) American Chemical Society." Insert appropriate information in place of the capitalized words.
- One-time permission is granted only for the use specified in your request. No additional uses are granted (such as derivative works or other editions). For any other uses, please submit a new request.

If credit is given to another source for the material you requested, permission must be obtained from that source.

Title: Quantum Dot Solar Cells. The Next Big Thing in Photovoltaics
Author: Prashant V. Kamat
Publication: Journal of Physical Chemistry Letters
Publisher: American Chemical Society
Date: Mar 1, 2013

PERMISSION/LICENSE IS GRANTED FOR YOUR ORDER AT NO CHARGE

This type of permission/license, instead of the standard Terms & Conditions, is sent to you because no fee is being charged for your order. Please note the following:

- Permission is granted for your request in both print and electronic formats, and translations.
- If figures and/or tables were requested, they may be adapted or used in part.
- Please print this page for your records and send a copy of it to your publisher/graduate school.
- Appropriate credit for the requested material should be given as follows: "Reprinted (adapted) with permission from (COMPLETE REFERENCE CITATION). Copyright (YEAR) American Chemical Society." Insert appropriate information in place of the capitalized words.
- One-time permission is granted only for the use specified in your request. No additional uses are granted (such as derivative works or other editions). For any other uses, please submit a new request.

If credit is given to another source for the material you requested, permission must be obtained from that source.

Title: Colloidal Nanocrystals with Molecular Metal Chalcogenide Surface Ligands

Author: Maksym V. Kovalenko,Marcus Scheele,Dmitri V. Talapin

Publication: Science

Publisher: The American Association for the Advancement of Science

Date: Jun 12, 2009

Order Completed

Thank you for your order.

This Agreement between Jagadeeswararao Metikoti ("You") and The American Association for the Advancement of Science ("The American Association for the Advancement of Science") consists of your license details and the terms and conditions provided by The American Association for the Advancement of Science and Copyright Clearance Center.

Your confirmation email will contain your order number for future reference.

Printable details.

License Number	4176551299577
License date	Aug 26, 2017
Licensed Content Publisher	The American Association for the Advancement of Science
Licensed Content Publication	Science
Licensed Content Title	Colloidal Nanocrystals with Molecular Metal Chalcogenide Surface Ligands
Licensed Content Author	Maksym V. Kovalenko,Marcus Scheele,Dmitri V. Talapin
Licensed Content Date	Jun 12, 2009
Licensed Content Volume	324
Licensed Content Issue	5933
Volume number	324
Issue number	5933
Type of Use	Thesis / Dissertation
Requestor type	Scientist/individual at a research institution
Format	Print and electronic
Portion	Figure
Number of figures/tables	1
Order reference number	
Title of your thesis / dissertation	Defect Manipulation in I-III-VI Metal Chalcogenide Semiconductor Nanocrystals for Luminescence and Solar Energy Applications
Expected completion date	Jan 2018
Estimated size(pages)	120
Requestor Location	Jagadeeswararao Metikoti IISER Pune Pashan New hostel-2 Pune, 411008 India Attn: Jagadeeswararao Metikoti
Billing Type	Invoice
Billing address	Jagadeeswararao Metikoti IISER Pune Pashan New hostel-2

Pune, India 411008
Attn: Jagadeeswararao Metikoti

Total 0.00 USD

ORDER MORE CLOSE WINDOW

Title:	Metal-free Inorganic Ligands for Colloidal Nanocrystals: S2–, HS–, Se2–, HSe–, Te2–, HTe–, TeS32–, OH–, and NH2– as Surface Ligands
Author:	Angshuman Nag, Maksym V. Kovalenko, Jong-Soo Lee, et al
Publication:	Journal of the American Chemical Society
Publisher:	American Chemical Society
Date:	Jul 1, 2011

PERMISSION/LICENSE IS GRANTED FOR YOUR ORDER AT NO CHARGE

This type of permission/license, instead of the standard Terms & Conditions, is sent to you because no fee is being charged for your order. Please note the following:

- Permission is granted for your request in both print and electronic formats, and translations.
- If figures and/or tables were requested, they may be adapted or used in part.
- Please print this page for your records and send a copy of it to your publisher/graduate school.
- Appropriate credit for the requested material should be given as follows: "Reprinted (adapted) with permission from (COMPLETE REFERENCE CITATION). Copyright (YEAR) American Chemical Society." Insert appropriate information in place of the capitalized words.
- One-time permission is granted only for the use specified in your request. No additional uses are granted (such as derivative works or other editions). For any other uses, please submit a new request.

If credit is given to another source for the material you requested, permission must be obtained from that source.

Title:	Origin of Photoluminescence and XAFS Study of (ZnS)1−x(AgInS2)x Nanocrystals
Author:	M. Jagadeeswara Rao, Tomohiro Shibata, Soma Chattopadhyay, et al
Publication:	Journal of Physical Chemistry Letters
Publisher:	American Chemical Society
Date:	Jan 1, 2014

PERMISSION/LICENSE IS GRANTED FOR YOUR ORDER AT NO CHARGE

This type of permission/license, instead of the standard Terms & Conditions, is sent to you because no fee is being charged for your order. Please note the following:

- Permission is granted for your request in both print and electronic formats, and translations.
- If figures and/or tables were requested, they may be adapted or used in part.
- Please print this page for your records and send a copy of it to your publisher/graduate school.
- Appropriate credit for the requested material should be given as follows: "Reprinted (adapted) with permission from (COMPLETE REFERENCE CITATION). Copyright (YEAR) American Chemical Society." Insert appropriate information in place of the capitalized words.
- One-time permission is granted only for the use specified in your request. No additional uses are granted (such as derivative works or other editions). For any other uses, please submit a new request.

Title:	Ligand-Free, Colloidal, and Luminescent Metal Sulfide Nanocrystals
Author:	Kiran P. Kadlag, M. Jagadeeswara Rao, Angshuman Nag
Publication:	Journal of Physical Chemistry Letters
Publisher:	American Chemical Society
Date:	May 1, 2013

PERMISSION/LICENSE IS GRANTED FOR YOUR ORDER AT NO CHARGE

This type of permission/license, instead of the standard Terms & Conditions, is sent to you because no fee is being charged for your order. Please note the following:

- Permission is granted for your request in both print and electronic formats, and translations.
- If figures and/or tables were requested, they may be adapted or used in part.
- Please print this page for your records and send a copy of it to your publisher/graduate school.
- Appropriate credit for the requested material should be given as follows: "Reprinted (adapted) with permission from (COMPLETE REFERENCE CITATION). Copyright (YEAR) American Chemical Society." Insert appropriate information in place of the capitalized words.
- One-time permission is granted only for the use specified in your request. No additional uses are granted (such as derivative works or other editions). For any other uses, please submit a new request.

Title: Defect-Mediated Electron–Hole Separation in Colloidal Ag2S–AgInS2 Hetero Dimer Nanocrystals Tailoring Luminescence and Solar Cell Properties

Author: Metikoti Jagadeeswararao, Abhishek Swarnkar, Ganesh B. Markad, et al

Publication: The Journal of Physical Chemistry C

Publisher: American Chemical Society

Date: Sep 1, 2016

PERMISSION/LICENSE IS GRANTED FOR YOUR ORDER AT NO CHARGE

This type of permission/license, instead of the standard Terms & Conditions, is sent to you because no fee is being charged for your order. Please note the following:

- Permission is granted for your request in both print and electronic formats, and translations.
- If figures and/or tables were requested, they may be adapted or used in part.
- Please print this page for your records and send a copy of it to your publisher/graduate school.
- Appropriate credit for the requested material should be given as follows: "Reprinted (adapted) with permission from (COMPLETE REFERENCE CITATION). Copyright (YEAR) American Chemical Society." Insert appropriate information in place of the capitalized words.
- One-time permission is granted only for the use specified in your request. No additional uses are granted (such as derivative works or other editions). For any other uses, please submit a new request.

Title: Nanocrystals for Luminescent Solar Concentrators

Author: Liam R. Bradshaw, Kathryn E. Knowles, Stephen McDowall, et al

Publication: Nano Letters

Publisher: American Chemical Society

Date: Feb 1, 2015

PERMISSION/LICENSE IS GRANTED FOR YOUR ORDER AT NO CHARGE

This type of permission/license, instead of the standard Terms & Conditions, is sent to you because no fee is being charged for your order. Please note the following:

- Permission is granted for your request in both print and electronic formats, and translations.
- If figures and/or tables were requested, they may be adapted or used in part.
- Please print this page for your records and send a copy of it to your publisher/graduate school.
- Appropriate credit for the requested material should be given as follows: "Reprinted (adapted) with permission from (COMPLETE REFERENCE CITATION). Copyright (YEAR) American Chemical Society." Insert appropriate information in place of the capitalized words.
- One-time permission is granted only for the use specified in your request. No additional uses are granted (such as derivative works or other editions). For any other uses, please submit a new request.

If credit is given to another source for the material you requested, permission must be obtained from that source.

BACK CLOSE WINDOW